Dissertation zur Erlangung des Doktorgrades

der Fakultät für Chemie und Pharmazie

der Ludwig-Maximilians-Universität München

Solvothermal *tert*-butanol syntheses of electrochemically active multinary metal oxide nanomorphologies

Peter Markus Zehetmaier

aus

Ebersberg, Deutschland

2019

Erklärung

Diese Dissertation wurde im Sinne von § 7 der Promotionsordnung vom 28. November 2011 von Frau Prof. Dr. Dina Fattakhova-Rohlfing betreut.

Eidesstattliche Versicherung

Diese Dissertation wurde eigenständig und ohne unerlaubte Hilfe erarbeitet.

München, 14.02.2019

Peter Markus Zehetmaier

Dissertation eingereicht am 22.02.2019

1. Gutachterin: Prof. Dr. Dina Fattakhova-Rohlfing

2. Gutachter: Prof. Dr. Thomas Bein

Mündliche Prüfung am 22.03.2019

Danksagung

Am Anfang will ich hier ein bisschen weißes Papier mit dem füllen, was meiner Meinung nach das Wichtigste nach Beendigung beschwerlicher Arbeit ist, nämlich Dankesworte. Dankesworte für all die einzigartigen Menschen, welche mir auf meiner Reise zur Promotion begegnet sind und mich inspiriert haben, welche mich begleitet und damit den Weg angenehmer gestaltet haben und welche mir tatkräftig geholfen haben.

Einer Person, die all die genannten Sachen erfüllt hat und noch viel mehr, will ich als erstes innigst danken: Meiner Doktormutter Prof. Dina Fattakhova-Rohlfing. Sie hat nicht nur früh Potential in mir gesehen und mich gefördert, in dem sie mir eine HIWI-Stelle und eine Masterarbeit angeboten hat, sondern hat mir schlussendlich auch noch ermöglicht die Forschung im Themenfeld der Energiespeicherung durch eine Doktorarbeit bei ihr zu intensivieren. Durch ihre elektrochemische Expertise, die sie mir vermittelt hat, ihre unermüdliche Unterstützung in allen Projekten und ihre Geduld mit meinem Schreibstil hat sie so viel dazu beigetragen, dass die Arbeit erfolgreich zum Abschluss gebracht wurde. Durch ihre Hilfe konnte ich auch die Projekte mehrfach bei internationalen Konferenzen interessierten Fachpublikum vorstellen.

Prof. Thomas Bein als meinem Zweitbetreuer möchte ich aus ganzem Herzen für die freundliche Aufnahme in die Gruppe danken und, dass er mir ermöglicht hat seine Labore und vor allem den beachtlichen Gerätefuhrpark für Analysen mitzubenutzen. Auch für seine steten fachlichen Anregungen im Rahmen der Group- und Subgroupmeetings und das Erstellen des Zweitgutachtens für diese Arbeit sei ihm recht herzlich gedankt.

Desweiteren möchte ich Hans danken, der mir immer ein guter Mentor war, der mir immer mit Rat und Tat zur Seite stand und mit dem ich zusammen erfolgreich das erste Projekt beenden konnte. In diesem Zusammenhang möchte ich auch Halina herzlich danken, einerseits für die Expertise, die sie in das erste Projekt eingebracht hat, als auch für ihren immerwährenden

Optimismus und ihre Gute Laune, welche sie auch nach dem Verlassen der Gruppe immer wieder bei Feiern versprüht hat. Krissi danke ich nicht nur, dass sie mir jahrelang als Bürokollegin den Rücken gestärkt hat, sondern auch für die erfolgreiche Zusammenarbeit im ATO Projekt. Hierzu hat auch Flozi sehr viel zum Gelingen beigetragen und ich bin glücklich, dass er die Tage von mir als Batterieeinzelgänger beendet hat und seit dem die Wege der Batterieforschung mit mir gemeinsam geht. Auch bin ich sehr glücklich, dass ich bei den vielen Fragestellungen, die sich bei den Projekten ergaben, nie lange suchen musste um geeignete Experten dafür zu finden. In allen Fragen, die TEM betrafen, war Markus immer ein williger und fundierter Ansprechpartner, aber auch Alex M. von der Gruppe von Prof. Scheu, Andi W. und Michi waren mir eine große Hilfe. Michi dank ich speziell auch für sein Können meine teils wirren Ideen in graphisch ansprechende Abbildungen zu überführen. Krissi und Wascht bin ich sehr dankbar für ihre exzellenten SEM Bilder, die sie von meinen Materialien gemacht haben. Patrick und vor allem Berni von Prof. Wintterlins Gruppe danke ich für die Mühe, die sie sich mit den XPS Spektren meiner Proben gemacht haben. Sabrina und Tina danke ich für das Messen von TGA und Sorption und Tina zusätzlich zusammen mit Regina und später Corinna, dass sie für mich gegen die Bürokratie und für die Ordnung gekämpft haben. Alesja dank ich noch, dass sie ihr Rezept für eine erfolgreiche NCC Synthese mit mir geteilt hat.

Ein riesig großer Dank gilt meinen Studenten (Erol, Arnaud, Pamina, Max, Franzi und Ceren), die mich unglaublich in meiner Forschungsarbeit unterstützt haben, bei deren Betreuung ich persönlich unglaublich gereift bin und die hoffentlich auch, nicht nur fachliches, für ihr Leben von mir gelernt haben. Ich bin froh, dass aus einigen später auch großartige Freunde wurden. Ein sehr großer Dank gilt allen meinen Kollegen im AK Bein ohne die die Promotionszeit wahrscheinlich nur halb so erträglich gewesen wäre. Wir haben legendäre Grill-, Weihnachts- und Verteildigungsfeiern miteinander verbracht. Da sich über die Jahre fast die ganze

Kollegenschar einmal komplett ausgetauscht hat, will ich nur exemplarisch dafür meinen Bürokollegen danken, die am meisten unter meinem baierischen Grant leiden mussten, aber auch immer Motivationssongs für mich gespielt haben (z.B. Queen oder Boilerroom): Ksenia, DannyB, Johannes (Beppi), Krissi, Flozi, Ceren, ChrisK, AndiJ, FloG, Sharath und Berninghard. Meiner Water Splitting Subgroup (Benni, Alesja, Dina, Markus, David, Ksenia, Krissi, Beppi, Ceren, Flozi, ChrisK, DannyB, AGH aka Hufi, Joni, Michi, Schuster, Waschtal) danke ich, dass wir Carlos in gemeinsamer Leistung befreien konnten und endlich mal zeigen konnten, dass wir nicht nur wissenschaftlich uns gegen die anderen Subgroups behaupten können, auch, wenn wir in den letzten Jahren an Multinationalität und Frauenanteil Einbußen hinnehmen mussten. Es wär noch so vielen Menschen zu danken, dem Jazz-Trio, den Radler-Boyz, den Perovschikas, meinen unermüdlichen Korrekturlesern (AndiJ, Noggi, Niklas, Flozi, DannyB), den Tappern, meiner App-unterstützten Sportgruppe, den Meso-Bios, den Fruit-Sharern, den Couch-Surfern, der Augustiner-Crew, der Bio-Mensa Gruppe, der Klinikumskasinogruppe und so vielen weiteren, aber irgendwann sollte man Schluß machen.

Last, but not least geht der größte Dank an die wichtigsten Menschen: meiner Familie. Meinen Nichten und Neffen dank ich fürs gemeinsam rumtollen, meinen Geschwistern besonders für die Fahrbereitschaft während Studium und Promotion und meinen Eltern für ihre Geduld, Verständnis und ständige Hilfsbereitschaft. Ein ganz besonder Dank gilt meinem Neffen Lorenz, er war der tägliche Sonnenschein während der strapazierenden Phase des Zusammenschreibens.

Danke

Abstract

This thesis deals with the synthesis of nanomaterials for electrochemical energy conversion and storage, with a special focus on materials for battery applications. Nanostructuring and nanoscaling are proven efficient means to enhance, and sometimes even to enable, the performance of electroactive materials. Processes involving transfer and transport of charges, which is the core of any electrochemical phenomena, greatly benefit from the increased surface areas and shortened diffusion pathways in nanomaterials.

Our group has focused for several years on exploring the electrochemical properties of extremely small metal oxide nanocrystals with a particle size down to 1-3 nm. To achieve this size range, our group has developed a novel synthesis approach based on solvothermal reactions in *tert*-butanol acting both as a solvent and a reactant. The *tert*-butanol route has demonstrated unique possibilities compared to other synthesis approaches, including other types of solvothermal reactions. One of the specific features of this process is an extremely small particles size that can be achieved; crystallinity; the dispersibility of nanoparticles in different solvents without additional surface stabilization; and the formation of metastable and non-stoichiometric phases, which could be attributed to the kinetic control of the reaction process. These features made the nanoparticles obtained *via* the *tert*-butanol route promising building blocks for low-temperature bottom-up syntheses of porous nanomaterials via surfactant-templated evaporation-induced self-assembly. Using the *tert*-butanol approach, numerous metal oxide compositions have been prepared so far, including binary oxides such as TiO_2, NiO, SnO_2 and FeOOH, doped oxides such as Nb-doped TiO_2, Fe-doped NiO, Sb-doped SnO_2 and doped FeOOH, and mixed and ternary oxides such as Co/NiO and $Li_4Ti_5O_{12}$ (LTO). The nanoparticles obtained *via* the *tert*-butanol approach and the nanomorphologies assembled have demonstrated strongly enhanced performance in dye-sensitized solar cells and electrocatalytic and photoelectrochemical water splitting, and the nanostructured LTO has shown record charging rates when used as an anode in lithium ion batteries (LIBs). The suitability of the *tert*-butanol route for the fabrication of cathode materials in LIBs has been however so far not been investigated, so it was one of the motivations of this work. Further unexplored challenges to investigate were the possibility of fabricating more complex chemical compositions such as multinary oxides, which are of importance for the

battery applications, and even more complex structures such as hybrid materials using the *tert*-butanol approach.

This thesis is mainly focussed on the extension of the solvothermal *tert*-butanol syntheses route for metal oxide nanoparticles towards multinary functional materials up to pseudo-quaternary oxides. Furthermore, the nanocrystals produced in this way are successfully assembled into nanocomposites and nanostructures, respectively, and embedded into devices with improved performance in photoelectrochemical water splitting and in particular as electrodes in LIBs. One special focus was on the synthesis of LIB cathode materials, which could be achieved for the first time with the *tert*-butanol solvothermal synthesis.

Chapter 1 introduces the principles of LIBs, the solvothermal nanoparticle synthesis and the relevant approaches towards nanostructures or compounds are depicted. Furthermore, it provides a short overview of the properties of the materials synthesized in this thesis. The basic principles of the techniques to characterize the morphology, the structure, the composition and the electrochemical behavior of the nanomaterials are described in Chapter 2.

In Chapter 3 the solvothermal synthesis in *tert*-butanol of crystalline, non-agglomerated nanoparticles of the binary material Co_3O_4 is described. The properties of the Co_3O_4 nanocrystals within the size range of 3-7 nm are investigated, and they are later implemented in devices for photo-driven water splitting. Due to the very small size of the nanoparticles and their high dispersibility, a homogenous deposition of the nanocrystals on mesoporous hematite layers is achieved. While the hematite acts as the photoactive absorber in the light-induced water splitting reaction, the Co_3O_4 nanoparticles are applied as co-catalysts. This surface treatment results in a distinct increase in photocurrent. The mechanisms involved are revealed by photoelectrochemical as well as transient absorption spectroscopy studies. The high performance is enabled as the Co_3O_4 nanoparticles help to suppress the surface electron-hole recombination on time scales of milliseconds to seconds.

Pseudo-binary oxide nanoparticles are produced within the tin oxide system by implementation of an additional metal, here antimony. The tin oxide and antimony-doped tin oxide (ATO) are synthesized in a microwave-assisted synthesis in *tert*-butanol in the presence of graphene oxide nanosheets to form nanocomposites where the ultrasmall metal oxide nanocrystals are anchored on the surface of reduced graphene oxide (rGO) sheets. These composite materials exhibit high

electrical conductivity and a high structural stability during lithium incorporation which makes them, in particular the ATO, novel high capacity anode materials for LIBs. The greatest advantage of the ATO/rGO nanocomposite in comparison to tin oxide or ATO bulk material is the efficient buffering of the volume changes associated with the electrochemical processes during charging/discharging. Here, a reversible high capacity of 577 mAh g^{-1} charging/discharging within one minute could be achieved. The syntheses of the nanocomposites as well as the electrochemical testing are described in Chapter 4.

In Chapters 5 and 6, the *tert*-butanol solvothermal synthesis of lithium containing multinary oxides as precursors for nanostructured cathode materials for LIBs is shown for the first time. Chapter 5 is focused on the syntheses of two different pseudo-binary metal oxide nanoparticles of the lithium cobalt system. In a first step ultrasmall nanocrystals of cubic rock-salt type $Li_{0.15}Co_{0.85}O$ are produced in *tert*-butanol. These nanoparticles themselves are not suitable as an effective cathode material in LIBs, but can be later transformed into high-performance nanostructured $LiCoO_2$ using block-copolymers as surfactant. Due to the nanostructuring, over 50% of the theoretical specific capacity can still be achieved even at extremely shortcharge/discharge times of 72 s.

In Chapter 6, the pseudo-binary lithium cobalt system is expanded to the pseudo-quaternary system of $Li_wNi_xCo_yMn_zO$. Herein, for the first time four different metals could be homogeneously integrated in ultrasmall metal oxide nanoparticles with 1-4 nm in size by the *tert*-butanol solvothermal synthesis route. Moreover, four different compositions in this system are deliberately synthesized, all adopting the cubic rock-salt structure. In a second step, the biotemplate nanocrystalline cellulose is used to create desert-rose structured $Li(Ni_xCo_yMn_z)O_2$ with fixed transition metal ratios. Although the synthesis approach *via* the rock-salt type nanoparticles favors the cation mixing between lithium and nickel and therefore drastically reduces the specific capacities achievable, the desert-rose structure shows promising stability for high power applications.

In summary, the *tert*-butanol route was significantly extended to produce different multinary metal oxide particles. These particles were then used either in compounds or together with surfactants to produce nanostructured materials for different applications, mainly as electrode materials in lithium ion batteries. These nanoparticles often showed significantly improved

performance, especially at high rate operations as compared to the materials reported in the literature.

Table of contents

1 Introduction

1.1 Lithium Ion Batteries (LIBs)

1.1.1 Principles of Battery Technology

A rapidly growing market of consumer electronic devices and electrical vehicles as well as the need for intermittent energy storage in smart grids demand the development of electrochemical energy storage technologies providing high storage capacity, high power density, long life-time and at the same time low production and operation costs.

In general, one distinguishes two major types of electrochemical energy storage devices, namely supercapacitors and batteries. Both types of devices consist of one or more electrically connected electrochemical cells, which typically consists of a negative and positive electrode, an electrolyte and a separator; they differ however in the basic mechanisms of energy storage. Supercapacitors store electrical energy in a form of electrostatic energy in a so called electrical double layer, which is built spontaneously on an interface of a solid charged electrode and the oppositely charged ions in an electrolyte. Due to a pure electrostatic nature of interactions and the absence of chemical transformations, the supercapacitors demonstrate very high power densities and can be reversibly charged and discharged for many thousands of cycles without deterioration. The energy is however stored only at the surface of the electrode and is therefore limited by the electrode surface area, which results in relatively low energy densities.[1, 2]

Batteries are a broad definition of electrochemical energy storage devices that store electrical energy in form of chemical energy (redox transformations of active materials on the electrodes). Primary batteries involve irreversible chemical transformations, so that the battery is discarded after the electrochemical reaction stops and no further energy supply is possible. Contrary to that, secondary batteries (also called rechargeable batteries or accumulators) involve reversible chemical transformations, so that the energy can be stored multiple times as chemical energy in the charged state and is released on purpose as electrical energy. During the discharge process (working cycle), an oxidation reaction takes place on the negative electrode (anode) and electrons are released into the external circuit. The electrons travel to the positive electrode (cathode) and drive a reduction reaction there. The ions of the electrolyte migrate in an electric field between

the anode and the cathode to ensure the total charge electroneutrality of the battery. Electrochemical cells also have ion permeable separators incorporated as a physical barrier between anode and cathode to prevent short circuits.[2] The function (being a cathode or an anode) of the electrodes in a rechargeable battery changes upon charge and discharge process. The common agreement in the battery research is therefore to define the electrodes and electrode materials according to their function during the working cycle, so that the terms anode and cathode are typically used for the negative and positive electrodes, respectively, during the discharge. Rechargeable battery cells are typically assembled in the discharged state and have to be charged prior to the first use. Rechargeable batteries generally offer a lower energy storage capability as compared to primary batteries since long time operation and recharging limit the number of suitable materials in comparison to primary cells.[2]

In order to compare the performance of different battery systems, one has to take into account the amount of electrical energy that can be stored and the time needed to release the stored energy. The possible / maximal amount of electrical energy stored in a battery can be expressed as weight dependent specific energy [Wh kg^{-1}], as volume dependent energy density [Wh L^{-1}] or as a product of the cell potential [V] and a capacity of a battery. The capacity (not to be confused with capacitance) is a measure of the charge that can be delivered by a battery and is either given as specific capacity [Ah kg^{-1}] or charge density [Ah L^{-1}].[3] The rate of the energy transfer can be expressed either as specific power [W kg^{-1}], power density [W L^{-1}] or as the charge and discharge rate, respectively. The so-called C-rate is commonly used in the battery research to describe the rate capability of batteries. Herein, C is reciprocally related to the theoretical number of hours necessary to fully charge a battery. For example, 1C means that the battery is charged from zero to full capacity within one hour and 20C implies that the charging takes 1/20 h or three minutes, respectively.[2-4] These features can be easily compared for different systems in a so called Ragone plot (Figure 1.1), in which specific energy and power are plotted against each other. The nominal cell voltage is defined by the thermodynamic properties of the active electrode materials and can slightly vary during cell operation because of kinetic effects. Batteries are normally operated in the range of defined cut-off voltages during charge and discharge to prevent irreversible chemical processes destroying the electrodes.

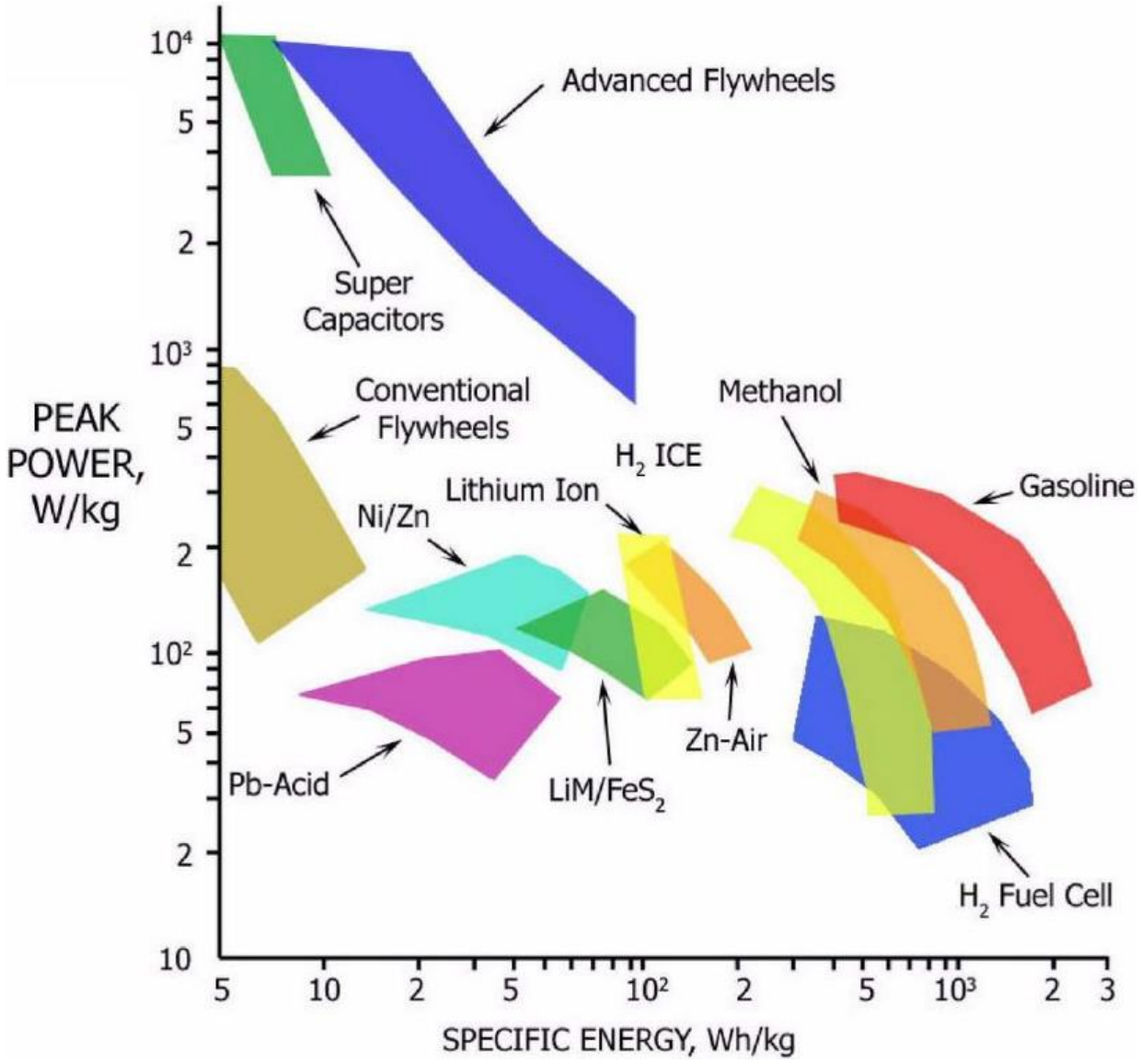

Figure 1.1: Ragone plot of different mechanical and electrochemical energy storage devices.[5]

Further important features to compare different secondary battery systems are the cycle lifetime, displaying the number of charge/discharge cycles, and the storage lifetime. The duration of both lifetimes is measured up to the point where the discharge capacity falls below 80% of the initial value. Finally, the costs of materials and processing are very important parameters greatly influencing the commercial success of different battery technologies.

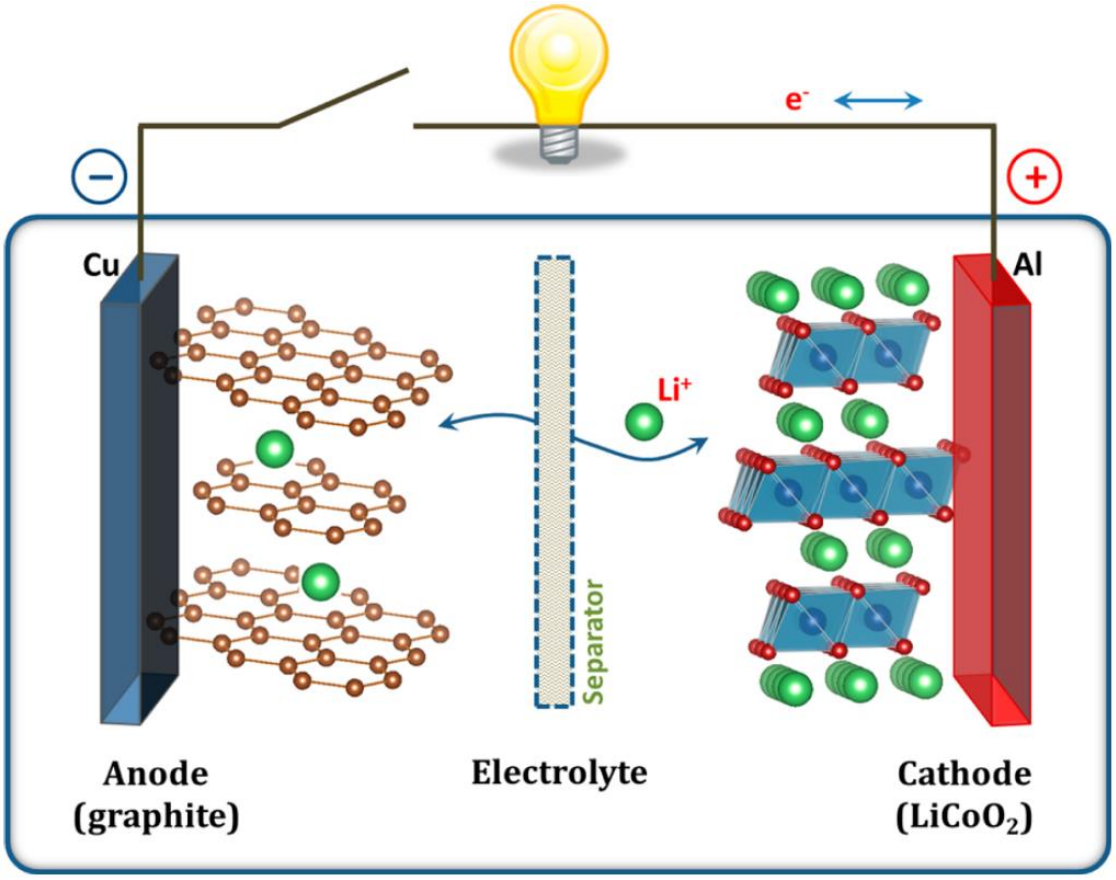

Figure 1.2: Scheme of the working principle of the first commercialized lithium ion battery.[6]

The old battery types such as carbon-zinc, alkaline, lead-acid and nickel-cadmium batteries, whose discovery goes back to the 19th century, are still actively used because of their robustness, reliable performance and extremely low costs. The energy and power densities of these battery chemistries are however significantly below the values dictated by the consumer needs of today. Continuous research has resulted in the invention of nickel-metal hydride accumulators and later in lithium ion batteries (LIBs).[7] LIBs are also known as "rocking chair" batteries since the lithium ions are "rocking" back and forth between the anode and the cathode. They were first commercialized in 1991 by SONY CORPORATION.[8] A scheme of the working principle of this first LIB using graphite and $LiCoO_2$ as electrodes is depicted in Figure 1.2.

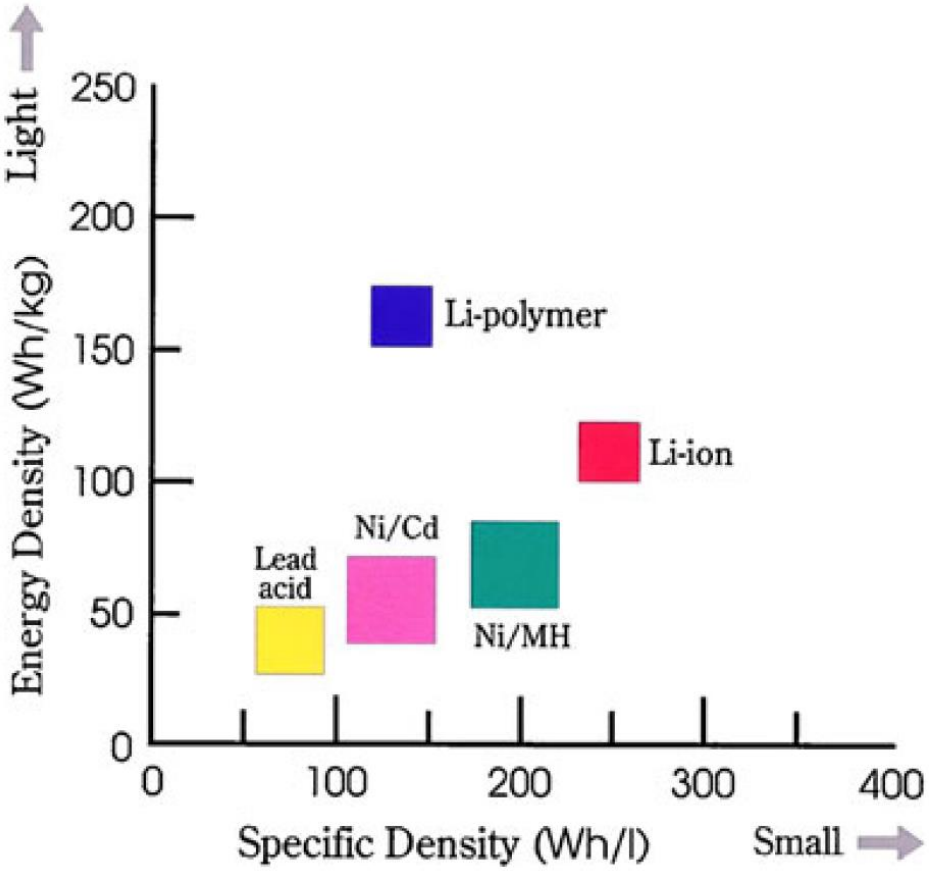

Figure 1.3: Ragone plot of different rechargeable battery systems.[7]

LIBs have a relatively low weight and show the highest energy and power densities compared to all other battery systems, which makes them the present technology of choice for electric vehicles and high-tech consumer electronics (Figure 1.3).[2, 9-11] However, the currently available LIBs can only hardly keep the pace of the growing demand of electric vehicles, stationary power ports and multimedia devices (see Figure 1.4). Research in the field of new materials for LIBs is mandatory, for example to extend the range of new electrically powered transportation systems without charging (higher energy density), to have faster acceleration and to allow for short charging times (higher power densities).[11] In the following chapters, the different components of LIBs are described in detail.

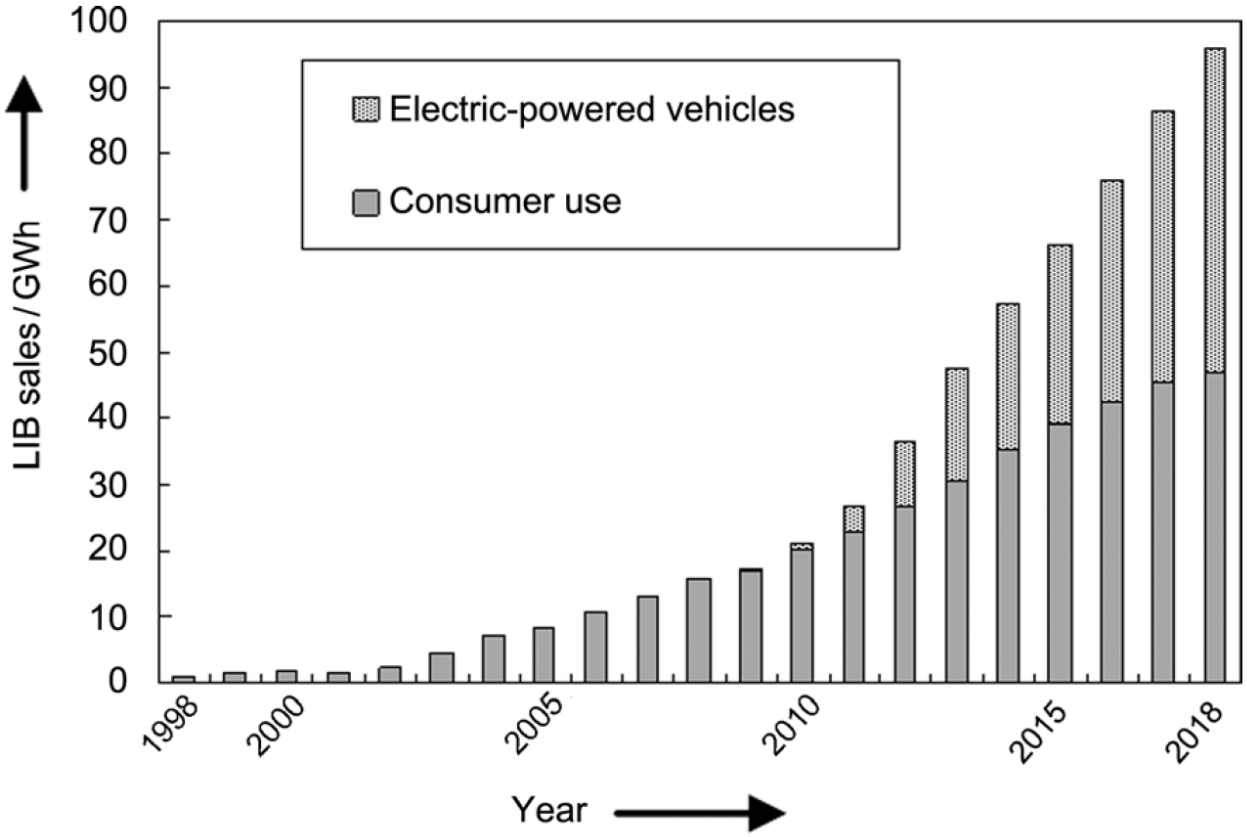

Figure 1.4: Rising market demand for lithium-ion batteries over years.[11]

1.1.2 Anode

1.1.2.1 Lithium Metal

The anode material in LIBs delivering the highest energy density is metallic lithium, due to the very high negative potential (-3.04 V versus standard hydrogen electrode) and the extreme low molar mass of lithium (M = 6.94 g mol^{-1}). Lithium metal has a theoretical specific capacity of 3842 mAh g^{-1} assuming that all of the lithium is accessible during discharge which is, however, not realistic, hence resulting in a lowered specific capacity.[12] The serious challenges of lithium metal anodes hampering their use in rechargeable cells are however mossy and dendritic lithium plating during the charging step, resulting in a low cycling stability of lithium metal batteries (only 150–200 cycles)[2, 3, 13] and even short circuiting due to the dendrite growth. One of the reasons for that are the properties of the so called solid electrolyte interface (SEI), which is always formed on the surface of electrode materials in organic electrolytes during the charge and discharge cycles. SEI generally plays a profound role in the battery performance acting as a spontaneously formed ion-permeable protection layer, which prevents the electrodes and the electrolyte from further decomposition and is greatly responsible for a long cycle life. The SEI on the lithium metal surface however does not provide the required protecting function, partially explained by the significant difference in their rigidity and mechanical properties. As a result, the SEI layer breaks apart leading to an inhomogeneous distribution of current density on the electrode surface and as a result the formation of needle-like or dendritic lithium (Figure 1.5). The growing dendrites can pierce the separator and create a direct contact between anode and cathode leading to short-circuit and overheating of the cell. This causes a melting of the lithium metal followed by the disappearance of the SEI, and consequently a direct contact of liquid lithium with the highly flammable organic electrolyte. Finally, this results in a so-called thermal runaway of the battery.[13] For this reason lithium metal, the most natural anode material for LIBs is so far only reasonable in primary, but not in rechargeable batteries.

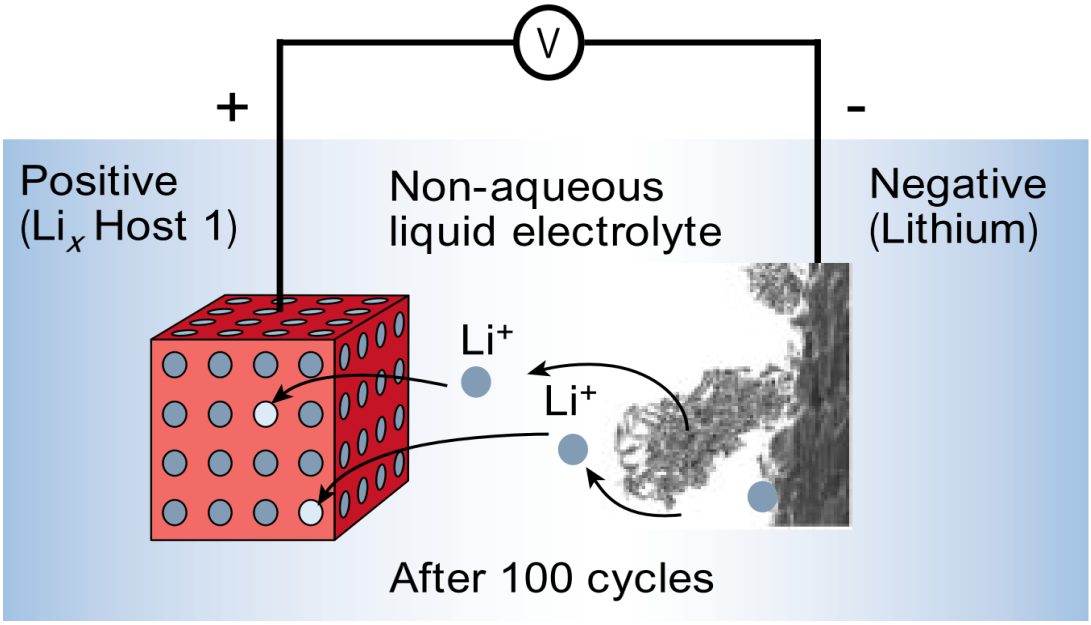

Figure 1.5: Dendrite formation upon repeated cycling.[3]

Beside lithium metal, many other materials can be used as anodes in the LIBs. They can be divided into three groups depending on the mechanism of lithium ion incorporation, namely insertion, alloying and conversion materials (Figure 1.6).[14, 15]

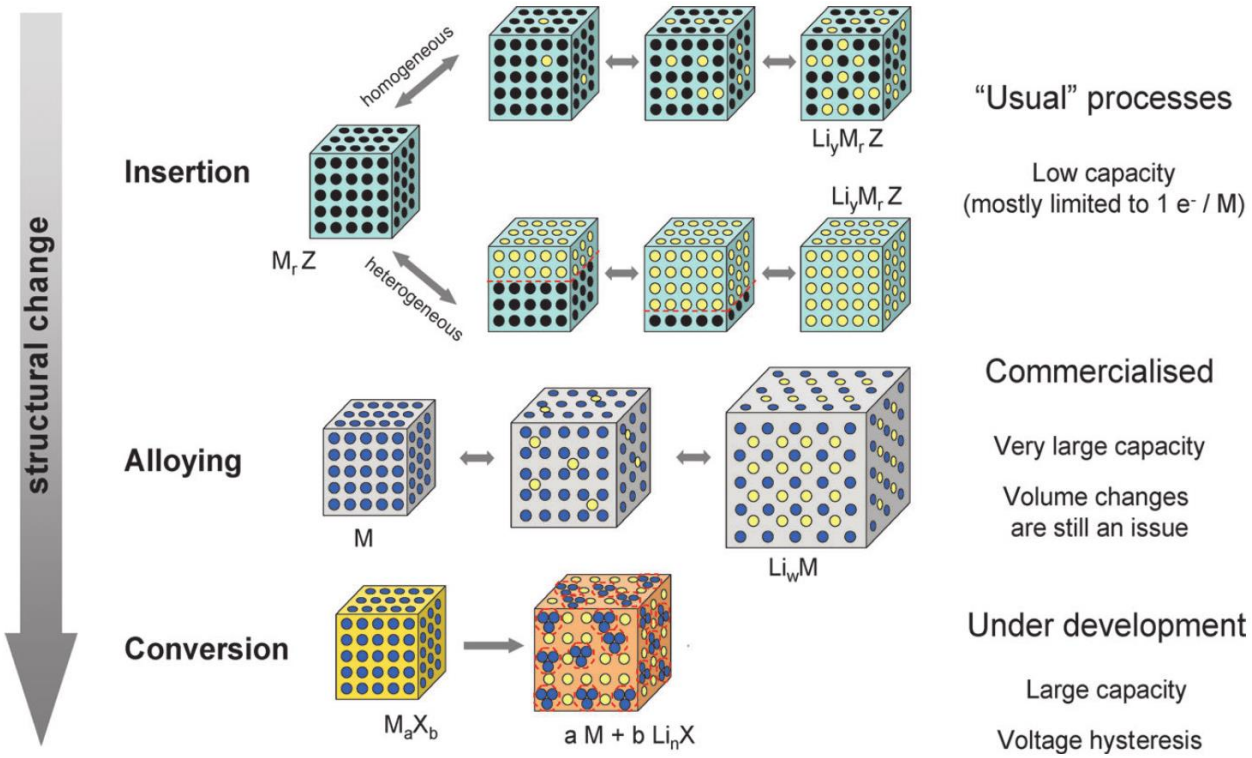

Figure 1.6: A schematic representation of the different reaction mechanisms observed in electrode materials for lithium batteries. Black circles: voids in the crystal structure, blue circles: metal, yellow circles: lithium.[15]

1.1.2.2 Insertion Materials

Insertion materials are compounds where lithium ions are incorporated in interstitial crystal positions, vacancies or between layers. A typical insertion-type material is the graphite, which is prevailingly used as an anode in the commercial LIBs because of the very low intercalation potential (slightly above lithium metal), cheap manufacturing, high cyclability, decent theoretical capacity of 372 mAh g^{-1} and the better safety as the dendrite formation is drastically reduced.[4, 8, 14, 15] Graphite undergoes the following electrochemical reaction (Equation 1.1):

$$\boldsymbol{6C + xLi^{+} + xe^{-} \rightleftharpoons Li_xC_6} \qquad 1.1$$

with $x \leq 1$.

Besides graphite, other carbonaceous materials can be used as anode material in LIBs:

- **Hard carbons** consist of a random alignment of graphene sheets providing multiple extra voids for lithium insertions which lead to higher reversible capacities than in graphite, but also hinder the Li^+-ion diffusion causing very poor rate capability.[14]
- **Carbon nanotubes** are highly ordered carbon nanostructures which show superior electronic and ionic conductivity as well as good mechanical and thermal stability. The theoretical reversible capacity of single-walled carbon nanotubes is 1116 mAh g^{-1} in LiC_2 stoichiometry, but has not been achieved in experiments yet.[14]
- **Graphene** can be described as independent single layers of graphite with a characteristic honey comb structure of sp^2 carbons. Graphene exhibits astonishing properties with high values for electrical conductivity, mechanical strength, charge carrier mobility and surface area. Depending on the assumed lithium ion insertion mechanism two different theoretical capacities can be obtained for graphene. If the Li^+-ions are absorbed on both sides of the graphene honey comb structure (Li_2C_6 stoichiometry), a gravimetric capacity of 780 mAh g^{-1} is calculated. If the lithium gets trapped in covalent bonds at the benzene rings (LiC_2 stoichiometry), a gravimetric capacity of 1116 mAh g^{-1} can be reached theoretically.[14]

Moreover, some metal oxides can also act as anodic host for lithium insertion, like titania (TiO_2) or a few spinel-like materials, with lithium titanate ($Li_4Ti_5O_{12}$, LTO) as the most promising candidate:[16]

- **Titania** has several polymorphs. The anatase structure (tetragonal, $I4_1/amd$) is regarded to be the most electroactive form with the potential ability to incorporate 1 mol lithium in 1 mol of TiO_2. This leads to a theoretical capacity of 330 mAh g^{-1} at an operative potential of around 1.5 V *versus* Li/Li^+, although only half of this capacity can be cycled reversibly. Furthermore, titania is abundant and chemically stable.[14]
- **LTO** is considered as the most appropriate titanium based oxide material for lithium insertion. The highly reversible reaction (Equation 1.2) at around 1.55 V *vs.* Li/Li^+ delivers a relatively low theoretical capacity of 175 mAh g^{-1}, but provokes almost no structural changes. It is regarded as a so-called “zero strain material”. Together with the high operating potential, this guarantees high safety, as the SEI and dendrite formations are drastically reduced.[14]

$$Li_4Ti_5O_{12} + xLi^+ + xe^- \rightleftharpoons Li_{4+x}Ti_5O_{12} \quad (1.2)$$

with $x \leq 3$.

Nevertheless, both titanium materials feature low electronic and ionic conductivity implying that high discharge or charge rates can only be achieved for nanosized materials.[17, 18]

1.1.2.3 Alloying Materials

The alloy/dealloy materials are a group of metals or semi-metals such as Sn, Al, Si, Sb, In, Zn, Pb, Bi, Ag, Pt, Au, Cd, As, Ga and Ge which can form alloys with lithium. Furthermore, intermetallic compounds containing one of the above listed elements such as Zn_xSb, SnSb, InSb, MnSb, Ag_xSb and AlSb can also show an alloying behavior, sometimes despite the competition with an insertion mechanism. When Li^+ is added to the metal, significant changes in the crystal structure are induced by forming Li_xM type alloys. Despite this fact, this mechanism can lead to a much higher degree of lithium incorporation as compared to insertion materials and consequently higher capacities. The higher stoichiometry of lithium causes huge volume changes that can hardly be buffered, which is the main drawback of the alloying materials. This enormous volume change during alloying leads to a loss of contact between the single grains and the current collector and the disintegration of the composite electrodes. In summary, the overall performance decreases drastically during cycling and results in a large voltage hysteresis and short cycle lives.[4, 14, 15]

Nevertheless, beside the drawbacks, the alloying materials bear a lot of potential because of the very high gravimetric capacities that can be achieved. For example, Si has a theoretical gravimetric capacity of 4211 mAh g^{-1} implying a maximum stoichiometry of $Li_{22}Si_5$, while Ge would provide 1623 mAh g^{-1} with an identical stoichiometry.[14, 15]

Specific oxides such as SiO_2, [19-22] SnO_2 and antimony doped tin oxide also incorporate lithium via an alloying mechanism, after the conversion (see next section) into the metal or intermetallic compound is fulfilled. This alloying step alone delivers a theoretical capacity of 783 mAh g^{-1} following this overall reaction (Equation 1.3): [14, 15]

$$Sn + 4.4Li^+ + 4.4e^- \rightleftharpoons Li_{4.4}Sn \qquad 1.3$$

1.1.2.4 Conversion Materials

The term conversion materials comprises all kinds of transition metal chalcogenides, halides and pnictogenides, in which a full reduction to the transition metal and the formation of the respective lithium salt matrix is involved according to Equation 1.4:

$$M_aX_b + yLi^+ + ye^- \rightleftharpoons aM + Li_yX_b \qquad 1.4$$

where *M* is a transition metal such as Mn, Ni, Fe, Co, Cu, Mo, Cr, Ru and *X* can be for example O, S, F, P and N.[14, 15]

These reactions deliver remarkably high capacity values and the potential of the reaction decreases with lower ionicity of the M-X bond, varying in most cases between 0.5 V and 1.0 V *vs*. Li/Li$^+$. Fluorides are exceptional due to the high potentials of nearly 3 V *vs*. Li/Li$^+$. The large voltage hysteresis between the discharge and the charge process of these binary compounds is one of the biggest drawbacks as it causes poor energy efficiency. Empirical studies showed that the magnitude of the hysteresis increases with stronger electronegativity of the anion and decreasing ionic conductivity of the lithium containing matrix.[14, 15]

Iron oxides, both hematite (α-Fe_2O_3) and magnetite (Fe_3O_4) are promising examples of oxide conversion materials because of their low cost, non-toxicity and high natural abundance. Hematite shows a theoretical capacity of 1007 mAh g^{-1} and magnetite of 926 mAh g^{-1}. Cobalt oxides CoO and Co_3O_4, which were synthesized as nanomaterials in this work, are also of great interest as they show theoretical capacities of 715 mAh g^{-1} and 890 mAh g^{-1}, respectively. As pointed out in the previous section, tin oxide-based materials can also be classified as conversion compounds, but the lithium incorporation does not end after the (reversible) conversion process. In fact, it is followed by a subsequent reversible alloying process. The second reaction almost doubles the theoretical capacity of the material and was further investigated in this work for tin and antimony doped tin oxide nanoparticles with and without the graphene as the supporting anode material. Drawbacks of all oxide materials are their poor cycling performance due to their low electrical conductivity, low diffusion lengths of Li$^+$-ions and high volume expansion.[14, 15]

In addition to the above mentioned metal oxides, nitrides and sulfides, metal phosphides have attracted special attention in the literature as new materials for LIB anodes since they can react with lithium, both in a conversion-type as well as in an insertion-type mechanism. The insertion mechanism greatly depends on the electrochemical nature of the transition metal and on the stability of the phosphorus bonding, as the conversion reaction entails the breaking of the metal-phosphorous bond. MP_x compounds generally have a low electrical conductivity and suffer from high volume changes upon charge/ discharge cycling. On the other hand, they have a lower insertion potential as compared to the oxide analogues, which is beneficial for their use as the anodes, and can deliver high theoretical capacities between 500 and 1800 mAh g^{-1}.[14, 15]

In Figure 1.7 different anode materials described in this chapter are compared regarding their theoretical capacities and reaction potentials in LIB.

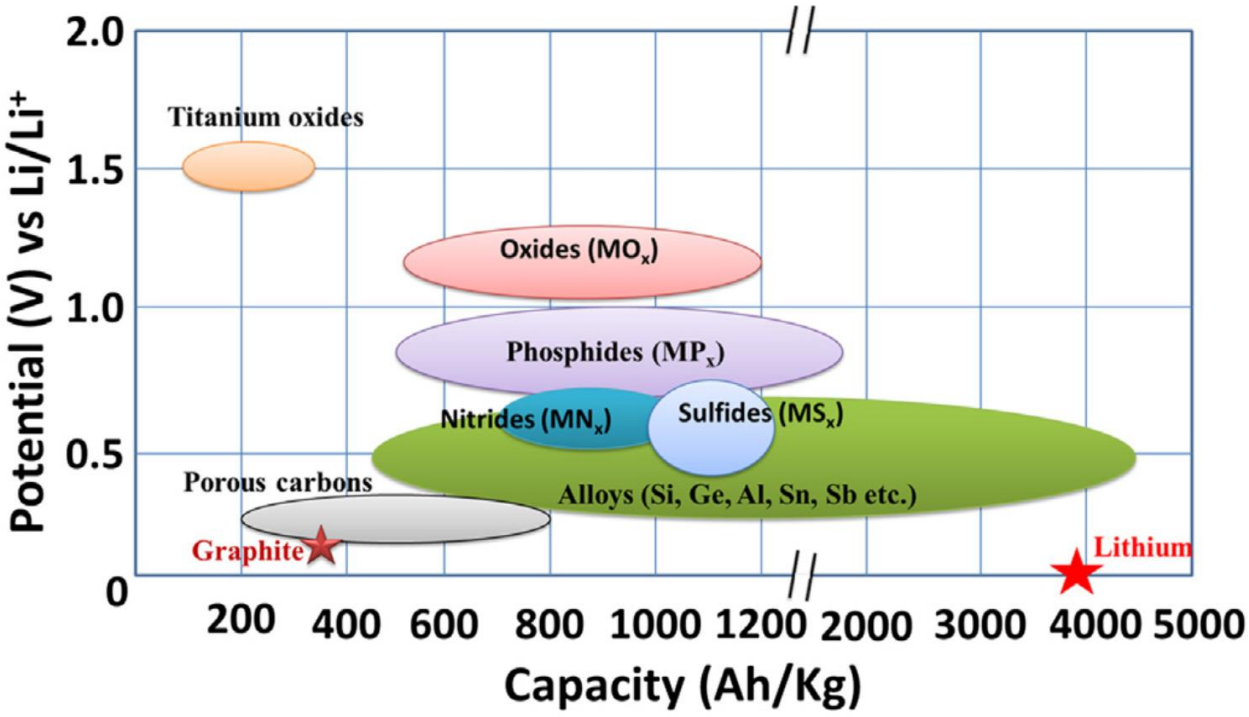

Figure 1.7: Schematic illustration of active anode materials for the next generation of lithium batteries. Potential *vs.* Li/Li^+ and the corresponding capacity density are shown.[14]

1.1.3 Electrolytes and Separators

The electrolyte is the medium responsible for the Li^+-ion transport between anode and cathode. The electrolyte should fulfill certain requirements such as being non-inflammable, exhibiting a high thermal stability within a relatively large temperature window between approximately -40 °C to 60 °C, low toxicity, low production costs and high Li^+-ion conductivity together with a negligible electron conductivity. The electrochemical stability of the electrolyte is generally governed by the kinetics of their reactions with the material of the electrodes rather than the thermodynamics of the system, although the cathodes and anodes have a strong oxidizing or reducing nature, respectively. The energy levels for an optimized electrolyte with respect to the anode (reductant) potential μ_A and the cathode (oxidant) potential μ_C are depicted in Figure 1.8. Furthermore, the SEI formation on both electrodes is strongly affected by the components of the electrolyte.[6, 15]

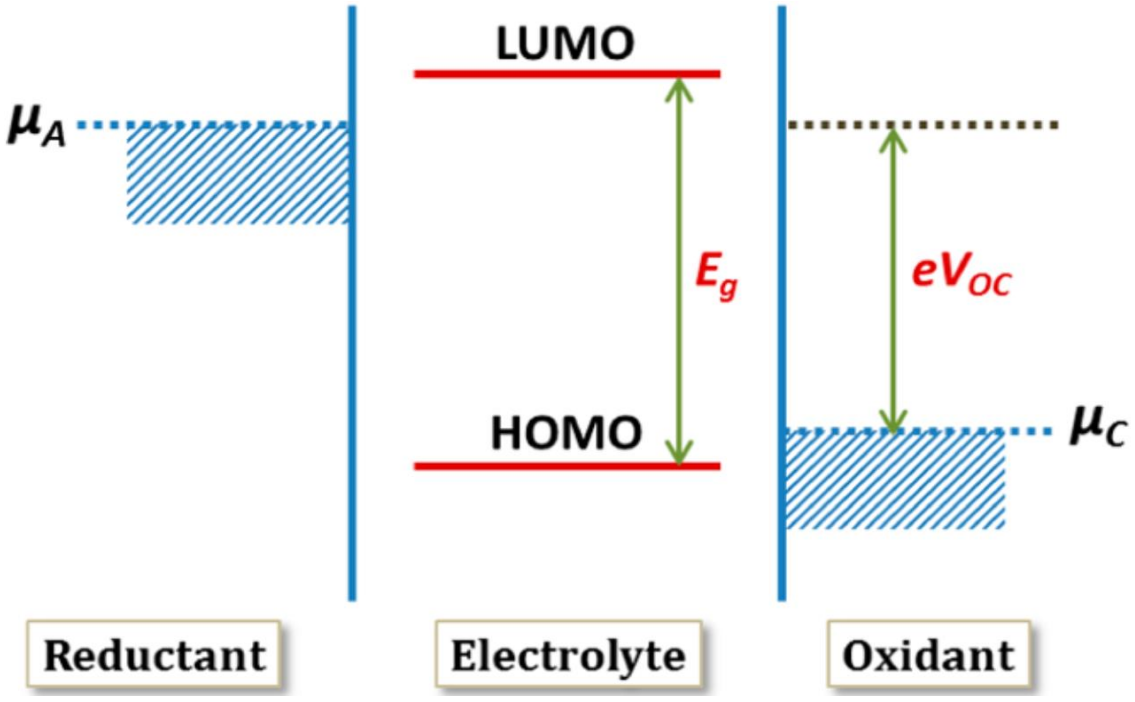

Figure 1.8: Relative energies of the electrolyte window *Eg* and the electrode electrochemical potentials μ_A and μ_C with no electrode/electrolyte reaction of a liquid electrolyte with solid electrodes.[6]

Electrolytes have to face large potential windows produced by the high potential difference of anode and cathode in high-energy LIBs. Because of this reason aqueous electrolytes are not favorable in LIBs as water exhibits a relatively small potential window of about 1.3 V, which can

be only slightly extended by special additives. Without the severe drawback of the small potential window, aqueous electrolytes fulfill most of the above stated requirements as electrolyte for LIBs.[23]

Organic solvents such as dimethoxy ethane and mainly carbonates including dimethyl carbonate (DMC), ethyl methyl carbonate (EMC), diethyl carbonate (DEC), ethylene carbonate (EC), fluoroethylene carbonate (FEC) and propylene carbonate (PC) are typically used in LIBs. They have a large potential window with an oxidation potential about 4.7 V and a reduction potential of around 1 V *vs.* Li/Li^+. Beside the large potential window, carbonates exhibit further advantages for the use in LIBs such as a relative low viscosity and the resultant relative high Li^+-mobility. In most cases electrolytes contain several solvents, mainly a mixture of different carbonates. Most of the mixtures contain EC, which is known to decompose at the anode forming a passivating SEI layer on the majority of low reduction potential anode materials. However, the carbonates are highly flammable with flash points below 30 °C, which can lead to an inflammation of the battery in case of short circuits.[23]

In addition to the solvent, the lithium ion conducting salt of an electrolyte has also to be stable against decomposition. Most of the commercial LIBs use lithium hexafluorophosphate ($LiPF_6$) as the conducting salt due to their relatively high conductivity and relatively low cost. However, $LiPF_6$ shows a poor thermal stability and a high sensitivity to moisture. A more expensive alternative with slightly lower ion mobility, but higher thermal stability and low sensitivity towards moisture is lithium bis (trifluoromethanesulfonyl) imide ($Li[N(CF_3SO_2)_2]$/LiTFSI). While $LiPF_6$ forms passivating layers with the aluminum current collector against the electrolyte, LiTFSI leads to a steady dissolution of the aluminum. This is the major drawback, which prevents LiTFSI from commercial use.[24]

Another set of electrolytes are room temperature ionic liquids (RTILs) such as imidazolium-based cations. All RTILs show a very high oxidation potential of about 5.3 V *vs.* Li/Li^+. Additionally, they are in general much safer as they are not inflammable, more chemically stable against elevated temperatures and relatively nontoxic. They enable a high solubility of lithium salt, however the Li^+-ion mobility is very low. Furthermore, the reduction potential is quite high leading to a low stability in combination with the majority of anode materials.[23]

All of the mentioned liquid electrolytes need a highly ion permeable and weakly electron conducting separator, which prevents an anode and a cathode from short circuiting. Typically, separators are made of glass fibers, inorganic ceramics or polyolefins like polyethylene or polypropylene.

Unlike liquid electrolytes, solid electrolytes do not need additional separators as they already integrate this function. Examples are lithium solid polymer electrolytes (Li-SPEs) that can stay in contact to the electrodes also during modest volume changes of the electrodes. Generally, polyethylene oxides (PEOs) with addition of a lithium ion conducting salt like $LiPF_6$ or $LiAsF_6$ are used. This type of solid electrolytes is light-weight, low-cost, nontoxic and chemical stable and, but they also exhibit very low Li^+-ion conductivity at room temperature. So, LIBs with Li-SPE electrolyte have to be operated at 80 °C for reasonable conductivity and therefore power applications. Swelling the Li-SPE electrolyte with a lithium salt containing liquid solvent produces lithium hybrid polymer electrolytes (Li-HPEs) with enhanced Li^+-ion conductivity which was first applied in plastic lithium ion batteries (PLiON).[23, 25]

Inorganic solid electrolytes can also be an alternative to organic electrolytes. Several materials such as garnets, perovskites, Li_3N, NASICON-type and lithium phosphorus oxynitrides (LiPONs) show reasonable ionic conductivities and huge potential windows. Using these materials can lead to an all solid state lithium ion battery. The major drawback related to the commercialization is the mechanically rigidity leading to contact loss during electrochemical induced volume changes of the electrodes.[23, 26]

1.1.4 Cathode

A material has to fulfill certain requirements to be suitable as a cathode material in LIB. Lithium should react reversibly with the cathode material or more explicitly the lithium ions should intercalate and de-intercalate without changing the structure of the host or causing other degradations. With an exception of emerging chemistries (such as sulfur), the prevailing part of cathode materials contains redox-active transition metal ions. The amount of these ions determines the maximum capacity a cathode material can deliver. The better electronically conducting the material is, the lower is the need for the addition of inactive conducting diluents such as carbon black that minimize the overall energy density. The easier lithium ions can be removed or inserted into the material, the higher is the overall power density of the material. Furthermore, the material should be cheap, abundant and environmentally harmless.[27]

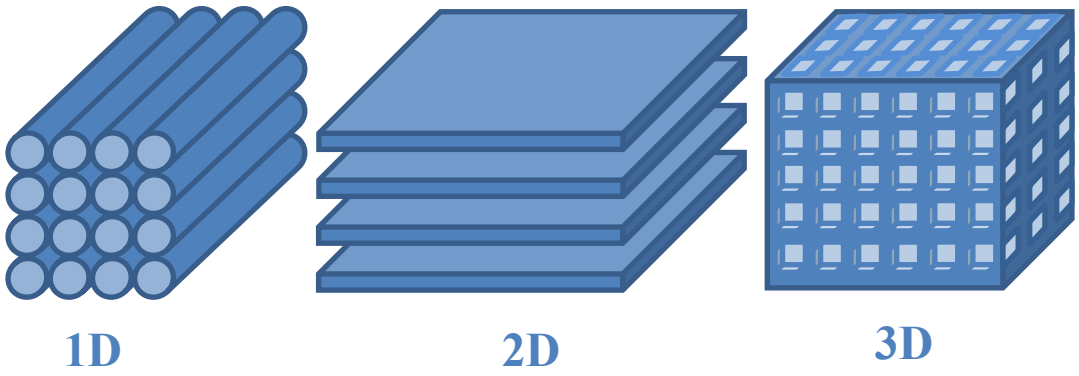

Figure 1.9: Schematic representation of void spaces in one-, two- or three-dimensional materials as cathode materials in lithium ion batteries (adapted from Winter *et al.*[4]).

In general, the insertion-type materials can be classified into three types with respect to their general structure, as schematically depicted in Figure 1.9.[4]

1.1.4.1 One-dimensional Materials

Transition metal trichalcogenides, such as TiS_3 and NbS_3, are examples for one-dimensional materials and were some of the earliest cathode materials investigated. They are built up of chains of face-sharing trigonal prismatic [MX_6] building units and the resulting ribbons are only linked together by weak van-der-Waals forces. The materials can insert three lithium ions per formula unit in the one-dimensional channels formed by the ribbons. The lithium insertion is partly irreversible in case of TiS_3 while, in contrast, for $NbSe_3$ it is totally reversible. Another advantage of this material is the metallic character of both, the lithium-free $NbSe_3$ and the fully-lithiated Li_3NbSe_3, which would allow electrodes of the pure material without the need to support the conductance with additives such as carbon black. Nevertheless, the rather low discharge potentials of around 1.8 V, the high toxicity, the high costs and the huge volume change during lithium insertion and extraction rule these materials out from commercialization nowadays.[4, 27]

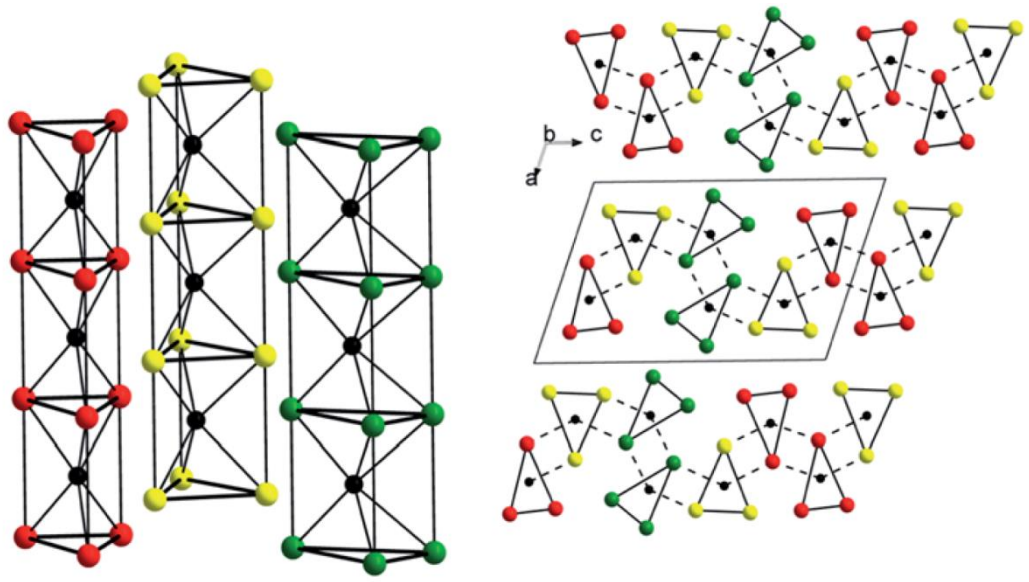

Figure 1.10: Structures of trichalcogenide NbSe3: the chains of coupled trigonal prisms [NbSe6/2] along the b axis (left) and structure projections on the ac plane (right). Different sorts of prismatic columns are marked with two- and three-color schemes.[28]

1.1.4.2 Two-dimensional Materials

In contrast to the one-dimensional materials, the two-dimensional layered materials are more promising as cathode materials in LIBs. The first 2D materials investigated were transition metal dichalcogenides MX_2 including all types of compounds of Ti, Nb, Ta, Mo and W with mostly S and Se atoms forming the layered CdI_2-structure. Lithium can intercalate between the sheets inducing quite a large structural expansion of 10% for TiS_2, the most promising material of the MX_2 group. The resulting $LiTS_2$ (LTS) was finally put on the market in batteries from 1977 - 1979 by EXXON to power watches and other small devices because of its high gravimetric energy density combined with long cycle life (1000+ cycles). The major drawback of LTS, beside the volume changes during insertion/extraction of lithium, is the rather low redox potential of around 2 V, which is not sufficient for high-energy applications.[4, 27, 29]

The layered oxides $LiMO_2$, all exhibiting the α-$NaFeO_2$ structure (Figure 1.11) are more promising. $LiCoO_2$ (LCO) is still used in the majority of LIBs and is also the cathode material used for the first commercialized LIB by SONY.[8, 29] LCO is attractive because of its theoretical capacity of about 140 mAh g^{-1} up to 4.2 V, the low self-discharge and good cycling performance. Due to these facts and in order to overcome some of the disadvantages, such as low thermal stability and fast capacity fading at high current rates or during deep cycling, this work includes a section about the synthesis of nanostructured LCO and its electrochemical performance as cathode material. Nevertheless, the major drawbacks of this material are the high cost and toxicity of cobalt within LCO. In order to overcome these problems without compromising the advantages, a lot of research has been conducted to substitute cobalt from the layered $LiMO_2$. Complete substitution of Co by Ni leads to $LiNiO_2$ (LNO) with, on the one hand, a similar specific capacity, a higher energy density and lower cost compared to LCO. On the other hand, LNO also exhibits an even higher thermal instability and the Ni^{2+}-ions have the tendency to substitute Li^{+}-sites during synthesis and delithiation and consequently block the lithium ion diffusion pathways. Using Mn as the only transition metal within LMO_2 leads to the low-cost layered $LiMnO_2$, which shows a high practical specific capacity of around 200 mAh g^{-1} as well as the problem of dissolution of Mn. This leads to a loss of the active material, to low cyclability and serious safety issues. The best strategy so far is the combination of different metals within the MO_2 layers of $LiMO_2$. The most important examples are the following:[4, 27, 29-31]

- **$LiNi_{0.8}Co_{0.15}Al_{0.05}O_2$** (NCA) combines the attractive properties of $LiNiO_2$ and $LiCoO_2$ and is already commercially used in PANASONIC batteries applied in TESLA electric vehicles (EVs) because of the high practical specific capacity of 200 mAh g^{-1} and the long storage calendar life. However, at temperatures above 40 °C severe capacity fading is reported.[4, 27, 29-31]
- **$LiNi_{0.5}Mn_{0.5}O_2$** delivers a high discharge capacity of about 200 mAh g^{-1} with a plateau potential of 3.8 V, but its practical application is limited through capacity decay, poor cycling stability and safety issues.[4, 27, 29-31]
- **$Li(Ni_xCo_yMn_z)O_2$** (NCM/NMC, with x+y+z = 1) with various compositions, for example $LiNi_{1/3}Mn_{1/3}Co_{1/3}O_2$ which is already commercialized, reflects attempts to combine the advantages of all of the above already mentioned layered oxides. The materials show promising properties including a more stable structure, a reasonable capacity and more economic costs. $LiNi_{0.8}Co_{0.1}Mn_{0.1}O_2$ shows an excellent capacity but a poor cycling stability. Within these compositions, different NCM materials can be synthesized and their properties can be tuned.[4, 27, 29-31] These facts make them an interesting and maybe trendsetting material. The synthesis of nanostructured NCMs of various compositions and their electrochemical performance is a part of this work.

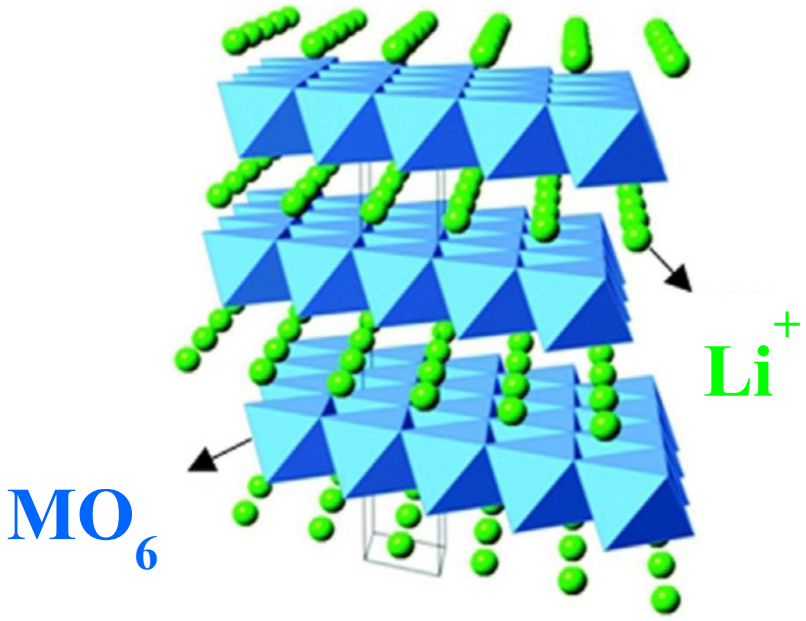

Figure 1.11: α-$NaFeO_2$ structure of a typical layered $LiMO_2$ material. [29]

1.1.4.3 Three-dimensional Materials

The most typical three-dimensional materials are spinels or polyanionic compounds (Figure 1.12).

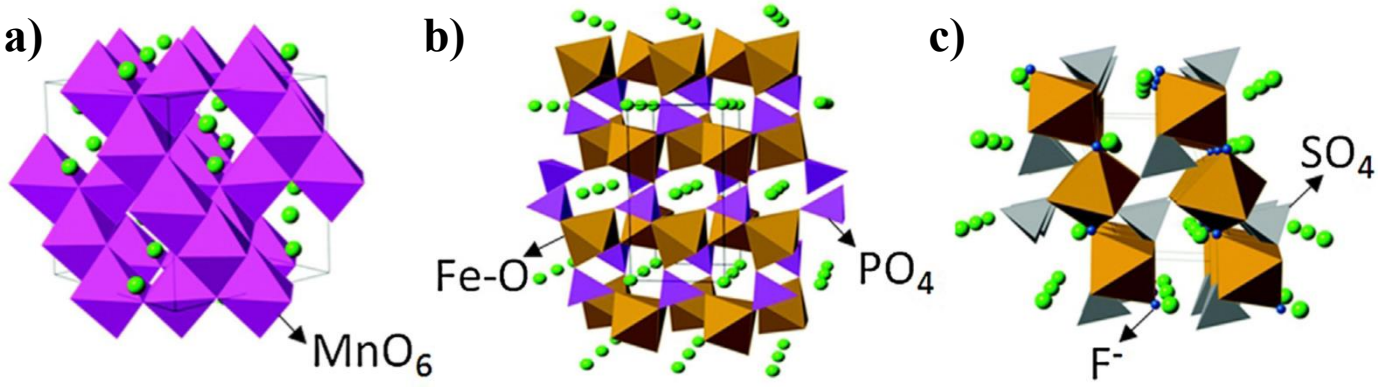

Figure 1.12: Structures of spinel- ($LiMn_2O_4$) (a), olivine- ($LiFePO_4$) (b) and tavorite- ($LiFeSO_4F$) (c) type materials. Li^+-ions are indicated in green.[29]

A prominent example of spinel-type materials in LIBs is $LiMn_2O_4$ (LMO), which is attractive due to the high abundance, low cost and environmental friendliness of Mn. In addition, it shows a high discharge potential but only a capacity of maximum 150 mAh g^{-1}. Further disadvantages are the dissolution of Mn similar to other manganese containing cathode materials and a transformation into a tetragonal phase, occurring especially at the surface. In order to extend the cyclability, doping with Ni to $LiMn_{1.5}Ni_{0.5}O_4$ can be performed. This also raises the discharge potential to about 4.7 V *vs.* Li/Li^+.[4, 27, 29-31]

The polyanions include the class of the $LiMPO_4$ phosphates (M = Fe, Co, Mn, Ni) usually crystallizing in the olivine structure. The complete family of $LiMPO_4$ olivines exhibits very poor electronic conductivity as well as slow lithium ion diffusion. On the other hand, the olivines are thermally and chemically highly stable. The discharge potential of $LiFePO_4$ (LFP) at around 3.4 V *vs.* Li/Li^+ can be increased by substituting Fe by Mn to yield $LiMnPO_4$ (LMP) with an average discharge potential of around 4.1 V *vs.* Li/Li^+, or Co leading to $LiCoPO_4$ (LCP) with an average discharge potential of around 4.8 V *vs.* Li/Li^+. The complete substitution for Mn or Co is however not feasible as it inherits the disadvantages of these elements such as the high costs for Co or the dissolution of Mn, respectively. The combination of different transition metals seems again to be a promising method for improvements.[4, 27, 29-31]

Tavorite-structured materials, such as $LiFeSO_4F$ (LFSF), are another interesting class of cathode materials. LFSF shows high cell voltage, a specific capacity of 151 mAh g^{-1} and reasonable ionic and electronic conductivity. The material is however relatively new and a lot of research on the specific properties and the implementation into LIBs has to be done yet.[29]

New upcoming candidates are polyanion materials such as silicates and borates as well as cathodic conversion materials like metal fluorides or chlorides such as FeF_3, CoF_3 or CuF_2, which are much further afield from commercialization than LFSF. In Figure 1.13, an overview of selected intercalation-type materials with their discharge potentials and specific capacities is given.[29]

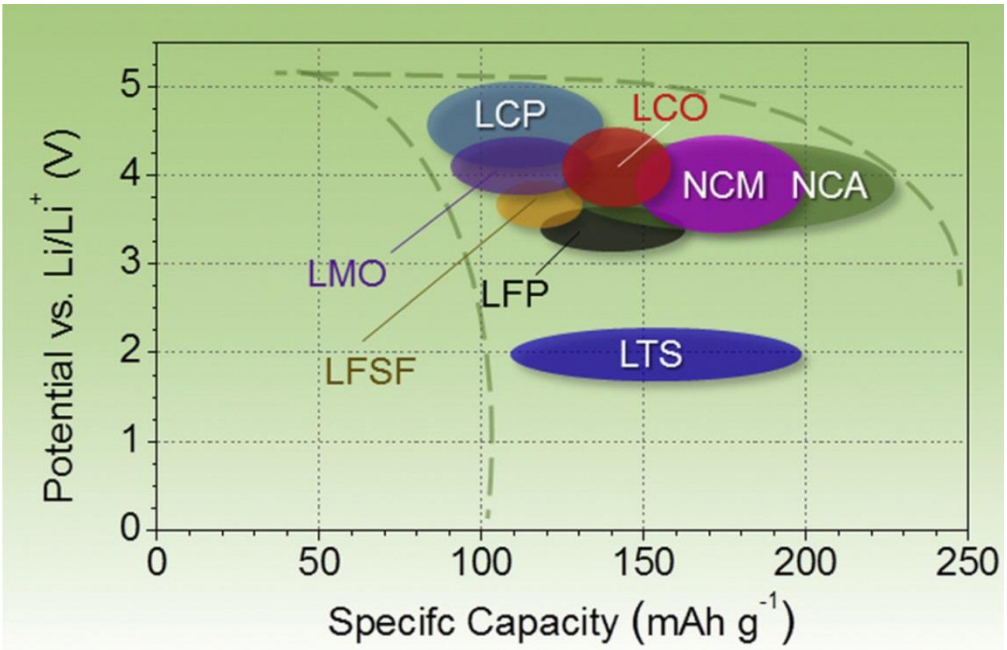

Figure 1.13: Approximate range of average discharge potentials and specific capacity of some of the most common intercalation-type cathodes.[29]

1.1.5 Nanostructured Lithium Ion Batteries

As already stated above, new upcoming applications and especially EVs make it necessary not only to increase the already quite high energy density of LIBs, but also the power density. This can in particular be achieved either by developing new materials or by nanostructuring.[9, 10] It is known that phase purity, particle distribution and size significantly influence the electronic and ionic transport and consequently the electrochemical performance of electrode materials. The most pronounced advantage brought by nanostructuring is a significantly enhanced electrochemical kinetics of lithium storage in nanostructured electrode materials. Since the Li^+-ion diffusion pathways drastically decrease in small nanoparticles, the rate of lithium insertion/removal rises considerably. The characteristic time constant τ for the diffusion is given in Equation 1.5:[31-33]

$$\tau = \frac{L^2}{D} \qquad 1.5$$

where L is the diffusion length and D - the diffusion coefficient.

While D is material inherent, L depends on the size of the particles. This implies that the time τ rapidly decreases for nanoparticles compared to particles with micrometer size.[33]

Besides the shortened diffusion pathways within the solid material described above, nanostructuring can bring also other benefits. One of them is a higher charge-discharge rate due to greater electrode/electrolyte contact area and hence a higher flux of Li+-ions from the electrolyte to the interface. The electronic transport in nanostructured electrodes can be further promoted by combining nanosized particles together with electronically conductive nanocoating shells.[31-33] Decreasing the size of active materials down to several nanometers influences the chemical potentials of lithium ions and electrons which can change the electrode potential as well as the working voltage of LIBs. Secondly, new electrode reactions can occur in nanosized materials and also materials which are inactive for Li^+-ion storage in micrometer size become active in nanometer size, such as $LiFeO_2$. Additionally, reactions that used to be irreversible in bulk can be reversible in nanoparticles like TiO_2. Furthermore, nanomaterials can more easily compensate strains and structural changes during cycling processes and the integrity of electrode materials can be preserved.[31-33] However, along with these benefits, nanoelectrodes carry some disadvantages, One of the practical challenges associated with the use of nanomaterials in

batteries is the increasing complexity of their synthesis and the difficulties to control their dimensions. The large electrolyte-electrode interface can also lead to an increasing amount of undesired reactions between the particle and the electrolyte making it difficult to maintain the inter-particle contact.[31-33]

Additionally, the density of nanopowders is less than that of micrometer-sized particles. Therefore, the volumetric capacities of nanomaterials are generally low due to the large surface and the open porous structure. A low thermodynamic stability can be caused by the presence of residual species such as organic surfactants on the surface of the nanomaterials, resulting in serious capacity fading and further serious safety problems at high temperatures.[31-33]

1.2 Synthesis of Metal Oxides with Different Nanomorphologies

1.2.1 Solvothermal Strategies towards Metal Oxide Nanoparticles

The reaction conditions are very important for the synthesis and crystallization of metal oxide nanoparticles. The size of the particles is influenced both by kinetics and thermodynamics of particle formation process. Thermodynamically, the critical energy ΔG^* is the most important measure, as it is the limiting energy that has to be overcome to enable crystal formation (Equation 1.6):

$$\Delta G^* = 16\pi \frac{\gamma}{(3\Delta G_v)^2} \qquad 1.6$$

where γ is the surface energy per unit area and ΔG_v - the Gibbs free energy per unit volume (Equation 1.7):

$$\Delta G_v = -\frac{kT}{\Omega}(1+\sigma) \qquad 1.7$$

where k is the Boltzmann constant, T - the temperature, Ω - the atomic volume and σ - the supersaturation of a solution.

From Equations 1.6and 1.7 it can be seen that an increase of the supersaturation as well as a diminished surface energy leads to a smaller ΔG^* value and consequently smaller crystal seeds are more stable. Therefore, for minimizing the surface energy special solvents that can interact with the particle surface or the addition of surface active agents (surfactants) can be beneficial. Surfactants can be all types of sterically demanding groups adhering on a surface. Moreover, a rapid decrease in the reaction temperatures typically enable a higher supersaturation and thus a lower critical energy.[34]

Different synthesis techniques, especially gas-phase and liquid-phase syntheses, give access to nanomaterials with a wide range of compositions, well-defined and uniform crystallite sizes and complex tuneable morphologies. The liquid-phase routes often provide more flexibility with regard to the controlled variation of structural, compositional and morphological features of the nanoparticles. Particularly, sol-gel processes are broadly used for the fabrication of nanomaterials. Sol-gel processes can be defined as the conversion of a precursor solution into an inorganic solid via inorganic polymerization reactions induced by the solvent. Synthesis

temperatures above the boiling points of the respective solvents are typically required to solubilize precursors, induce polymerization, and/or convert amorphous nanoparticles to the crystalline form. A method in which water or organic solvents can be used at temperatures above their particular boiling points is called the solvothermal synthesis. Such reactions are carried out in sealed vessels for example autoclaves or bombs (see Figure 1.14).[35, 36] Solvothermal processes are defined by both chemical parameters, such as the type of reactants and the solvent, and thermodynamic parameters like temperature and pressure.[37] The heating of solvents beyond their boiling point within such autoclaves produces high pressure and this entails, in turn, elevated solvent boiling points.

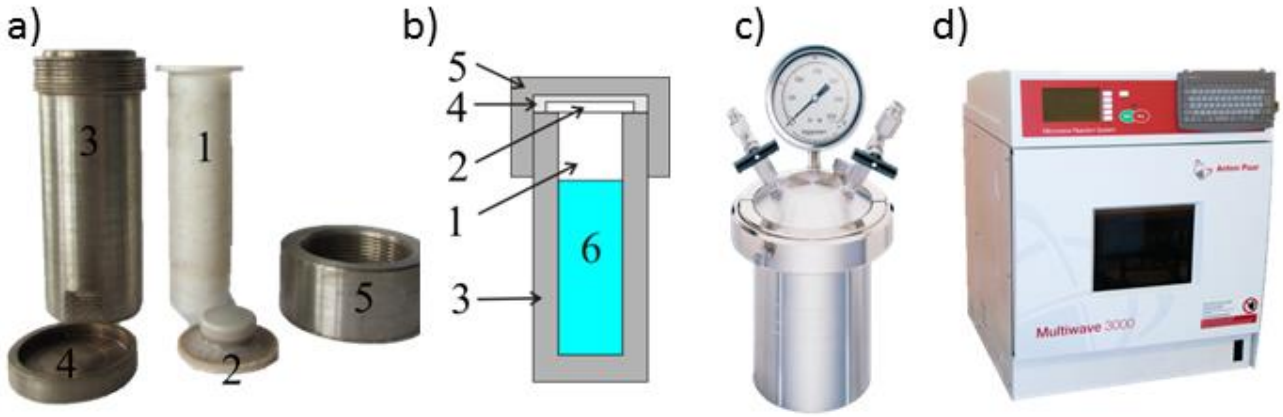

Figure 1.14: Overview of different autoclave techniques used for solvothermal syntheses in this thesis. Small self-made stainless steel autoclave (a) and its assemblage (b): Reaction solution (6) is filled in a Teflon liner (1) and sealed with a Teflon lid (2). Both are used to prevent the stainless steel autoclave (3), an additional cover (4) and the lid (5) from corrosion. These types of autoclaves can be heated in ovens up to 200 °C. Commercial stainless steel autoclaves (c) can be heated independently by a heating jacket, are equipped with pressure and temperature sensors and the reaction solution within can be stirred. Special autoclaves made of ceramics or polymers can be heated in lab microwave ovens (d).

The choice of a solvent has a profound influence on the properties of the products of solvothermal reactions. Depending on the solvent, such reactions are also referred to as hydrothermal (water), ammonothermal (ammonia), glycothermal (glycols) or alcothermal (alcohols). Among alcothermal processes, solvothermal in benzyl alcohol as a solvent were shown to be particularly suitable for the synthesis of nanosized crystalline metal oxide nanoparticles. Benzyl alcohol is non-toxic, has a high boiling point and its special reactivity is based on the aromatic stabilized intermediate states. This route was first established by Niederberger and co-workers.[38, 39] The benzyl alcohol in this synthesis route fulfills different tasks as it is solvent, surfactant and oxygen supply at the same time. Herein, the reacting metal salts including halides, alkoxides and acetylacetonates react with the benzyl alcohol and small

nanoparticles in the size range of 2 nm to 80 nm are formed. The solvent alone leads, without the addition of any surfactant, to highly crystalline particles with uniform sizes and shapes due to its capping properties. A further advantage of this method is that a broad variety of metal oxides can be synthesized also including binary, ternary and multinary ones.[38-43] Furthermore, this route was also successfully extended to the synthesis of metal sulfide nanoparticles.[44] However, this method also shows drawbacks as stabilizers or surfactants have to be added to the solvents to redisperse the nanoparticles for reassembly such as nanostructured metal oxide films. Furthermore, it is challenging to remove the highly-stable aromatic benzyl alcohol ligands from the surface of the nanoparticles in order to implement them into devices for electronics, catalysis or electrochemistry.[39, 45]

Albeit the benzyl alcohol route is a very successful and often used method for nanoparticle syntheses, the disadvantages namely the device integration motivated our group for an alternative approach. The different transition metal oxide nanoparticles described in this thesis were either directly solvothermally synthesized using our novel *tert*-butanol route or were produced by calcining─pre-synthesized nanoparticles in *tert*-butanol. Screening towards the optimized synthesis of nanosized transition metal oxides within the *tert*-butanol solvothermal route was one of the main parts of this thesis. The synthesis using *tert*-butanol exhibits all the advantages of the benzyl alcohol strategy, but manages to overcome some of its disadvantages. For example, as *tert*-butanol is non-aromatic, the residual *tert*-butoxide groups on the surface of the nanoparticles can be more easily removed by moderate heating as compared to the benzyl alkoxide groups. Moreover, the *tert*-butyl groups build up a sufficient steric hindrance to prevent the nanoparticles from fast growth and aggregation. This was already shown by the successful syntheses of TiO_2,[17] Nb-doped TiO_2,[46] $Li_4Ti_5O_{12}$,[18] NiO,[47] In-doped SnO_2,[48] Co_3O_4,[49] Fe-doped NiO,[50] Sb-doped SnO_2[51] and Co-doped NiO nanoparticles.[52] All those examples show that the *tert*-butanol route is a feasible pathway to produce ultrasmall particles.[53]

1.2.2 Synthesis of Nanomaterials using Templating Strategies

Besides the dimensions of the bulk phase, the performance of materials for battery applications critically depends upon spatial arrangement of the solid and empty components (nanomorphology). An important characteristic of nanomorphology is porosity (including pore size distribution, pore shape, and pore volume) as it has a strong impact on the accessibility of active sites and mass transfer conditions (both electrons and ions) in the electrode networks. Therefore, an ability to control and tune the nanostructure and the parameters of porosity is an important step in optimization of materials for energy storage applications.

Synthesis strategies to obtain nanostructured materials can be divided into spontaneous and template approaches. Spontaneous approaches are generally more beneficial for large scale fabrication because of the synthesis simplicity and lower costs, but they provide as a rule less flexibility in producing desired nanostructures. Thus, deposition of particles typically always results in porous materials featuring so called textural porosity produced by the voids in between the nanoparticle packing. Depending on the size of the particles, the porosity can cover the whole scale of micro-, meso- and macroporosity (for a detailed definition of these terms read further at Section 2.7 Sorption). The porosity obtained in this way is however disordered, featuring a broad distribution of pore shape and size. More defined structures can be reached by using so called templating agent defining the spatial arrangement of the pores and governing the nanostructure formation. Hereby, soft and hard templating methods can be distinguished. The hard templating approach relies on shape-persistent templates such as spheres of different sizes made of silica, latex or poly (methyl methacrylate) (PMMA).[54] The soft templating approach uses ionic surfactant or amphiphilic block copolymer molecules that can self-assemble to micellar aggregates[55-57] after reaching a critical micellar concentration (CMC).[58, 59] Natural objects such as starch or nanocrystalline cellulose (NCC) can also be used as templates for nanoporosity.[60-62]

By using soft templates together with building blocks for a targeted material, nanostructured films or materials can be produced. The choice of building blocks depends on the material and can be salts, oligomers, sols or pre-synthesized nanocrystals. The building blocks have to be mobile during assembly to arrange around the templates (typically solutions or colloidal dispersions of the smaller building blocks are used), but have to be solidified after the assembly using physical or chemical ways to yield the targeted porous scaffold. One of the versatile

approaches to fabricate nanostructured materials using soft templates is a so called evaporation induced self-assembly (EISA), which is particularly suitable for the fabrication of thin films because of the low viscosity of the initial solutions. In an EISA process, the concentration of the surfactant molecules in the dispersion mixture is below the CMC of the surfactant and therefore no micelles are present in the beginning. Only after coating the dispersion on a substrate, either by simple drop-casting, doctor-blading, spin- or dip-coating and the evaporation of the solvent, the CMC is reached. For the micelle structure formation two main processes have been suggested how the surfactant molecules can interact with the building blocks. The so-called liquid crystal templating (LCT) is one of the mechanisms. Herein, the nanoparticles cover already formed micelles or other stabilized surfactant phases. The other mechanism is the cooperative self-assembly (CSA), where the surfactant molecule and the building blocks bind in a first step to each other by weak forces to form hybrid intermediates. In a second step, these intermediates act as independent surfactants and form micelles themselves. In reality both mechanisms are likely to occur simultaneously as they are both influenced by the chemistry of the system and the processing parameters. After complete solvent evaporation, the nanostructures can be obtained by calcination, where the templates are combusted and the nanostructured network is stabilized as the nanoparticles at least partly sinter together.[63, 64] A schematic drawing of the overall EISA process and the calcination can be seen in Figure 1.15. In general, films with very high specific surface area are achieved with this soft chemical approach, but most times this technique is limited to very thin film thicknesses. With thicker films the probability of crack formation or even film delamination is vastly increased.[63]

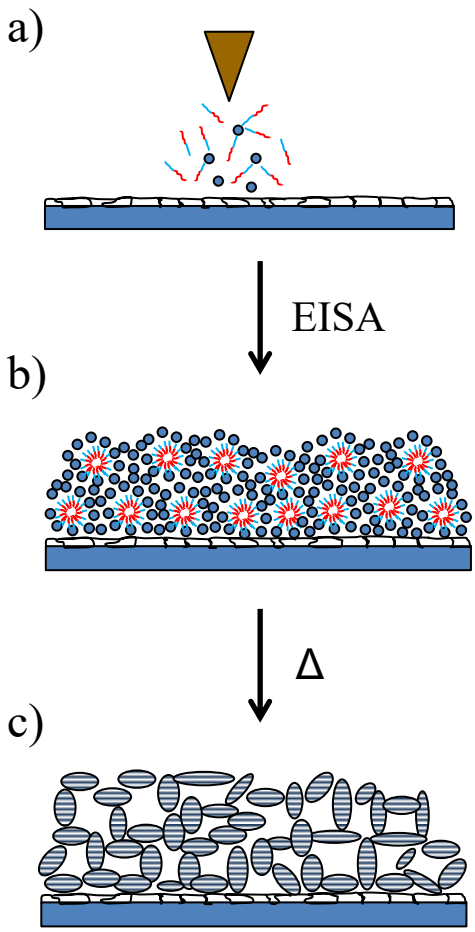

Figure 1.15: Nanoparticles and surfactant molecules are simultaneously coated in the same solvent suspension on a substrate (a). Nanoparticles arrange around micelles during the EISA process (b). During calcination the rest of the solvent evaporates, the template combusts, the nanocrystals grow, sinter together and finally result in a nanostructured film (c).

1.2.2.1 Block Copolymer

One of the most common surfactant molecules for soft templating via the EISA process are block copolymers. They are amphiphilic, i.e. containing hydrophilic as well as hydrophobic parts. The hydrophilic parts typically consist of poly (ethylene oxide) (PEO) whereas the hydrophobic parts are made of poly (propylene oxide), poly (ethylene-co-butylene) (KL), polystyrene (PS) or polybutadiene (PB). In polar solvents such as water or ethanol the hydrophilic parts try to keep contact with the solvent, while the hydrophobic parts turn towards the solvent-free interior of the formed micelle. Depending on the nature of the block copolymer, the solvent and the concentration, the micelles can self-assemble to different periodic mesophases such as lamellar, cubic, hexagonal ones or many others (see Figure 1.16). The size of the micelles can normally be influenced by the length of the hydrophobic chain and after combustion of the block copolymer, this templated porous structure is more or less preserved.[34, 55, 58, 59]

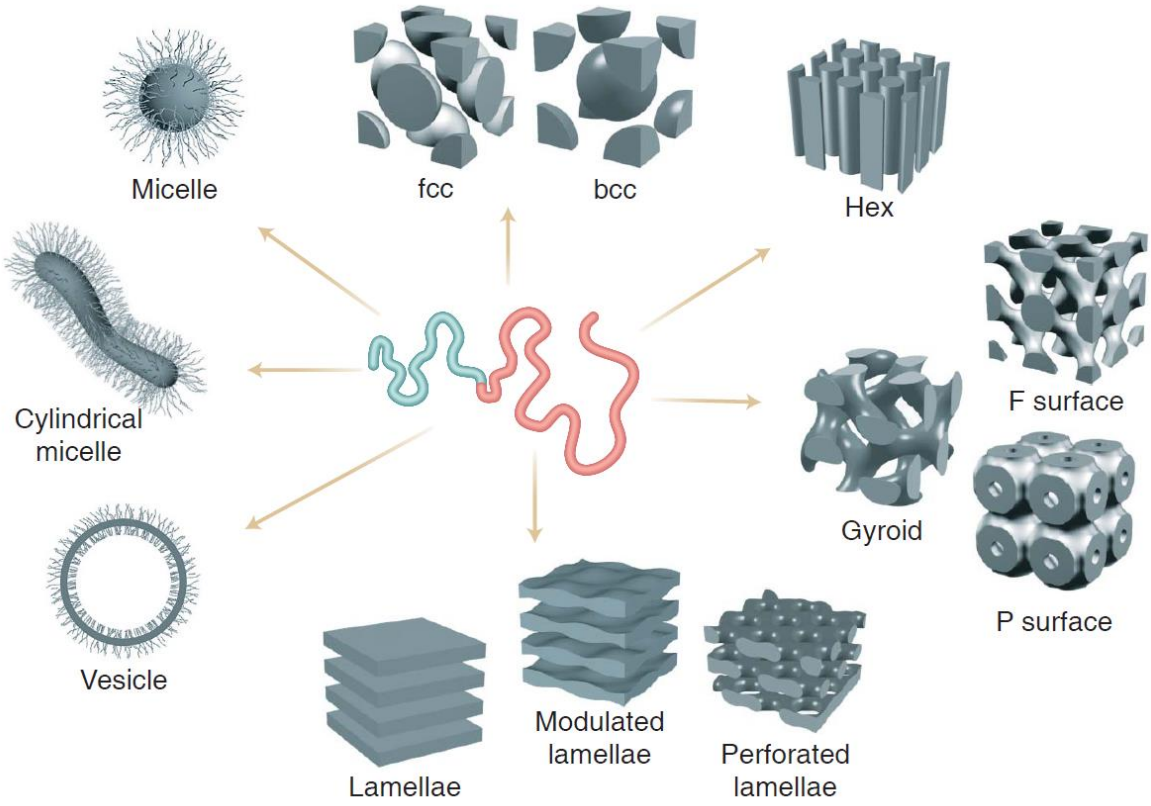

Figure 1.16: Self-organization of block copolymers. Block copolymers can form spherical and cylindrical micelles, vesicles, spheres with face-centered cubic (fcc) and body-centered cubic (bcc) packing, hexagonally packed cylinders, minimal surfaces (gyroid, F surface, and P surface), simple lamellae and modulated and perforated lamellae.[55]

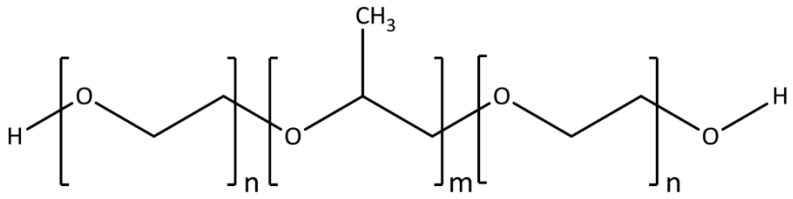

Figure 1.17: Structure of a poly(alkylene oxide) triblock copolymer of Pluronic® family.[65]

Some of the most common block copolymers are amphiphilic poly (alkylene oxide) triblock copolymers of the Pluronic® family, whose general structure can be seen in Figure 1.17. Pluronic® P123 is a type of triblock copolymer with 20 ethylene glycol units (n = 20) and 70 propylene glycol units (m = 70). For Pluronic® F127, the values change to n = 106 and m = 60.[66]

1.2.2.2 Nanocrystalline Cellulose

Figure 1.18: The cellulose-rich cotton fibers surrounding the cotton seeds.

Nanocrystalline cellulose (NCC), often named also cellulose nanocrystals, cellulose nanowhiskers, cellulose nanocrystallites and crystalline nanocellulose is a subunit of the natural cellulose within plants such as cotton (Figure 1.18) and bacteria.[67] Cellulose is solely built up of *β*-1,4-linked D-glucopyranose rings, where two *β*-D-glucopyranose rings form a so-called cellobiose unit as depicted in Figure 1.19. Herein, the *β*-D-glucopyranose units are rotated with respect to each other in a way that the glucosidic oxygens of adjacent rings point in different directions.[67]

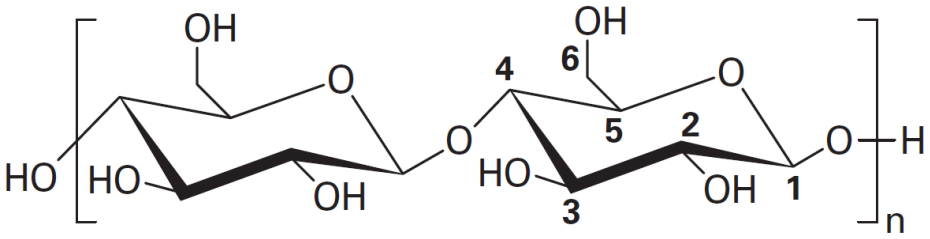

Figure 1.19: Basic chemical structure of cellulose.[67]

Natural cellulose consists of around 2000 – 27000 cellobiose units depending on the source, e.g. 5000 cellobiose units for wood cellulose and around 7500 for native cotton cellulose.[67] Furthermore, the presence of many hydroxyl groups along the *β*-D-glucopyranose backbone of the cellulose leads to the formation of inter- and intramolecular hydrogen bonds (see Figure 1.20) as well as the development of van-der-Waals forces between layers of connected chains.[67]

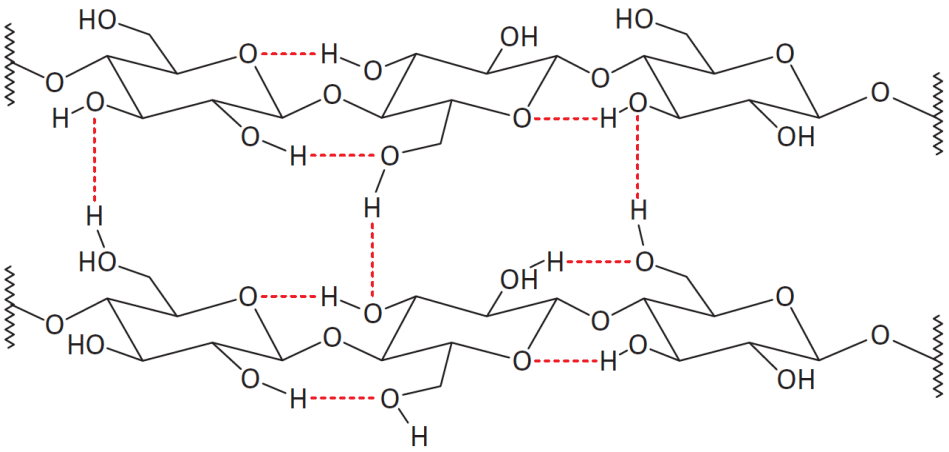

Figure 1.20: Hydrogen bond formation within and between cellulose chains.[67]

These two types of forces cause the formation of well-defined, ordered and crystalline microfibrils. Such microfibrils again agglomerate in larger fibrils which finally lead to the cellulose structure. In Figure 1.21 the hierarchy of cellulose and the supramolecular organization are schematized.[67]

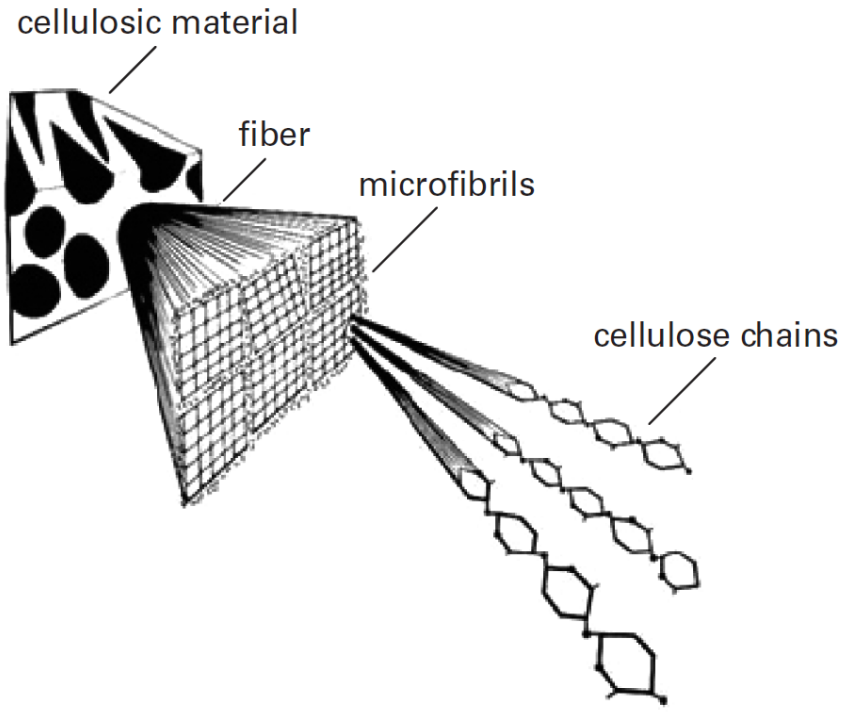

Figure 1.21: Hierarchical structure of cellulose.[67]

The width, the length, the shape as well as the crystallinity of the microfibrils depend on the source of the cellulose. However, cellulose microfibrils always show rod- or needle-like

morphology. The crystalline regions within cotton are 5-10 nm in width and 100-300 nm in length and can be isolated by acidic hydrolysis, for example with concentrated sulfuric acid. Amorphous, disordered or para-crystalline regions are hydrolyzed preferentially before the crystalline microfibril regions that stay intact. This product is called the NCC and is collected after the hydrolysis by subsequent dilution, precipitation, washing and centrifugation steps. Sulfuric acid as the hydrolyzation agent has the advantage of yielding well-dispersible NCC crystals due to the sulfurization of hydroxide groups with the formation of sulfate esters on the NCC surface. Deposition of NCC dispersions in solution (mainly aqueous) results either in randomly distributed NCC, or their self-assembly to chiral nematic phases. The self-assembly is strongly influenced by the concentration of NCC in the solution, by the ionic strength of other species in the solution as well as by temperature.[68]

The high dispersibility and the natural abundance of NCC make it an interesting templating agent for different materials such as metal oxides. Bio-templates like NCC act in a similar way as surfactant micelles. The metal oxide nanoparticles assemble around the NCC crystals that leave porosity after their combustion. NCC has been already successfully implemented in our group to template various oxides such as titania[60, 62] or hematite.[61] In Chapter 6 of this thesis the NCC biotemplation of NCM in various compositions is described.

1.3 Metal Oxides for LIBs

As already mentioned in section 1.1, a lot of metal oxides are promising candidates as anodes and cathodes for LIBs. In the following, the basic properties of metal oxides that were synthesized and used in this thesis are shortly described.

1.3.1 Cobalt (II) Oxide CoO and Derivatives

Cobalt(II)-oxide crystallizes in the rock-salt type crystal structure (see Figure 1.22). The Co^{2+}-ions occupy the octahedral voids within the face centered cubic lattice of the oxygen ions.

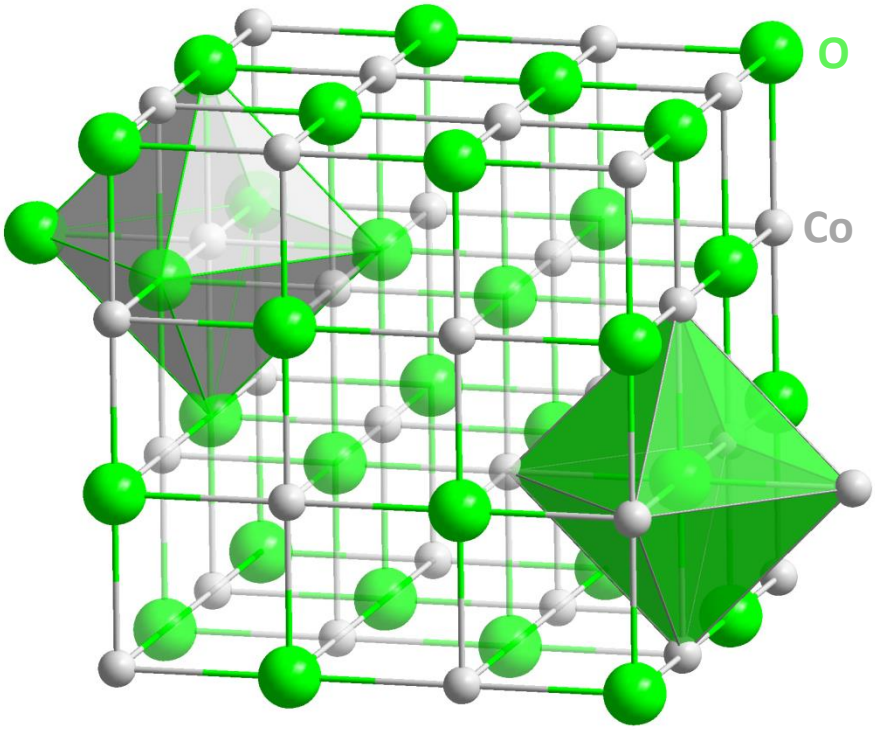

Figure 1.22: Schematic presentation of the CoO crystal structure including the respective coordination polyhedra.[69]

The properties of CoO, for instance its color that varies from olive green to red, depend on the particle size. . Commercially available CoO is mostly grayish.[70] Furthermore, bulk CoO shows antiferromagnetism, while CoO nanocrystals are weakly ferromagnetic or superparamagnetic.[71] CoO is a semiconductor with a band gap of approximately 2.5 eV.[72] When Co^{2+} ions in CoO are partly replaced by Li^{+}, the overall structure is preserved, but the adjacent cobalt ions are oxidized to Co^{3+} to compensate the charge and the band gap decreases to 2.0 eV for $Li_{0.2}Co_{0.8}O$.[72]

CoO can be used as an electrocatalyst for oxygen as well as the hydrogen evolution reaction in water splitting setups and are consequently potential electrode materials for overall water splitting devices.[73]

Moreover, CoO is a promising next-generation anode material for LIBs due to its high theoretical specific capacity of 716 mAh g^{-1} in the bulk caused by the conversion reaction described in Equation 1.8:[74]

$$\boldsymbol{CoO + 2Li^{+} + 2e^{-} \rightleftharpoons Co + Li_2O} \qquad 1.8$$

Until now, a practical use in LIBs is hindered by the significant volume change induced during the conversion reaction. This problem can possibly be solved by nanostructuring approaches.[74]

The synthesis of ultrasmall dispersible $Li_{0.15}Co_{0.85}O$ nanoparticles, their electrochemical applicability as a cathode and their use as precursor for the production of lithium cobalt oxide $LiCoO_2$ is described in Chapter 5.

Furthermore, in Chapter 6 the synthesis of ultrasmall nanoparticles of several derivatives of CoO through simultaneous substitution of different amounts of Co by Li, Ni and Mn is shown. The different rock-salt type $Li_wNi_xCo_yMn_z$ nanoparticles are used to produce lithium nickel cobalt manganese oxide $LiNi_xCo_yMn_zO_2$.

1.3.2 Cobalt (II, III) Oxide Co_3O_4

Co_3O_4 is normally a black solid and its formula can also be written as $Co^{II}Co^{III}{}_2O_4$. This makes it easily visible that it crystallizes in the typical spinel structure AB_2O_4.[75] Hereby, the O^{2-}-ions build up a cubic closed packing of a face centered cubic lattice, where the high-spin Co^{2+}-ions occupy one eighth of the tetrahedral sites and the low-spin Co^{3+}-ions half of the octahedral sites (see Figure 1.23).[76]

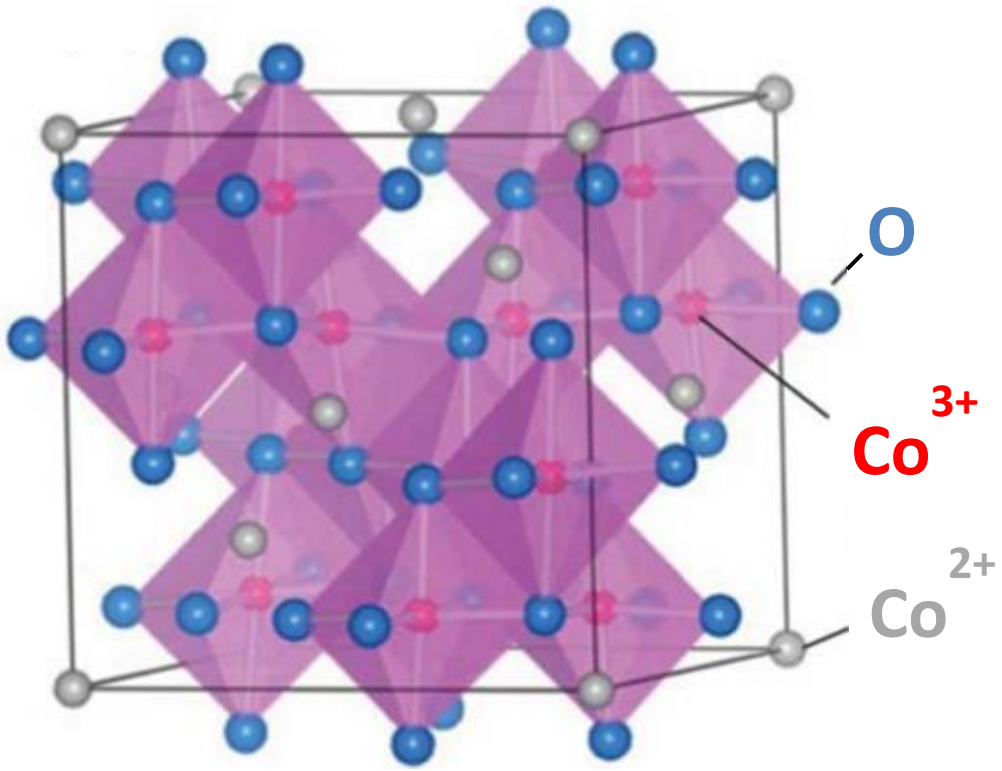

Figure 1.23: Schematic presentation of the spinel structure of Co_3O_4. The octahedral sites are highlighted.[77]

Since all electrons in Co^{3+} are paired, only three unpaired electrons of the Co^{2+} contribute to the overall magnetic moment. Co_3O_4 is paramagnetic at room temperature, but becomes antiferromagnetic below 30–40 K due to a coupling of the opposite spins of adjacent Co^{2+}-ions. For nanoparticles, the Néel temperature is lower with 26 K in comparison to the bulk material.[78-80]

Co_3O_4 exhibits an indirect band gap of 1.60–1.65 eV and a direct band gap of 2.10 -2.40 eV, and due to that it has been considered as a charge transfer insulator. However, p-doping at room temperature or other intrinsic effects at higher temperatures make it conductive.[81] The indirect

band gap is caused by a d-d electron transfer between the Co^{3+} and the Co^{2+}. A charge transfer process between the 2p level of O^{2-} and the d-orbitals of Co^{2+} produces the direct band gap. Another electron transition was detected at 2.80 eV that is attributed to an exchange of O^{2-} 2p and the energetically higher d-levels of Co^{3+}.[72, 76, 82]

Co_3O_4 is of great interest as an anode material in lithium ion batteries due to the high theoretical specific capacity of 892 mAh g^{-1} as a bulk.[74, 83-86] Herein, the conversion reaction is according to Equation 1.9:[74]

$$\boldsymbol{Co_3O_4 + 8Li^+ + 8e^- \rightleftharpoons 3Co + 4Li_2O} \qquad 1.9$$

The conversion reaction in bulk Co_3O_4 suffers however from the same shortcomings as other conversion-type compounds, namely large volume expansion and therefore a low initial coulombic efficiency and a poor cycling stability. This drawbacks can be efficiently mitigated by nanoscaling the Co_3O_4 phase. In fact, the research on Co3O4 for battery applications is focused mainly on the nanostructured materials. Other applications for Co_3O_4 are for example found as heterogeneous catalysts,[87, 88] in solar cells,[89] as magnetic materials,[90] as ceramic pigments[91] and as a compound in electrochromic devices.[92] Furthermore, Co_3O_4 recently gained attraction as a co-catalyst in the photoelectrochemical oxygen evolution reaction.[93-96] Especially, at photoanodes based on a mixture of Co_3O_4 and hematite a more efficient charge separation at the interface was found.[94, 97, 98] In Chapter 3 of this thesis the synthesis of ultrasmall Co_3O_4 nanoparticles and their performance as electrochemical water splitting material is elucidated.

1.3.3 Tin(IV) Oxide SnO_2 and Antimony(V)-doped Tin(IV) Oxide $Sb_xSn_{1-x}O_2$ (ATO)

SnO_2 crystallizes in several different polymorphs. The rutile-type ($P4_2/mnm$) is the most commonly available and stable phase (see Figure 1.24).[99] A low percentage of Sn^{4+}-ions (r = 0.69 Å) can be easily substituted in this structure by Sb^{5+}-ions (r = 0.60 Å). Only higher doping concentrations can lead to an occupation of Sb ions at interstitial sites and the fraction of Sb^{3+} species (r = 0.76 Å) increases with respect to Sb^{5+}.[100, 101]

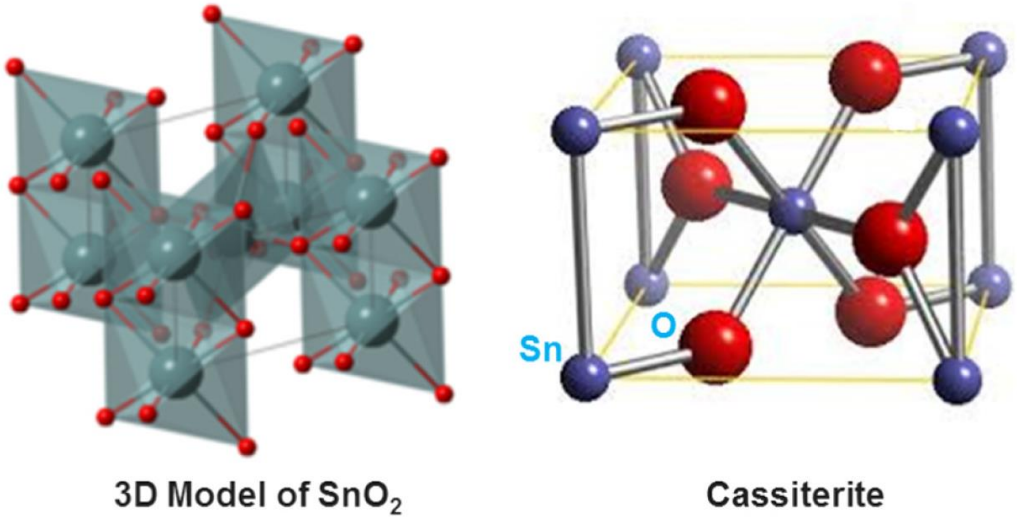

Figure 1.24: Rutile-type structure of cassiterite SnO_2.[102]

SnO_2 is an n-type semiconductor with a large band gap of 3.6 eV. Nevertheless, the formation energy of oxygen vacancies as well as tin interstitials is very low.[99, 100] This phenomenon explains the rather good conductivity that SnO_2 mostly exhibits. The conductivity of SnO_2 can be increased even more by using extrinsic dopants such as the already mentioned antimony.[100, 103, 104] Hereby, the incorporation of Sb^{5+}-ions introduces donor states located close to the conduction band of SnO_2 and causes the formation of additional charge carriers. The integration of Sb^{3+}-ions in contrast leads to the creation of acceptor states. Since the donor and the acceptor states might compensate each other, the overall Sb concentration and the consequent ratio of Sb^{5+} to Sb^{3+} has an important impact on the conductance.[100, 104] The relatively large band gap leads to transparency and the material exhibits a rather good conductivity which is a characteristic especially for Group IV elements of the periodic table. Their resulting oxides are normally referred to as transparent conducting oxides (TCO).[99]

Because of these remarkable properties, the SnO_2–based TCO (mainly fluorine-doped SnO_2, FTO as a commercial product) and ATO can be found in a broad range of applications such as solar cells,[105-109] chemical sensors[110-114] or catalytic support materials.[115, 116] Besides the transparency, the conductivity is an interesting feature for possible application as anode material in LIBs. Furthermore, SnO_2 also shows a low discharge potential and a high specific capacity.[117] The anodic reaction contains a conversion (Equation 1.10) and a consequent alloying step (Equation 1.11) that can be described as follows:

$$\boldsymbol{SnO_2 + 4Li^+ + 4e^- \rightleftharpoons Sn + 2Li_2O} \qquad 1.10$$

$$\boldsymbol{Sn + 4.4Li^+ + 4.4e^- \rightleftharpoons Li_{4.4}Sn} \qquad 1.11$$

In bulk SnO_2 only the alloying reaction is reversible, leading to a specific reversible capacity of 782 mAh g^{-1}.[117, 118] If nanosized SnO_2 is used, even the conversion reaction is reversible or at least partly reversible with an overall specific capacity for both steps of 1494 mAh g^{-1}.[118, 119] The reversibility and the electrochemical performance in general can be further improved by increasing the conductivity of SnO_2, for example by doping with Sb. The ATO reacts with lithium (Equation 4.1 and 4.2) in a similar way as it was mentioned for the pure SnO_2.[120]

The major drawback of SnO_2 or ATO is the huge volume change of up to 300% during the alloying step leading to a pulverization and re-aggregation of the active particles. As a consequence, every additional cycle leads to a deterioration of the electrical contact between the active material and the surrounding conducting matrix of the electrode ink, finally resulting in a poor cyclability of the SnO_2 and ATO based LIBs.[117, 121] Making composites of SnO_2 and ATO, respectively, and flexible carbonaceous supports, such as graphene, can help to solve the large volume change as this can be buffered by the support material and the lifetime of the LIB is prolonged (Figure 1.25).[122] This is further discussed in Chapter 4 of this thesis, where the synthesis as well as the electrochemical superior performance of SnO_2/graphene and even more of ATO/graphene composites is demonstrated.

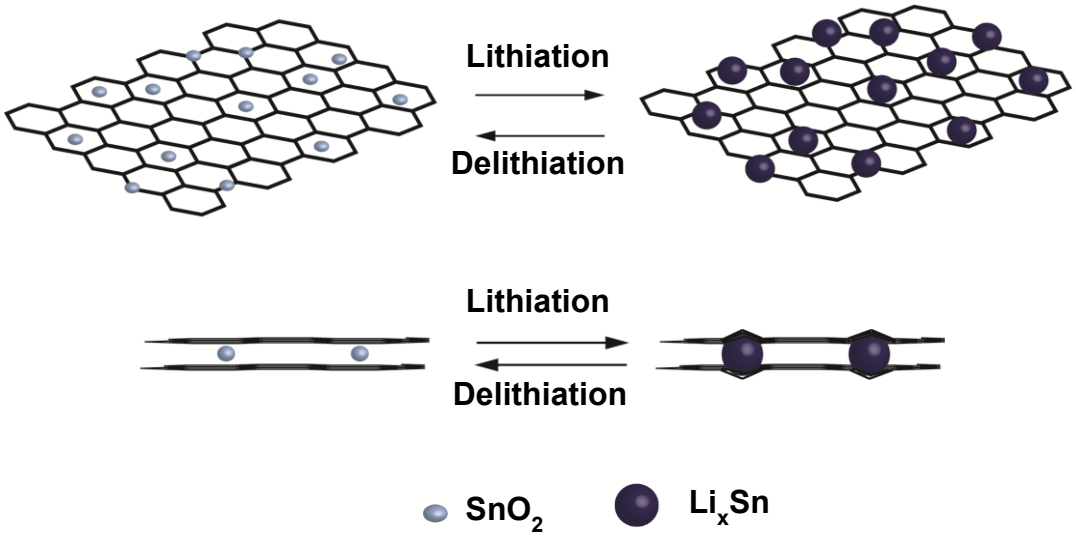

Figure 1.25: Schematic description of the lithiation/delithiation process in SnO_2/graphene composites.

1.3.4 Lithium Cobalt(III) Oxide $LiCoO_2$ (LCO)

$LiCoO_2$ crystallizes in two main polymorphs that are named after the different synthesis temperatures they were synthesized originally. The structures of both phases, high-temperature (HT) and low-temperature (LT) are depicted in Figure 1.26.

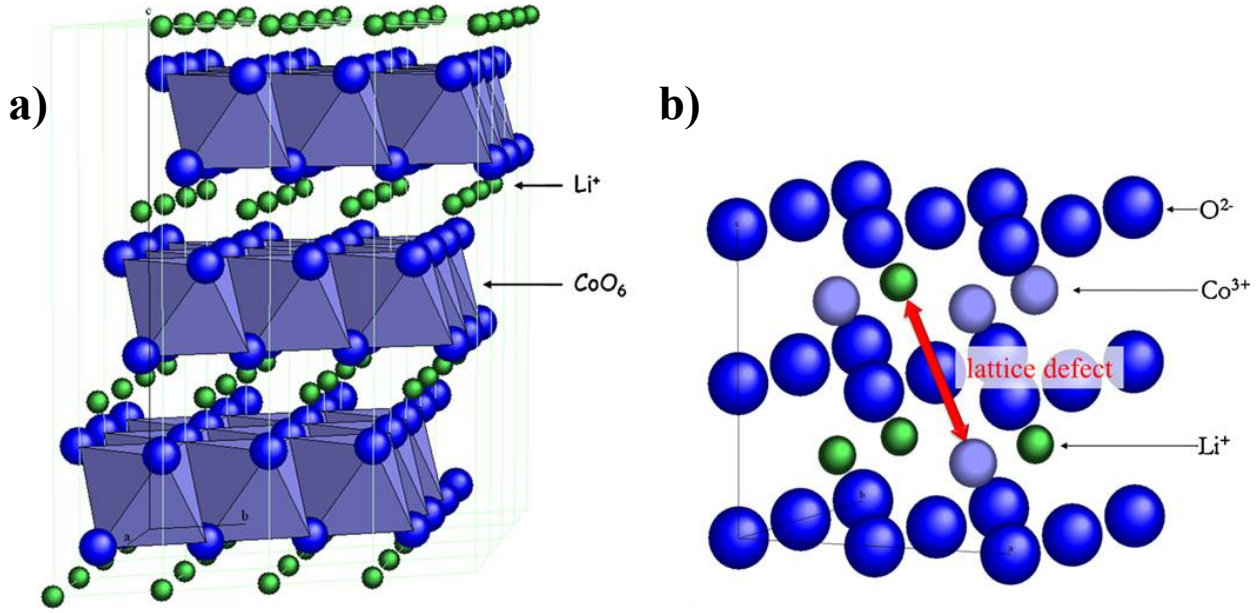

Figure 1.26: Schematic structure for HT-LCO (a) and LT-LCO (b).[123]

HT-LCO crystallizes in the α-$NaFeO_2$ or also known as the layered rock-salt structure type. It was originally synthesized in a solid state reaction above 850 °C by calcination of the respective metal carbonates.[124, 125] The space group of this structure is $R\bar{3}m$, where Li^+- and Co^{3+}-ions are distributed at interstitial octahedral sites of a cubic close packed oxygen array. This leads to CoO_2 layers of edge-sharing [CoO_6] octahedrons where the Li^+-ions are distributed in between.[4] Modifications are produced by different stacking of the CoO_2 layers, whereby the ABC stacking or O3 type is the most stable modification.[126]

In contrast to this, LT-$LiCoO_2$ can be synthesized in solid state reactions at lower temperatures at around 400 °C and crystallizes in the $Li_2Ti_2O_4$-type structure.[125, 127] It is a modified cubic spinel structure since both Li^+- and the Co^{3+}-ions are at the interstitial octahedral sites of the face centered cubic array of oxygens and not at the tetrahedral sites, like in a normal spinel. Furthermore, the Li^+- and Co^{3+}-ions can also randomly mix, which means that pure cation layers of the same type will not form (see Figure 1.26b).[128-130]

In both modifications, Co^{3+}-ions are in a non-magnetic ground state because of the low-spin electron modification, resulting in the pairing of all valence electrons. LCO is a semiconductor with a band gap of around 2.4 eV.[72, 129, 131]

Especially in HT-LCO, an oxygen-mediated 4p-3d intersite hybridization can occur between single cobalt ions, which is more likely with decreasing particle size. Consequently, particles with a size smaller than the critical 15 nm can have a drastically reduced electrochemical efficiency of the lithium insertion/extraction process.[132] Additionally, below this critical size a lattice expansion due to a reduction of the Co^{3+}- to Co^{2+}-ions at the surface worsens the performance of such extremely small nanoparticles. [132-135] In opposite to that, the intersite hybridization does not occur in such an extent in LT-LCO since the CoO_6 clusters are more isolated.[129]

HT-LCOs is mainly used as a cathode material in LIBs. Mizushima *et al.* showed for the first time the reversible extraction of lithium ions from the HT-LCO host structure and later this material was implanted in the first commercial LIB.[8, 136] Theoretically, the construction of a Li/HT-LCO cell would lead to discharge voltages up to 4.7 V and a specific capacity of around 280 mAh g^{-1} for an extraction of 93% lithium. However, practically only about the half of Li^+-ions can be extracted to guarantee a good reversibility which limits the overall specific capacity to around 140 mAh g^{-1} and the maximum potential to around 4.2 V.[4] During the delithiation step Co^{3+} is oxidized to Co^{4+}, which exhibits a d^5 low-spin configuration, and the space between the CoO_2 layers increases due to electrostatic repulsion. This leads to an increased lattice constant *c* by around 2%. In opposite to that, the Co-Co distances decrease and interactions across the edge-shared CoO_6 octahedrons arise because of the partially filled t_{2g} of the Co^{4+}-ions. Here, a dispersion of the electronic energy bands happens and hence an overlap of valence and conduction bands. After the extraction of around 25% of the Li^+-ions, HT-LCO is no longer a semiconductor, but shows metallic character. [4, 130, 137-143] It is also assumed that the metallic behavior of HT-Li_xCoO_2 caused by the lithium removal in the first cycle does not revert to its original insulating state in the following redox cycles.[141] The reversibility of HT-LCO is destroyed above 4.2 V *versus* Li/Li^+ when over 50% of all Li^+-ions are extracted. This can cause the formation of the modified spinel type on the surface and a large concentration of the unstable Co^{4+}-ions destroys the crystallinity of the material.[27, 137] Additionally, at higher positive voltages the probability of the electrolyte combustion at the surface of the HT-LCO increases significantly

resulting in the formation of CO_2, CO, methane, ethylene, water, ethane, oxygen and a cathodic SEI on HT-LCO with components such as ROLi and $ROCO_2Li$ and Co_3O_4, which drastically affects the electrochemical performance of the LIB. [144-146]

In opposite to the HT-LCO, the structure of modified spinel of LT-LCO is more stable and only undergoes volume changes of a factor of 0.2% between 3.4 V and 3.7 V which corresponds to a lithium extraction of up to 50%. These potential values are below those of HT-LCO and also the lithium ion diffusion coefficient within LT-LCO is by magnitudes lower than that of HT-LCO. All these points and the reduced reversibility of lithium insertion/extraction during multiple cycling make HT-LCO the polymorph of choice as cathode material for LIBs.[13, 127, 147]

In Chapter 5 of this thesis, the synthesis of HT-LCO nanoparticles is described which show excellent performance at high power conditions.

1.3.5 Lithium Nickel Cobalt Manganese Oxide $Li[Ni_xCo_yMn_z]O_2$ (NCM/NMC)

$Li[Ni_xCo_yMn_z]O_2$ (NCM*abc*, $x = a/10$, $y = b/10$, $z = c/10$) with x + y +z = 1, can be derived from HT-LCO just by partially or fully replacing cobalt ions by manganese and/or nickel ions. This compound can be seen as a solid solution of $LiCoO_2$, $LiNiO_2$ (LNO) and $LiMnO_2$ (LMO) in different ratios.[148] Hereby, the hexagonal layered α-$NaFeO_2$ structure with the space group $R\bar{3}m$ of HT-LCO is preserved, but manganese and especially nickel can also occupy lithium sites and not only cobalt sites during substitution.[149-152] This disorder effect of the metal ions is explained with the similarity of the ionic radii of Ni^{2+} (69 pm) and Li^+ (76 pm) in octahedral coordination which even increases with rising nickel content.[150, 152-154] Reaching a Ni content of only 2% in the Li layers limits the Li^+-ion diffusion significantly and therefore decreases the capacity and finally the cycle lifetime.[155-159] The substitution is a way to reduce the overall costs of the HT-LCO material, since cobalt is very rare in the geosphere (37ppm) in contrast to nickel (0.015wt.%) and manganese (0.085wt.%).[160] However, the products of total substitution, LNO and LMO, suffer from different issues. Thus, pure LNO cannot be used as a cathode because of high oxygen pressure at low lithium content generated at positive potentials. The generated oxygen can react with the electrolyte of the LIB in a highly exothermal reaction which is a serious safety concern. Furthermore, LNO undergoes multiple phase reactions during electrochemical cycling that cause drastic structural degradation. The major drawback of LMO is its electrochemical transformation into the spinel structure (space group $Fd\bar{3}m$).[161-163]

The combination of the three transition metals within one compound is an opportunity to compensate the different disadvantages every element exhibits on its own and to harness the positive properties each element brings in.[27, 164-168] Nickel, for example, features high capacity but poor thermal stability, whereas manganese maintains excellent cycle performance and safety but provides lower capacity, while cobalt offers good rate capability. It is always a trade-off between capacity and safety (see Figure 1.27). On the one hand, for higher specific discharge capacities the Ni content should be elevated in NCM materials, as Ni is the main redox species. On the other hand, Ni negatively affects the cyclability due to an increasing interfacial resistance, since phase transitions and surface degradation take place during cycling.[161-163, 169]

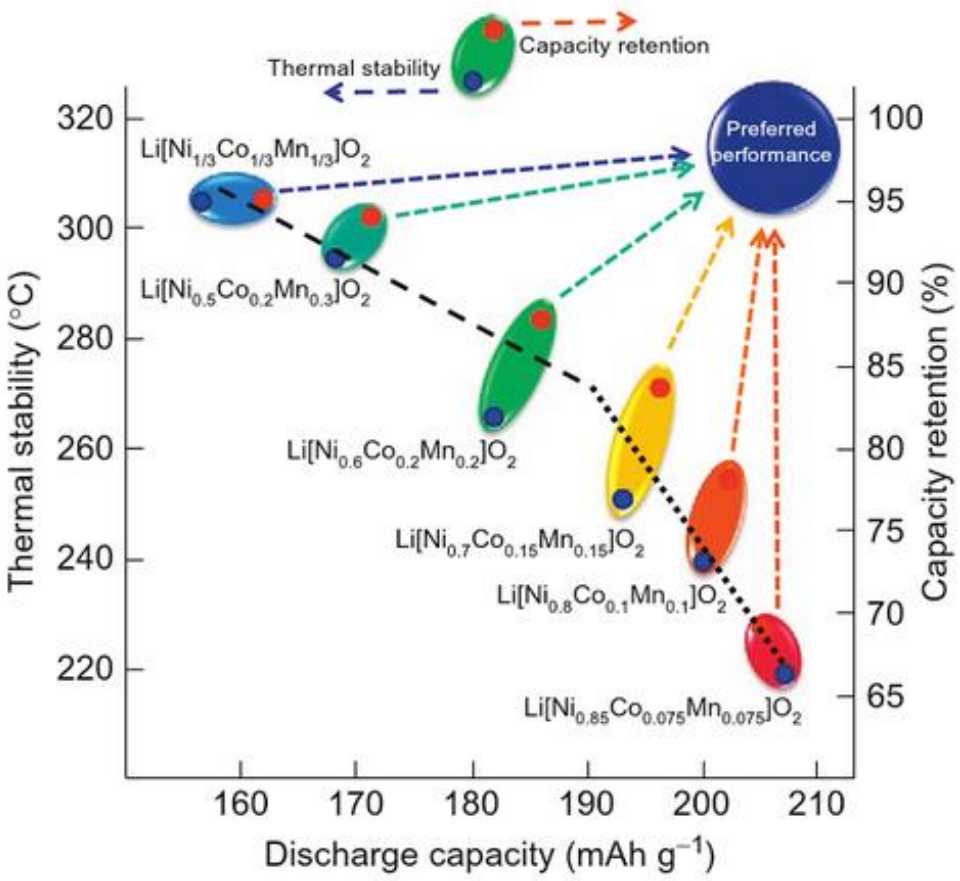

Figure 1.27: Map of the relationship between discharge capacity, thermal stability and capacity retention of $Li/Li(Ni_xMn_yCo_z)O_2$.[170]

For $Li(Ni_{1/3}\ Co_{1/3}Mn_{1/3})O_2$ or NCM333 X-ray photoelectron spectroscopy (XPS) studies revealed that the predominant oxidation states for Ni, Co and Mn in this compound are +II, +III, and +IV, respectively. Consequently, the redox processes found in NCM333 correspond to Ni^{2+}/Ni^{4+} and Co^{3+}/Co^{4+}, while Mn^{4+} does not take part in the redox process.[171] The redox inactivity of Mn^{4+} is the major reason for its structure-stabilizing function. Mn^{4+} stabilizes the crystal structure of NCM, minimizes volume changes and prevents phase transitions.[172, 173] With decreasing Co and increasing Ni content the oxidation states change more and more to +III for all transition metals. For NCM424, 80% of the nickel and manganese are present as Ni^{2+} and Mn^{4+}, and remaining 20% of Mn and all cobalt ions are present in a +III state.[174] Furthermore, X-ray absorption near edge structure (XANES) spectra of NCM811showed only oxidation states of +III for Ni, Co and Mn.[169]

As NCMs are of great interest as cathode materials, the achievable capacities are important for the practical use. In general, one would estimate theoretical specific capacities for all NCMs

around 280 mAh g^{-1} for full delithiation, but the practical values are always smaller. NCM333, for example, can deliver specific capacities from 150 mAh g^{-1} to 188 mAh g^{-1} for cycling up to 4.2 V or 4.6 V *vs.* Li/Li^+, respectively, which is more than for pure LCO. Moreover, NCM333 shows more stable cycling at high voltage.[166, 175] For NCM811 even values of up to 192 mAh g^{-1} for cycling between 2.7 V and 4.3 V *vs.* Li/Li^+ are reached.[176]

In Chapter 6 of this thesis, the synthesis of novel nanocellulose-templated NCM nanostructures with different compositions is described.

1.4 References

[1] C. Liu, F. Li, L. P. Ma, H. M. Cheng. *Adv Mater* **2010**, *22*, E28-62.
[2] M. Winter, R. J. Brodd. *Chem Rev* **2004**, *104*, 4245-4269.
[3] J.-M. Tarascon, M. Armand. *Nature* **2001**, *414*, 359-367.
[4] M. Winter, J. O. Besenhard, M. E. Spahr, P. Novák. *Adv Mater* **1998**, *10*, 725-763.
[5] A. F. Ghoniem. *Progress in Energy and Combustion Science* **2011**, *37*, 15-51.
[6] J. B. Goodenough, K.-S. Park. *J Am Chem Soc* **2013**, *135*, 1167-1176.
[7] B. Scrosati. *Journal of Solid State Electrochemistry* **2011**, *15*, 1623-1630.
[8] K. Ozawa. *Solid State Ionics* **1994**, *69*, 212-221.
[9] M. T. McDowell, S. W. Lee, W. D. Nix, Y. Cui. *Adv Mater* **2013**, *25*, 4966-4985.
[10] K. Kang, Y. S. Meng, J. Breger, C. P. Grey, G. Ceder. *Science* **2006**, *311*, 977-980.
[11] A. Yoshino. *Angewandte Chemie International Edition* **2012**, *51*, 5798-5800.
[12] A. Eftekhari. *ACS Sustainable Chemistry & Engineering* **2018**.
[13] M. Winter, J. O. Besenhard. *Chemie in unserer Zeit* **1999**, *33*, 320-332.
[14] S. Goriparti, E. Miele, F. De Angelis, E. Di Fabrizio, R. Proietti Zaccaria, C. Capiglia. *Journal of Power Sources* **2014**, *257*, 421-443.
[15] M. R. Palacín. *Chemical Society Reviews* **2009**, *38*, 2565-2575.
[16] E. Ferg, R. J. Gummow, A. de Kock, M. M. Thackeray. *Journal of The Electrochemical Society* **1994**, *141*, L147-L150.
[17] J. M. Szeifert, J. M. Feckl, D. Fattakhova-Rohlfing, Y. Liu, V. Kalousek, J. Rathousky, T. Bein. *J Am Chem Soc* **2010**, *132*, 12605-12611.
[18] J. M. Feckl, K. Fominykh, M. Döblinger, D. Fattakhova-Rohlfing, T. Bein. *Angewandte Chemie International Edition* **2012**, *51*, 7459-7463.
[19] B. Guo, J. Shu, Z. Wang, H. Yang, L. Shi, Y. Liu, L. Chen. *Electrochemistry Communications* **2008**, *10*, 1876-1878.
[20] Y. Yao, J. Zhang, L. Xue, T. Huang, A. Yu. *Journal of Power Sources* **2011**, *196*, 10240-10243.
[21] P. Lv, H. Zhao, J. Wang, X. Liu, T. Zhang, Q. Xia. *Journal of Power Sources* **2013**, *237*, 291-294.
[22] J. Meng, Y. Cao, Y. Suo, Y. Liu, J. Zhang, X. Zheng. *Electrochimica Acta* **2015**, *176*, 1001-1009.
[23] J. B. Goodenough, Y. Kim. *Chemistry of Materials* **2010**, *22*, 587-603.
[24] V. Aravindan, J. Gnanaraj, S. Madhavi, H.-K. Liu. *Chemistry – A European Journal* **2011**, *17*, 14326-14346.
[25] M. Armand, J. M. Tarascon. *Nature* **2008**, *451*, 652-657.
[26] F. Zheng, M. Kotobuki, S. Song, M. O. Lai, L. Lu. *Journal of Power Sources* **2018**, *389*, 198-213.
[27] M. S. Whittingham. *Chemical reviews* **2004**, *104*, 4271-4302.
[28] V. E. Fedorov, S. B. Artemkina, E. D. Grayfer, N. G. Naumov, Y. V. Mironov, A. I. Bulavchenko, V. I. Zaikovskii, I. V. Antonova, A. I. Komonov, M. V. Medvedev. *Journal of Materials Chemistry C* **2014**, *2*, 5479-5486.
[29] N. Nitta, F. Wu, J. T. Lee, G. Yushin. *Materials Today* **2015**, *18*, 252-264.
[30] W. Li, B. Song, A. Manthiram. *Chemical Society Reviews* **2017**, *46*, 3006-3059.
[31] R. Chen, T. Zhao, X. Zhang, L. Li, F. Wu. *Nanoscale Horizons* **2016**, *1*, 423-444.
[32] P. G. Bruce, B. Scrosati, J.-M. Tarascon. *Angewandte Chemie International Edition* **2008**, *47*, 2930-2946.

[33] P. Roy, S. K. Srivastava. *Journal of Materials Chemistry A* **2015**, *3*, 2454-2484.
[34] G. Cao. *Nanostructures & Nanomaterials: Synthesis, Properties & Applications*. Imperial College Press: London, 2004.
[35] M. Rajamathi, R. Seshadri. *Current Opinion in Solid State and Materials Science* **2002**, *6*, 337-345.
[36] K. Byrappa, T. Adschiri. *Progress in Crystal Growth and Characterization of Materials* **2007**, *53*, 117-166.
[37] M. Niederberger, N. Pinna. *Metal Oxide Nanoparticles in Organic Solvents: Synthesis, Formation, Assembly and Application*. Springer London, 2009.
[38] M. Niederberger, M. H. Bartl, G. D. Stucky. *Chemistry of Materials* **2002**, *14*, 4364-4370.
[39] M. Niederberger, M. H. Bartl, G. D. Stucky. *J Am Chem Soc* **2002**, *124*, 13642-13643.
[40] N. Pinna, M. Antonietti, M. Niederberger. *Colloids and Surfaces A: Physicochemical and Engineering Aspects* **2004**, *250*, 211-213.
[41] M. Niederberger, G. Garnweitner, J. Buha, J. Polleux, J. Ba, N. Pinna. *Journal of Sol-Gel Science and Technology* **2006**, *40*, 259-266.
[42] N. Pinna, M. Karmaoui, M.-G. Willinger. *Journal of Sol-Gel Science and Technology* **2011**, *57*, 323-329.
[43] B. Ludi, M. J. Süess, I. A. Werner, M. Niederberger. *Nanoscale* **2012**, *4*, 1982-1995.
[44] B. Ludi, I. Olliges-Stadler, M. D. Rossell, M. Niederberger. *Chemical Communications* **2011**, *47*, 5280-5282.
[45] N. Shi, W. Cheng, H. Zhou, T. Fan, M. Niederberger. *Chemical Communications* **2015**, *51*, 1338-1340.
[46] Y. Liu, J. M. Szeifert, J. M. Feckl, B. Mandelmeier, J. Rathousky, O. Hayden, D. Fattakhova-Rohlfing, T. Bein. *ACS Nano* **2010**, *4*, 5373-5381.
[47] K. Fominykh, J. M. Feckl, J. Sicklinger, M. Döblinger, S. Böcklein, J. Ziegler, L. Peter, J. Rathousky, E.-W. Scheidt, T. Bein, D. Fattakhova-Rohlfing. *Advanced Functional Materials* **2014**, *24*, 3123-3129.
[48] Y. Liu, K. Peters, B. Mandlmeier, A. Müller, K. Fominykh, J. Rathousky, C. Scheu, D. Fattakhova-Rohlfing. *Electrochimica Acta* **2014**, *140*, 108-115.
[49] J. M. Feckl, H. K. Dunn, P. M. Zehetmaier, A. Müller, S. R. Pendlebury, P. Zeller, *et al.* *Advanced Materials Interfaces* **2015**, *2*, 1500358-n/a.
[50] K. Fominykh, P. Chernev, I. Zaharieva, J. Sicklinger, G. Stefanic, M. Döblinger, A. Müller, A. Pokharel, S. Böcklein, C. Scheu, T. Bein, D. Fattakhova-Rohlfing. *ACS Nano* **2015**, *9*, 5180-5188.
[51] K. Peters, P. Zeller, G. Stefanic, V. Skoromets, H. Němec, P. Kužel, D. Fattakhova-Rohlfing. *Chemistry of Materials* **2015**, *27*, 1090-1099.
[52] K. Fominykh, G. C. Tok, P. Zeller, H. Hajiyani, T. Miller, M. Döblinger, R. Pentcheva, T. Bein, D. Fattakhova-Rohlfing. *Advanced Functional Materials* **2017**, *27*, 1605121-n/a.
[53] G. Garnweitner, M. Niederberger. *Journal of the American Ceramic Society* **2006**, *89*, 1801-1808.
[54] Y. Ren, Z. Ma, P. G. Bruce. *Chemical Society Reviews* **2012**, *41*, 4909-4927.
[55] D. G. Bucknall, H. L. Anderson. *Science* **2003**, *302*, 1904-1905.
[56] S. W. Boettcher, J. Fan, C.-K. Tsung, Q. Shi, G. D. Stucky. *Accounts of Chemical Research* **2007**, *40*, 784-792.
[57] C. Sanchez, C. Boissière, D. Grosso, C. Laberty, L. Nicole. *Chemistry of Materials* **2008**, *20*, 682-737.
[58] S. Förster, M. Antonietti. *Adv Mater* **1998**, *10*, 195-217.
[59] C. J. Brinker, Y. Lu, A. Sellinger, H. Fan. *Adv Mater* **1999**, *11*, 579-585.

[60] A. Ivanova, D. Fattakhova-Rohlfing, B. E. Kayaalp, J. Rathouský, T. Bein. *J Am Chem Soc* **2014**, *136*, 5930-5937.
[61] A. Ivanova, K. Fominykh, D. Fattakhova-Rohlfing, P. Zeller, M. Döblinger, T. Bein. *Inorg Chem* **2015**, *54*, 1129-1135.
[62] A. Ivanova, M. C. Fravventura, D. Fattakhova-Rohlfing, J. Rathouský, L. Movsesyan, P. Ganter, T. J. Savenije, T. Bein. *Chemistry of Materials* **2015**, *27*, 6205-6212.
[63] M. Zukalová, A. Zukal, L. Kavan, M. K. Nazeeruddin, P. Liska, M. Grätzel. *Nano Lett* **2005**, *5*, 1789-1792.
[64] B. F. R. Smarsly, D. Evaporation-Induced Self-Assembly for the Preparation of Porous Metal Oxide Films. In: D. B. Mitzi (ed). *Solution Processing of Inorganic Materials*, 2008.
[65] J. Sicklinger. Master thesis, LMU Munich **2013**.
[66] A. A. Ismail, D. W. Bahnemann. *Journal of Materials Chemistry* **2011**, *21*, 11686-11707.
[67] A. Dufresne. *Nanocellulose, From Nature to High Performance Tailored Materials*, 2012.
[68] Y. Habibi, L. A. Lucia, O. J. Rojas. *Chem Rev* **2010**, *110*, 3479-3500.
[69] https://upload.wikimedia.org/wikipedia/commons/c/c0/NaCl_polyhedra.png (retrieved 10.09.2018 16:00).
[70] D. L. Perry. *Handbook of Inorganic Compounds, Second Edition*. CRC Press, 2016.
[71] K. Sinkó, G. Szabó, M. Zrínyi. *J Nanosci Nanotechnol* **2011**, *11*, 4127-4135.
[72] J. van Elp, J. Wieland, H. Eskes, P. Kuiper, G. Sawatzky, F. de Groot, T. Turner. *Physical Review B* **1991**, *44*, 6090-6103.
[73] H. Wang, H.-W. Lee, Y. Deng, Z. Lu, P.-C. Hsu, Y. Liu, D. Lin, Y. Cui. *Nature Communications* **2015**, *6*, 7261.
[74] S. Xiong, J. S. Chen, X. W. Lou, H. C. Zeng. *Advanced Functional Materials* **2012**, *22*, 861-871.
[75] W. L. Smith, A. D. Hobson. *Acta Cristallographica Section B* **1973**, *29*, 362-363.
[76] K. J. Kim, Y. R. Park. *Solid State Communications* **2003**, *127*, 25-28.
[77] K. Mukai, Y. Ikedo, K. Kamazawa, J. H. Brewer, E. J. Ansaldo, K. H. Chow, M. Månsson, J. Sugiyama. *RSC Advances* **2013**, *3*, 11634-11639.
[78] W. L. Roth. *Journal of Physics and Chemistry of Solids* **1963**, *25*, 1-10.
[79] P. Dutta, M. S. Seehra, S. Thota, J. Kumar. *Journal of Physics: Condensed Matter* **2008**, *20*, 015218.
[80] W. Kündig, M. Kobelt, H. Appel, G. Constabaris, R. H. Lindquist. *Journal of Physics and Chemistry of Solids* **1969**, *30*, 819-826.
[81] A. Kaczmarska, Z. Grzesik, S. Mrowec. *High Temperature Materials and Processes* **2012**, *31*.
[82] V. R. Shinde, S. B. Mahadik, T. P. Gujar, C. D. Lokhande. *Applied Surface Science* **2006**, *252*, 7487-7492.
[83] X. W. Lou, D. Deng, J. Y. Lee, J. Feng, L. A. Archer. *Adv Mater* **2008**, *20*, 258-262.
[84] X. W. Lou, D. Deng, J. Y. Lee, L. A. Archer. *Journal of Materials Chemistry* **2008**, *18*, 4397-4401.
[85] D. Liu, X. Wang, X. Wang, W. Tian, Y. Bando, D. Golberg. *Sci Rep* **2013**, *3*.
[86] Y. Li, B. Tan, Y. Wu. *Nano Lett* **2008**, *8*, 265-270.
[87] J. E. Bailie, C. H. Rochester, G. J. Hutchings. *Journal of the Chemical Society, Faraday Transactions* **1997**, *93*, 4389-4394.
[88] K. Schmidt-Szałowski, K. Krawczyk, J. Petryk. *Applied Catalysis A: General* **1998**, *175*, 147-157.
[89] A. J. Nozik. *Physica E: Low-dimensional Systems and Nanostructures* **2002**, *14*, 115-120.

[90] S. A. Makhlouf. *Journal of Magnetism and Magnetic Materials* **2002**, *246*, 184-190.
[91] E. Matijevic. *Chemistry of Materials* **1993**, *5*, 412-426.
[92] T. Maruyama, S. Arai. *Journal of The Electrochemical Society* **1996**, *143*, 1383-1386.
[93] F. E. Osterloh. *Chemistry of Materials* **2007**, *20*, 35-54.
[94] C. S. Chua, D. Ansovini, C. J. J. Lee, Y. T. Teng, L. T. Ong, D. Chi, T. S. A. Hor, R. Raja, Y.-F. Lim. *Physical Chemistry Chemical Physics* **2016**, *18*, 5172-5178.
[95] X. Deng, H. Tüysüz. *ACS Catalysis* **2014**, *4*, 3701-3714.
[96] N. H. Chou, P. N. Ross, A. T. Bell, T. D. Tilley. *ChemSusChem* **2011**, *4*, 1566-1569.
[97] L. Xi, P. D. Tran, S. Y. Chiam, P. S. Bassi, W. F. Mak, H. K. Mulmudi, S. K. Batabyal, J. Barber, J. S. C. Loo, L. H. Wong. *The Journal of Physical Chemistry C* **2012**, *116*, 13884-13889.
[98] J. Gan, X. Lu, Y. Tong. *Nanoscale* **2014**, *6*, 7142-7164.
[99] S. Das, V. Jayaraman. *Progress in Materials Science* **2014**, *66*, 112-255.
[100] J. Robertson, B. Falabretti. Electronic Structure of Transparent Conducting Oxides. In: D. S. Ginley (ed). *Handbook of Transparent Conductors*. Springer US: Boston, MA, 2011, pp 27-50.
[101] M. M. Koebel, D. Y. Nadargi, G. Jimenez-Cadena, Y. E. Romanyuk. *ACS Appl Mater Interfaces* **2012**, *4*, 2464-2473.
[102] R. Varala, V. Narayana, S. R. Kulakarni, M. Khan, A. Alwarthan, S. F. Adil. *Arabian Journal of Chemistry* **2016**, *9*, 550-573.
[103] Ç. Kılıç, A. Zunger. *Physical Review Letters* **2002**, *88*, 095501.
[104] M. Batzill, U. Diebold. *Progress in Surface Science* **2005**, *79*, 47-154.
[105] S. R. Vishwakarma, Rahmatullah, H. C. Prasad. *Journal of Physics D: Applied Physics* **1993**, *26*, 959.
[106] V. Vasu, A. Subrahmanyam. *Semiconductor Science and Technology* **1992**, *7*, 320.
[107] K. Tennakone, G. R. R. A. Kumara, I. R. M. Kottegoda, V. P. S. Perera. *Chemical Communications* **1999**15-16.
[108] S. Ito, Y. Makari, T. Kitamura, Y. Wada, S. Yanagida. *Journal of Materials Chemistry* **2004**, *14*, 385-390.
[109] A. S. Ferlauto, G. M. Ferreira, J. M. Pearce, C. R. Wronski, R. W. Collins, X. Deng, G. Ganguly. *Journal of Applied Physics* **2002**, *92*, 2424-2436.
[110] O. K. Varghese, L. K. Malhotra. *Sensors and Actuators B: Chemical* **1998**, *53*, 19-23.
[111] E. Comini, G. Faglia, G. Sberveglieri, Z. Pan, Z. L. Wang. *Applied Physics Letters* **2002**, *81*, 1869-1871.
[112] H. Huang, O. K. Tan, Y. C. Lee, T. D. Tran, M. S. Tse, X. Yao. *Applied Physics Letters* **2005**, *87*, 163123.
[113] P. Balaji, L. D. Don, R. W. Mark, C. Richard, S. Steve. *Nanotechnology* **2001**, *12*, 336.
[114] J. G. Partridge, M. R. Field, J. L. Peng, A. Z. Sadek, K. Kalantar-zadeh, J. D. Plessis, D. G. McCulloch. *Nanotechnology* **2008**, *19*, 125504.
[115] D. Aaron, M. Allan, S. Martin, T. Takuya. *Nanotechnology* **2006**, *17*, 692.
[116] D. R. Pyke, R. Reid, R. J. D. Tilley. *Journal of the Chemical Society, Faraday Transactions 1: Physical Chemistry in Condensed Phases* **1980**, *76*, 1174-1182.
[117] L. Yin, S. Chai, F. Wang, J. Huang, J. Li, C. Liu, X. Kong. *Ceramics International* **2016**, *42*, 9433-9437.
[118] Y. Deng, C. Fang, G. Chen. *Journal of Power Sources* **2016**, *304*, 81-101.
[119] P. Lian, X. Zhu, S. Liang, Z. Li, W. Yang, H. Wang. *Electrochimica Acta* **2011**, *56*, 4532-4539.
[120] Y. Wang, T. Chen. *Electrochimica Acta* **2009**, *54*, 3510-3515.

[121] M. Zhang, Z. Sun, T. Zhang, D. Sui, Y. Ma, Y. Chen. *Carbon* **2016**, *102*, 32-38.
[122] F. Ye, B. Zhao, R. Ran, Z. Shao. *Chemistry – A European Journal* **2014**, *20*, 4055-4063.
[123] H. Porthault, R. Baddour-Hadjean, F. Le Cras, C. Bourbon, S. Franger. *Vibrational Spectroscopy* **2012**, *62*, 152-158.
[124] W. D. Johnston, R. R. Heikes, D. Sestrich. *Journal of Physics and Chemistry of Solids* **1958**, *7*, 1-13.
[125] J. N. Reimers, W. Li, E. Rossen, J. R. Dahn. *Solid State Ionics III* **1993**, *293*, 3-13.
[126] C. Delmas, C. Fouassier, P. Hagenmuller. *Physica B* **1980**, *99*, 81-85.
[127] R. J. Gummow, M. M. Thackeray, W. I. F. David, S. Hull. *Materials Research Bulletin* **1992**, *27*, 327-337.
[128] M. Antaya, K. Cearns, J. S. Preston, J. N. Reimers, J. R. Dahn. *Journal of Applied Physics* **1994**, *76*, 2799-2806.
[129] K. Kushida, K. Kuriyama. *Solid State Communications* **2002**, *123*, 349-352.
[130] H. Gabrisch, R. Yazami, B. Fultz. *Journal of The Electrochemical Society* **2004**, *151*, A891.
[131] F. Xiong, H. J. Yan, Y. Chen, B. Xu, J. X. Le, C. Y. Ouyang. *International Journal of Electrochemical Science* **2012**, *7*, 9390-9400.
[132] L. Simonelli, N. L. Saini, M. Moretti Sala, M. Okubo, I. Honma, T. Mizokawa, G. Monaco. *Applied Physics Letters* **2013**, *103*, 083111.
[133] M. Okubo, E. Hosono, J. Kim, M. Enomoto, N. Kojima, T. Kudo, H. Zhou, I. Honma. *J Am Chem Soc* **2007**, *129*, 7444-7452.
[134] L. Maugeri, A. Iadecola, B. Joseph, L. Simonelli, L. Olivi, M. Okubo, I. Honma, H. Wadati, T. Mizokawa, N. L. Saini. *Journal of Physics: Condensed Matter* **2012**, *24*, 335305.
[135] L. Maugeri, L. Simonelli, A. Iadecola, B. Joseph, M. Okubo, I. Honma, H. Wadati, T. Mizokawa, N. L. Saini. *Journal of Power Sources* **2013**, *229*, 272-276.
[136] K. Mizushima, P. C. Jones, P. J. Wiseman, J. B. Goodenough. *Materials Research Bulletin* **1980**, *15*, 783-789.
[137] J. N. Reimers, J. R. Dahn. *Journal of The Electrochemical Society* **1992**, *139*, 2091-2097.
[138] A. Van der Ven, M. K. Aydinol, G. Ceder. *Journal of The Electrochemical Society* **1998**, *145*, 2149-2155.
[139] X. Q. Yang, X. Sun, J. McBreen. *Electrochemistry Communications* **2000**, *2*, 100-103.
[140] B. Park, Y. J. Kim, J. Cho. CATHODES BASED ON LiCoO2 AND LiNiO2. In: G. A. Nazri, G. Pistoia (eds). *Lithium Batteries: Science and Technology*. Springer: Berlin, 2003.
[141] M. Menetrier, I. Saadoune, S. Levasseur, C. Delmas. *Journal of Materials Chemistry* **1999**, *9*, 1135-1140.
[142] Z. Chen, Z. Lu, J. R. Dahn. *Journal of The Electrochemical Society* **2002**, *149*, A1604-A1609.
[143] S. Venkatraman, A. Manthiram. *Journal of Solid State Chemistry* **2004**, *177*, 4244-4250.
[144] H. Li, Z. Wang, L. Chen, X. Huang. *Adv Mater* **2009**, *21*, 4593-4607.
[145] N. Liu, H. Li, Z. Wang, X. Huang, L. Chen. *Electrochemical and Solid-State Letters* **2006**, *9*, A328.
[146] J. Choi, A. Manthiram. *Electrochemical and Solid State Letters* **2005**, *8*, C102-C105.
[147] B. Garcia, J. Farcy, J. P. Pereira-Ramos, N. Baffier. *Journal of The Electrochemical Society* **1997**, *144*, 1179-1184.
[148] Y. Koyama, Y. Makimura, I. Tanaka, H. Adachi, T. Ohzuku. *J Electrochem Soc* **2004**, *151*.

[149] A. M. A. Hashem, A. E. Abdel-Ghany, A. E: Eid, J. Trottier, K. Zaghib, A. Mauger, C. M. Julien. *J Power Sources* **2011**, *196*, 8632-8637.
[150] A. M. Hashem, R. S. El-Taweel, H. M. Abuzeid, A. E. Abdel-Ghany, A. E. Eid & H. Groult, A. Mauger, C. M. Julien. *Ionics* **2012**, *18*, 1-9.
[151] J. Kim, C. Park, Y. Sun. *Solid State Ionics* **2003**, *164*, 43.
[152] S.-C. Yin, Y.-H-Rho, I. Swainson, L. F. Nazar. *Chem Mater* **2006**, *18*, 1901-1010.
[153] H. Kim, S. M. Oh, B. Scrosati, Y. K. Sun. 9 - High-performance electrode materials for lithium-ion batteries for electric vehicles. In: B. Scrosati, J. Garche, W. Tillmetz (eds). *Advances in Battery Technologies for Electric Vehicles*. Woodhead Publishing, 2015, pp 191-241.
[154] R. D. Shannon. *Acta Crystallogr Sect A: Found Crystallogr* **1976**, *32*, 751-767.
[155] A. Rougier, P. Gravereau, C. Delmas. *J Electrochem Soc* **1996**, *143*.
[156] J. P. Peres, C. Delmas, A. Rougier, M. Broussely, F. Perton, P. Biensan, P. Willmann. *J Phys Chem Solids* **1996**, *57*.
[157] K. M Shaju, P. G. Bruce. *J Power Sources* **2007**, *174*.
[158] K.-S. Lee, S.-T. Myung, J. Prakash, H. Yashiro, Y.-K. Sun. *Electrochim Acta* **2008**, *53*.
[159] S. Jouanneau, K. W. Eberman, L. J. Krause, J. R. Dahn. *J Electrochem Soc* **2003**, *150*.
[160] H. H. Binder. *Lexikon der chemischen Elemente: das Periodensystem in Fakten, Zahlen und Daten*. Hirzel, 1999.
[161] K. M. Shaju, G. V. Subba Rao, B. V. R. Chowdari. *Electrochimica Acta* **2002**, *48*, 145-151.
[162] S. H. Kang, J. Kim, M. E. Stoll, D. Abraham, Y. K. Sun, K. Amine. *Journal of Power Sources* **2002**, *112*, 41-48.
[163] M. Ma, N. A. Chernova, B. H. Toby, P. Y. Zavalij, M. S. Whittingham. *Journal of Power Sources* **2007**, *165*, 517-534.
[164] P. K. Nayak, J. Grinblat, M. Levi, Y. Wu, B. Powell, D. Aurbach. *Journal of Electroanalytical Chemistry* **2014**, *733*, 6-19.
[165] J. Yan, X. Liu, B. Li. *RSC Advances* **2014**, *4*, 63268-63284.
[166] S. Park, C. Yoon, S. Kang, H.-S. Kim, S.-I. Moon, Y.-K. Sun. *Electrochimica Acta* **2004**, *49*, 557-563.
[167] P. K. Nayak, J. Grinblat, M. Levi, O. Haik, E. Levi, S. Kim, J. W. Choi, D. Aurbach. *ChemElectroChem* **2015**, *2*, 1957-1965.
[168] S.-M. Bak, E. Hu, Y. Zhou, X. Yu, S. D. Senanayake, S.-J. Cho, K.-B. Kim, K. Y. Chung, X.-Q. Yang, K.-W. Nam. *ACS Appl Mater Interfaces* **2014**, *6*, 22594-22601.
[169] M. Park, X. Zhang, M. Chung, G. B. Less, A. M. Sastry. *Journal of Power Sources* **2010**, *195*, 7904-7929.
[170] H.-J. Noh, S. Youn, C. S. Yoon, Y.-K. Sun. *Journal of Power Sources* **2013**, *233*, 121-130.
[171] J. C. Garcia, J. Bareño, J. Yan, G. Chen, A. Hauser, J. R. Croy, H. Iddir. *The Journal of Physical Chemistry C* **2017**, *121*, 8290-8299.
[172] K. Ben-Kamel, N. Amdouni, A. Mauger, C. M. Julien. *J Alloys Compd* **2012**, *528*, 91-98.
[173] L. Q. Wang, L. F. Jiao, H. T. Yuan, J. Guo, M. Zhao, H. X. Li, Y. M. Wang. *J Power Sources* **2006**, *162*, 1367- 1372.
[174] J. K. Ngala, N. A. Chernova, M. Ma, M. Mamak, P. Y. Zavalij, M. S. Whittingham. *Journal of Materials Chemistry* **2004**, *14*, 214-220.
[175] T. Ohzuku, Y. Makimura. *Chemistry Letters* **2001**642-643.
[176] L.-j. Li, X.-h. Li, Z.-x. Wang, H.-j. Guo, P. Yue, W. Chen, L. Wu. *Powder Technology* **2011**, *206*, 353-357.

2 Characterization

This chapter briefly discusses the theoretical background for main characterization techniques used in this work to analyze nanomaterials and their properties. The combination of the used methods provides comprehensive information about the composition, crystalline structure, morphology and electrochemical properties of different nanomaterials synthesized in this work and their respective composites. Typically, different complementary techniques were used to provide the most accurate values of different parameters and to minimize the uncertainties inherent for each method. For example, X-ray diffraction, dynamic light scattering and transmission electron microscopy were utilized to determine the size of the nanocrystals. Additionally, the specific setup and the experimental details of the measurements for each technique are listed.

2.1 X-ray Diffraction (XRD)

X-ray diffraction is an important non-destructive analytical technique in material sciences. Using this method, unknown materials can be identified by comparing their diffractograms with those in a database. It is possible to get information about the crystallinity of substances, for example the orientations of single crystals, the texture of polycrystalline materials, stresses and defects. In this technique, X-rays with a wavelength usually in the range of 0.7 Å (Mo-K_α) up to 2 Å (Fe-K_α) are used. These wavelengths are approximately in the same order of magnitude as the interplanar spacings of the crystal lattice, therefore scattering of the X-rays can occur. The measured intensity of the diffracted X-rays is a function of the diffraction angle 2θ and the specimen orientation. The X-rays are scattered elastically or inelastically at single atoms of the materials. The conditions for constructive elastic scattering result from Bragg's law (Equation 2.1):

$$\boldsymbol{n\lambda = 2d_{hkl}sin\theta} \qquad 2.1$$

where n is the order of diffraction, λ - the wavelength of the X-rays, d_{hkl} - the crystal lattice spacing and θ - the incident angle. In Figure 2.1, Bragg's law is illustrated.

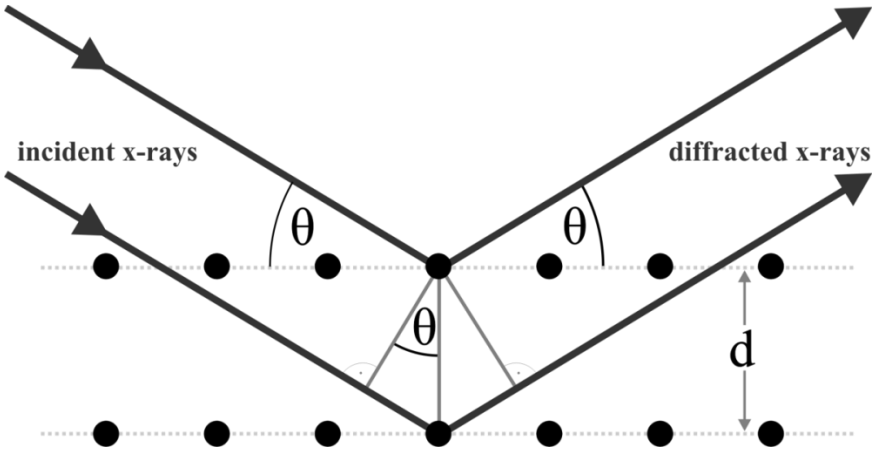

Figure 2.1: Illustration of Bragg's law.[1]

X-ray diffraction can also be used to estimate the size of particles. The crystal lattice, and therefore the number of scattering centers, is no longer quasi-infinite, since nanoparticles are very small. Hence, the interference condition is getting more diffuse and the reflections broaden. This peak broadening can be used to calculate the particle size by using Scherrer's formula (Equation 2.2):

$$\boldsymbol{D = \frac{K\lambda}{B cos\theta}} \qquad 2.2$$

where D is the crystallite size, K - the shape-dependent proportionality factor (approximated to 0.9 for spherical particles), λ - the wavelength of the X-rays, B - the full width at half maximum (FWHM) of a single reflection and θ - the Bragg angle.[2, 3]

Wide angle X-ray diffraction analysis of the powders was performed on two setups. For transmission mode (Debye-Scherrer geometry), a *STOE STADI P* diffractometer was used, with a Ge(111) single crystal monochromator for either Cu-$K_{\alpha 1}$ (λ = 1.54060 Å) or Mo-$K_{\alpha 1}$-radiation (λ = 0.709300 Å) and a solid state strip detector (*DECTRIS MYTHEN 1K*). Measurements in reflection mode (Bragg-Brentano) were performed on microscopy slides using a *BRUKER D8 DISCOVER* diffractometer with Ni-filtered Cu-K_{α}-radiation and a position-sensitive detector (*LynxEye*).

In order to identify the phases within the measured sample, the obtained diffractograms were compared with archived ones from the database of the International Centre for Diffraction Data (ICDD).

2.2 Raman Spectroscopy

Raman spectroscopy is an analytical method which is very sensitive to the length, strength, polarizability and arrangement of chemical bonds. Therefore, it is used to determine vibrational modes of single molecules, which can be translated into phonon modes in a crystal lattice. Raman spectroscopy can be very sensitive for solid state materials such as metal oxides towards small changes in the crystal lattice, the distances between the ions and the coordination of ions.[4] Therefore, it enables us to distinguish different phases of the same compound even in trace amounts. Monochromatic laser light in the visible or near infrared region is used in a typical Raman experiment to excite the electrons of a chemical bond to a virtual higher vibrational energy state. The different processes occurring are depicted in Figure 2.2. Most of the energy of the virtual excited states is emitted at the same wavelength as that of the incident light beam. This elastically scattering process is called Rayleigh scattering. The smaller part of the excited molecules does not relax to the ground state but to a higher vibrational state, thus light of longer wavelength is radiated. This phenomenon is called Stokes Raman scattering. Another possibility is that an excited vibrational state (in the electronic ground state) is excited to a higher virtual vibrational state. The relaxation of this state hence releases more energy than of the incident photon, which leads to shorter wavelength light. This situation is known as anti-Stokes Raman scattering.

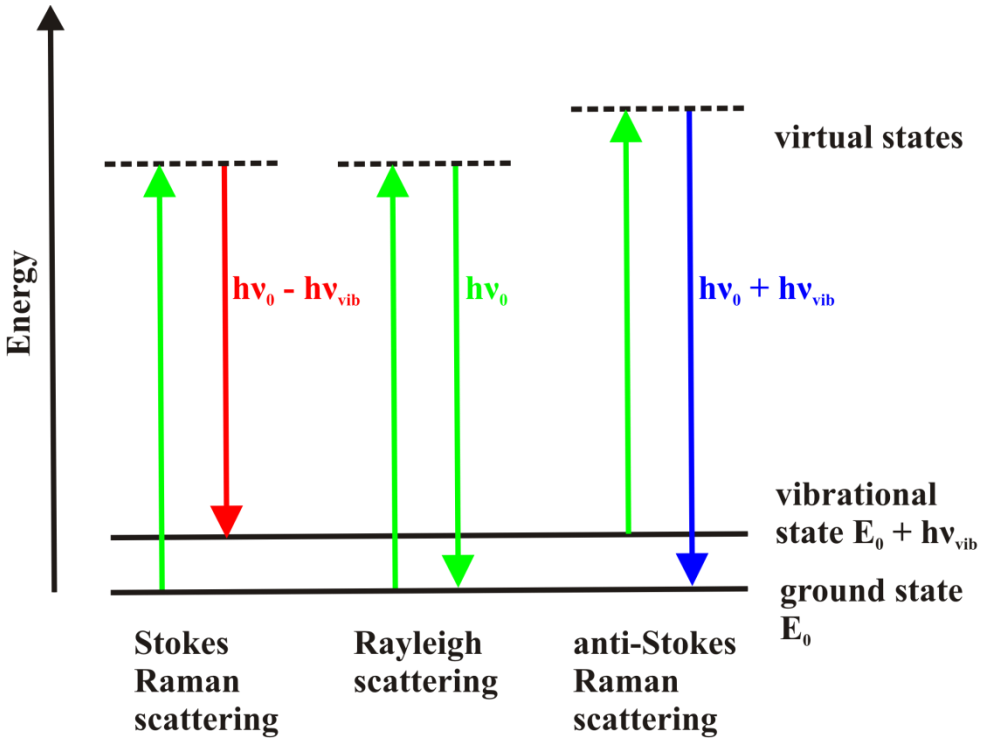

Figure 2.2: Vibrational energy states and transition processes during Raman spectroscopy.[1]

The probability of transitions decreases from Rayleigh, Stokes to anti-Stokes scattering. The probability of Rayleigh scattering is three orders of magnitude higher than that of the other transitions, since this two particle process is more likely to occur than a three particle process (Stokes and anti-Stokes scattering). Furthermore, the probability of anti-Stokes Raman transitions is less than that of the Stokes transitions as the initial state is energetically higher and therefore less occupied than the ground state at room temperature. Despite the peak differences, Stokes and anti-Stokes Raman lines are mirrored at the Rayleigh frequency.[2]

Raman spectra were acquired with a *Jobin Yvon Horiba HR800 UV* Raman microscope (*OLYMPUS BX41*) using a HeNe laser (632.8 nm) and a *SYMPHONY CCD* detection system. Spectra were recorded using a microscope objective with 10 or 100 times magnification. To prevent the samples of local heating, the power of the laser beam was normally adjusted to about 8.5 mW and for extremely sensitive samples to 1.7 mW with filters of various optical densities.

2.3 Dynamic Light Scattering (DLS)

Dynamic light scattering (DLS) is a fast, non-destructive and undemanding technique to determine the size of sub-micron particles in a suspension. The random movement of particles in a fluid, also called Brownian motion, is measured with a laser beam. The incident laser light is scattered in all directions *via* a Rayleigh mechanism at the very small particles in the dispersion. At all times a detector records the resulting intensity pattern composed of the constructive and destructive interferences of the scattered light. As this pattern changes with time, the Brownian motion can be determined by using an autocorrelation function. Finally, the derived particle diffusion and the properties of the dispersion medium are offset with the Stokes-Einstein equation (Equation 2.3) to gain the size of the nanoparticles in the respective medium:

$$\boldsymbol{d(H) = \frac{kT}{3\pi\eta D}} \qquad 2.3$$

where *d(H)* is the hydrodynamic diameter, *k* - the Boltzmann`s constant, *T* - the absolute Temperature, η - the viscosity of the medium, and *D* - the translational diffusion coefficient.[5]

Finally, the hydrothermal diameter only delivers information on the combined size of the actual particle together with any kind of adsorbed species on the surface including hydration, organic and ionic shells.

The dynamic light scattering experiments on the various dispersed metal oxide nanoparticles were performed using a *Malvern Zetasizer Nano* with a 4 mW HeNe laser (632.8 nm) and an avalanche photodiode detector in backscattering mode (173°). The scattering data were evaluated on particle number.

2.4 Inductively Coupled Plasma-Optical Emission Spectroscopy (ICP-OES)

Inductively Coupled Plasma-Optical Emission Spectroscopy (ICP-OES) is an analytical technique to qualitatively and quantitatively determine the elemental composition of materials. Herein, the sample has to be solved and the liquid is then injected into radiofrequency induced argon plasma using a nebulizer. The sample mist reaching the plasma is quickly dried, vaporized and the contained atoms are energized through collisional excitation at high temperature. During relaxation of the excited atoms photons of characteristic energies are emitted. These are recorded by a wavelength selective device. The specific wavelengths are characteristic for each element and the intensity of the emission indicates the concentration of the element within the sample.[6]

In this work, measurements were performed with a Varian Vista RL CCD Simultaneous ICP-OES spectrometer.

2.5 Electron Microscopy

Electron microscopy is a powerful tool to study the structure of materials as well as their compositions and their morphologies especially on the nanoscale. Herein, accelerated electrons emitted by a field emission gun are focused by an electromagnetic lens system onto the sample. As the wavelength of the electrons (e^-) in the focused beam is by far smaller than of visible light, the diffraction limit of electron microscopes is much smaller than in a common optical light microscope.

The maximum achievable resolution *R* depends on the numerical aperture *N.A.* of the lens system and on the wavelength λ of the electrons (Equation 2.4).[2]

$$\boldsymbol{R = \frac{\lambda}{2N.A.}} \qquad 2.4$$

Furthermore, the wavelength of the e^--beam is determined according to Equation 2.5 using the Planck`s constant *h*, the electron mass m_e and the acceleration energy E_{acc}:

$$\boldsymbol{\lambda = \frac{h}{\sqrt{2m_eE_{acc}}}} \qquad 2.5$$

Generally, the electron beam is accelerated with 1 kV-300 kV, which, as seen above, directly affects the maximum theoretical resolution limit. In contrast to that, spherical aberrations, chromatic aberrations and the astigmatism of the lenses restrict the effective resolutions.

Furthermore, when the e^--beam hits the sample, it interacts with the specimen by producing different signals as it can be noticed in Figure 2.3. These different signals are used for various recording and analyzing tools, yielding different information depending on the sample composition.

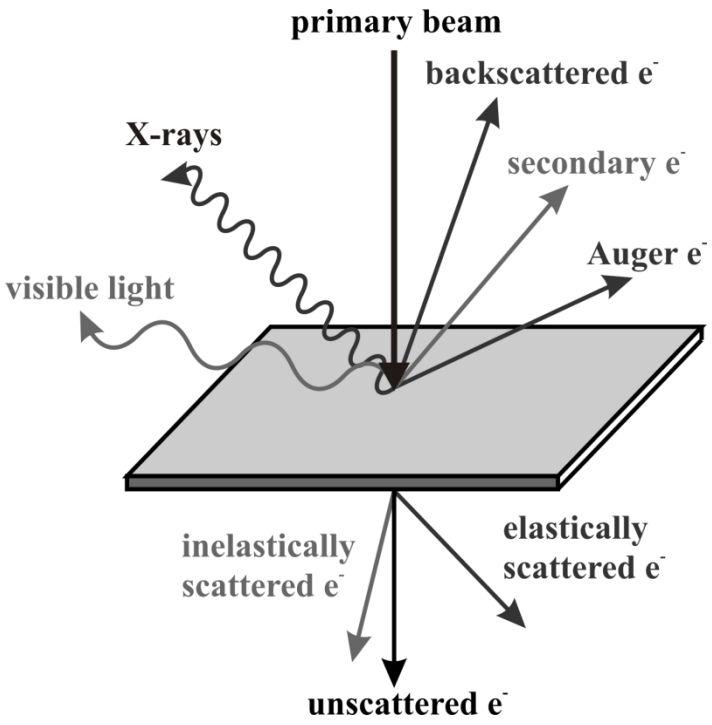

Figure 2.3: Interactions of the electron beam with a sample in electron microscopy.[1]

Two different types of electron microscopy were used in this work: scanning and transmission electron microscopy. Additionally, electron microscopy analytics such as energy dispersive X-ray spectroscopy (EDX) and electron energy loss spectroscopy (EELS) were applied to gain information about the sample compositions.

2.5.1 Scanning Electron Microscopy (SEM)

Scanning electron microscopy (SEM) is an important tool to obtain high-magnification images of the sample surface and morphology. Normally, morphological details as small as 1 nm can be resolved by SEM.

To get information about the structure and the morphology of a sample, the accelerated (1-30 kV) e^--beam is focused by electromagnetic lenses onto the specimen (Figure 2.4). The sample is scanned with the e^--beam in a grid-like pattern. Here, the secondary electrons or the backscattered electrons carry important information about the morphology of the sample's surface. With backscattered electrons not only topographical information is gathered, but also the Z contrast is obtained which, in general, correlates to the atomic mass of the material.

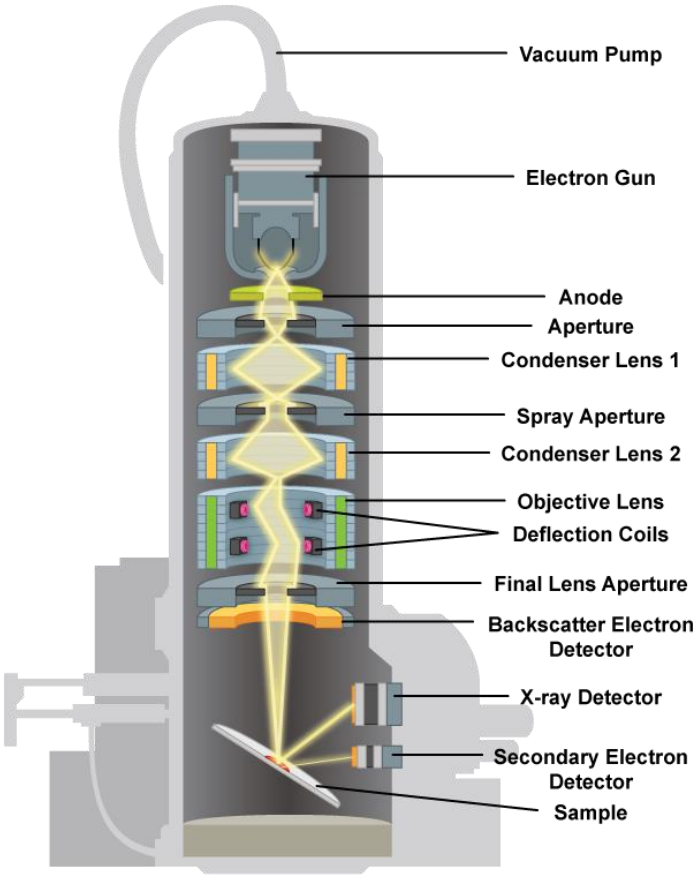

Figure 2.4: Schematic representation of the parts and the principle electron beam path of a SEM.[7]

SEM was carried out either on a *JEOL JSM-6500F* scanning electron microscope equipped with a field emission gun operating at 5 kV or an *FEI Helios NanoLab G3 UC* scanning electron microscope equipped with a field emission gun usually operated at 3 kV.

2.5.2 Transmission Electron Microscopy (TEM)

Transmission electron microscopy (TEM) is a very important tool to obtain information about the internal structure of a sample. The smallest observable feature size of 0.1 nm is achieved in high resolution TEM (HRTEM), as the wavelength of the electrons λ is only several pm. Generally, the electron beam is accelerated with 60 -300 kV, focused by electromagnetic condenser lenses and penetrates a specimen (Figure 2.5). This is the most pronounced difference to the SEM. The samples used in TEM have to be prepared very thin, below 200 nm, to allow the electrons to pass through the sample as they strongly interact with the probed material.

The transmitted electrons are then displayed on a fluorescent screen or a CCD camera. The image contrast in this mode is a complex mixture between mass-thicknesses and the phase contrast resulting from the interference between diffracted e^- on a crystalline sample. If the optical path is altered by modifying the intermediate electromagnetic lenses, the mode can be switched from imaging to diffraction. Herein, a diffraction pattern of the sample can be obtained by Bragg scattering of the electron beam. For crystalline samples, this can be used to identify the crystal phase of the specimen.

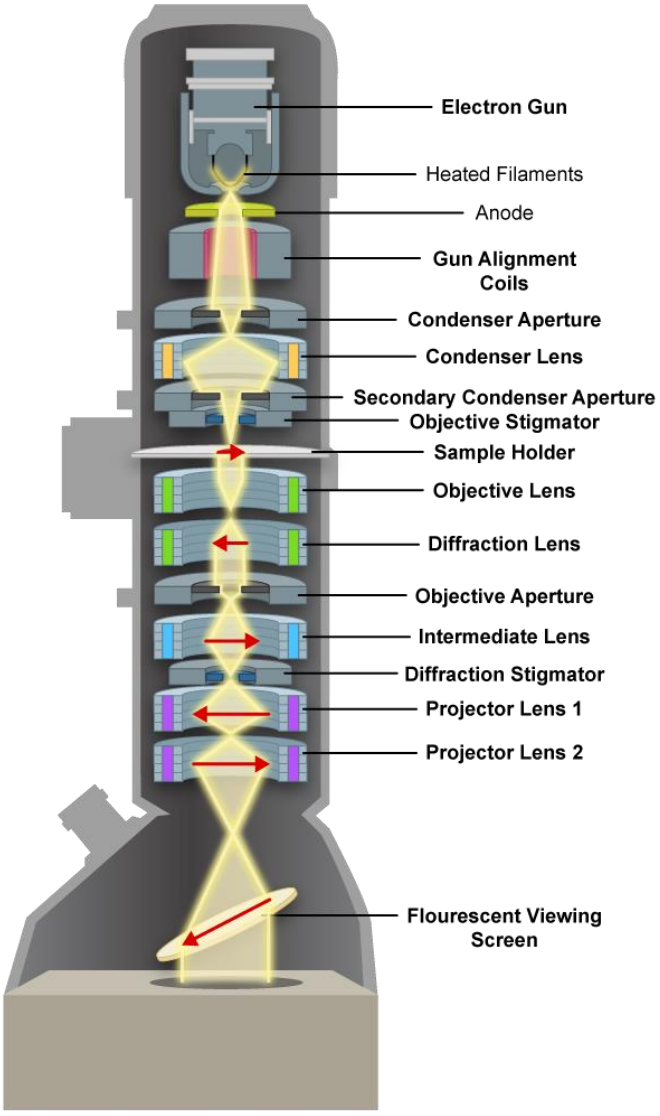

Figure 2.5: Schematic representation of the main parts and the principle electron beam path of a TEM.[7]

Similar to SEM, the strongly focused e^--beam can be used to scan the sample which is called scanning transmission electron microscopy (STEM) accordingly. With an annular detector placed

around the optical axis of the microscope, images with a very high mass contrast can be achieved. Here, only electrons that are heavily diffracted at a high angle are detected. This method is called high-angle annular dark field (HAADF) imaging.

Generally, samples were drop-casted on a holey-carbon coated copper grid out of a diluted nanoparticle-containing dispersion or the grid was loaded with very little material scratched of a film. The following TEM analyses were carried out on an *FEI Titan* Themis 300, an *FEI Tecnai G2 20 S-TWIN* or *FEI Titan 80-300 (S)TEM* equipped with a high angle annular dark field (HAADF) detector, an *EDAX* energy-dispersive X-ray spectrometer and a *Gatan* EELS spectrometer.

2.5.3 Energy-dispersive X-ray Spectroscopy (EDX)

Energy-dispersive X-ray spectroscopy (EDX) uses the X-rays generated by inelastic scattering of the incident e^--beam on the sample. When electrons of the inner atomic shell are removed by the primary e^--beam, electrons of the outer shell can fill the inner vacancies. The characteristic X-rays for each element are emitted as the difference of the energy of the involved shells. The energy and intensity of the different characteristic X-rays are recorded in EDX detectors both equipped in SEM and TEM instruments. Software then assigns the gathered signals to the different elements involved. With this spectroscopy method the composition of samples can be determined and also the elemental distribution within a sample can be spatially resolved to a certain point.

2.5.4 Electron Energy Loss Spectroscopy (EELS)

In electron energy loss spectroscopy (EELS) the e^- of the primary beam that are inelastically scattered by the sample are collected and the amount of energy loss is measured *via* an electromagnetic prism. Different inelastic interactions such as phonon excitations, inter- and intraband transitions, plasmon excitations or inner shell ionizations cause the electron energy loss. In particular, the inner shell ionizations energies are used in EELS to determine the chemical composition of the investigated specimen.

2.6 Thermogravimetric Analysis (TGA) and Differential Scanning Calorimetry (DSC)

Both thermogravimetric analysis (TGA) and differential scanning calorimetry (DSC) reveal properties of a material as a function of temperature.

TGA uses a microbalance to determine the change in mass of a sample with respect to time and temperature. For this purpose, the sample is placed in an inert crucible and heated at a specific rate in a selectable atmosphere such as synthetic air or nitrogen. During heating several processes can alter the mass of a material, for example desorption or evaporation of solvents, the release of crystal water, combustion of organic materials and oxidation processes within the sample.[8]

DSC, in contrast, measures the difference in expended enthalpy to keep the sample and an inert reference at the same temperature. The heat flux between the investigated material and the reference at each respective temperature is recorded and enables to distinguish endothermic processes like evaporation of adsorbed molecules and exothermic reactions e.g. combustion, melting or crystallization. Furthermore, phase transitions can be recognized by coupling to TGA, as there is normally no mass change at the transition points.[8]

Thermogravimetric analysis (TGA) and differential scanning calorimetry (DSC) were carried out with a *NETZSCH STA 440 C TG/DSC* instrument (heating rate 10 K min^{-1}) in a stream of synthetic air of about 25 mL min^{-1}.

2.7 Sorption

Sorption measurements are used to get information about the accessible surface of porous materials as well as the characteristics of the pores. At a constant temperature the amount of gas molecules (adsorptive) adsorbing to the surface of the investigated material (adsorbent) is measured with respect to the relative pressure p/p_0. The isotherms obtained can be drawn for the adsorption as well as the desorption process. Various models with different assumptions deal with the different aspects of sorption. One commonly used model is the Brunauer-Emmett-Teller (BET) theory. Here, the assumption is made that the adsorptive only interacts by weak van-der-Waals forces with the adsorbent, so only physisorption is present and no chemical bonds are formed between the gas molecule and the surface of the material. Further assumptions are that there are no interactions in between the adsorbed molecules of one layer and that the adsorption enthalpy of the first monolayer is different to the one of the multilayer formation.[9, 10]

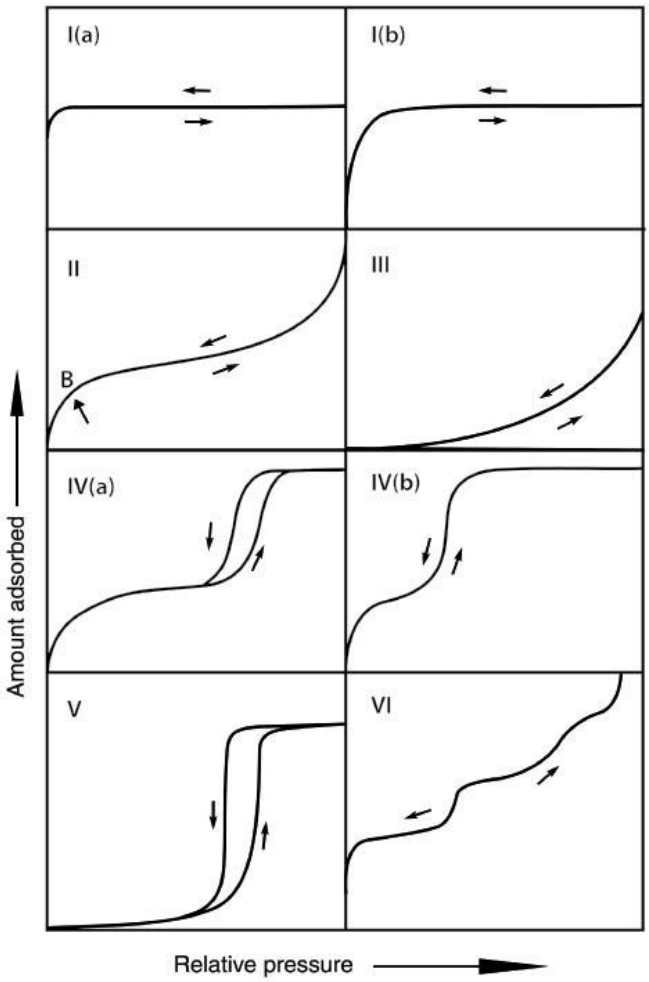

Figure 2.6: Classification of physisorption isotherms according to IUPAC.[10]

The BET method uses the point of the completed monolayer formation B at rather low relative pressures in the isotherm and the volume occupied by a single adsorptive molecule to determine the surface area. The International Union of Pure and Applied Chemistry (IUPAC) distinguishes six main types of gas sorption isotherms as seen in Figure 2.6.

Type I isotherms are examples for microporous (<2 nm) materials where basically only one monolayer can be adsorbed. In contrast to that, Type II and Type III isotherms represent macro- (>50 nm) or nonporous materials. Additionally, Type IV isotherms are typical for mesoporous (2-50 nm) materials showing the completed monolayer adsorption with subsequent multilayer adsorption until all pores are completely filled. Adsorption and desorption branch exhibit a hysteresis loop ascribed to capillary condensation of the adsorptive in the mesopores and relative to the pressure of the delayed evaporation process.[11]

Nitrogen sorption measurements were performed at 77 K with the scratched powders using a *QUANTACHROME Autosorb iQ* instrument. The powders were degassed at 120-150 °C for at least 12 h before the measurement. The data was evaluated with the *ASiQwin* software. The specific surface area was determined with the Brunauer-Emmett-Teller method and the pore size distribution was calculated using a non-local density functional theory (NLDFT) approach on silica cylindrical pores.

2.8 X-ray Photoelectron Spectroscopy

X-ray photoelectron spectroscopy (XPS) is a surface-sensitive technique that allows determining the elemental composition and the nature of the electronic states. Its principle is based on the photoelectric effect, where electrons are liberated from their bound state in the atomic shells by an incident electromagnetic wave. The binding energy of the electrons in their shells E_B can be calculated with XPS by using the relation in Equation 2.6:

$$\boldsymbol{E_{kin} = h\nu - E_B - e\varphi_{sp}} \qquad 2.6$$

where E_{kin} is the kinetic energy of the liberated electron, h - the Planck`s constant, ν – the X-ray frequency , $e\varphi_{sp}$ – the work function of the spectrometer.

The sketch in Figure 2.7 illustrates the different energy levels involved in this process.

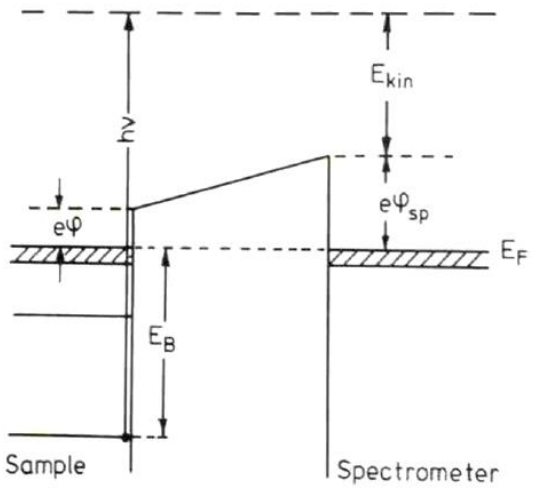

Figure 2.7: Diagram on the different energy levels involved in the XPS measurement.[12]

When the spectrometer is calibrated, only the kinetic energies of the liberated electrons are unknown and have to be measured to determine the binding energies. In order to analyze and collect the electrons escaping from the surface of the sample, the mean free path length of the electrons must be high enough to reach the detector. The XPS chamber is hereby kept under ultra-high vacuum (UHV) with a pressure below 10^{-7} Pa. The liberated electrons are gathered *via* electron optics and counted and sorted by kinetic energy in a hemispherical energy analyzer (see Figure 2.8). The output of the XPS experiment is a photoemission spectrum, where the number of electrons is correlated with their binding energies calculated from the measured kinetic energies. The binding energy of the electrons is not only correlated to the respective shell they are in, but

also from the electronic/oxidation state of atoms. Hence, in XPS not only information about the atomic ratio of elements, but also about their oxidation states is gained.[12]

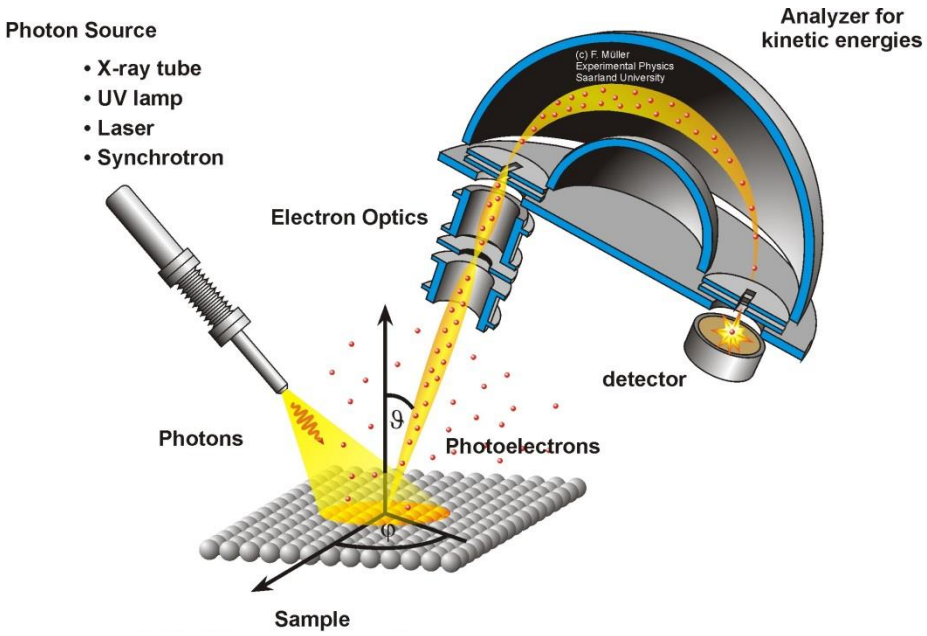

Figure 2.8: Schematic representation of the instruments involved and the principle of a XPS measurement.[13]

XPS analysis of the particles was performed on pure or gold-coated silicon substrates using a *VSW HA 100* electron analyzer and the K_α radiation provided by a non-monochromatized Mg anode system (Mg-K_α = 1253.6 eV). The sample surfaces were cleaned by Ar^+ sputtering (*VSW AS10* ion source).

2.9 Nuclear Magnetic Resonance

Nuclear magnetic resonance spectroscopy (NMR) uses the magnetic properties of atomic nuclei to obtain information about the structure of materials and the chemical surrounding of certain elements. The principle of NMR is based on the fact that some atomic nuclei show a spin $I \neq 0$. In this case, the spin states can split when exposed to an external magnetic field, also known as the Zeeman effect. The transitions between these spin states are specific to particular nuclides and their chemical environment, as the nucleus can be shielded by the surrounding electron cloud. Hence, the magnetic field at the atomic nuclei of the same type can be different depending on the individual chemical surrounding, which can lead to a differently strong splitting of the spin states. In a typical NMR experiment, an electromagnetic pulse is applied and the energy for the transitions within the spin states is absorbed by the nuclei. Furthermore, each individual nuclide absorbs at its own specific frequency. Therefore, each possible isotope is measured in a separate experiment, namely ^{1}H-NMR, ^{7}Li-NMR, ^{13}C-NMR, ^{59}Co-NMR, for example. The individual response of each system to the electromagnetic pulse is detected and amplified to get the free induction decay (FID) of the relaxation. The FID is then converted by a computer program to construct the NMR spectrum: intensity of the signals versus their specific resonance frequencies. As these frequencies depend on the magnetic field strength of the used instrument, it is more practicable to use chemical shift values instead to make spectra independently comparable. The chemical shift δ can be expressed as follows (Equation 2.7):

$$\boldsymbol{\delta = \frac{\nu_{sample} - \nu_{ref}}{\nu_{ref}}} \qquad 2.7$$

where ν_{sample} is the resonance frequency of the probed nucleus and ν_{ref} - the resonance frequency of a reference standard of the same nucleus.[14, 15]

For solid state samples, the magic angle spinning (MAS) experiment is used in ss-NMR. Herein, multiple anisotropic interactions are averaged that occur in non-oriented solid state powder samples. In liquid samples, for example for molecules in solution, these interactions are already averaged by the Brownian motion of the molecules. In the MAS experiment (see Figure 2.9), the powder sample rotates with a frequency of several kHz around an axis at the magic angle of 54.74° with regard to the direction of the external applied magnetic field.[16]

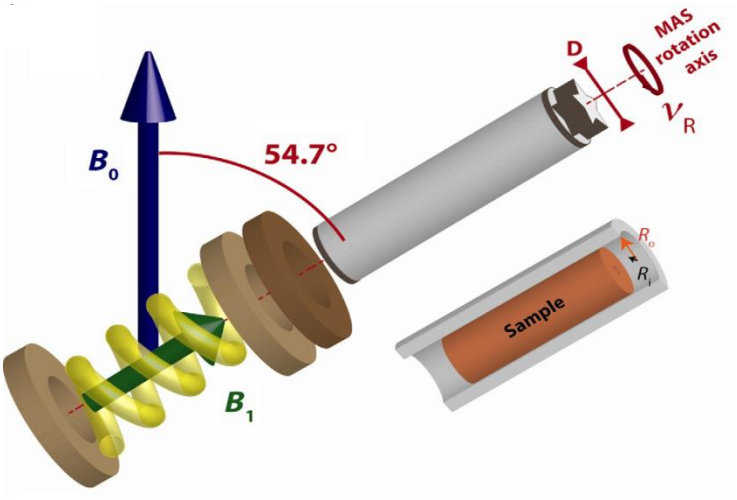

Figure 2.9: Schematic representation of the MAS-NMR experiment.[16]

^{7}Li magic angle spinning solid state nuclear magnetic resonance (MAS-NMR) was recorded on a *Bruker DSX Avance 500 FT* spectrometer with a magnetic field of 11.7 T. The zirconia rotor with an outer diameter of 2.5 mm was spun at a rotation frequency of 12 kHz.

2.10 Electrochemical Measurements

The electrochemical lithium insertion/extraction properties and their underlying mechanisms were investigated by cyclic voltammetry and galvanostatic measurements. In the former, a potential and in the latter method a constant current is applied to the sample electrodes.

2.10.1 Cyclic Voltammetry (CV)

Cyclic voltammetry (CV) is an electroanalytical technique that is used to investigate the electrochemical properties of materials, as it can deliver information about fairly complicated electrode reactions. In a CV experiment, a linearly changing potential is applied to the electrode and the current during the potential scan is measured. The resulting current-potential curve is called cyclic voltammogram or CV curve (Figure 2.10). The applied potential varies linearly over time with a certain scan or sweep rate [V s^{-1}] between an initial and a switching potential where the potential direction is reversed until the starting potential is reached. The potential scan can be performed multiple times.

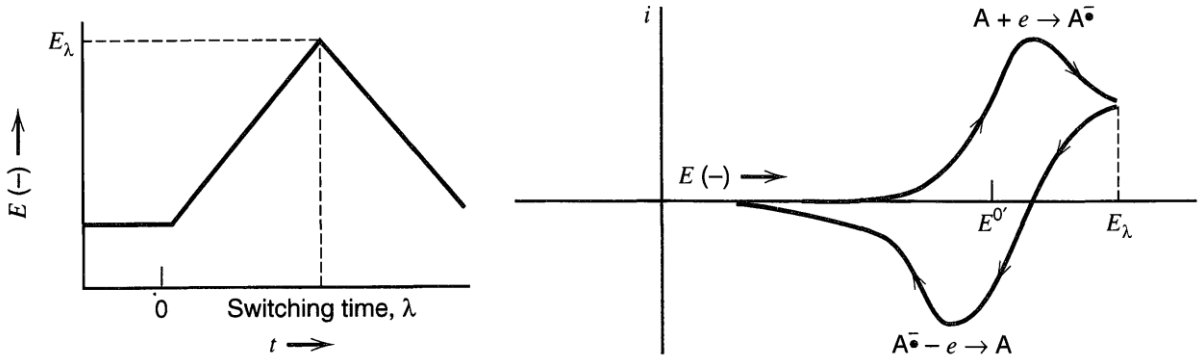

Figure 2.10: A typical curve of the applied voltage (left) and an exemplary CV curve (right).[17]

In an electrochemical setup, a three electrode arrangement is usually used to obtain the CV curve. A typical cell consists of a working electrode (WE), where the electrochemical process of interest takes place, a counter electrode (CE) and a reference electrode (RE) with a defined potential to control the potential of the WE. All three electrodes are electrically connected *via* an ionically conducting electrolyte. During the whole procedure, the current between the WE and the CE is recorded in dependence to the applied potential. The electrolyte is typically not stirred during the CV experiment. Therefore, mass transport occurs by non-stationary diffusion.

From cyclic voltammograms, information about both thermodynamic and kinetic properties of processes at the electrode-electrolyte interface can be derived, for example, the reaction potential, the charge transfer rate, the reversibility of reactions and the amount of charge carriers involved. The detected current is a sum of all currents flowing through the electrode interface. Two basic charge transport mechanisms contribute to the overall current. First, there are non-Faradaic currents which correspond to the charging of a double layer forming at the electrode interface. Second, there are Faradaic currents due to the transfer of electrons through the electrode interface such as redox reactions. The voltammograms of the Faradaic processes typically show peaks that are defined by the peak current and the peak potential, for example anodic peak potential E_{pa} and cathodic peak potential E_{pc}. The resulting shape depends on the character of the electrode reaction. According to Equation 2.8 the difference between E_{pa} and E_{pc} defines the reversibility of the electron transfer reaction.

$$\boldsymbol{\Delta E = E_{pc} - E_{pa} \sim \frac{0.059}{n}\ (V)} \qquad 2.8$$

where n is the number of electrons transferred in the reaction. Hence, for a one electron process ΔE has to be about 0.059 V to indicate a reversible reaction. Higher values indicate quasi-reversible reaction and slow charge transfer processes. The peak currents are limited by the diffusion of the electroactive species to the electrode surface.

In battery research the CV is broadly used to determine the basic electrochemical characteristics of active materials such as the reduction and oxidation potentials during lithium insertion/extraction, the insertion capacity, the reaction reversibility, the reaction kinetics and the reaction mechanism. The CV can also provide information about the presence of side phases if their electrochemical fingerprint is known. Typically, the initial scanning process represents the charging of the material, whereas the reverse direction shows the discharge process. The amount of transferred electrons (charge), which for battery materials is typically expressed as gravimetric capacity (charge per gram of the materials) can be determined by integrating the area under the CV curve. Information about the cycling stability of an electrode material can be gained by repeating the charge-discharge cycle. The decrease in E_{pa} and E_{pc} during multiple cycling, for example, can be a sign for capacity fading.[17, 18]

2.10.2 Galvanostatic Charge-discharge Experiments

Galvanostatic charge-discharge experiments are examples of chronopotentiometric methods. Herein, a constant current is applied between the counter and the working electrode and the change of the overall cell potential over time with respect to the reference electrode is monitored (Figure 2.11).

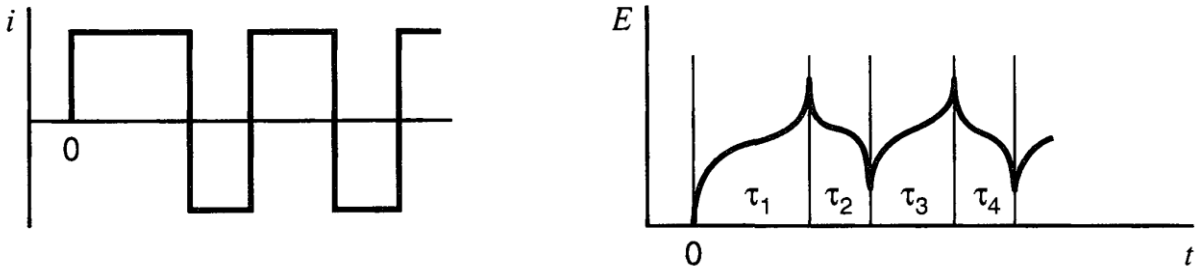

Figure 2.11: A typical curve of the applied current (left) and possible signals for the resulting potential (right).[17]

The applied constant current induces the migration of the lithium ions in the electrolyte and thus depending on the direction of the current, insertion or extraction of lithium ions at the WE. The typical experiment starts with a constant charging current and runs until a defined cut-off potential followed by a short potentiostatic step to minimize effects due to the cell resistance. Afterwards, the direction of the current is reversed until the start potential is reached. For more discharge cycles, the procedure is repeated. The gravimetric capacity C in [mAh g^{-1}] of the investigated active electrode material can then be determined using Equation 2.9:

$$C = \frac{I \cdot t}{m} \qquad 2.9$$

where I is the applied current, t - the duration of the charge or discharge process until the cut-off voltage is reached and m – the mass of the active electrode material.[17]

The relation of applied current to the investigated active mass of the electrode can define the kinetics of the experiment and is often given as C-rates. Herein, 1C is defined as the rate to fully charge or discharge a material within 1 h with regard to its theoretical possible capacity. As the C-rate convention is reciprocal to time, a rate of 0.5C corresponds to an experimental duration of 2 h and a rate of 6C to a duration of 10 min.

Furthermore, similar to CV the potentials of different redox processes during charging and discharging can be figured out by plateaus in the capacity-potential plots. The location and occurrence of each plateau is depending on the redox potential of the electrochemical active species, the type of the electron transfer process and the C-rate. As in the CV, multiple cycling of the active electrode material can give information about the electrode stability, the quality of the electrode composite and the lifetime of the cell.

Electrochemical measurements were performed in a three-electrode setup using an *AUTOLAB* potentiostat/galvanostat *PGSTAT302N* with *FRA32M* module operating with *Nova 1.10.4* software.

Thin film electrodes were typically prepared by simply drop-casting a certain amount of a dispersion on a defined area, 1.0 cm x 1.5 cm, of a 1.0 cm x 3.0 cm FTO glass substrate. The specimen were calcined under air by heating up with a heat rate of 3 °C min^{-1} to the respective calcination temperature and a dwell time of 5 h. Afterwards the samples cooled down to room temperature with an estimated cooling rate of about 1 °C min^{-1}. To provide good electrical contact to the attached electrodes a small strip of silver varnish was attached to the upper part of the uncoated side of the FTO glass substrate. The thin film electrodes on FTO were then measured in a custom-made three-electrode setup (Figure 2.12) with lithium sheets as both, RE (3) and CE (2), and the nanostructured LCO film as WE(1). A 1 M $LiN\text{-}(SO_2CF_3)_2$ solution in a mixture of ethylene carbonate (EC) and 1,2-dimethoxyethane (DME) (1:1 by weight) that was dried over 3 Å molecular sieves for at least 24 h was used as electrolyte.

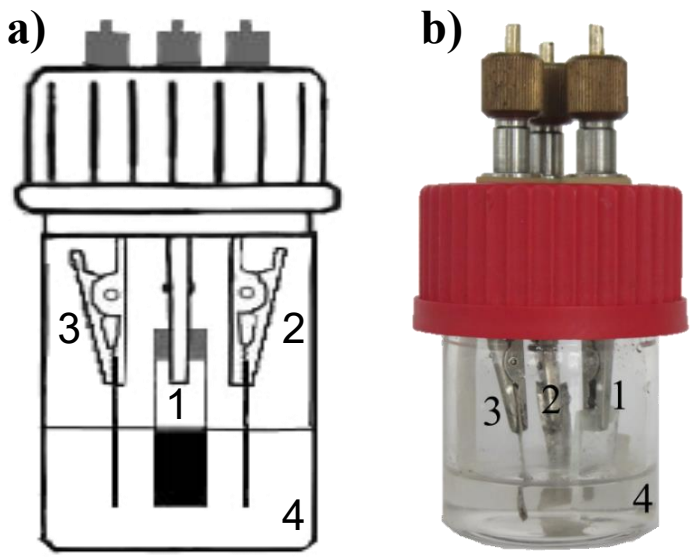

Figure 2.12: Sketch (a) and photograph (b) of the custom-made three-electrode setup for thin film measurements on FTO substrates (1) with lithium sheets as both, CE (2) and RE (3).[1]

Compound electrodes were typically prepared by mixing the powders of the nanostructured active material together with carbon black Super C65 purchased from TIMCAL and poly(vinylidene fluoride) (PVdF) from Aldrich in a ratio of 80:10:10. Small amounts of 1-methyl-2-pyrrolidinone purchased from Sigma-Aldrich (99% purity) was added to the mixture to produce a slightly viscose mixture called ink. The ink was stirred overnight and treated for at least 20 min with an ultrasonic horn (Vibra Cell VC 250 of Sonics Materials) at half power and/or a vortexer. A wet film of 100 µm of the ink was normally coated on the respective metal foil by an automatic film applicator coater ZAA 2300 from Zehntner with a coating speed of 5 mm s^{-1} and dried afterwards at 60 °C for 3 h. Circular electrodes of 18 mm in diameter were punched out and then dried at 120 °C for 5 h under vacuum.

Compound electrodes were measured in an *EL-CELL ECC-PAT-Core* three-electrode setup (**Figure 2.13** on the left). The cathode material compounds were coated on Al-foil and the anode material compounds on Cu-foil. The electrodes of the investigated active materials were separated from the Li metal foil anode by an insulation sleeve equipped with a *WHATMAN* glass-fiber separator and a lithium metal reference ring (**Figure 2.13** on the right). We used as electrolyte the commercially available *PuriEL* with 1.15 M $LiPF_6$ in EC/ethyl-methyl-carbonate (EMC)/dimethylcarbonate (DMC) in a 2:2:6 volume to volume ratio and 1.0 wt% fluoroethylene carbonate (FEC) purchased from *Soulbrain MI*.

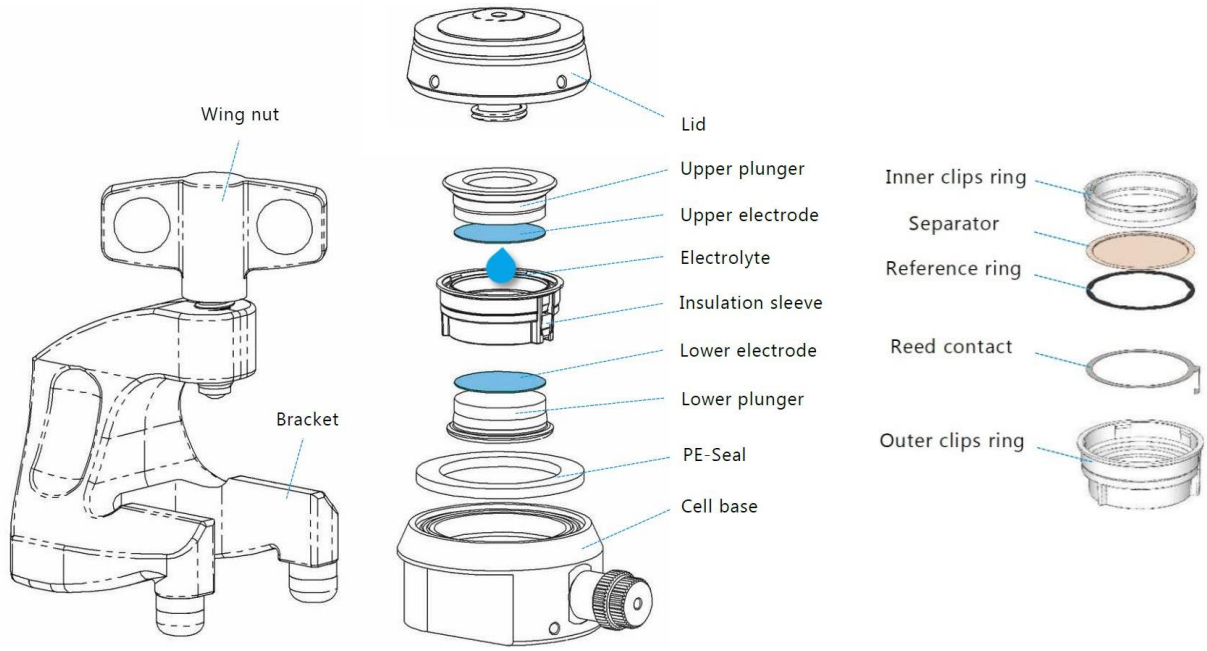

Figure 2.13: Schematic assembly of the EL-CELL ECC-PAT-Core (left) and of the insulation sleeve in particular (right).[19]

2.11 References

[1] P. M. Zehetmaier. Master thesis, University of Munich (LMU) **2014**.

[2] G. Cao. *Nanostructures & Nanomaterials: Synthesis, Properties & Applications*. Imperial College Press: London, 2004.

[3] E. J. Mittemeijer, U. Welzel. *Modern Diffraction Methods*. Wiley, 2013.

[4] M. A. G. Soler, F. Qu. Raman Spectroscopy of Iron Oxide Nanoparticles. In: C. S. S. R. Kumar (ed). *Raman Spectroscopy for Nanomaterials Characterization*. Springer Berlin Heidelberg: Berlin, Heidelberg, 2012, pp 379-416.

[5] R. Pecora. *Journal of Nanoparticle Research* **2000**, *2*, 123-131.

[6] S. Ghosh, V. L. Prasanna, B. Sowjanya, P. Srivani, M. Alagaraja, D. Banji. *Inductively coupled plasma - Optical emission spectroscopy: A review*, vol. 3, 2013.

[7] https://openoregonstate.pressbooks.pub/microbiology/chapter/microscopes/ (retrieved 16.04.2018 18:00).

[8] A. W. Coats, J. P. Redfern. *Analyst* **1963**, *88*, 906-924.

[9] S. Brunauer, P. H. Emmett, E. Teller. *J Am Chem Soc* **1938**, *60*, 309-319.

[10] M. Thommes, K. Kaneko, V. Neimark Alexander, P. Olivier James, F. Rodriguez-Reinoso, J. Rouquerol, S. W. Sing Kenneth. *Pure and Applied Chemistry* **2015**, *87*, 1051.

[11] M. Thommes, K. Kaneko, V. Neimark Alexander, P. Olivier James, F. Rodriguez-Reinoso, J. Rouquerol, S. W. Sing Kenneth. Physisorption of gases, with special reference to the evaluation of surface area and pore size distribution (IUPAC Technical Report). *Pure and Applied Chemistry*; 2015. p. 1051.

[12] J. K. G. Ertl. *Low energy electrons and surface chemistry*, 2 edn. VCH Verlagsgesellschaft: Weinheim 1985.

[13] http://www.rowbo.info/XPS.html (retrieved 18.04.2018 13:00).

[14] A. Unkel. *Basic Knowledge of Nuclear Magnetic Resonance Spectroscopy (NMR)*. OpenStax CNX, 2012.

[15] B. Blümich. *TrAC Trends in Analytical Chemistry* **2016**, *83*, 2-11.

[16] M. Deschamps. Chapter Three - Ultrafast Magic Angle Spinning Nuclear Magnetic Resonance. In: G. A. Webb (ed). *Annual Reports on NMR Spectroscopy*, vol. 81. Academic Press, 2014, pp 109-144.

[17] A. J. Bard, L. R. Faulkner. *Electrochemical Methods: Fundamentals and Applications*. Wiley, 2000.

[18] J. Heinze. *Angewandte Chemie* **1984**, *96*, 823-916.

[19] https://el-cell.com/products/test-cells/standard-test-cells/pat-cell#1489054119432-11ba84bf-d8c3 (retrieved 19.04.2018 15:30).

3 Ultrasmall Co_3O_4 nanoparticles drastically improving solar water splitting on mesoporous hematite

This chapter is based on the following publication:

Ultrasmall Co_3O_4 Nanocrystals Strongly Enhance Solar Water Splitting on Mesoporous Hematite

Feckl, J. M.*, Dunn, H. K.*, Zehetmaier. P. M., Müller, A., Pendlebury, S. R., Zeller, P., Fominykh, K., Kondofersky, I., Döblinger, M., Durrant, J. R., Scheu, C., Peter, L., Fattakhova-Rohlfing, D., Bein, T., *Adv. Mater. Interfaces* **2015**, *2*, 1500358.

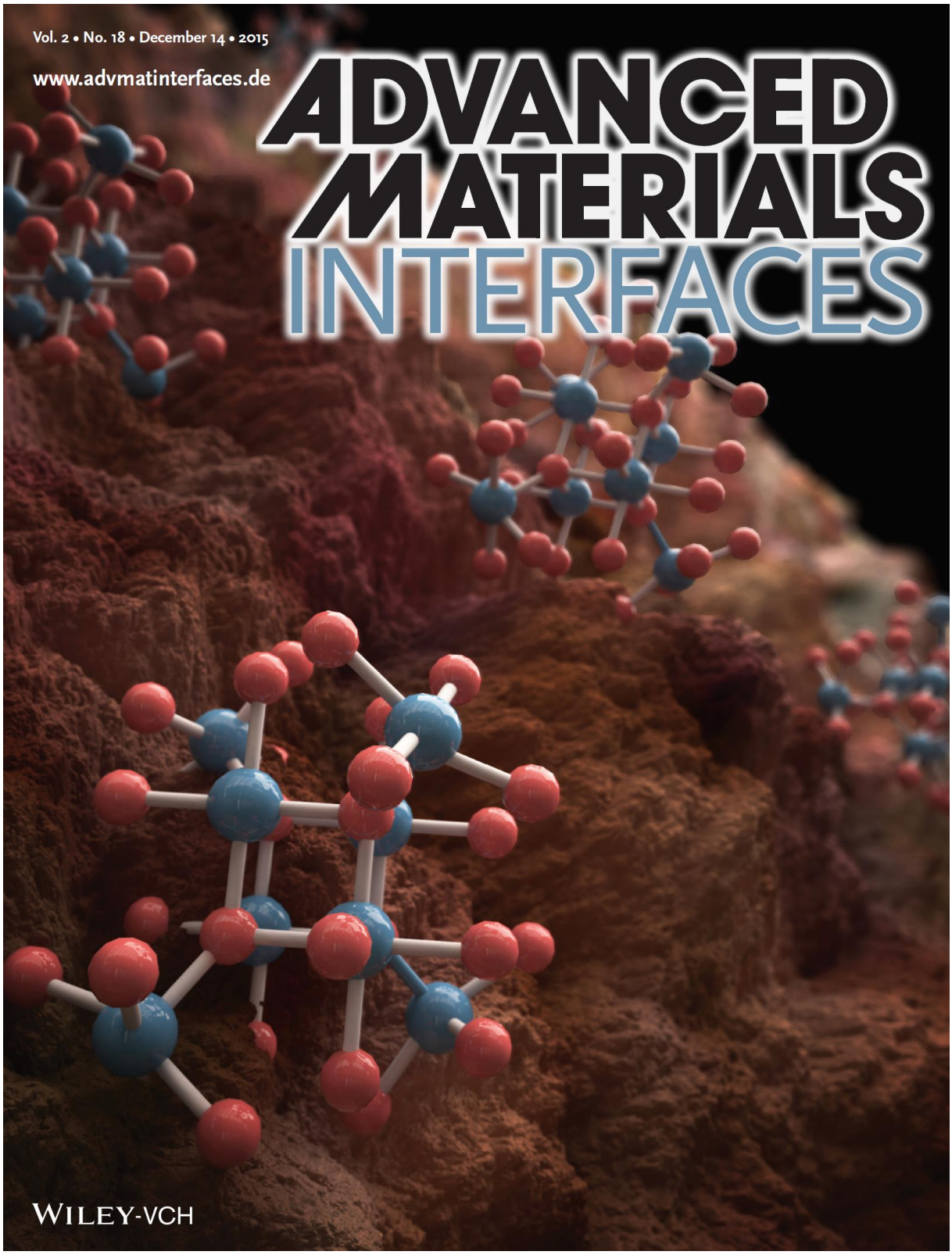

Figure 3.1: Image created by Christoph Hohmann (Nanosystems Initiative Munich, NIM) published as front cover in Adv. Mater. Interfaces 18/2015 (used with permission from the publisher).

3.1 Abstract

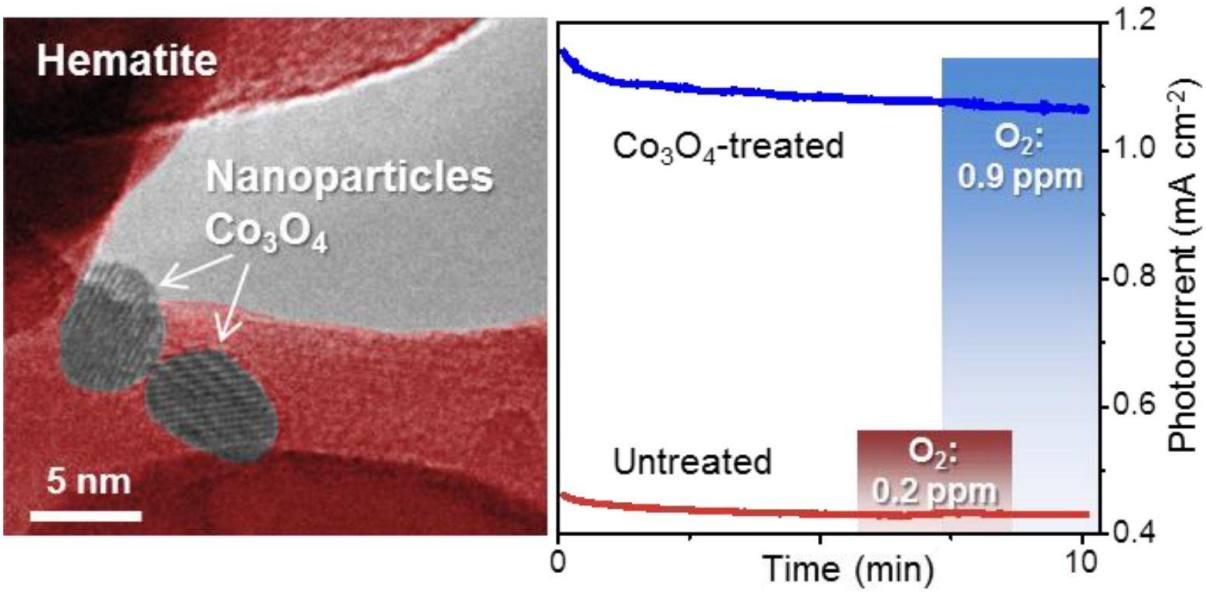

Figure 3.2: ToC image: Ultrasmall dispersible Co3O4 nanocrystals with an average size of 3 - 7 nm are prepared by a solvothermal reaction in tert-butanol. The small size and high dispersibility of the nanoparticles enable their homogeneous deposition on nanostructured Sn-doped hematite serving as a photoanode in light-driven water splitting. This surface treatment leads to a striking photocurrent increase.

The synthesis of crystalline, nonagglomerated, and perfectly dispersible Co_3O_4 nanoparticles with an average size of 3 - 7 nm using a solvothermal reaction in *tert*-butanol is reported. The very small size and high dispersibility of the Co_3O_4 nanoparticles allow for their homogeneous deposition on mesoporous hematite layers serving as the photoactive absorber in the light-driven water splitting reaction. This surface treatment leads to a striking photocurrent increase. While the enhancement of hematite photoanode performance by cobalt oxides is known, the preformation and subsequent application of well-defined cobalt oxide nanoparticles are novel and allow for the treatment of arbitrarily complex hematite morphologies. Photoelectrochemical and transient absorption spectroscopy studies show that this enhanced performance is due to the suppression of surface electron–hole recombination on time scales of milliseconds to seconds.

3.2 Introduction

The spinel Co_3O_4 is interesting for applications such as gas sensing,[1] electrochemical lithium ion storage,[2-6] and as a catalyst for lithium air batteries,[7] for the combustion of CH_4,[8] for the oxidation of CO,[9] for the oxygen reduction reaction in fuel cells,[10, 11] or for electrochemical water oxidation.[12] Co_3O_4 has the highest turnover frequency for dark electrochemical water oxidation among the various cobalt oxides, and the catalytic activity is enhanced with decreasing crystallite size.[12] Interest in Co_3O_4 for photoelectrochemical water splitting was sparked by the work of Kanan and Nocera,[13] and several other groups demonstrated the high efficiency of various cobalt compounds,[14-20] including Co_3O_4,[21-23] as oxygen evolving catalysts. The effect is pronounced in combination with Fe_2O_3 hematite photoanodes. Hematite offers several features attractive for solar water splitting,[24-27] but also suffers from serious limitations including the sluggish kinetics of the oxygen evolution reaction (OER)[28-30] and the high rate of electron–hole recombination at the surface.[19, 26, 31-33] The photoelectrochemical water splitting efficiency of hematite photoanodes was found to improve significantly upon surface treatment with different cobalt compounds.[14-19, 34] The role of these surface treatments is not yet fully understood,[34] although some of them were found to suppress surface recombination but not to catalyze the hole transfer.[18, 35, 36] The reported synthetic methods rely either on electrochemical deposition,[14-17] in situ growth,[18, 23, 37] or atomic layer deposition.[19, 34] However, the former methods are sensitive to the growth conditions or surface properties of the photoabsorber material and not always applicable to complex electrode geometries, while the latter is not easily and economically scalable. [14-17] Consequently, the development of a facile procedure for the low-temperature deposition of Co_3O_4 with well-defined properties on any type of photoabsorber substrate, independent of surface properties or morphology, is very desirable. Dispersible nanoparticles are particularly interesting for this purpose, as their deposition from solution can easily be controlled.

Compared to an in situ growth process, the formation of nanocrystals in a separate process allows for a much better control of properties such as size, shape, and chemical composition. Although several Co_3O_4 morphologies such as nanotubes,[6, 38] needles,[4] rods,[11] wires,[5] hollow spheres,[8] nanoboxes,[39] and nanoparticles[12, 37, 40-45] are synthetically available, it appears that none of these have so far been applied to photoabsorbers for water splitting. Here, we report the solvothermal synthesis of dispersible, non-agglomerated, and crystalline Co_3O_4 nanoparticles

with sizes in the range of 3–7 nm. The nanoparticles can be dispersed in ethanol and homogeneously distributed on the surface of mesoporous hematite photoanodes by a simple drop-casting process. This treatment leads to a more than fivefold increase in photocurrent under AM 1.5 illumination compared to the untreated hematite electrodes. The performance enhancement is more pronounced for thicker films, suggesting that the reason for the increased photocurrents is enhanced electron collection in the mesoporous nanoparticle-containing hematite electrodes rather than acceleration of hole transfer at the hematite–solution interface. Efficient extraction of photogenerated electrons from a mesoporous photoanode requires retardation of their recombination with the photogenerated holes (and with intermediates in the water oxidation reaction), resulting in significantly more long-lived surface-accumulated holes, which are required for water oxidation on hematite. This observation was supported by transient absorption spectroscopy (TAS), which showed an increased lifetime of long-lived (ms to s time scale) photogenerated holes at or near the hematite surface.

3.3 Results and Discussion

For the synthesis of dispersible crystalline Co_3O_4 nanoparticles we developed a solvothermal procedure in *tert*-butanol. This solvent has already been shown to be suitable for the preparation of dispersible, crystalline, and ultrasmall metal-oxide nanoparticles such as different titania compounds, NiO, and tin oxide.[46-51] For the preparation of Co_3O_4 nanoparticles, $Co(OAc)_2$ was dispersed in a solution of Pluronic P123 in *tert*-butanol. After the addition of concentrated nitric acid to the reaction solution, the mixture was autoclaved at 120 °C for 17 h. Only a combination of $Co(OAc)_2$, nitric acid, and Pluronic P123 led to the formation of small non-agglomerated particles. The use of $Co(NO_3)_2$ as an alternative precursor causes the fast growth of larger nanocrystals whose size cannot be decreased by changing reaction conditions or by adding stabilizing ligands. On the other hand, using $Co(OAc)_2$ as a precursor leads to the formation of mostly amorphous material. We believe that the combination of $Co(OAc)_2$ with nitric acid leads to the *in situ* formation of reactive $Co(NO_3)_2$ that can form Co_3O_4. It seems reasonable to assume that the particles are capped by acetate ligands, limiting the particle growth. The presence of Pluronic P123 additionally stabilizes and limits the particle growth.

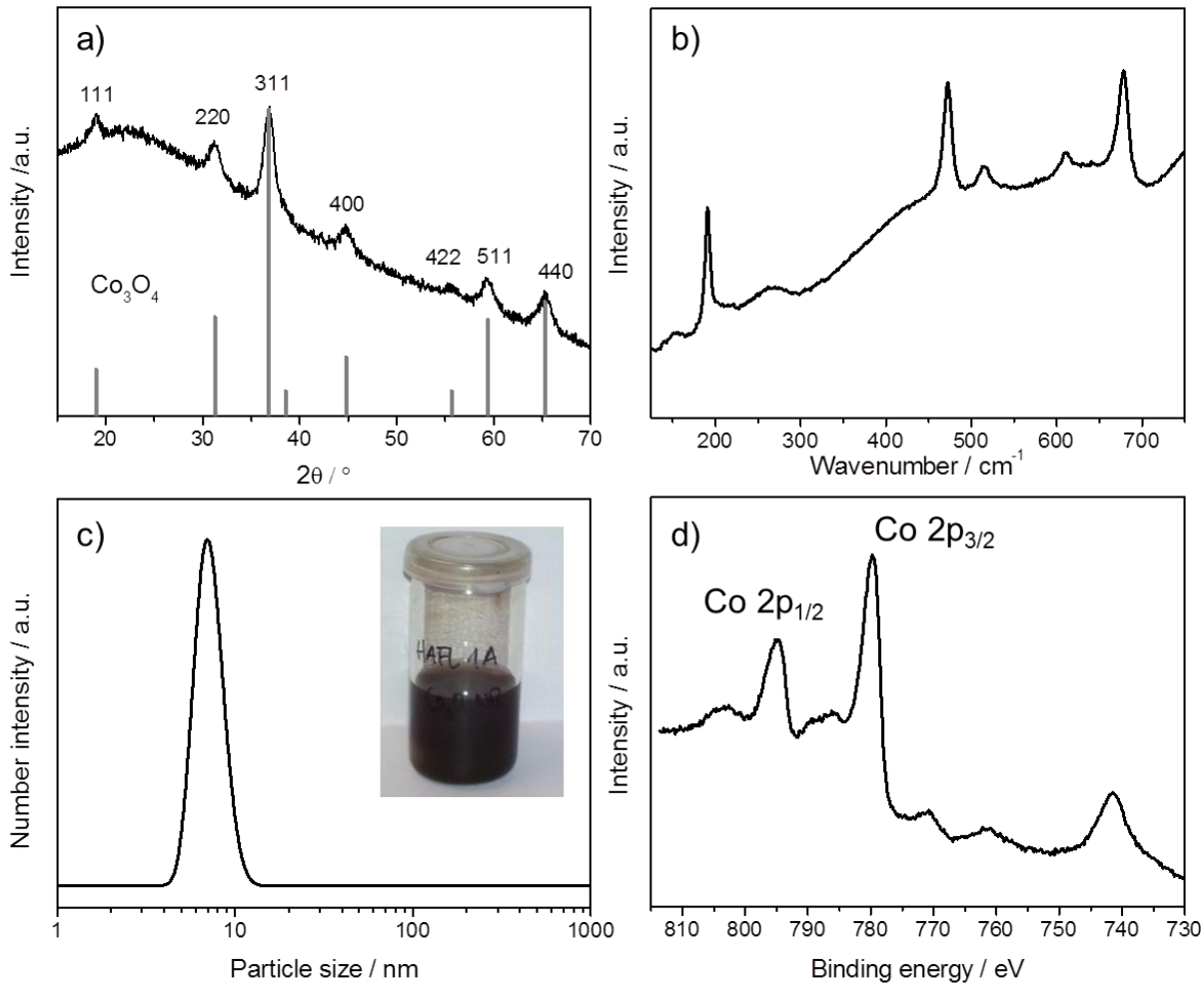

Figure 3.3: Morphology and composition of as-synthesized Co_3O_4 nanoparticles prepared via the *tert*-butanol route: a) XRD pattern of nanoparticles with the corresponding ICDD card 00-043-1003 of Co_3O_4 and b) Raman spectrum of the Co_3O_4 nanoparticles. The peaks at 190.7 (F_{2g}), 472.7 (E_g), 513.1 (F_{2g}), 610.0 (F_{2g}), and 678.6 (A_{1g}) cm^{-1} correspond to the Raman modes characteristic of Co_3O_4.[52] c) DLS measurement of a diluted Co_3O_4 nanoparticle dispersion; the inset shows a photograph of a dispersion with a concentration of 22.8 mg Co_3O_4 nanoparticles after drying, dispersed in 4 mL ethanol; and d) XPS spectrum of Co_3O_4 nanoparticles showing the Auger transitions of oxygen at 742 eV and 761 eV and the Co 2p signals, which are split by spin–orbit coupling into Co $2p_{3/2}$ (779.9 eV) and $2p_{1/2}$ (795.0 eV).

After cooling to room temperature, the nanoparticles could be collected simply by centrifugation or by drying the processed solution. X-ray diffraction of the obtained solid proves the formation of about 7 nm small Co_3O_4 nanoparticles (size calculated according to the Scherrer´s equation from the broadening of the 311 reflection; Figure 3.3a). The high background in the XRD pattern is attributed to the fluorescence common for cobalt-containing materials when using Cu-K_α radiation. Additionally, the Raman spectrum of the nanoparticles shows modes characteristic of Co_3O_4 (Figure 3.3b).[52] The solid is easily redispersible in ethanol by adding a drop of

concentrated acetic acid. This was proven by dynamic light scattering (DLS) measurements in Figure 3.3c, which show a narrow peak at around 7 nm.

X-ray photoelectron spectroscopy measurements were performed to determine the oxidation states of the cobalt oxide nanoparticles. Figure 3.3d shows the Auger transitions of oxygen at 742 and 761 eV and the Co 2p signals that are split by spin–orbit coupling into Co $2p_{3/2}$ and $2p_{1/2}$. The binding energy of the Co $2p_{3/2}$ peak (779.9 eV) and the absence of a satellite at about 786 eV (which would indicate CoO) identify the samples as Co_3O_4.[53] The XPS spectra before and after electrochemical testing look very similar, suggesting no significant changes in the material during the electrochemical reactions (see Figure 3.4).

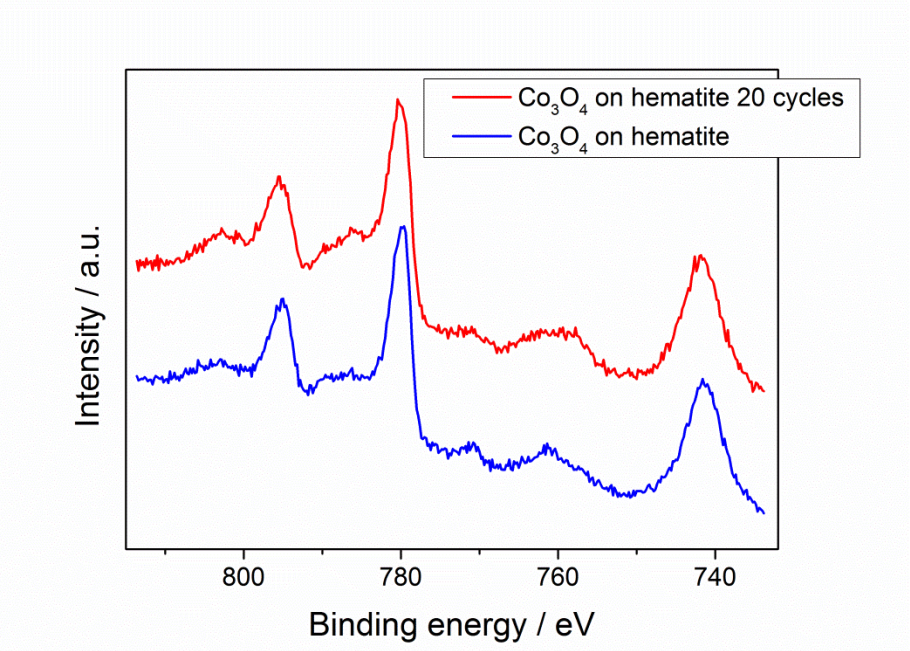

Figure 3.4: XPS spectra of cobalt oxide nanoparticles deposited on top of Sn-doped hematite electrodes before and after 20 cyclic voltammetry scans under 455 nm illumination, incident photon flux 10^{17} $cm^{-2}s^{-1}$. The XPS spectra exhibit the Auger transitions of oxygen at 742 eV and 761 eV and the Co 2p signals that are split by spin-orbit coupling into Co $2p_{3/2}$ (779.9 eV) and $2p_{1/2}$ (795.0 eV).

In good agreement with the data obtained by XRD and DLS, high-resolution transmission electron microscope images show monocrystalline nanoparticles with *d*-spacings typical of Co_3O_4 (Figure 3.5). The particles sized 3-7 nm are non-agglomerated and evenly distributed on the surface of the TEM grid, indicating high dispersibility in ethanol (Figure 3.5a).

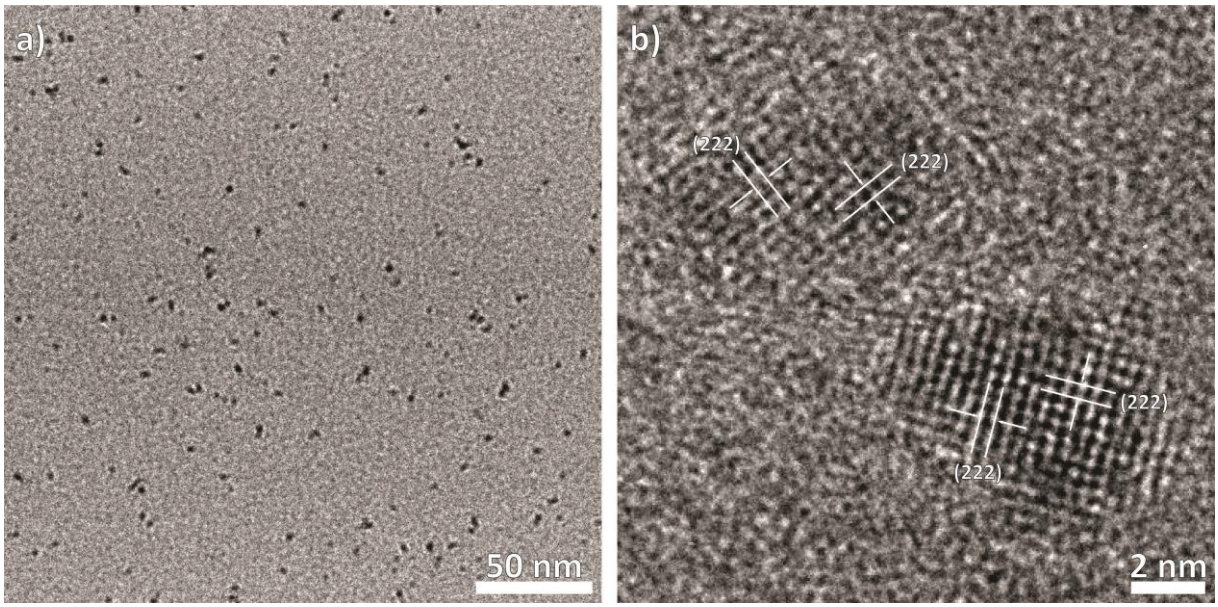

Figure 3.5: a) TEM image of finely dispersed Co3O4 nanoparticles. b) HRTEM image of two individual Co_3O_4 nanoparticles.

The ultrasmall and dispersible Co_3O_4 nanoparticles were applied as a surface treatment to mesoporous, Sn-doped hematite layers prepared by a wet chemical deposition described by Dunn et al.[54] The hematite electrodes prepared in this way feature a disordered mesoporous structure composed of elongated crystalline nanoparticles with an average size of around 40 × 80 nm. The thickness of the electrodes can be varied from about 50 to 400 nm by repetitive coating.[54] Even though the photocurrents are lower than those of state-of-the-art hematite photoelectrodes,[55] the morphology and photocurrents of the hematite films used in this study are similar to those prepared by other solution-based synthetic routes and therefore provide an excellent model system.[56] The Co_3O_4 nanoparticles were deposited onto the mesoporous hematite electrodes by drop-casting from an ethanolic dispersion. The degree of coating of the hematite photoanodes by Co_3O_4 could easily be controlled by diluting the particle dispersions to the desired concentration. After the deposition step, the samples were heated to 180 °C. This step was necessary to provide good adhesion of the nanoparticles to the mesoporous layer. TEM analysis showed that the Co_3O_4 nanoparticles (which could be identified by lattice spacings, energy-dispersive X-ray spectroscopy measurements, and size) were for the most part homogenously distributed throughout the whole volume of the mesoporous hematite layer. For a rather low nanoparticle loading depicted in Figure 3.6, individual, non-agglomerated nanoparticles are evenly distributed on the hematite crystals, which can be attributed to their excellent dispersibility.

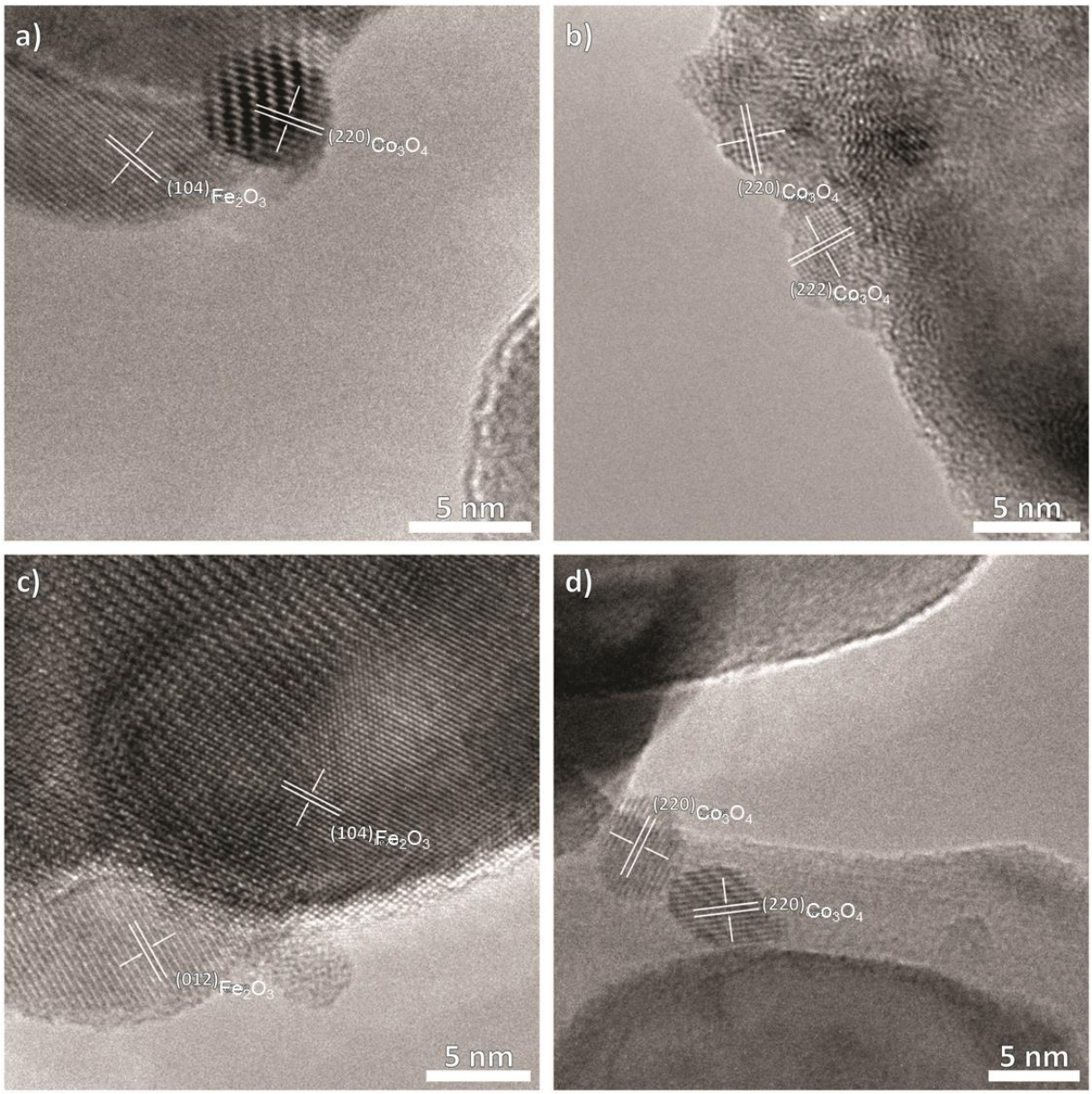

Figure 3.6: HR-TEM images of the cobalt oxide nanoparticle-treated mesoporous hematite layers removed from the substrate. Rare occurrences of agglomerates (c) that could be observed in addition to individual nanoparticles (b) are most likely a result of nanoparticles being caught in pores during the drop-casting process.

The Co_3O_4-treated hematite films fabricated as described above were tested as photoanodes for the photoelectrochemical OER. The current–voltage curves obtained under AM 1.5 illumination are displayed in Figure 3.8 for a 350 nm thick mesoporous hematite film with and without the Co_3O_4 nanoparticle surface treatment. The photocurrent of the hematite electrodes with deposited Co_3O_4 nanoparticles is significantly higher than that of the untreated hematite films. The increase in photocurrent depends on the illumination direction, a phenomenon that will be discussed later. The increase in photocurrent is accompanied by an increase in the amount of detected oxygen

(see Figure 3.7), indicating that the observed effect stems from the water oxidation process and not from any other reactions such as photocorrosion or the oxidation of organics. We detect a cathodic shift in the photocurrent onset potential, although the observed effect is small compared to other reported cobalt treatments.[32, 57-59] Such a shift can indicate either catalysis of charge transfer or a lowering of surface recombination; the analysis of possible effects will be given below.

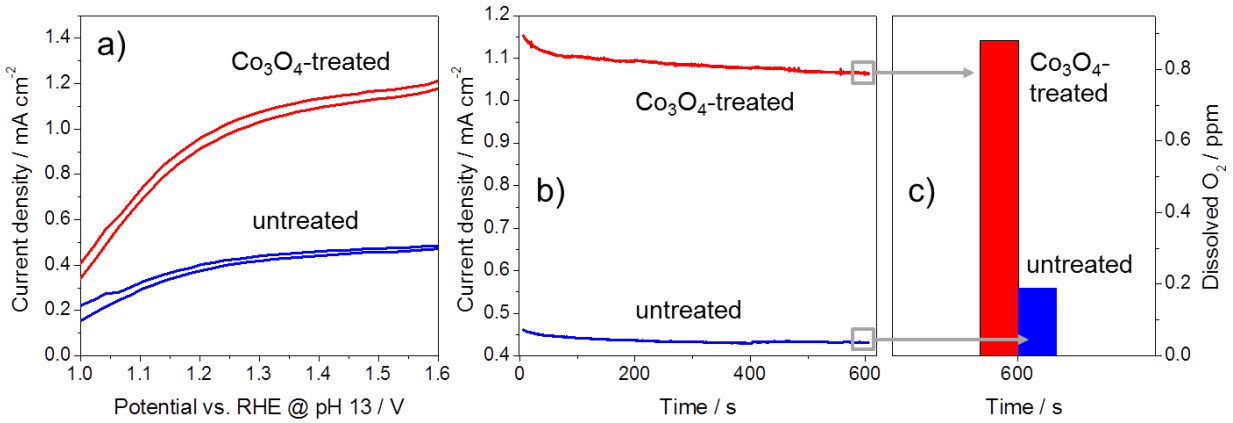

Figure 3.7: (a) Cyclic voltammetry curves of tin-doped hematite films on FTO with (red line) and without (blue line) Co_3O_4 treatment. (b) Potentiostatic measurements on untreated (blue) and Co_3O_4-treated (red) tin-doped hematite samples at 1.56 V vs. RHE over 10 minutes. (c) Amount of dissolved oxygen in electrolyte after 10 minute measurement at 1.56 V vs. RHE and under illumination (455 nm LED, with ca. 10^{17} $cm^{-2}s^{-1}$ intensity).

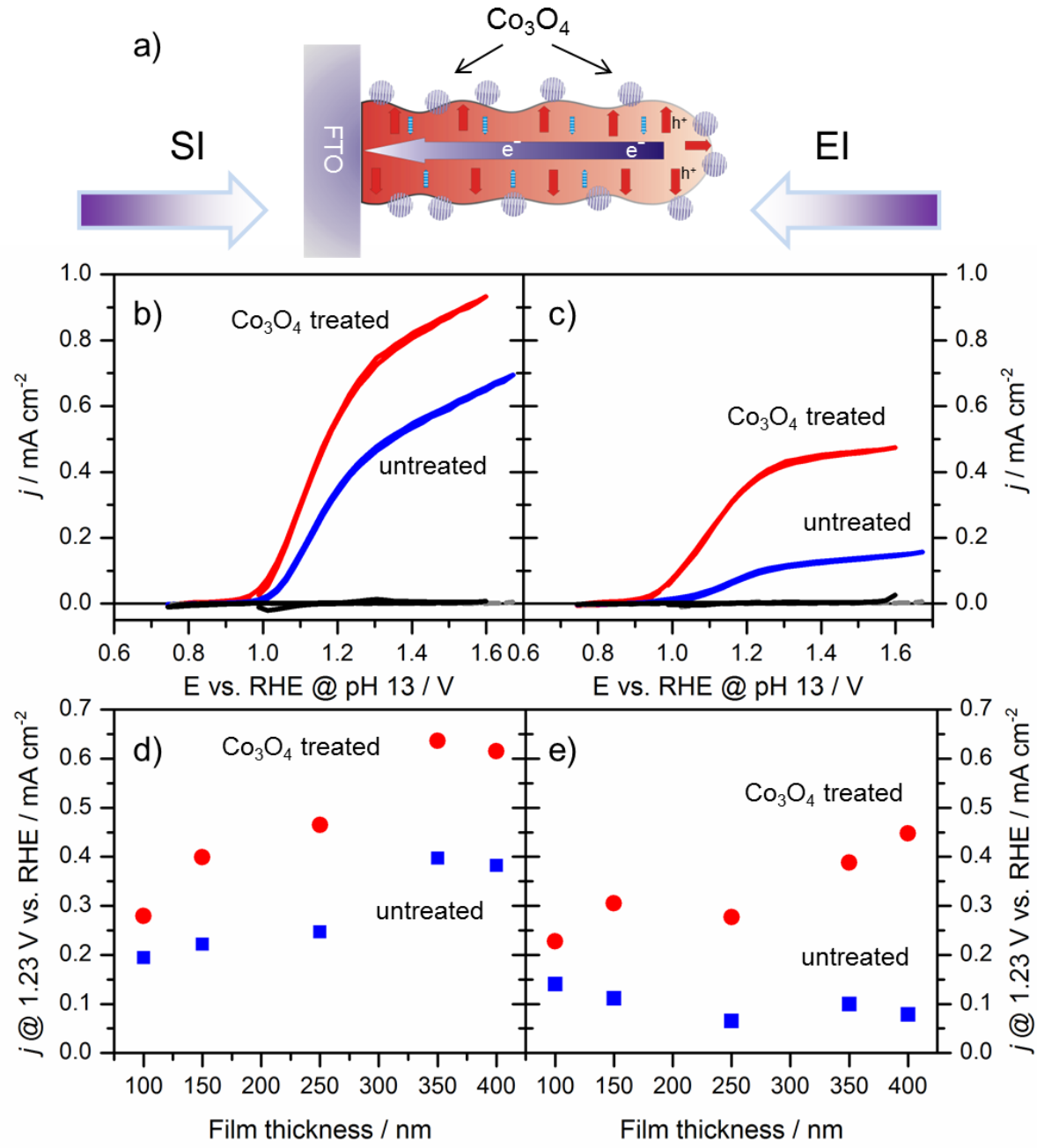

Figure 3.8 a) Simplified illustration of the processes taking place in a porous hematite electrode during illumination. Red arrows indicate diffusion of the photogenerated holes to the hematite surface, the blue arrow indicates diffusion of photogenerated electrons to the substrate (current collector), and striped blue arrows represent their recombination with positive species, such as holes; illumination direction is indicated as SI (substrate illumination) and EI (electrolyte illumination). Current density–voltage curves for 350 nm nanostructured hematite films with (full red lines) and without (dashed blue lines) Co_3O_4 nanoparticle treatment under simulated AM 1.5 illumination through b) the substrate and c) the electrolyte. Dark *j–V* curves are also shown for the Co_3O_4 treated film (full black line) and untreated film (dashed gray line). Photocurrent at 1.23 V versus RHE of films of varying thicknesses with (red circles) and without the Co_3O_4 treatment (blue squares), when illumination is provided through the d) substrate and e) electrolyte.

When deposited directly onto FTO, the Co_3O_4 nanoparticles do not produce any photocurrent, indicating that the observed improvements originate from the synergy between the hematite and the nanoparticles (see Figure 3.9). We note that the Co_3O_4 nanoparticles lower the onset potential of water oxidation in the dark, acting as catalysts for electrochemical water oxidation. To quantify the dark electrocatalytic activity, we prepared thin films by depositing particle dispersions on the Au electrodes of piezoelectric quartz crystal microbalance (QCM) chips. Using Au/QCM crystals as substrates allows for an accurate determination of the mass loading[60] and the direct calculation of turnover frequencies (TOF) from voltammetric data (Figure 3.10). The TOF values can either be calculated based on the mass loading of Co_3O_4, assuming that all Co atoms are catalytically active (TOF_{min}), or by using the BET surface area based on the assumption that the catalytically active sites are located only on the surface of the electrode (TOF_{max}). We applied both methods to compute the TOF values for our Co_3O_4 nanoparticles. For example, the TOF_{min} values at overpotentials of $\eta = 300$ mV and $\eta = 400$ mV are 0.003 and 0.01 s^{-1}, respectively. The TOF_{max} at the same overpotentials were calculated as 0.021 and 0.63 s^{-1}, which is an order of magnitude higher than the corresponding TOF_{min}. The obtained results indicate that Co_3O_4 nanoparticles act as a reasonably good dark catalyst for the OER, although the TOF values do not surpass those of other cobalt oxide structures reported in the literature.[21, 58, 59, 61, 62] It should also be noted that good dark catalysts do not necessarily act as catalysts when deposited on photoelectrodes.[58, 63] The explanation for this possibly lies in the different mechanisms of the light and dark OER, as the former involves minority carriers, whereas the latter involves majority carriers.

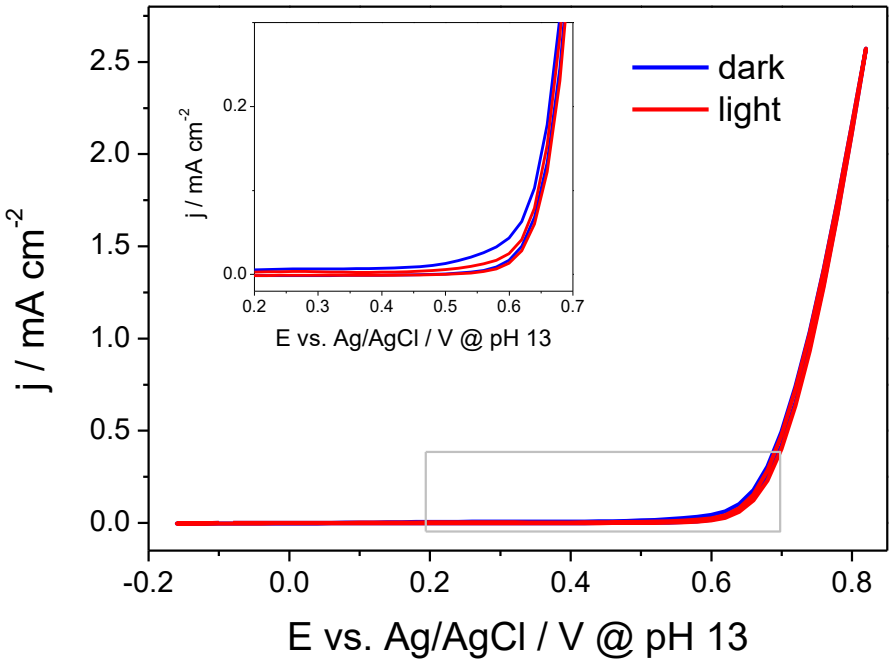

Figure 3.9: Cyclic voltammograms of a Co_3O_4 treated (red) FTO electrode in the dark (blue) and under illumination (455 nm LED, with ca. 10^{17} $cm^{-2}s^{-1}$ intensity) (red). An inset shows a zoomed area marked in grey.

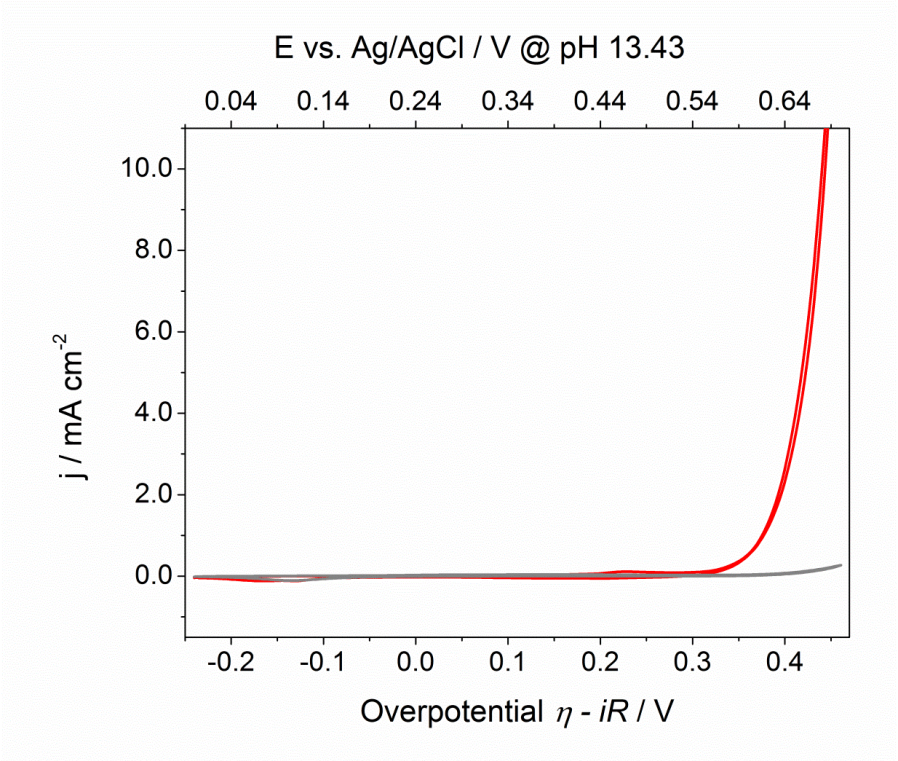

Figure 3.10: Dark CV curves of a Co_3O_4 electrode prepared on a Au/QCM crystal (red line) and a bare Au/QCM crystal (grey line). The electrodes were cycled vs. Ag/AgCl in 0.5 M KOH with the scan rate of 20 mV s^{-1}. The reduction peak at the potential of ca. 0.1 V vs. Ag/AgCl corresponds to the Au electrode and is visible in both CV curves.

To elucidate how the Co_3O_4 nanoparticles improve the performance of hematite photoanodes, we compared their effect on the photocurrent for substrate (SI) and electrolyte (EI) side illumination. A scheme illustrating the various pathways of photogenerated charges in a mesoporous electrode is shown in Figure 3.8a. In porous hematite layers made up of particles of the same size, photogenerated holes (red arrows in Figure 3.8a) travel the same short distance to reach the oxide–solution interface, independent of the illumination direction. Photogenerated electrons, in contrast, must travel through the porous layer to the FTO substrate, and for strongly absorbed light (i.e., at wavelengths where the penetration depth of the light is much less than the film thickness), the average distance travelled therefore depends on the illumination direction. Under EI, electron–hole pairs are generated far away from the substrate and electrons have a long collection pathway through the thickness of the film (blue arrow in Figure 3.8a). This leaves them vulnerable to recombination with surface species such as trapped holes (this loss pathway is depicted by blue striped arrows). Under SI, we expect more efficient electron collection, since the charges are generated very close to the FTO substrate. The comparison of the photocurrent under EI and SI thus gives insight into electron–hole recombination in porous electrodes;[55, 64] the description of this method for AM 1.5 illumination will be published separately.

For the untreated hematite electrode, the photocurrent measured when illuminating by an AM 1.5 solar simulator through the electrolyte is approximately a quarter of that obtained when illuminating through the substrate (Figure 3.8b,c). According to the arguments outlined above, this indicates that a considerable portion of photogenerated electrons is not collected when generated far from the FTO substrate. However, when applying Co_3O_4 nanoparticles to 100-400 nm thick mesoporous hematite layers, the photocurrent when illuminating through the substrate strongly increases by a factor of 1.6 compared to the untreated hematite electrode, reaching 0.64 mA cm^{-2} at 1.23 V versus the reversible hydrogen electrode (RHE) for the 350 nm thick electrode (Figure 3.8b,d). Much higher increases of up to a factor of nearly five are observed for EI (Figure 3.8c,e). Given that the losses to recombination under EI are expected to scale with the film thickness, one can expect a more dramatic effect of the Co_3O_4 nanoparticles on thicker films. Figure 3.8 illustrates the photocurrent at 1.23 V versus RHE of films of varying thickness under SI (Figure 3.8d) and EI (Figure 3.8e), with and without the Co_3O_4 nanoparticle treatment. Due to electron–hole recombination losses, the deviation between EI and SI increases

as a function of thickness. However, the effect is reduced for Co_3O_4-treated photoanodes, indicating a significant reduction of this loss pathway.

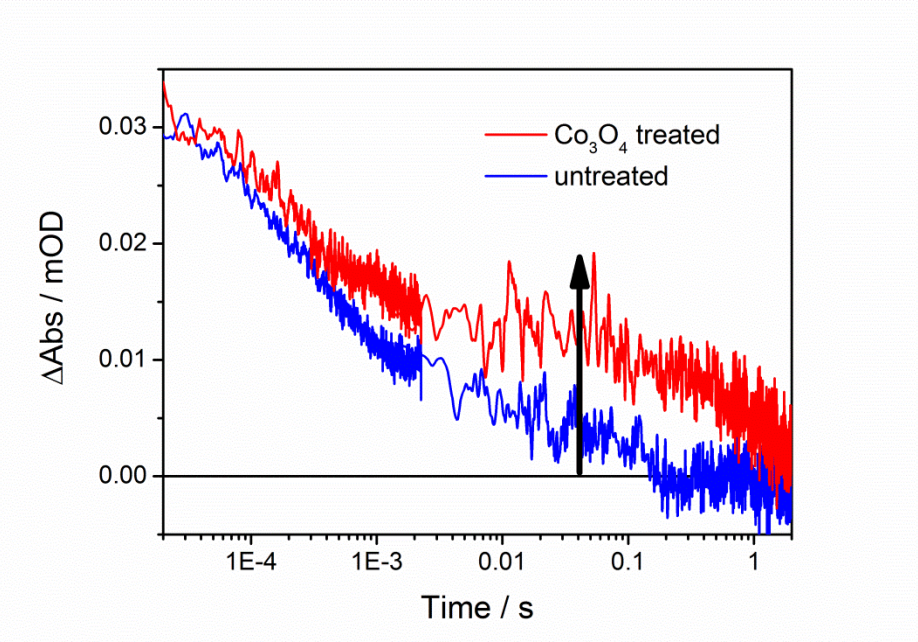

Figure 3.11 Photogenerated hole dynamics in untreated (blue) and Co_3O_4 treated (red) thin (50 nm) hematite photoanodes at open circuit in 1 M NaOH, excited at 455 nm and probed at 650 nm. The arrow indicates the increase in lifetime of photogenerated holes after treatment with Co_3O_4 nanoparticles.

The transient absorption dynamics of photogenerated holes at or near the hematite surface (probed at 650 nm, in accordance with previous studies[30] in untreated and Co_3O_4-treated hematite at open circuit are shown in Figure 3.11 (the same data shown on a linear time axis are presented in Figure 3.12). It is apparent that the Co_3O_4 treatment significantly increases the lifetime of the photogenerated hole signal on millisecond to second time scales. These results are consistent with the effect of other Co-based treatments (such as Co–Pi and cobalt nitrate) on the lifetime of surface-accumulated holes in hematite as studied by transient absorption spectroscopy and intensity modulated photocurrent spectroscopy. [35, 36] The increase in lifetime of photogenerated holes (of $\approx$ 500 ms) on these long time scales indicates that electron–hole recombination at the semiconductor surface has been retarded by the Co_3O_4 treatment.[33] These results are consistent with the photocurrent increase by Co_3O_4 treatment. Interestingly, treatment with cobalt nitrate, which has been reported to increase photocurrents of different hematite photoelectrodes[32, 57] by retarding recombination,[36] had little influence on the performance (see Figure 3.13).

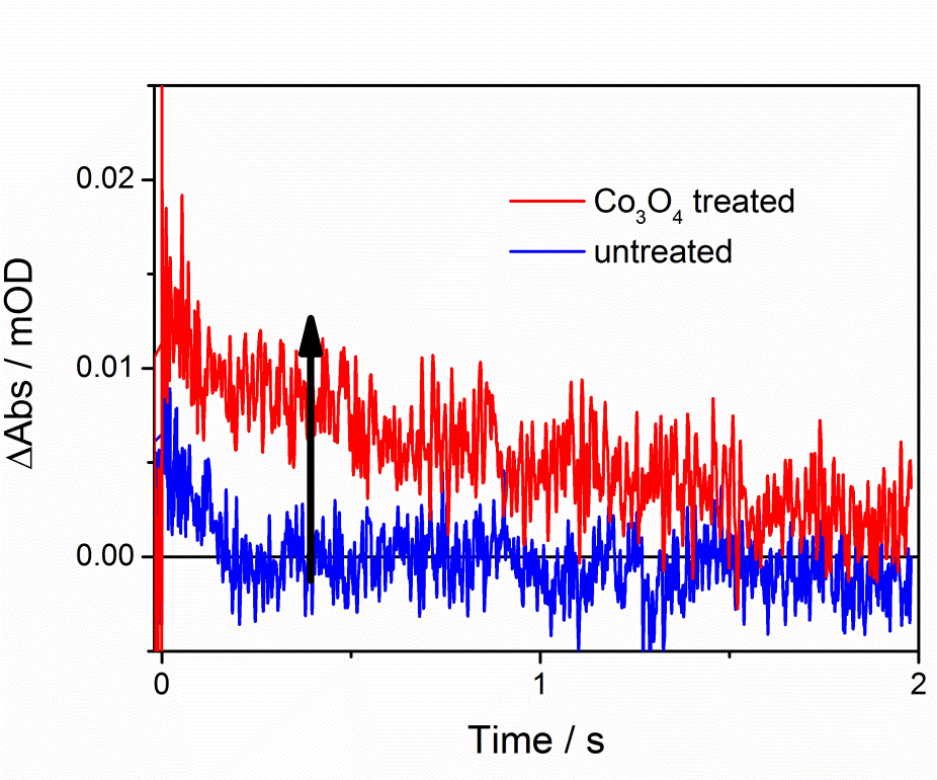

Figure 3.12: Dynamics of surface-accumulated photogenerated holes in untreated (blue) and Co_3O_4 treated (red) thin (50 nm) hematite photoanodes at open circuit in 1 M NaOH, excited at 455 nm and probed at 650 nm, shown on a linear time-axis. The arrow indicates the increase in lifetime of photogenerated holes after treatment with Co_3O_4.

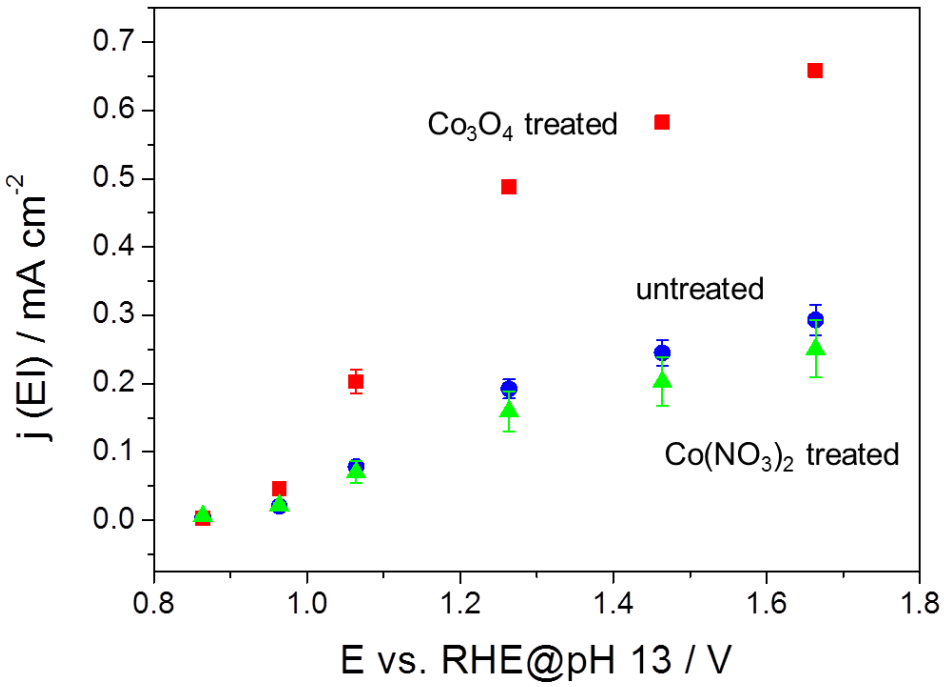

Figure 3.13: Steady state photocurrent under 455 nm illumination with about 10^{17} $cm^{-2}s^{-1}$ intensity from the electrolyte side of 150 nm Sn-doped hematite films (blue), as well as identical films treated with Co_3O_4 (red) and $Co(NO_3)_2$ (green).

The observed improvement in photocurrent depends on the mass loading of the Co_3O_4 nanoparticles in the mesoporous hematite electrodes, as shown in Figure 3.14. The best performance is observed for samples with a low loading of Co_3O_4 nanoparticles. TEM investigation of the best-performing samples demonstrates that the porous hematite layers contain homogeneously distributed nonagglomerated Co_3O_4 nanoparticles, with only a few Co_3O_4 nanoparticles observed on the hematite crystals (Figure 3.14a and Figure 3.6). In contrast, hematite photoanodes treated with concentrated nanoparticle dispersions show suppressed photocurrents compared to the nontreated photoanodes. Examination of such samples by TEM reveals a dense coverage with Co_3O_4 nanoparticles, leaving very little exposed Fe_2O_3. We tentatively attribute the suppressed photocurrent in such densely decorated hematite films to the reduced exposed surface area and an increased parasitic light absorption by the black Co_3O_4.[65]

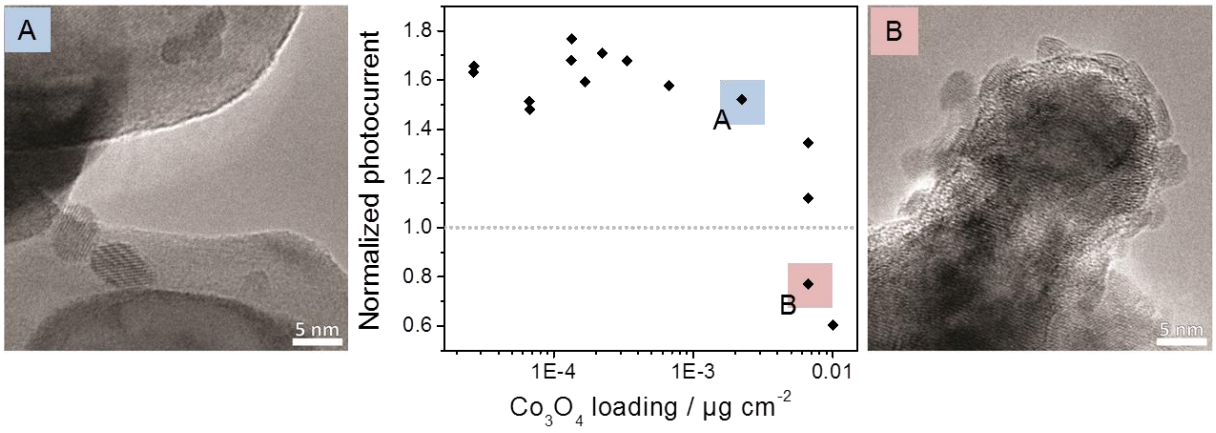

Figure 3.14 Normalized photocurrent at 1.164 V versus RHE (pH 13) under 455 nm illumination with ≈10^{17} $cm^{-2}s^{-1}$ intensity, of Co_3O_4-treated 150 nm Sn-doped hematite films as a function of Co_3O_4 nanoparticle loading on the active area of the electrodes. The normalized current is displayed as a ratio of photocurrent of Co_3O_4 nanoparticle–treated electrodes to that of an untreated electrode of the same thickness. On the left and right side the corresponding TEM images are shown to illustrate the different surface coverage.

The obtained results demonstrate that the postsynthetic Co_3O_4 nanoparticle treatment significantly improves the electron collection in mesoporous hematite photoanodes.

Photoelectrochemical and transient absorption spectroscopy studies suggest that this enhanced performance is due to the suppression of surface electron–hole recombination and not due to the catalysis of charge transfer. However, the way by which Co_3O_4 nanoparticles retard electron–hole

recombination at the semiconductor surface is not fully understood and additional studies are needed to elucidate the mechanism of this effect.

3.4 Conclusion

Ultrasmall Co_3O_4 nanoparticles were synthesized via a newly developed *tert*-butanol solvothermal synthesis protocol. The high dispersibility and very small size of these particles were proven by XRD, DLS, and TEM measurements and allow for the efficient distribution of these monocrystalline nanoparticles on mesoporous hematite films by a drop-casting process. This treatment leads to striking improvements in photoelectrochemical water oxidation rates, increasing the obtained photocurrent by a factor of nearly five. The improvement is attributed to a significant reduction in electron–hole recombination processes on millisecond to second time scales at the surface of the mesoporous network, and strongly depends on the degree of surface coverage by the Co_3O_4 nanoparticles. This demonstrates the importance of a homogeneous distribution of the applied nanoparticles on the highly porous host materials, which can easily be achieved with the stable colloidal dispersions presented in this study.

3.5 Experimental Section

Co_3O_4 Nanoparticle Synthesis: Co_3O_4 nanoparticles were synthesized in *tert*-butanol. All chemicals were purchased from Sigma-Aldrich and used as received. *tert*-Butanol was dried over a 4 Å molecular sieve at 28 °C and filtered prior to use (Sartorius minisart cellulose acetate membrane, 220 nm). In a typical reaction, 50 mg (0.2 mmol) of $Co(OAc)_2$ tetrahydrate was dispersed in a solution of 58 mg Pluronic P123 in 14 mL *tert*-butanol and treated for 45 min in an ultrasonic bath at room temperature. To accelerate the synthesis, 48 mg of concentrated nitric acid was added to the reaction solution. The reaction mixture was transferred into a Teflon lined steel autoclave (20 mL volume) and kept at 120 °C for 17 h. The nanoparticles can be collected by simply drying the processed solution or by centrifugation. The Co_3O_4 content of the resulting centrifuged solid after drying at 180 °C (equivalent to the heat treatment after the deposition of the nanoparticles on the nanostructured hematite electrodes) was determined as 70 wt% by TGA. The pellet was treated with one drop of concentrated acetic acid (35 mg acetic acid per 22.8 mg solid) and then redispersed in ethanol (1 mL ethanol for 1 mg solid). This dispersion was filtered with a 220 nm syringe filter and the concentration of Co_3O_4 nanoparticles in the resulting dispersion was determined by ICP-OES to be 0.667 mg mL^{-1}, which agrees well with the inorganic amount of 70 wt% determined by TGA. This dispersion was then diluted with ethanol (1:50) for DLS measurements, the preparation of TEM samples, and the photoelectrochemical water splitting experiments.

Electrode Preparation: The electrodes were prepared by spin-coating of the cobalt oxide nanoparticle dispersions on Au/QCM crystals (KVG 10 MHz QCM devices with gold electrodes from Quartz Crystal Technology GmbH). In a typical procedure, 10 µL of the cobalt oxide dispersion were deposited on a masked QCM crystal covering an area of 0.196 cm^2 and spun at 1000 rpm for 10 s. The electrodes were subsequently heated in a laboratory oven to 200 °C with a heating ramp of 4 °C min^{-1} and a dwell time of 2 h.

The mass loading was calculated from the change in the resonance frequency of the QCM crystals before and after coating using the Sauerbrey equation (Equation 3.1):

$$\Delta f = -C_f \times \Delta m \qquad 3.1$$

where Δf is the change in frequency, C_f - the sensitivity factor of the QCM crystal and Δm - the change in mass.[60]

Photoelectrode Preparation: Sn-doped hematite electrodes were prepared according to a procedure described in detail elsewhere,[54] resulting in mesoporous films of about 50 nm thickness after calcination at 600 °C. Thicker films were obtained by repeating the complete procedure. The mesoporous morphology of the films obtained in this way is illustrated in a TEM cross-section image shown in Figure 3.15.

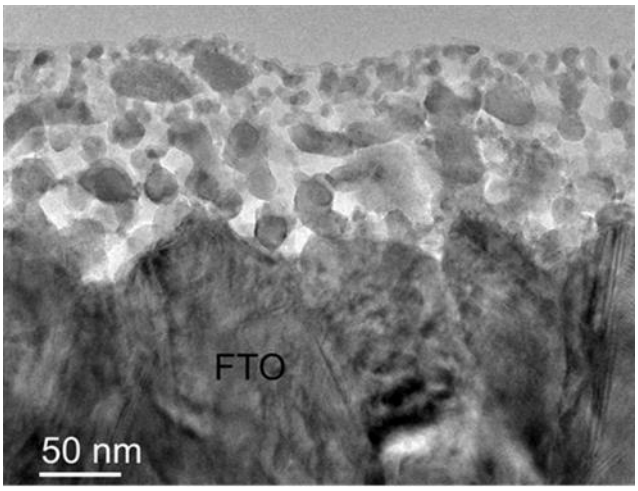

Figure 3.15: Cross-section TEM image of mesoporous Sn-containing hematite film on FTO substrate.

A Co_3O_4 nanoparticle surface treatment was applied to the Sn-containing mesoporous hematite thin films by drop-casting. After depositing 10 µL of the Co_3O_4 nanoparticle dispersion in ethanol as described above onto a projected electrode area of 2.25 cm^2, the films were heated to 180 °C for 30 min. This step was necessary to provide a good adhesion of the nanoparticles to the mesoporous layer. All data reported herein are representative of several samples of each type (hematite film thickness and nanoparticle loading).

Materials characterization: X-ray diffraction analysis of the powders on microscopy slides was carried out in reflection mode (Bragg-Brentano) using a Bruker D8 Discover diffractometer with Ni -filtered Cu-Kα-radiation and a position-sensitive detector (LynxEye).

Raman spectra were recorded with a Jobin Yvon Horiba HR800 UV Raman microscope using a HeNe laser emitting at 632.8 nm.

Scanning electron microscopy was performed on a JEOL JSM-6500F scanning electron microscope equipped with a field emission gun.

TEM analysis was carried out on a FEI Titan 80-300 (S)TEM with a Fischione Instruments (Model 3000) high angle annular dark field (HAADF) detector and an EDAX Energy-dispersive X-Ray Spectroscopy detector. All measurements were conducted at an acceleration voltage of 300 kV. Pure Co3O4 nanoparticles were drop-coated on a copper grid with a holey carbon film, whereas of the treated hematite film material was removed and deposited on such a copper grid.

X-ray photoelectron spectroscopy analysis was performed using a VSW HA 100 hemispherical analyzer and a VSW TA10 X-ray source providing non-monochromatized Mg-Kα-radiation (Mg-Kα = 1253.6 eV).

Dynamic light scattering of the cobalt oxide nanoparticles was performed using a Malvern Zetasizer-Nano equipped with a 4 mW He-Ne laser (633 nm) and an avalanche photodiode detector. The scattering data were weighted based on particle number.

Thermogravimetric analysis was performed on a Netzsch STA 440 C TG/DSC.

Inductively coupled plasma atomic emission spectroscopy was carried out with a VARIAN VISTA RL CCD Simultaneous ICP-OES.

Electrochemical measurements: Cyclic voltammetry measurements were performed at a scan rate of 20 mV s−1 between 0 V and 0.8 V in a three-electrode setup using an Autolab potentiostat/galvanostat PGSTAT302N with FRA32M module operating with Nova 1.10.2 software. A 0.5 M KOH solution (Sigma-Aldrich, volumetric solution, pH 13.43) was used as electrolyte in all measurements. Pt mesh (1 cm2) was used as a counter electrode. Au/quartz crystals coated with Co3O4 nanoparticles were used as working electrodes. All potentials were measured vs. Ag/AgCl/KCl (sat.) reference electrode with a potential of +0.989 V vs. the reversible hydrogen electrode (RHE) at pH 13.43 (+0.197 V vs. NHE). The overpotential η was calculated using Equation 3.2:

$$\boldsymbol{\eta = E - E_{OER} - iR_S} \qquad 3.2$$

where E is the potential recorded vs. Ag/AgCl reference electrode, E_{OER} - the reversible potential of the OER vs. Ag/AgCl reference electrode (0.240 V at pH 13.43), i - the current, and R_s - the uncompensated resistance.

R_s was determined by measuring the minimum total impedance in the frequency mode between 10 and 50 kHz at open circuit conditions at a potential of 0.2 V vs. Ag/AgCl, and was typically around 11-14 Ohm. All data were corrected for 95% of the measured resistance. Current densities were calculated using the unmasked surface area of 0.196 cm^2 of the Au/quartz electrode.

The turnover frequency (TOF) was calculated according to Equation 3.3:

$$\boldsymbol{TOF = \frac{i}{4 \cdot F \cdot n}} \qquad 3.3$$

where i is the current, F - the Faraday constant and n - the amount of Co on the electrode determined either from the total amount of Co atoms using the mass loading (TOF_{min}) or from the number of surface Co atoms calculated using the BET surface area and the density of surface cobalt atoms in cobalt oxide of $6.1 \cdot 10^{18}$.[61]

Photoelectrochemical characterization: Hematite photoelectrodes were masked with a Teflon-coated glass fiber adhesive tape leaving a circular area of 1 cm in diameter exposed to a 0.1 M NaOH aqueous electrolyte. All electrochemical measurements were carried out with glass or quartz cells using a μ-Autolab III potentiostat equipped with a FRA2 impedance analyzer connected to a saturated Ag/AgCl reference electrode (Sigma Aldrich, 0.197 V vs. the standard hydrogen electrode) and a Pt mesh counter electrode. Potentials versus the reversible hydrogen electrode, V_{RHE}, were calculated from those measured at pH 13 versus the Ag/AgCl electrode, $V_{Ag/AgCl}$, according to Equation 3.4:

$$\boldsymbol{V_{RHE} = V_{Ag/AgCl} + 0.197 + 0.059\,pH} \qquad 3.4$$

The light intensity was measured inside the cells using a 4 mm^2 photodiode, which had been calibrated against a certified Fraunhofer ISE silicon reference cell equipped with a KG5 filter.

The current–voltage characteristics of the films were obtained by scanning from negative to positive potentials in the dark or under illumination, with a 20 mV s^{-1} sweep rate. Illumination, which was either provided by a high power light-emitting diode (LED, Thorlabs, 455 nm), or an AM1.5G solar simulator (Solar Light Model 16S) at 100 mW cm^{-2}, was incident either through

the substrate or the electrolyte. A detailed description of the method for quantification of the electron diffusion length will be described in a following publication.

The dissolved O_2 was determined with an HANNA dissolved oxygen bench meter (HI 2400 DO Meter) using the setup described above. The electrolyte solution was purged with N_2 before each measurement until the dissolved oxygen in solution reached 0ppm. During electrochemical measurements N_2 was purged above the solution. The films were illuminated through the electrolyte side using a blue diode (455 nm at 10^{17} $s^{-1}cm^{-2}$).

Current–voltage (*I–V*) curves were obtained by scanning from negative to positive potentials in the dark or under illumination at a 20 mV s^{-1} sweep rate. Further chronoamperometric measurements were carried out at 1.56 V versus RHE over 10 min while determining the concentration change of dissolved oxygen over time.

Transient Absorption Spectroscopy: The dynamics of photogenerated holes in untreated and Co_3O_4-treated hematite photoanodes were measured using microsecond to second timescale TAS. Band gap excitation of hematite was achieved using a 455 nm pulsed laser (0.35 Hz, 210 μJ cm^{-2} $pulse^{-1}$, <20 ns pulse width), generated from the third harmonic (355 nm) of an Nd:YAG laser (Quantel Ultra, Lambda Photometrics) via an optical paramagnetic oscillator (Opolette, Opotek Inc.). This “pump” pulse was transmitted to the sample by a liquid light guide. A 100 W tungsten lamp (IL 1, Bantham) equipped with a monochromator (OBB-2001, Photon Technology International) was employed as the probe beam; holes in hematite were probed at 650 nm, in accordance with previous studies.[30] The sample was illuminated from the EI side (electrolyte–electrode). The transmitted probe light was filtered by several long-pass filters and a band-pass filter in order to remove scattered light from the laser before being focused on a silicon photodiode detector (S3751, Hamamatsu). Microsecond to millisecond timescale data were amplified and filtered (Costronics) and collected by an oscilloscope (TDS 2012c, Tektronics); millisecond to second timescale data were collected with a DAQ card (NI USB-6211, National Instruments). All data were acquired using home-built LabVIEW software. Each trace shown is the average of 300–500 individual measurements. Signals due to laser scatter were subtracted from μs to ms timescale data.

3.6 References

[1] D. W. Su, H. Liu, H. J. Ahn, G. X. Wang. *J Nanosci Nanotechnol* **2013**, *13*, 3354-3359.
[2] D. Liu, X. Wang, X. Wang, W. Tian, Y. Bando, D. Golberg. *Sci Rep* **2013**, *3*.
[3] X. W. Lou, D. Deng, J. Y. Lee, J. Feng, L. A. Archer. *Adv Mater* **2008**, *20*, 258-262.
[4] X. W. Lou, D. Deng, J. Y. Lee, L. A. Archer. *Journal of Materials Chemistry* **2008**, *18*, 4397-4401.
[5] Y. Li, B. Tan, Y. Wu. *Nano Lett* **2008**, *8*, 265-270.
[6] N. Du, H. Zhang, B. Chen, J. Wu, X. Ma, Z. Liu, Y. Zhang, D. Yang, X. Huang, J. Tu. *Adv Mater* **2007**, *19*, 4505-4509.
[7] C. Sun, F. Li, C. Ma, Y. Wang, Y. Ren, W. Yang, Z. Ma, J. Li, Y.-J. Chen, Y. Kim, L. Chen. *Journal of Materials Chemistry A* **2014**, *2*, 7188-7196.
[8] C.-A. Wang, S. Li, L. An. *Chemical Communications* **2013**, *49*, 7427-7429.
[9] X. Xie, Y. Li, Z.-Q. Liu, M. Haruta, W. Shen. *Nature* **2009**, *458*, 746-749.
[10] J. Xiao, Q. Kuang, S. Yang, F. Xiao, S. Wang, L. Guo. *Sci Rep* **2013**, *3*, 2300.
[11] J. Xu, P. Gao, T. Zhao. *Energy & Environmental Science* **2012**, *5*, 5333-5339.
[12] N. H. Chou, P. N. Ross, A. T. Bell, T. D. Tilley. *ChemSusChem* **2011**, *4*, 1566-1569.
[13] M. W. Kanan, D. G. Nocera. *Science* **2008**, *321*, 1072-1075.
[14] M. Barroso, A. J. Cowan, S. R. Pendlebury, M. Grätzel, D. R. Klug, J. R. Durrant. *J Am Chem Soc* **2011**, *133*, 14868-14871.
[15] B. Klahr, S. Gimenez, F. Fabregat-Santiago, J. Bisquert, T. W. Hamann. *J Am Chem Soc* **2012**, *134*, 16693-16700.
[16] D. K. Zhong, D. R. Gamelin. *J Am Chem Soc* **2010**, *132*, 4202-4207.
[17] D. K. Zhong, J. Sun, H. Inumaru, D. R. Gamelin. *J Am Chem Soc* **2009**, *131*, 6086-6087.
[18] C. Y. Cummings, F. Marken, L. M. Peter, A. A. Tahir, K. U. Wijayantha. *Chemical Communications* **2012**, *48*, 2027-2029.
[19] S. C. Riha, B. M. Klahr, E. C. Tyo, S. Seifert, S. Vajda, M. J. Pellin, T. W. Hamann, A. B. F. Martinson. *ACS Nano* **2013**, *7*, 2396-2405.
[20] V. Artero, M. Chavarot-Kerlidou, M. Fontecave. *Angewandte Chemie International Edition* **2011**, *50*, 7238-7266.
[21] J. D. Blakemore, H. B. Gray, J. R. Winkler, A. M. Müller. *ACS Catalysis* **2013**, *3*, 2497-2500.
[22] F. Jiao, H. Frei. *Angewandte Chemie International Edition* **2009**, *48*, 1841-1844.
[23] L. Xi, P. D. Tran, S. Y. Chiam, P. S. Bassi, W. F. Mak, H. K. Mulmudi, S. K. Batabyal, J. Barber, J. S. C. Loo, L. H. Wong. *The Journal of Physical Chemistry C* **2012**, *116*, 13884-13889.
[24] T. W. Hamann. *Dalton Transactions* **2012**, *41*, 7830-7834.
[25] Y. Lin, G. Yuan, S. Sheehan, S. Zhou, D. Wang. *Energy & Environmental Science* **2011**, *4*, 4862-4869.
[26] K. Sivula, F. Le Formal, M. Grätzel. *ChemSusChem* **2011**, *4*, 432-449.
[27] M. J. Katz, S. C. Riha, N. C. Jeong, A. B. F. Martinson, O. K. Farha, J. T. Hupp. *Coordination Chemistry Reviews* **2012**, *256*, 2521-2529.
[28] J. R. Bolton, S. J. Strickler, J. S. Connolly. *Nature* **1985**, *316*, 495-500.
[29] J. Brillet, J.-H. Yum, M. Cornuz, T. Hisatomi, R. Solarska, J. Augustynski, M. Graetzel, K. Sivula. *Nature Photonics* **2012**, *6*, 824-828.
[30] S. R. Pendlebury, A. J. Cowan, M. Barroso, K. Sivula, J. Ye, M. Gratzel, D. R. Klug, J. Tang, J. R. Durrant. *Energy & Environmental Science* **2012**, *5*, 6304-6312.

[31] I. Cesar, A. Kay, J. A. Gonzalez Martinez, M. Grätzel. *J Am Chem Soc* **2006**, *128*, 4582-4583.
[32] A. Kay, I. Cesar, M. Grätzel. *J Am Chem Soc* **2006**, *128*, 15714-15721.
[33] F. Le Formal, S. R. Pendlebury, M. Cornuz, S. D. Tilley, M. Grätzel, J. R. Durrant. *J Am Chem Soc* **2014**, *136*, 2564-2574.
[34] D. R. Gamelin. *Nat Chem* **2012**, *4*, 965-967.
[35] M. Barroso, C. A. Mesa, S. R. Pendlebury, A. J. Cowan, T. Hisatomi, K. Sivula, M. Grätzel, D. R. Klug, J. R. Durrant. *Proceedings of the National Academy of Sciences* **2012**, *109*, 15640-15645.
[36] L. M. Peter, K. G. U. Wijayantha, A. A. Tahir. *Faraday Discussions* **2012**, *155*, 309-322.
[37] Y. Liang, Y. Li, H. Wang, J. Zhou, J. Wang, T. Regier, H. Dai. *Nat Mater* **2011**, *10*, 780-786.
[38] L. Zhuo, J. Ge, L. Cao, B. Tang. *Crystal Growth & Design* **2008**, *9*, 1-6.
[39] T. He, D. Chen, X. Jiao, Y. Wang. *Adv Mater* **2006**, *18*, 1078-1082.
[40] D. Yuming, H. Kun, Y. Lin, Z. Aimin. *Nanotechnology* **2007**, *18*, 435602.
[41] M. Staniuk, O. Hirsch, N. Kränzlin, R. Böhlen, W. van Beek, P. M. Abdala, D. Koziej. *Chemistry of Materials* **2014**, *26*, 2086-2094.
[42] S. Farhadi, J. Safabakhsh, P. Zaringhadam. *Journal of Nanostructure in Chemistry* **2013**, *3*, 69.
[43] T. He, D. Chen, X. Jiao. *Chemistry of Materials* **2004**, *16*, 737-743.
[44] N. R. Jana, Y. Chen, X. Peng. *Chemistry of Materials* **2004**, *16*, 3931-3935.
[45] N. Shi, W. Cheng, H. Zhou, T. Fan, M. Niederberger. *Chemical Communications* **2015**, *51*, 1338-1340.
[46] J. M. Feckl, K. Fominykh, M. Doblinger, D. Fattakhova-Rohlfing, T. Bein. *Angewandte Chemie International Edition* **2012**, *51*, 7459-7463.
[47] K. Fominykh, J. M. Feckl, J. Sicklinger, M. Döblinger, S. Böcklein, J. Ziegler, L. Peter, J. Rathousky, E.-W. Scheidt, T. Bein, D. Fattakhova-Rohlfing. *Advanced Functional Materials* **2014**, *24*, 3123-3129.
[48] Y. Liu, J. M. Szeifert, J. M. Feckl, B. Mandlmeier, J. Rathousky, O. Hayden, D. Fattakhova-Rohlfing, T. Bein. *ACS Nano* **2010**, *4*, 5373-5381.
[49] J. M. Szeifert, J. M. Feckl, D. Fattakhova-Rohlfing, Y. Liu, V. Kalousek, J. Rathousky, T. Bein. *J Am Chem Soc* **2010**, *132*, 12605-12611.
[50] K. Fominykh, P. Chernev, I. Zaharieva, J. Sicklinger, G. Stefanic, M. Döblinger, A. Müller, A. Pokharel, S. Böcklein, C. Scheu, T. Bein, D. Fattakhova-Rohlfing. *ACS Nano* **2015**, *9*, 5180-5188.
[51] K. Peters, P. Zeller, G. Stefanic, V. Skoromets, H. Němec, P. Kužel, D. Fattakhova-Rohlfing. *Chemistry of Materials* **2015**, *27*, 1090-1099.
[52] V. G. Hadjiev, M. N. Iliev, I. V. Vergilov. *Journal of Physics C: Solid State Physics* **1988**, *21*, L199-L201.
[53] M. C. Biesinger, B. P. Payne, A. P. Grosvenor, L. W. M. Lau, A. R. Gerson, R. S. C. Smart. *Applied Surface Science* **2011**, *257*, 2717-2730.
[54] H. K. Dunn, J. M. Feckl, A. Müller, D. Fattakhova-Rohlfing, S. G. Morehead, J. Roos, L. M. Peter, C. Scheu, T. Bein. *Physical Chemistry Chemical Physics* **2014**DOI: 10.1039/c1034cp03946g.
[55] I. Cesar, K. Sivula, A. Kay, R. Zboril, M. Grätzel. *The Journal of Physical Chemistry C* **2008**, *113*, 772-782.
[56] K. Sivula, R. Zboril, F. Le Formal, R. Robert, A. Weidenkaff, J. Tucek, J. Frydrych, M. Grätzel. *J Am Chem Soc* **2010**, *132*, 7436-7444.

[57] K. J. McDonald, K.-S. Choi. *Chemistry of Materials* **2011**, *23*, 4863-4869.
[58] F. Lin, S. W. Boettcher. *Nat Mater* **2014**, *13*, 81-86.
[59] T. J. Mills, F. Lin, S. W. Boettcher. *Physical Review Letters* **2014**, *112*, 148304.
[60] G. Sauerbrey. *Zeitschrift für Physik* **1959**, *155*, 206-222.
[61] A. J. Esswein, M. J. McMurdo, P. N. Ross, A. T. Bell, T. D. Tilley. *The Journal of Physical Chemistry C* **2009**, *113*, 15068-15072.
[62] L. Trotochaud, J. K. Ranney, K. N. Williams, S. W. Boettcher. *J Am Chem Soc* **2012**, *134*, 17253-17261.
[63] X. Yang, C. Du, R. Liu, J. Xie, D. Wang. *Journal of Catalysis* **2013**, *304*, 86-91.
[64] S. Soedergren, A. Hagfeldt, J. Olsson, S.-E. Lindquist. *The Journal of Physical Chemistry* **1994**, *98*, 5552-5556.
[65] L. Trotochaud, T. J. Mills, S. W. Boettcher. *The Journal of Physical Chemistry Letters* **2013**, *4*, 931-935.

4 Making Ultrafast High-Capacity Anodes for Lithium-Ion Batteries via Antimony Doping of Nanosized Tin Oxide/Graphene Composites

This chapter is based on the following publication:

Making Ultrafast High-Capacity Anodes for Lithium-Ion Batteries via Antimony Doping of Nanosized Tin Oxide/Graphene Composites

Florian Zoller*, Kristina Peters*, Peter Zehetmaier, Patrick Zeller, Markus Döblinger, Thomas Bein, Zdeněk Sofer, Dina Fattakhova-Rohlfing, *Adv. Funct. Mater.***2018**, *28*, 1706529

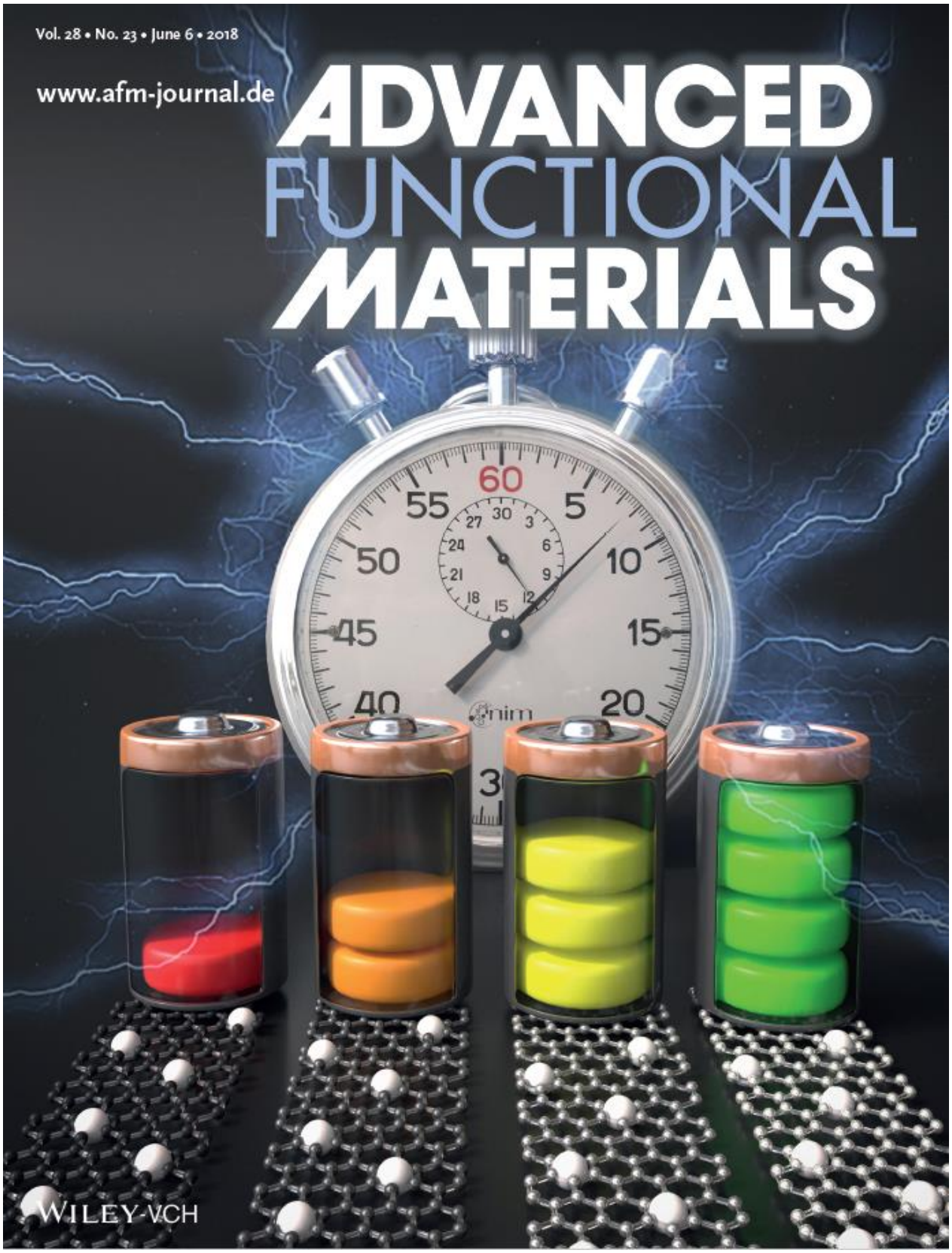

Figure 4.1: Image created by Christoph Hohmann (Nanosystems Initiative Munich, NIM) published as front cover in Adv. Funct. Mater. 23/2018 (used with permission from the publisher).

4.1 Abstract

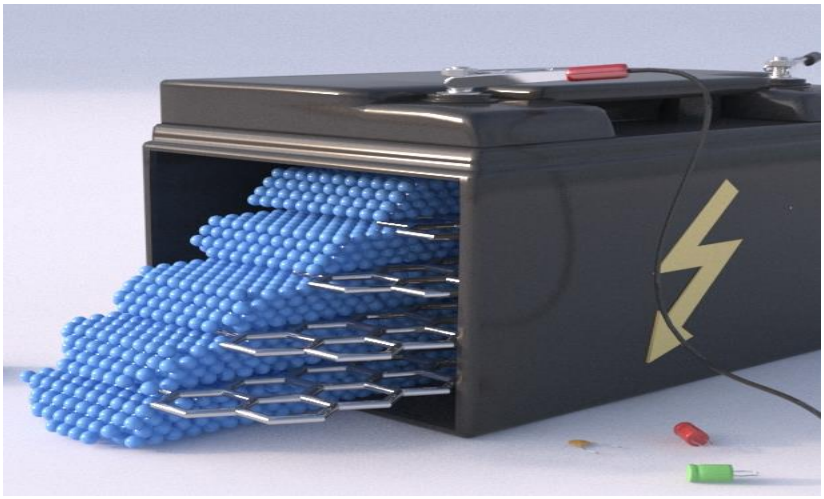

Figure 4.2: ToC image: Antimony doped tin oxide/graphene nanocomposites are synthesized in a microwave-assisted solvothermal approach in tert-butyl alcohol. The resulting nanocomposites consist of laminated graphene oxide sheets homogeneously decorated with ATO nanoparticles. The hybrid structures reveal a very high gravimetric capacity and drastically improved rate performance and cycling stability, making them attractive as ultrafast high capacity anodes in lithium ion batteries.

Tin oxide based materials attract increasing attention as anodes in lithium ion batteries due to their high theoretical capacity, low cost and high abundance. Composites of such materials with a carbonaceous matrix such as graphene are particularly promising, as they can overcome the limitations of the individual materials. We describe the fabrication of antimony-doped tin oxide (ATO)/graphene hybrid nanocomposites with high reversible capacity and superior rate performance using a microwave assisted in-situ synthesis in tert-butyl alcohol. This reaction enables the growth of ultrasmall ATO nanoparticles with sizes below 3 nm on the surface of graphene, providing a composite anode material with a high electric conductivity and high structural stability. Antimony doping results in greatly increased lithium insertion rates of this conversion-type anode and an improved cycling stability, presumably due to the increased electrical conductivity. The uniform composites feature gravimetric capacity of 1226 mAh g^{-1} at the charging rate 1C and still a high capacity of 577 mAh g^{-1} even at the very high charging rates of up to 60C, as compared to 93 mAh g^{-1} at 60C for the undoped composite synthesized in a similar way. At the same time the antimony-doped anodes demonstrate excellent stability with a capacity retention of 77% after 1000 cycles.

4.2 Introduction

Lithium-ion batteries (LIBs) represent the most advanced electrochemical energy-storage technology with energy and power densities superior to that of other rechargeable battery systems.[1-5] Still, there is an ever increasing need for Li-ion batteries with significantly higher energy densities and faster charging rates able to meet the growing demands of portable consumer devices with advanced functionalities and long-range electric vehicles.[1, 6]

The state-of-the-art LIBs are based on insertion-type electrode materials such as graphite anodes and transition metal oxide cathodes.[1] The redox transformations of these materials involve the reversible incorporation of lithium ions without major structural changes, resulting in high cycling stability.[1, 7, 8] A lot of efforts have been made to use the spinel $Li_4Ti_5O_{12}$ (LTO), also an insertion-type material, as an anode material in LIBs. Especially nanosized and nanostructured LTO electrodes exhibit a high power capability and an extreme good cycle life, also at very high current densities.[9-13] However, the penalty for the structural stability of such insertion-type electrode materials is a rather moderate specific capacity, in the case of LTO 175 mAh g^{-1}, which is limited by the amount of available lithium ion vacancies in the host structure.[1, 7-9] The use of electrode materials with different charge storage chemistry, such as for example alloying/de-alloying or conversion-type materials, is a promising way to increase the storage capacity.[1, 7, 8] Among numerous candidates, tin dioxide (SnO_2) is a very attractive anode material for replacing conventional graphite anodes due to the very high lithium insertion capacity and low working potential.[8, 14, 15] The lithiation of SnO_2 involves its full conversion to metallic Sn followed by alloying/dealloying of tin with lithium, with a total transfer of 8.4 Li per one SnO_2 formula unit and a very high theoretical capacity of 1494 mAh g^{-1}.[1, 8, 16] However, the practical insertion capacity of SnO_2 is much lower reaching only 783 mAh g^{-1} due to the irreversibility of the conversion step and the large volume change of 358% accompanying the structural transformation. The latter factors are also responsible for a very low cycling stability and a fast capacity fading observed for macroscopic SnO_2 materials.[17] Nonetheless, these shortcomings can be successfully addressed by using nanosized SnO_2 stabilized in a carbonaceous matrix, which is currently an established strategy to achieve high capacity and cycling stability of SnO_2 electrodes.[1, 8, 18] Nanoscaling of SnO_2 minimizes the strain during volume changes and results in a significantly enlarged contact area with the electrolyte, providing a high lithium ion flux across the interface. Consequently, the diffusion path length is decreased, enhancing the lithium ion

diffusion kinetics and hence the power density of batteries.[1, 18, 19] Furthermore, incorporation of nanosized SnO_2 in a carbonaceous conductive matrix buffers the volume changes and improves the electrical conductivity of the composites. Up to now, various types of carbonaceous materials including meso- and macroporous carbons,[15, 20] carbon nanotubes,[21, 22] carbon hollow particles[23] and graphene[14, 16, 17, 21-31] have been investigated in SnO_2 composites. Especially graphene-based nanocomposites have gained extensive attention due to the outstanding properties of graphene nanosheets (GNS) such as a high theoretical capacity (744 mAh g^{-1}), excellent conductivity, large surface area, high mechanical flexibility and chemical stability.[8] The reported synthetic strategies for such composites include hydro-/solvothermal *in-situ* synthesis of the nanoparticles on GNS[16, 17, 24-26], the self-assembly of preformed nanoparticles and GNS sheets[14, 27, 28], mechanochemical ball milling[29], electrostatic spray deposition (ESD)[30] and atomic layer deposition (ALD)[31].

Significant progress has been achieved in recent years regarding the preparation of tin oxide-based composite electrodes with a specific capacity close to the theoretical one and high cycling stability.[17, 24] However, such high capacities could only be reached at low current densities corresponding to long charging or discharging times. At higher charging/discharging rates the capacity decreased rapidly. The major reasons for the poor rate performance are the significant structural changes involving several steps with a large reorganization energy, as well as resistances arising from the low conductivity of tin oxide and the contact resistances in the composite material. So far only few groups have investigated the performance of SnO_2-based anodes at high current densities. Li *et al.*[25] prepared SnO_2 nanoparticles anchored on vertically aligned graphene, which retain a moderate specific capacity of 145 mAh g^{-1} at a current density of 20 A g^{-1}. Zhou *et al.*[32] reported a higher reversible capacity of 417 mAh g^{-1} for SnO_2/N-doped graphene composites at the same current density. Sun *et al.*[33] prepared SnO_2/C nanocapsules by an arc discharge method, which maintained an even higher capacity of 590 mAh g^{-1} at a current density of 20 A g^{-1}.

Several groups have attempted to improve the lithiation rate of tin oxide based electrodes by increasing the electrical conductivity of SnO_2 via doping.[14, 34-36] SnO_2 based anodes were doped with Sb,[14, 21, 22, 34-37] In,[38] Zn,[39] Co,[40, 41] Fe,[42] Mo,[43] Ti,[44] W,[45] and F,[40, 46] however no improvement in the rate capability was observed. In- and W- doped SnO_2/graphene composites reported by Liu *et al.*[38] and Wang *et al.*[45] reach only 200 mAh g^{-1} and 300 mAh g^{-1} at a current

densities of 7.8 A g^{-1} and 7 A g^{-1}, respectively. Sb doped SnO_2 (ATO)/graphene hybrid structures prepared by Zhao *et al.*[14] show a capacity of 483 mAh g^{-1} at a current density of 5 A g^{-1}.

Here, we demonstrate that antimony-doping of ultrasmall SnO_2 nanoparticles directly grown on graphene sheets significantly increases the cycling stability and the rate performance of the composite conversion-type anodes. The ATO/graphene nanocomposites prepared using a new *in-situ* microwave-assisted solvothermal route show a very high capacity, good cycling stability and an exceptionally high rate capability.

4.3 Results and Discussion

Antimony doped tin oxide/graphene oxide (ATO/GO) nanocomposites were fabricated *in-situ* using a one-step solvothermal reaction in *tert*-butyl alcohol.[35] In a typical procedure, tin(IV) and antimony(III) chlorides were dissolved at a molar ratio of 90:10 in *tert*-butyl alcohol, mixed with an aqueous graphene oxide dispersion and heated in hermetically sealed autoclaves; the resulting brown nanocomposites were separated and washed by repeated redispersion and centrifugation. Furthermore, SnO_2/GO composites and pure ATO particles were prepared in a similar way but without addition of antimony or graphene oxide, respectively (see Experimental part for further details).

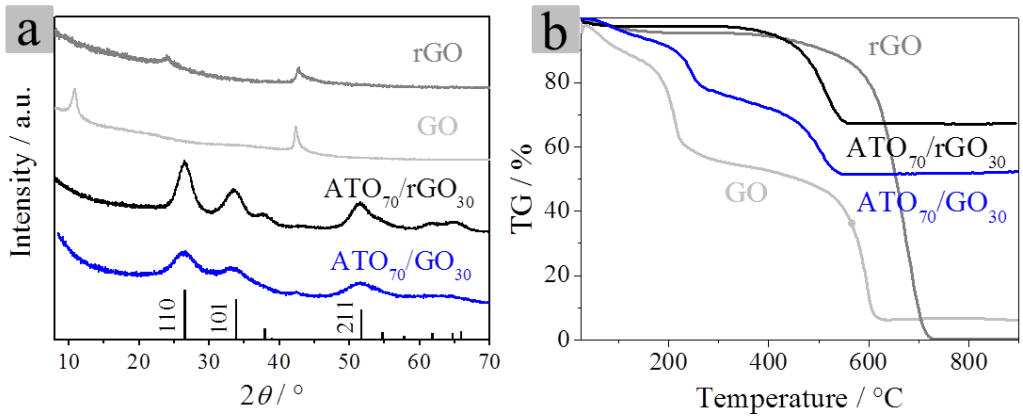

Figure 4.3: a) XRD patterns and b) TGA curves measured in air of a microwave synthesized ATO_{70}/GO_{30} nanocomposite and of pure GO before and after pyrolysis. The bars in the bottom of the XRD patterns (a) mark the position and the intensity of the diffraction lines of the SnO_2 cassiterite structure (space group $P4_2/mnm$, JCPDS card No.41-1445).

The reaction can be performed in a laboratory oven at temperatures between 80 and 150 °C; in this case it takes about 20 h to fully convert the precursors. However, the reaction time is significantly shortened to 90 min when the reactions are performed in a microwave reactor. X-ray diffraction patterns (XRD) of washed and dried ATO/GO (Figure 4.3a and Figure 4.4a-c) and SnO_2/GO (Figure 4.4d) nanocomposites demonstrate three distinct diffraction peaks corresponding to the (110), (101) and (211) reflections of tetragonal SnO_2. The particle size (calculated from the line broadening of the 110 reflection) strongly depends on the synthesis temperature and the way of heating. At the same reaction temperature (but after different heating times), the particle sizes of microwave-heated ATO and SnO_2 nanoparticles are smaller compared to the oven heated samples. Thus, at the reaction temperature of 80 °C the size of the ATO/SnO_2

nanoparticles within the composites is 3.7/3.5 nm for the oven-heated samples and only 2.5/2.0 nm for the microwave-heated samples.

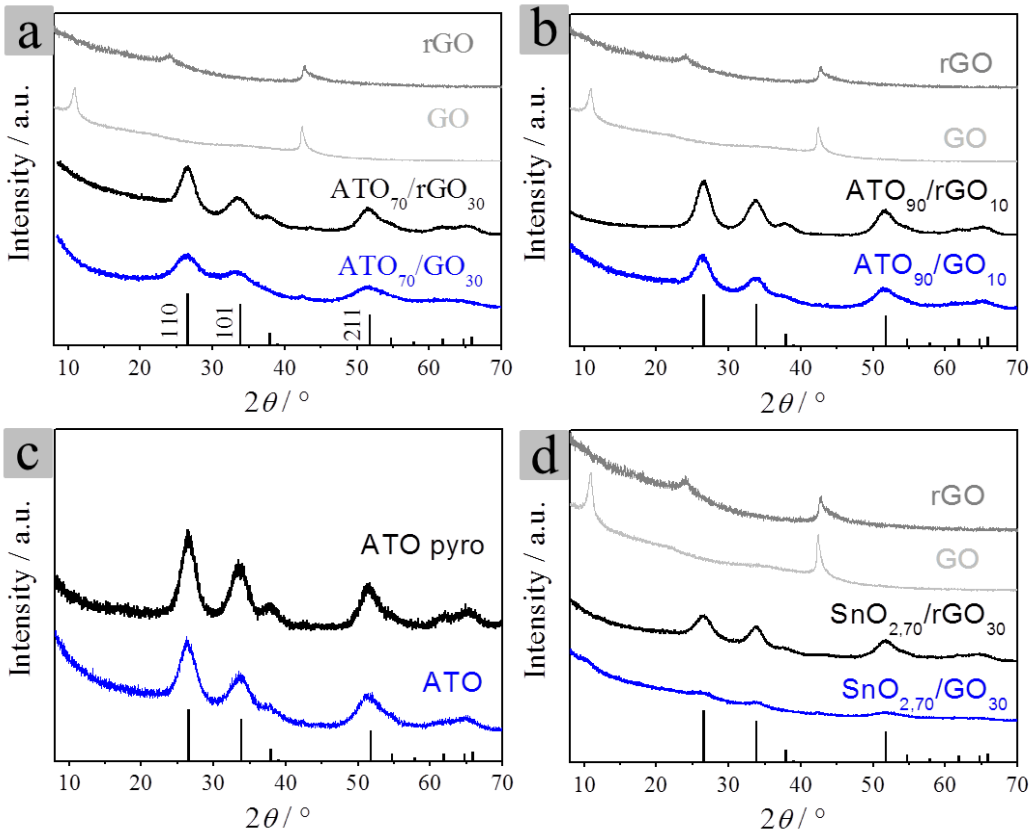

Figure 4.4: XRD patterns of microwave (a, c, d) and oven (b) synthesized ATO_{70}/GO_{30} (a), ATO_{90}/GO_{10} (b), pure ATO (c) and $SnO_{2,70}/GO_{30}$ (d) before (blue line) and after pyrolysis (black line). The bars in the bottom of the XRD pattern mark the position and the intensity of the diffraction lines of SnO_2 cassiterite (space group $P4_2/mnm$, JCPDS File Card No. 41-1445).

The composites were pyrolyzed at 400 °C in nitrogen to remove organic residues and to reduce GO to reduced graphene oxide (termed ‘rGO’); the reduction process can be observed by the color change from brown to black. The composites were pyrolyzed at 400 °C in nitrogen to remove organic residues and to reduce GO to reduced graphene oxide (termed ‘rGO’); the reduction process can be observed by the color change from brown to black. The nanocomposites were analyzed by Raman spectroscopy before and after this pyrolysis step (Figure 4.5).

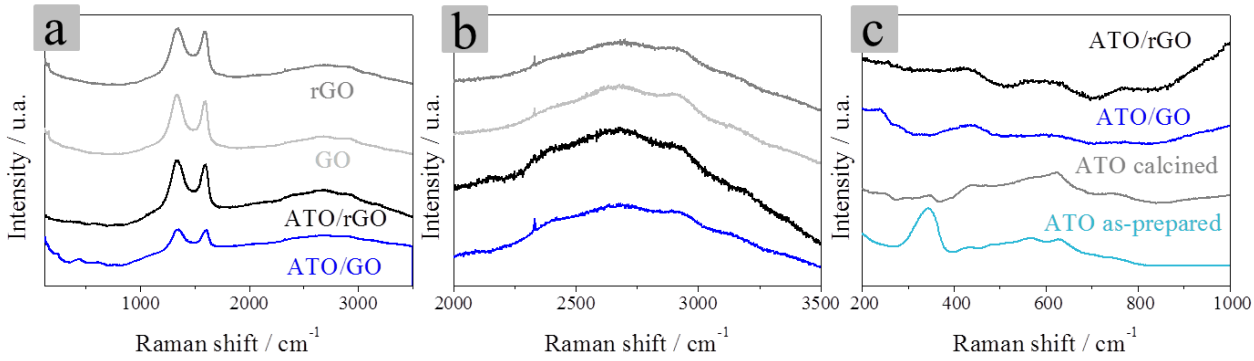

Figure 4.5: Raman spectra: a) Overview of the ATO_{70}/GO_{30} nanocomposites and pure GO before and after pyrolysis. b) Zoom-in in the high shift region of the spectra showing the 2D and D+G bands. c) Comparison of pure ATO nanoparticles with ATO_{70}/GO_{30} nanocomposites, showing the typical bulk vibration modes corresponding to rutile-type SnO_2, namely A_{1g} (630 cm^{-1}), B_{2g} (775 cm^{-1}) and E_g (477 cm^{-1}). The surface vibrations modes typical for nanosized SnO_2, namely *S1* (333 cm^{-1}) and *S2/S3* (500 – 570 cm^{-1}), are only visible for pure, as-prepared ATO nanoparticles.

Raman spectroscopy is often used to verify the degree of the GO reduction by evaluating the intensity ratio of the *D* band and the *G* band, denoted as I_D/I_G. However, this approach is not applicable to all nanocomposites, as reported by King *et al.*.[47] They reported that using the I_D/I_G ratio as a quality criterion of graphene is problematic for both GO and rGO, as this method relies on the analysis of the G peak, which is in fact a superposition of two peaks (*G* and *D'*).[1] This is in good agreement with our results, which show almost no changes in the I_D/I_G ratio even after the thermal reduction step. All ATO/SnO_2 containing samples exhibited the typical bulk vibration modes of rutile-type SnO_2 (A_{1g} (630 cm^{-1}), B_{2g} (775 cm^{-1}) and E_g (477 cm^{-1})). Pure as-prepared ATO also exhibited the surface vibration modes (*S1* (333 cm^{-1}) and *S2/S3* (500 – 570 cm^{-1})), which are typical for nanosized ATO.[36] In the nanocomposites, the surface vibration modes are apparently suppressed due to particle growth and attachment to graphene.

The results of XRD measurements (Figure 4.3a), thermogravimetric analysis (TGA) (Figure 4.3b) and X-ray photoelectron spectroscopy (XPS) (Figure 4.6) confirm that this treatment is sufficient for a reduction of GO to rGO. XRD patterns of pure GO exhibit a typical reflection (002) at 11.7° 2θ corresponding to the interlayer distance between GO sheets and a second reflection (100) around 42.2° 2θ indicating a short range order in stacked layers.[48, 49] For rGO the (002) reflection is shifted to higher 2θ values and broadened, indicating a decreased interlayer distance due to the removal of oxygen groups and a poor ordering of the sheets along the stacking direction, respectively.[48, 50] Upon pyrolysis the nanoparticles synthesized using microwave heating (80 °C) grow from 2.5 nm to 3.8 nm and from 2.3 nm to 3.5 nm for ATO/GO and SnO_2/GO nanocomposites, respectively. In contrast to the nanocomposites synthesized in an

oven, weak diffraction peaks of GO or rGO could be observed in microwave synthesized composites, which is probably associated with the GO content in the composites and will be discussed in the following section.

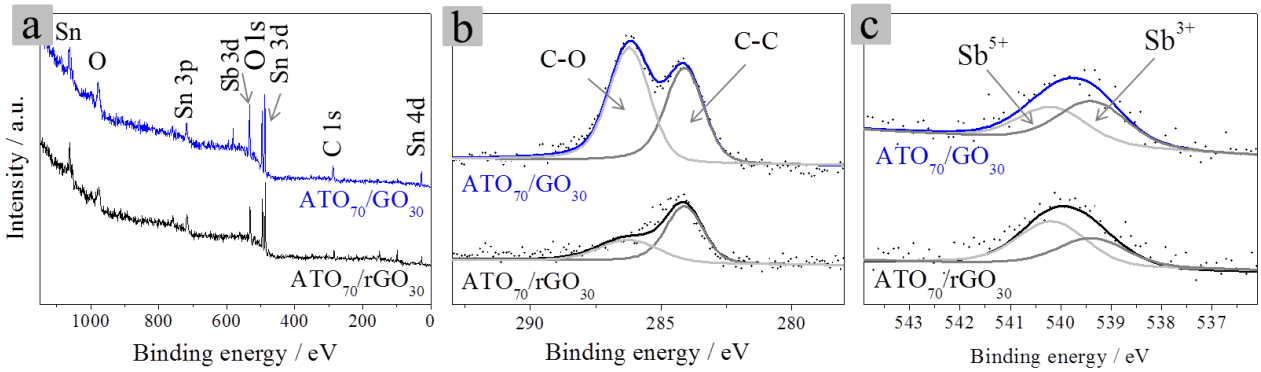

Figure 4.6: XPS spectra of ATO_{70}/GO_{30} nanocomposites before (blue lines) and after pyrolysis (black lines): an overview (a), the C 1s peak (b) and the Sb $3d_{3/2}$ peak (c). The solid black squares in b) and c) correspond to the experimental spectra. b) The peak fits for C–O components (285.5–288.6 eV, light grey line) and C–C components (284.6 eV, dark grey line). c) The peak fits for Sb^{5+} (540.0 eV, light grey line) and Sb^{3+} (539.2 eV, dark grey line).

The TGA curves of GO in air show a weight loss at around 200 °C and between 500 °C and 600 °C (Figure 4.3b) due to the combustion of oxygen-containing groups and the gradual decomposition of the GO, respectively.[51] In contrast, rGO shows practically no weight loss in the range of 25 °C to 250 °C due to the absence of oxygen groups and only a small amount of adsorbed or weakly bound residues. The ATO/GO and ATO/rGO composites demonstrate similar behavior; the weight loss associated with the rGO combustion was used for quantification of rGO in the pyrolyzed composites. For nanocomposites synthesized at temperatures of 100 °C or higher, the weight loss corresponds to the initial content of GO in the reaction mixture (Figure 4.7). However, for nanocomposites prepared at 80°C the mass fraction of the carbon phase is higher. The resulting ATO/rGO and SnO_2/rGO composites synthesized at 80°C (microwave) with an initial GO content of 10% contained 30% rGO after pyrolysis (see Figure 4.3b). One possible reason is that a certain fraction of the ATO precursors remained unreacted and was removed after washing and centrifugation, resulting in a higher relative GO content. In the following, these pyrolyzed composites are labeled as ATO_{70}/rGO_{30} and $SnO_{2,70}/rGO_{30}$, respectively.

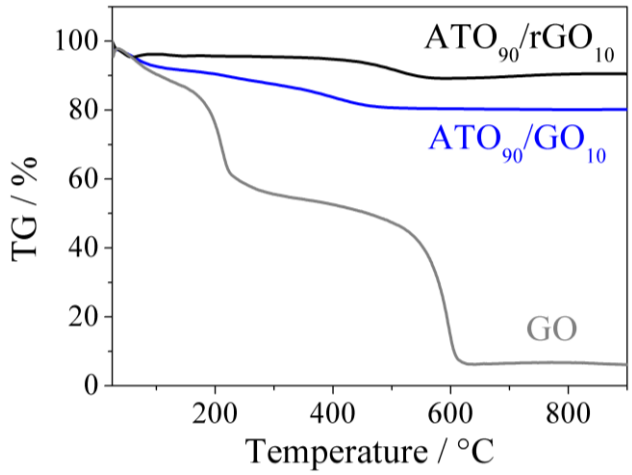

Figure 4.7: TGA curves of an oven-synthesized (100°C) ATO_{90}/GO_{10} nanocomposite compared with pure GO. The weight loss associated with the rGO decomposition was used for quantification of the rGO content in the pyrolyzed composites. The weight loss corresponds to the initial ratio of GO in the reaction mixture.

The elemental composition as well as the oxidation states of elements in the nanocomposites were studied by XPS (Figure 4.6a). The antimony content found in the nanocomposite corresponds to the initial precursor content of 10 % Sb used in the reaction, equaling 9.8% and 10.6% for ATO_{70}/GO_{30} and ATO_{70}/rGO_{30}, respectively. The electrical conductivity of the ATO nanoparticles is generally influenced by the antimony content and its valence state in the tin oxide lattice, with Sb^{5+} ions acting as donor species beneficial for conductivity and the Sb^{3+} ions acting as electron traps, respectively. The ratio of Sb^{5+} species increases from 44.5 mol% to 61.1 mol% upon pyrolysis (Figure 4.6c, light grey line), pointing to an improved conductivity of the composites after the pyrolysis.[35] After pyrolysis in nitrogen the C 1s components associated with carbon-oxygen bonds significantly decrease (Figure 4.6b, light grey line) proving the successful reduction of most of the carboxyl and hydroxyl functional groups in the ATO_{70}/rGO_{30} nanocomposite.[14, 17, 49, 50]

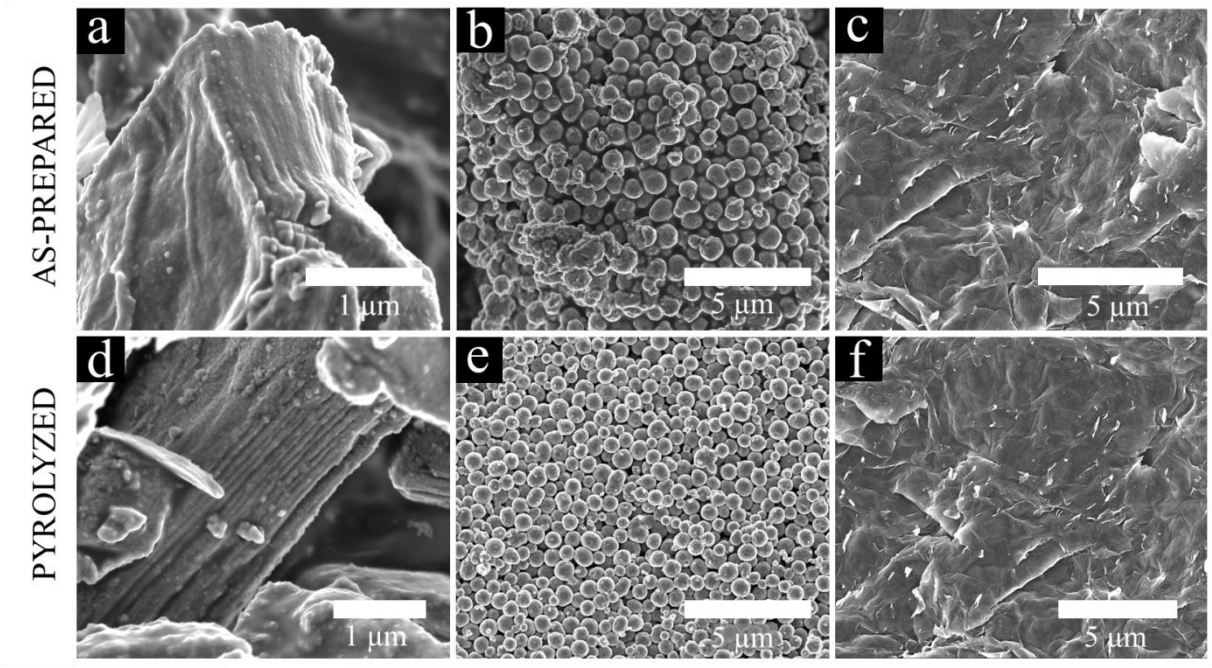

Figure 4.8: SEM images of ATO_{70}/GO_{30} nanocomposites (a, d), pure ATO nanoparticles (b, e), graphene (c) and reduced graphene (f). Top (a-c): as-prepared; bottom (d-f): pyrolyzed samples (in nitrogen at 400 °C).

The morphology of the nanocomposites and of individual components was studied by scanning electron microscopy (SEM). Interestingly, the ATO nanoparticles synthesized without GO form spherical agglomerates of small nanocrystals. The agglomerates are porous as demonstrated by nitrogen sorption measurements showing type IV isotherms typical for mesoporous materials and a BET surface area of 224 $m^2 g^{-1}$ (Figure 4.10c and Table 4.1). The spherical agglomerates retain their morphology also after pyrolysis (Figure 4.8b), whereby the BET surface area decreases to 140 $m^2 g^{-1}$. The morphology of pure GO shows crumpled, paper-like structures with smooth edges before and after the solvothermal treatment and the pyrolysis (Figure 4.8c); here the surface area also decreased upon pyrolysis, from 54 $m^2 g^{-1}$ to 26 $m^2 g^{-1}$ (Figure 4.10d and Table 4.1). In contrast, the morphology of ATO_{70}/rGO_{30} composites differs significantly from that of the individual components (Figure 4.8a). The SEM images of ATO_{70}/rGO_{30} composites show the presence of laminated graphene sheets decorated with ATO nanoparticles, which appear to be uniformly distributed on the surface of the rGO and as a result separating the sheets from each other. Upon pyrolysis the agglomeration between the ATO decorated rGO sheets is reduced due to removal of organic residues between the single rGO layers of the nanocomposite, which can be seen by comparing SEM images of as-prepared and pyrolyzed samples in Figure 4.8a,d. None of the spherical agglomerates of pure ATO was found in the composites, pointing to a homogeneous

distribution of ATO nanoparticles between the rGO sheets (see low magnification SEM images in Figure 4.9). The porous morphology and high specific surface area of the nanocomposites were also confirmed by type IV nitrogen sorption isotherms with a hysteresis between the adsorption and desorption branches that is typical for mesoporous materials with relatively narrow pores (Figure 4.10a). The BET surface area of the nanocomposites remained stable around 265 $m^2 g^{-1}$ for the as-prepared and pyrolyzed samples, respectively (see Figure 4.10 and Table 4.1). The mean pore size increased from 2.6 nm for the as-prepared to 4.3 nm for the pyrolyzed ATO nanoparticles and remained stable at 6 nm for the as-prepared ATO_{70}/GO_{30} and the pyrolyzed ATO_{70}/rGO_{30} nanocomposites.

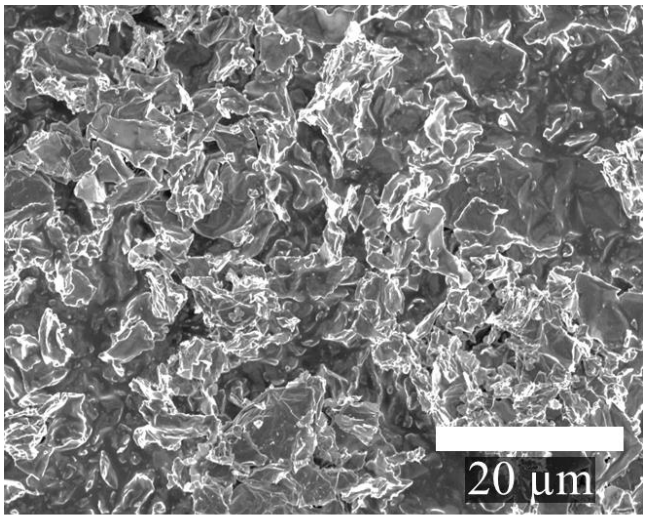

Figure 4.9: Low magnification SEM image of a pyrolyzed ATO_{70}/rGO_{30} nanocomposite illustrating the homogeneity of the material, as shown by the absence of spherical ATO agglomerates.

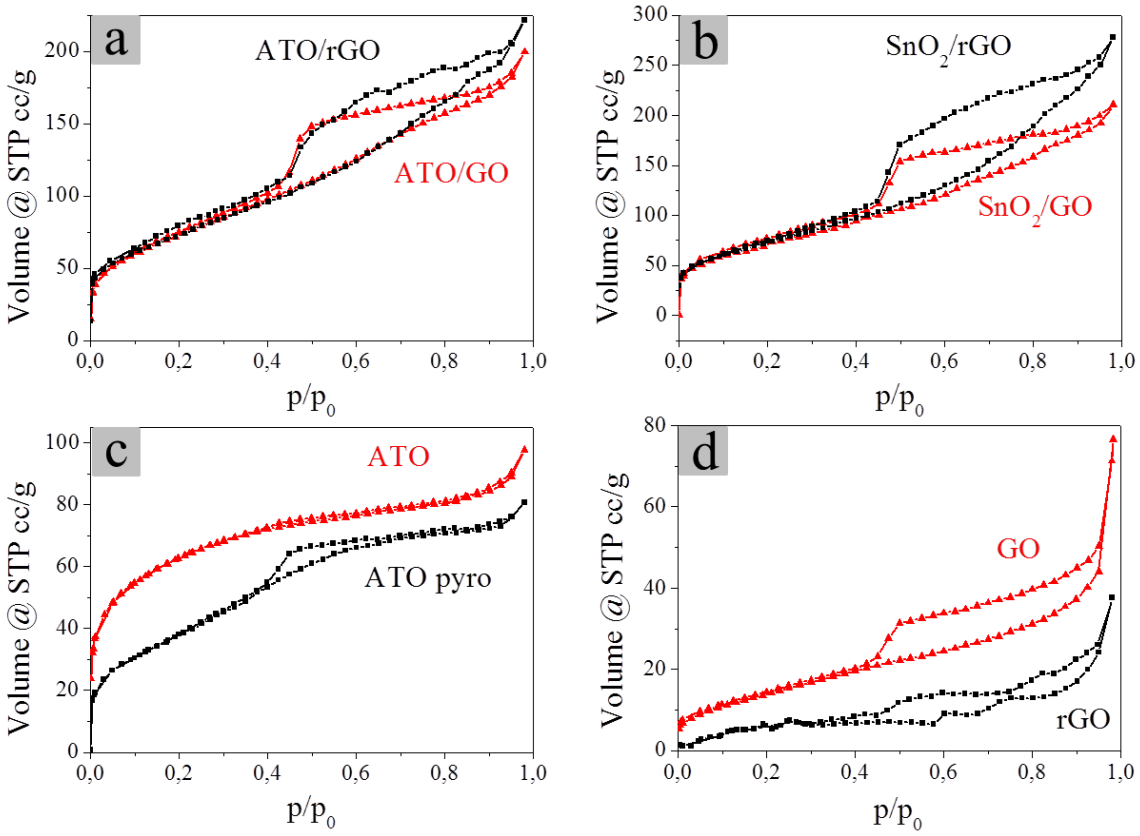

Figure 4.10: Nitrogen adsorption-desorption isotherms of ATO_{70}/GO_{30} (a), $SnO_{2,70}/GO_{30}$ (b), pure ATO nanoparticles (c) and GO (d) before (▲ red line) and after pyrolysis (■ black line), respectively. The corresponding BET surface areas and pore sizes are summarized in the following Table (Table 4.1).

Table 4.1: Textural parameters of ATO_{70}/GO_{30} (a), $SnO_{2,70}/GO_{30}$ (b), pure ATO nanoparticles (c) and GO (d) before and after pyrolysis extracted from nitrogen adsorption–desorption isotherms from Figure 4.10. The specific surface areas were determined with the BET method and the pore size distribution was calculated using a nonlocal density functional theory (NLDFT) adsorption model with cylindrical/spherical pores.

Panel of Figure 4.10	Sample name	BET surface area [$m^2\ g^{-1}$]	Pore size [nm]
a (▲)	ATO_{70}/GO_{30}	270	5.8
a (■)	ATO_{70}/rGO_{30}	263	6.0
b (▲)	$SnO_{2,70}/GO_{30}$	260	6.0
b (■)	$SnO_{2,70}/rGO_{30}$	266	6.0
c (▲)	ATO	224	2.6
c (■)	ATO pyro	140	4.1
d (▲)	GO	54	3.8
d (■)	rGO	26	7.3

High-resolution transmission electron microscopy (HRTEM) analysis as well as selected area electron diffraction (SAED) patterns of the ATO_{70}/rGO_{30} nanocomposite show the presence of highly crystalline ATO nanoparticles (see Figure 4.11 and Figure 4.12). The SAED pattern (Figure 4.11c) is in good agreement with the tetragonal cassiterite structure of ATO deduced from XRD data. The particle size determined from TEM analysis (3-4 nm) also agrees with that calculated from the line broadening of the 110 reflection of ATO in the XRD pattern (3.8 nm, Figure 4.3a). Due to a very low elemental contrast, graphene is not visible in the TEM. The graphene sheets were visualized only when they were aligned perpendicular to the TEM grid (as indicated by the red arrows in Figure 4.11a) or if the sheets were overlapping (see low magnification TEM images in Figure 4.12), which causes a different contrast depending on the amount of overlapping lamellae. However, the presence of rGO can be clearly confirmed based on the sharp hexagonal diffraction spots in the SAED pattern of the nanocomposite (Figure 4.11c), which match the d-value of graphene (2.1 Å)[52, 53]. From the combined SEM and TEM/SAED analyses we can conclude that the GO sheets are completely decorated with nanoparticles forming very homogeneous composites.

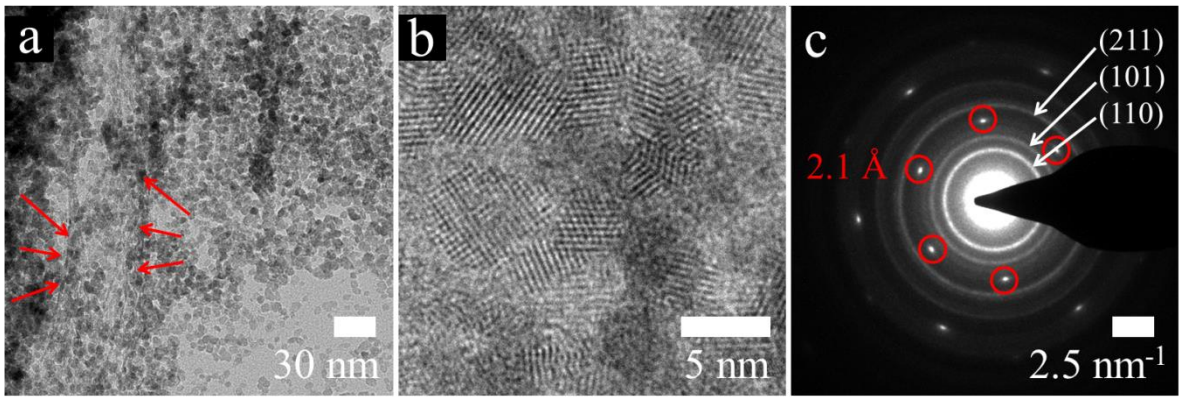

Figure 4.11: HRTEM images (a, b) and SEAD pattern (c) of a pyrolyzed ATO_{70}/rGO_{30} nanocomposite showing crystalline ATO nanoparticles on the graphene surface. The red arrows in a) mark graphene sheets aligned about perpendicular to the TEM grid. The SEAD pattern (c) show typical rings corresponding to ATO (d-values: 3.3 (110), 2.7 (101), and 1.8 Å (211)) and sharp hexagonal spots for rGO (d-values: 2.1 Å).[52, 53]

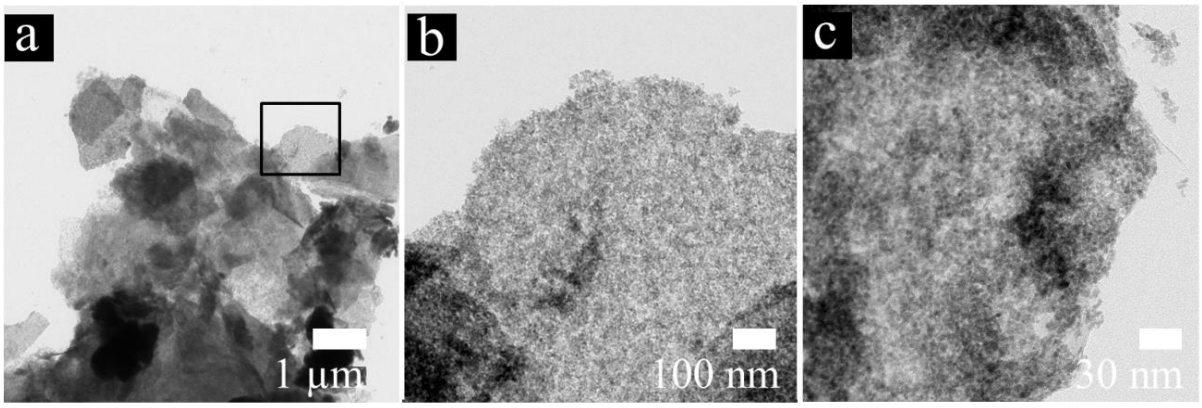

Figure 4.12: TEM images of an ATO_{70}/rGO_{30} nanocomposite pyrolyzed in nitrogen at 400 °C. a) Low magnification TEM showing overlapping graphene flakes and b) zoom-in of the marked area in a). c) TEM images taken from another area showing crystalline, small ATO nanoparticles decorating the graphene nanosheets.

The electrochemical performance of the ATO/GO nanocomposites was investigated using cyclic voltammetry and galvanostatic charge/discharge measurements. Generally, the electrochemical lithium insertion in SnO_2 (or $Sb_{0.1}Sn_{0.9}O_2$) proceeds via several steps, such as conversion (Equation 4.1) and alloying/ dealloying (Equation 4.2) reactions according to the following reactions:[26]

Conversion: 4.1

$$SnO_2 + 2Li^+ + 2e^- \rightleftharpoons SnO + Li_2O \qquad E_1 = 1.7\,V$$

$$SnO + 2Li^+ + 2e^- \rightleftharpoons Sn + Li_2O \qquad E_2 = 0.9\,V$$

$$Sn_{0.90}Sb_{0.10}O_2\ (ATO) + 4Li^+ + 4e^- \rightleftharpoons 0.90Sn + 0.10Sb + 2Li_2O$$

Alloying/ dealloying: 4.2

$$0.90Sn + 3.96Li^+ + 3.96e^- \rightleftharpoons 0.90Li_{4.4}Sn \qquad E_3 = 0.4\,V$$

$$0.1Sb + 0.30Li^+ + 0.30e^- \rightleftharpoons 0.10Li_3Sb \qquad E_4 = 0.4\,V$$

$$0.90Sn + 0.10Sb + 4.26Li^+ + 4.26e^- \rightleftharpoons 0.90Li_{4.4}Sn + 0.10Li_3Sb$$

The overall electrochemical process involves the transfer of 8.4 or 8.26 Li^+ ions per one SnO_2 or ATO ($Sb_{0.1}Sn_{0.9}O_2$) formula unit with a theoretical capacity of 1494 $mAhg^{-1}$ and 1466 $mAhg^{-1}$, respectively. For bulk materials, however, the conversion reactions (1) are widely believed to be irreversible due to the drastic volume changes, resulting in a lower capacity of around 783 $mAhg^{-1}$ stemming from the reversible alloying/dealloying process.[8, 34]

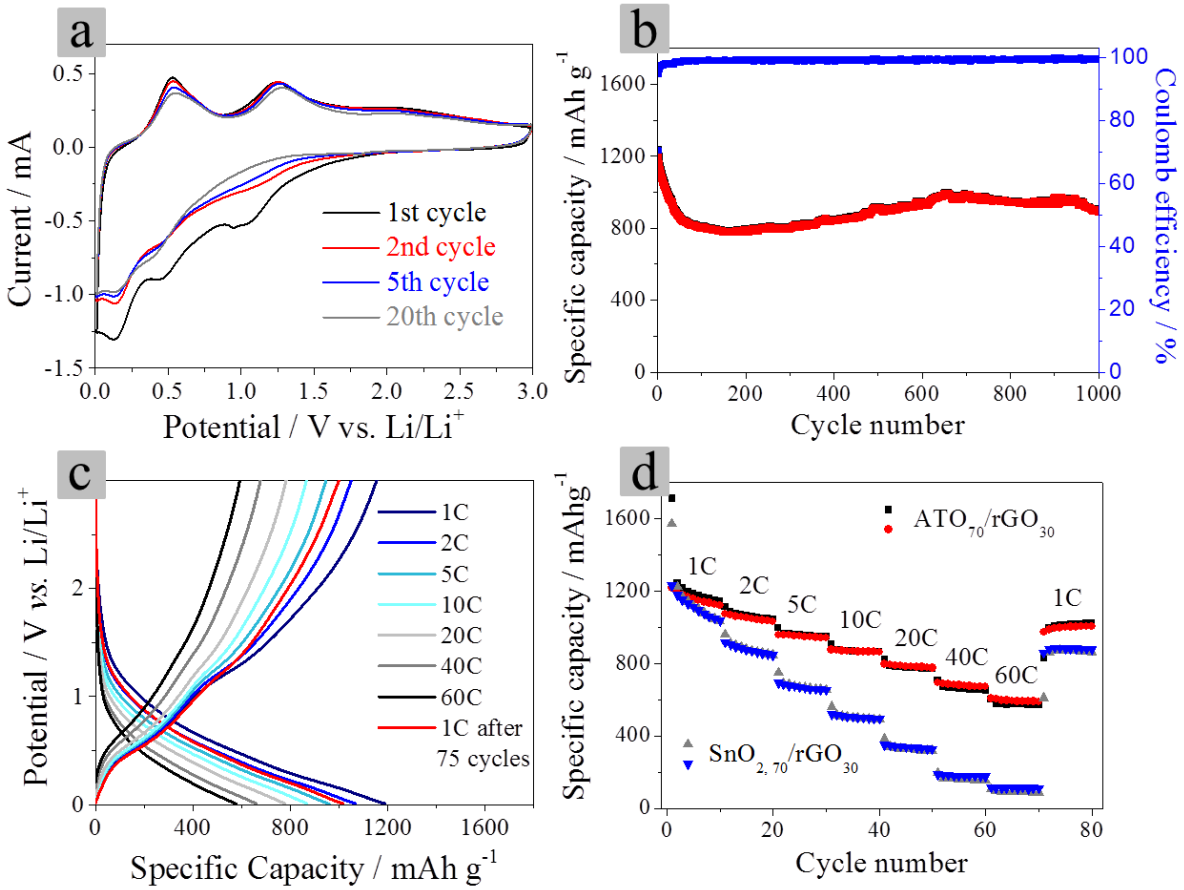

Figure 4.13: a) CV curves of an ATO_{70}/rGO_{30} electrode recorded with a scan rate of 0.5 mV s^{-1} and a step potential of 2.44 mV in the range of 0.01 – 3 V vs. Li/Li^+. b) Multicycling stability of an ATO_{70}/rGO_{30} electrode at 1C and the corresponding Coulombic efficiencies (■ blue labels). c) Discharge/charge profiles of ATO_{70}/rGO_{30} at increasing C-rates (1C – 60C) each recorded in the 5th, 15th, 25th etc. cycle. d) Rate performance of ATO_{70}/rGO_{30} and $SnO_{2,70}/rGO_{30}$: The charge capacities correspond to the red (●) and blue (▼) labels, while the discharge capacities are displayed with black (■) and grey (▲) labels.

In the cyclic voltammograms (CV) of the ATO_{70}/rGO_{30} nanocomposite (Figure 4.13a), of the $SnO_{2,70}/rGO_{30}$ nanocomposite (Figure 4.14a) and of the ATO nanoparticles (Figure 4.12b) obtained in this work show a dominant cathodic peak around 1.2 V in the first discharge curve, which can be attributed to the irreversible formation of a solid electrolyte interface (SEI) layer and disappears in the following scans.[17] The CVs of all ATO and SnO_2 based samples demonstrate a couple of peaks at around 0.4 V ascribed to the reversible alloying/de-alloying process.[1, 2, 26] Moreover, the pair of peaks at around 0.9 V and 1.7 V correspond to the conversion of ATO to Sn and Sb and the simultaneous formation of Li_2O (1). The presence of these two pairs of peaks, which have only been observed for nanosized SnO_2 or ATO particles,[26, 28, 54] is commonly interpreted as an indication of the reversibility of the conversion reaction. This result in a higher theoretical capacity for our nanosized ATO/SnO_2 nanoparticles

(1466 mAh g^{-1}/1494 mAh g^{-1}) compared to the macroscopic ATO/SnO_2 (756 mAh g^{-1}/783 mAh g^{-1}).[1, 8, 16, 26, 27]

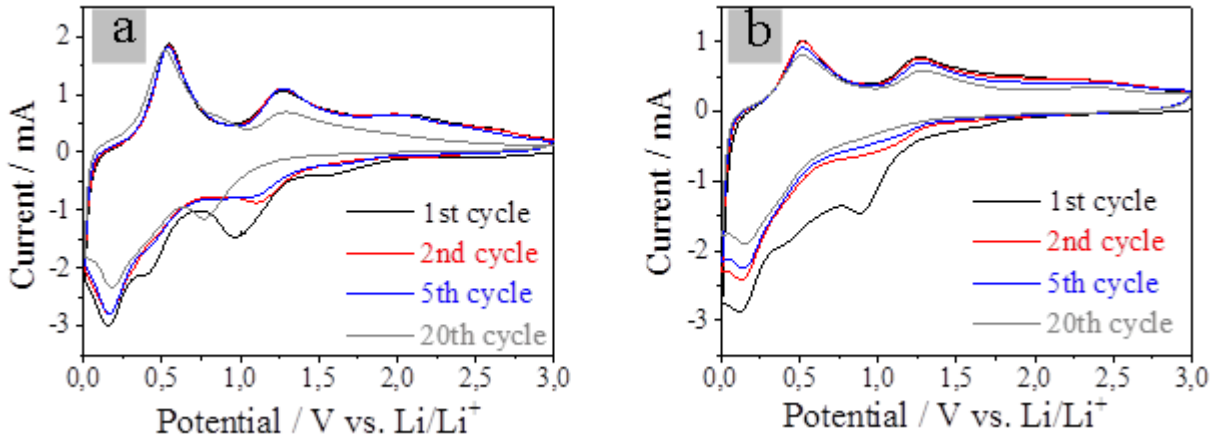

Figure 4.14: Cyclic voltammograms of $SnO_{2,70}$/rGO_{30} nanocomposites (a) and pure ATO nanoparticle based electrodes (b) showing their cycling stability. The CVs were recorded with a scan rate of 0.5 mV s^{-1} and a step potential of 2.44 mV in the range of 0.01 – 3 V vs. Li/Li^+. The first discharge curve corresponding to the lithium ion insertion process differs significantly from the subsequent cycles due to the irreversible formation of a solid electrolyte interface (SEI) layer that disappears in the following scans.

Although the ATO nanoparticles and the ATO/rGO_{30} and $SnO_{2,70}$/rGO_{30} nanocomposites show similar CV features and a comparable specific capacity in the first cycles, they differ significantly in their cycling stability. The ATO nanoparticles-only based electrodes show significant capacity fading, which is the highest among the three investigated systems (Figure 4.14b).

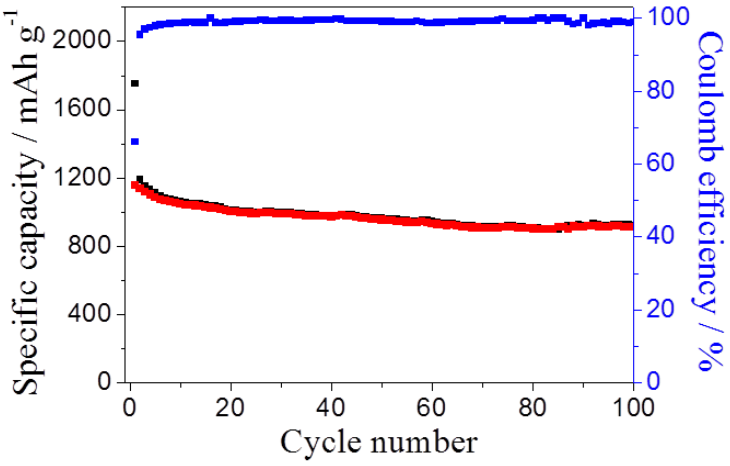

Figure 4.15: Multicycling stability of an $SnO_{2,70}/rGO_{30}$ electrode (loading 0.2 mg cm^{-2}) at a rate of 1C and the corresponding Coulombic efficiencies (■ blue labels). Charge and discharge capacities correspond to the red (●) and black (■) labels, respectively. The specific capacity reaches 1188 mAh g^{-1}/1135 mAh g^{-1} (discharge/charge) in the second cycle, which is close to the theoretical lithium insertion capacity of the composite (1269 mAh g^{-1}), and reaches 918 mAh g^{-1} after 100 cycles.

Galvanostatic charge/discharge measurements of the ATO_{70}/rGO_{30} nanocomposite (loading 0.2 mg cm^{-2}) performed at different current densities (C-rates) (Figure 4.13) show three typical plateau regions in good agreement with the corresponding CV curves. The first discharge/charge capacities reach 1696/1194 mAh g^{-1} at 1C (corresponding to a current density of 1249 mA g^{-1}) (Figure 4.13b), which is higher than the theoretical capacity due to SEI formation on the electrode surface. This results in an initially low initial Coulombic efficiency of 70%. However, the Coulombic efficiency increases to around 97% after the first three cycles (see blue line in Figure 4.13b) and remains stable above 99% after the 40th cycle. The specific capacity reaches 1237 mAh g^{-1}/1175 mAh g^{-1} (discharge/charge) in the second cycle, which is close to the theoretical lithium insertion capacity of the composite (1249 mAh g^{-1}), and remains quite stable reaching 813 mAh g^{-1} after 100 cycles (Figure 4.13b). Strikingly, the capacity fading of the unsupported ATO nanoparticles was far more pronounced (Figure 4.17) compared to the graphene-supported ATO and SnO_2 (918 mAh g^{-1} after 100 cycles, see Figure 4.15), reaching only 77 mAh g^{-1} after 100 cycles. Even after 1000 charge and discharge cycles at 1C, the ATO_{70}/rGO_{30} nanocomposite shows a very stable cycling behavior reaching 894 mAh g^{-1} corresponding to an irreversible capacity loss of 23% (compared with the 5th cycle (Figure 4.13b)).

Table 4.2: Specific discharge capacities of ATO_{70}/rGO_{30}, $SnO_{2,70}/rGO_{30}$, pure ATO and ATO_{70}/rGO_{30} 'dispersion-mixing' electrodes at different C-rates (1C – 60C) each recorded in the 5th, 15th, 25th etc. The capacity retention was calculated by setting the measured capacity at 1C in the 5th cycle to 100%.

	Specific discharge capacity [mAh g^{-1}] and the corresponding capacity retention								Loading [mg cm^{-2}]
C-rate	1C	2C	5C	10C	20C	40C	60C	1C	
Cycle	5	15	25	35	45	55	65	75	
ATO_{70}/rGO_{30}	1186	1066	959	868	778	661	577	1014	0.2
	100%	90%	81%	73%	66%	56%	49%	85%	
ATO_{70}/rGO_{30}	1260	1092	909	762	550	335	235	1031	0.6
	100%	87%	72%	60%	44%	27%	19%	82%	
$SnO_{2,70}/rGO_{30}$	1120	881	672	503	328	161	93	865	0.2
	100%	79%	60%	45%	29%	14%	8%	77%	
ATO	1132	838	647	477	327	173	20	573	0.2
	100%	74%	57%	42%	29%	15%	2%	51%	
ATO_{70}/rGO_{30} 'dispersion-mixing'	1213	1058	867	663	426	211	114	688	0.2
	100%	87%	71%	55%	35%	17%	9%	55%	

The most remarkable feature of the ATO_{70}/rGO_{30} nanocomposite is, however, their excellent rate capability. The charging and discharging rates of pure ATO as well as of $SnO_{2,70}/rGO_{30}$ and ATO_{70}/rGO_{30} electrodes are summarized in Table 4.2 in the experimental part. Comparison between three types of electrodes with a similar thickness of 10 µm and a moderate loading of 0.2 mg cm^{-2} highlights the superior rate performance and higher cycling stability of ATO_{70}/rGO_{30} material compared to the ATO nanoparticles and the undoped $SnO_{2,70}/rGO_{30}$ nanocomposite. The specific capacities at different C-rates are summarized in Table 4.2 and Figure 4.13c, d. The ATO_{70}/rGO_{30} electrodes deliver close to theoretical specific discharge capacities of 1186 mAh g^{-1}

at the 1C rate and very high capacity values at the rates up to 40C. Even at a rate of 60C (corresponding to a theoretical charging and discharging within one minute) 49% of the initial capacity is achieved. The capacity of the composite remains much higher than the capacity of the state-of-the-art anode material graphite (372 mAh g^{-1}). Remarkably, the capacity fading with increasing C-rates is reversible, as the capacity recovers to 1014 mAh g^{-1} when the C-rate returns to 1C. Furthermore, thicker ATO_{70}/rGO_{30} electrodes with a loading of 0.6 mg cm^{-2} still demonstrate a high rate capability, as shown in Figure 4.16. When cycled at 60C, such an electrode still retains a capacity of 235 mAh g^{-1} and restores to a capacity of 1032 mAh g^{-1} when set back to 1C.

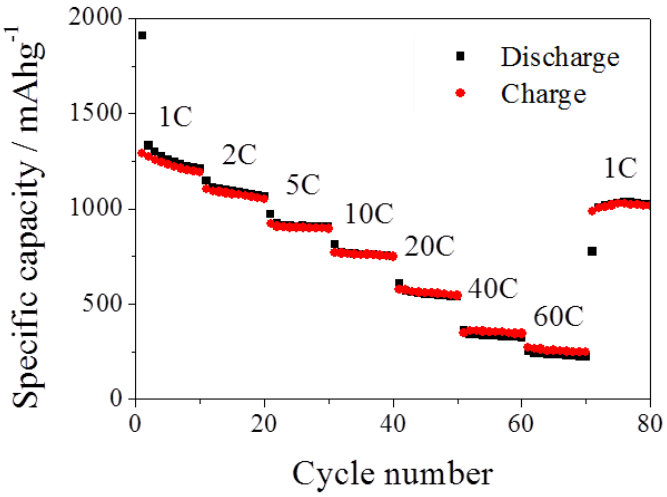

Figure 4.16: Rate performance of an ATO_{70}/rGO_{30} electrode with a loading of 0.6 mg cm^{-2} at different rates ranging from 1 to 60C (ten cycles at each C-rate). Charge and discharge capacities correspond to the red (●) and black (■) labels, respectively. The electrodes deliver specific discharge capacities of 1260 mAh g^{-1} (1C; 5th cycle),1092 mAh g^{-1} (2C; 15th cycle), 909 mAh g^{-1} (5C; 25th cycle), 762 mAh g^{-1} (10C; 35th cycle), 550 mAh g^{-1} (20C; 45th cycle), 335 mAh g^{-1} (40C; 55th cycle) and 235 mAh g^{-1} (60C; 65th cycle), respectively. These values correspond to a capacity loss of 13% (2C), 28% (5C), 40% (10C), 56% (20C), 73% (40C) and 81% (60C) compared to the initial capacity at 1C (1260 $mAhg^{-1}$). The capacity is recovered to a level of 1031 mAh g^{-1} after 80 cycles between 1C and 60C, which corresponds to 82% of the initial capacity.

Notably, the electrochemical performance of undoped $SnO_{2,70}/rGO_{30}$ nanocomposites is much worse, featuring a strongly pronounced capacity fading at higher C-rates compared to their antimony-doped counterparts (see Figure 4.13d). The initial capacity of 1120 mAh g^{-1} (1C) decreases rapidly 93 mAh g^{-1} (60C) (see Table 4.2). For the undoped $SnO_{2,70}/rGO_{30}$ nanocomposite the capacity also recovers when the C-rate is set back to 1C, but it reaches only a lowered value of 865 mAh g^{-1}, The capacity fading of the unsupported ATO nanoparticles at higher C-rates was even more pronounced (Figure 4.17b) compared to the graphene supported ATO and SnO_2 (see Figure 4.13d). Pure ATO nanoparticles reached only a capacity of 20 mAh g^{-1} at 60C (see Table 4.2). When the C-rate was set back to 1C, a capacity retention to

only 573 mAh g^{-1} in the 80th cycle could be observed, which corresponds to an irreversible capacity loss of 49%. The lower cycling stability of pure ATO nanoparticles could be caused by the greater volume expansion of the unsupported nanoparticles causing delamination and pulverization and removal of the active material from the electrode.[41]

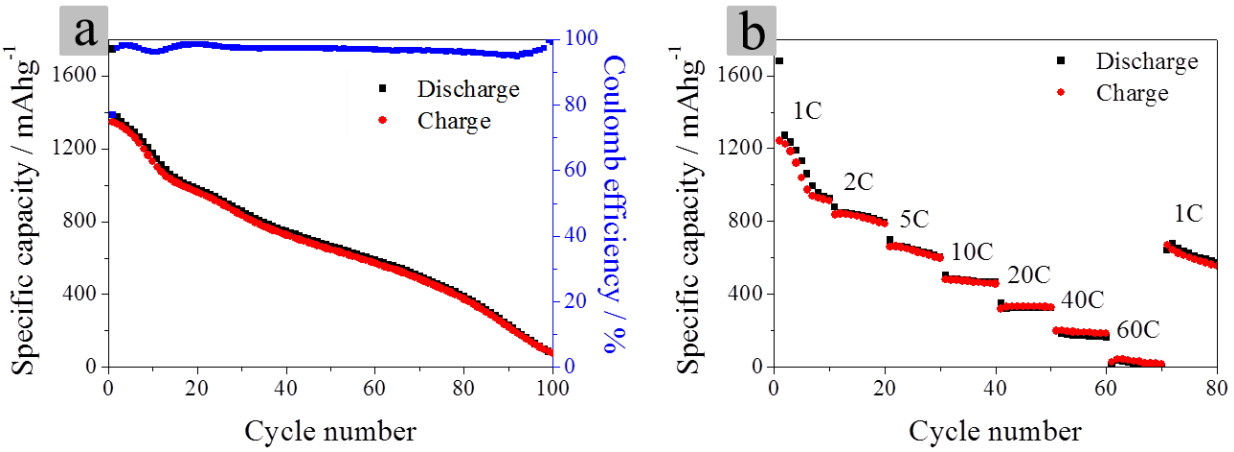

Figure 4.17: a) Multicycling stability of an ATO electrode (loading 0.2 mg cm^{-2}) at a rate of 1C and the corresponding Coulombic efficiencies (■ blue labels). Charge and discharge capacities correspond to the red (●) and black (■) labels, respectively. After 100 cycles at 1C, the electrode maintains a capacity of only 77 mAh g^{-1}. b) Rate performance of an ATO electrode at different rates ranging from 1 to 60C (ten cycles at each C-rate). The electrodes deliver specific discharge capacities of 1132 mAh g^{-1} (1C; 5th cycle), 838 mAh g^{-1} (2C; 15th cycle),647 mAh g^{-1} (5C; 25th cycle), 477 mAh g^{-1} (10C; 35th cycle), 327 mAh g^{-1} (20C; 45th cycle), 173 mAh g^{-1} (40C; 55th cycle) and 20 mAh g^{-1} (60C; 65th cycle). These values correspond to a capacity loss of 26% (2C), 43% (5C), 61% (10C), 71% (20C), 85% (40C) and 98% (60C) compared to the initial capacity at 1C (1132 $mAhg^{-1}$). The capacity retrieves to 573 mAh g^{-1} after 80 cycles between 1C and 60C, which corresponds to an irreversible capacity loss of 49%.

Additionally to the 'in-situ' synthesis, we also tested a 'dispersion-mixing' approach to fabricate ATO_{70}/rGO_{30} nanocomposites by simply mixing the dispersed pure nanoparticles with dispersed graphene oxide sheets (see experimental part for further details). The 'dispersion-mixed' nanocomposites showed an inferior electrochemical behavior compared to 'in-situ' synthesized ones, as summarized in Table 1 and shown in Figure 4.18. The specific discharge capacity drops to 211 mAh g^{-1} at 60C compared to 577 mAh g^{-1} for the 'in-situ' synthesized nanocomposite. Also the capacity retention is with only 55% lower than the for the 'in-situ' synthesized nanocomposites, which reach 85%. The lower cycling stability could be attributed to an inferior electrical contact between the ATO nanoparticles and the graphene sheets and hence a decreased conductivity.

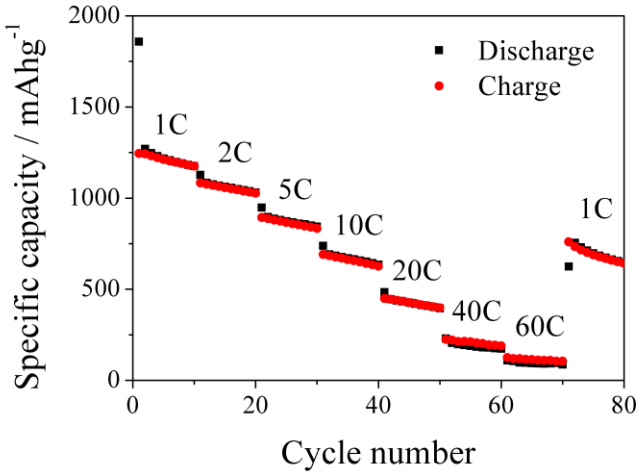

Figure 4.18: Rate performance of an ATO70/rGO30 nanocomposite prepared in a 'dispersion-mixing' approach. (mass loading: 0.2 mg cm-2) at different rates ranging from 1 to 60C (ten cycles at each C-rate). Charge and discharge capacities correspond to the red (●) and black (■) labels, respectively. The electrodes deliver specific discharge capacities of 1213 mAh g^{-1} (1C; 5th cycle),1058 mAh g^{-1} (2C; 15th cycle), 867 mAh g^{-1} (5C; 25th cycle), 663 mAh g^{-1} (10C; 35th cycle), 426 mAh g^{-1} (20C; 45th cycle), 221 mAh g^{-1} (40C; 55th cycle) and 114 mAh g^{-1} (60C; 65th cycle), respectively. The capacity is recovered to a level of 643 mAh g^{-1} after 80 cycles which corresponds to 55% of the initial capacity.

Generally; the comparison of the rate performance of different electrodes is somewhat ambiguous, as the performance strongly depends on the electrode thickness and the mode of the electrode fabrication. Furthermore, direct comparison with literature data is complicated because of different mass loadings on the electrodes, for example ranging between 0.11 mg cm^{-2} and 10 mg cm^{-2},[19, 32, 33, 55] or even missing information about the electrode loading. To the best of our knowledge, the ATO_{70}/rGO_{30} nanocomposite electrodes presented here show the highest ever reported capacity values at such high charging/discharging rates (60C = 75 A g^{-1}) among the reported related electrodes. SnO_2/carbon composites reported previously did not reach such a high current density with a reasonably high specific capacity of 550 mAh g^{-1} at 10 A g^{-1} (Chen *et al.*, unknown loading),[19] 574 mAh g^{-1} at 10 A g^{-1} (Chen *et al.*, 1 mg cm^{-2}),[55] 428 mAh g^{-1} at 10 A g^{-1} (Sher Shah *et al.*, 1.12 mg cm^{-2}),[18] 590 mAh g^{-1} at 20 A g^{-1} (Sun *et al.*, unknown loading),[33] 417 mAh g^{-1} at 20 A g^{-1} (Zhou *et al.*, 10 mg cm^{-2}),[32] and 145 mAh g^{-1} at 20 A g^{-1} (Li *et al.*, 0.11 mg cm^{-2})[25] (see also Table 4.3). Compared to low loadings of 0.11 mg cm^{-2} reported by Li *et al.*[25], our electrodes (0.2 mg cm^{-2}) deliver a five times higher capacity at 10 A g^{-1} (≈ 8C).

Table 4.3: Electrochemical performance of various ATO and SnO_2/carbon containing composites.

Anode materials	Rate performance			Cycling performance			Loading [mg cm^{-2}]	Ref.
	Discharge capacity [Ah g^{-1}]	Current density [A g^{-1}]	cycle	Discharge capacity [Ah g^{-1}]	Current density [A g^{-1}]	cycle		
ATO/NG/TEPA	1.23 0.48	0.1 5	2 32	0.89	0.5	142	-	[14]
C/ATO/CNF	≈0.80 0.41 0.71	0.1 2 0.1	5 55 70	0.35	0.1	2000	10.7	[37]
ATO/MWCNT	-	-	-	753	1C	100	-	[21]
SnO_2/graphene	≈1.20 0.55 1.02	0.5 10 0.1	5 40 45	0.95	0.5	200	-	[19]
SnO_2 nanoparticles/ graphene	0.91 0.57	0.5 10	2 120	1.45	2	1200	1	[55]
C/SnO_2/rGO	≈1.05 0.43 ≈0.11	0.1 10 0.01	5 32 40	1.24	0.01	210	1.12	[18]
SnO_2/graphite layers	1.18 0.59 1.03	0.5 20 0.5	5 55 70	1.25	0.5	500	-	[33]
SnO_2 nanocrystals/ *N*-doped graphene	1.07 0.42 1.03	0.5 20 0.5	5 55 65	1.35	0.5	500	10	[32]
SnO_2 nanoparticles/ vertically aligned graphene	≈1.10 0.15 ≈1.10	0.08 20 0.08	5 60 125	1.00 0.21	0.08 9	100 5000	0.11	[25]
SnO_2/ honeycomb-like CNFs	0.84 ≈0.55	0.1 2	2 45	0.37	1	500	0.65	[56]

Mesoporous SnO_2/rGO	1.13 0.75	0.05 0.3	5 20	0.99	0.01	100	0.56	[57]
SnO_2/ CNT/graphene	≈1.40 0.79 1.22	0.1 5 0.1	5 55 100	0.87	0.2	200	-	[58]
SnO_2/3D carbon network	0.62 0.28 0.63	0.05 10 0.05	10 65 80	0.64	0.1	50	-	[59]
SnO_2/graphene	≈1.20 ≈0.60 ≈1.15	0.1 1 0.1	5 135 160	0.68	1	1000	0.8	[17]

4.4 Conclusion

The one-step in-situ solvothermal reaction in *tert*-butyl alcohol enables the facile fabrication of ATO/GO nanocomposites containing ultrasmall crystalline ATO nanoparticles of about 3 nm in size. The nanocomposites can be synthesized in a conventional oven or via microwave-assisted synthesis, whereby the reaction time could be significantly reduced. The nanoparticle size could be tuned by adjusting the reaction temperature. Prior to the electrode fabrication, the nanocomposites were pyrolyzed in nitrogen to improve the conductivity of the hybrid materials by reducing GO to rGO. The resulting nanocomposites consist of laminated graphene oxide sheets homogeneously decorated with ATO nanoparticles. They show a superior charge storage capacity of 1226 mAh g^{-1} at 1C, which is close to the maximum theoretical capacity of the composite. Furthermore, the hybrid structures reveal an excellent cycling stability even at high current densities, reaching a capacity of 577 mAh g^{-1} at 60 C. By comparing ATO_{70}/rGO_{30} with undoped $SnO_{2,\,70}/rGO_{30}$ and pure ATO control samples, we could show the beneficial effect of antimony doping and of the intricate graphene nanocomposites on the overall electrode performance. We attribute the excellent performance to the following factors: (1) the high capacity arises from the small size of the nanoparticles, which results in a high reversibility of the conversion reaction due to decreased activation energy in nanosized ATO. (2) The higher surface area of the nanocomposites (265 m^2/g) compared to pure ATO (140 m^2/g) or rGO (26 m^2/g) results in an enlarged effective contact area between electrode and liquid electrolyte, leading to a reduced path-length for Li^+ transport and therefore a better rate performance. (3) The hybrid structure formed by the direct growth of ATO on the graphene provides a strong contact of the nanoparticles with the surface of the graphene sheets and therefore increases the overall conductivity, improves the tolerance towards volume changes and alleviates agglomeration/pulverization during the lithium insertion/de-insertion. (4) The use of ATO-based nanocomposites is advantageous compared to SnO_2 composites, as they feature a significantly higher conductivity compared to pure SnO_2 resulting in a superior cycle stability and rate capability.

4.5 Experimental Section

Materials. Tin(IV) chloride (Sigma-Aldrich), antimony(III) chloride (abcr), *tert*-butyl alcohol (99%, Sigma-Aldrich), poly(vinylidene fluoride) (PVDF, Sigma-Aldrich), graphite microparticles (2–15 μm, 99.9995%, from Alfa Aesar), black carbon (Super C65, Timcal), 1-methyl-2-pyrrolidone (NMP, Sigma-Aldrich), PuriEL electrolyte (1.15 M $LiPF_6$ in EC/EMC/DMC = 2:2:6 v/v + 1.0%wt FEC, *soul*brain MI) and lithium metal (Rockwood) were used as received. Sulphuric acid (98%), phosphoric acid (85%), potassium permanganate (99.5%), hydrogen peroxide (30%), barium nitrate (99.5%) and N,N-dimethylformamide (DMF) were obtained from Penta, Czech Republic.

Fabrication of graphene oxide. Graphene oxide was prepared by the oxidation of graphite by potassium permanganate in sulphuric/phosphoric acid as described by Marcano *et al.*.[53] For that purpose, graphite (3.0 g) and subsequently potassium permanganate (18.0 g) were added to a cooled (under 0 °C) mixture of concentrated sulphuric acid and phosphoric acid in a volume ratio of 9:1 (360 mL : 40 mL). The reaction mixture was stirred and heated at 50 °C for 12 h. Afterwards the mixture was cooled to room temperature and poured on ice (400 g) with hydrogen peroxide (3.0 mL) to remove excess permanganate ions and manganese dioxide. After the ice was dissolved, 30% hydrogen peroxide (20 mL) and water (2500 mL) were added to remove remaining unreacted potassium permanganate and manganese dioxide. Finally the obtained graphite oxide was purified by repeated centrifugation and redispersion in deionized water until a negative reaction on sulfate ions with $Ba(NO_3)_2$ was achieved. The graphite oxide slurry was ultrasonicated for 1 h (400 W; 20 °C) in order to exfoliate it to graphene oxide sheets. The concentration of graphene oxide in suspension used for composite synthesis was measured by gravimetric analysis.

Fabrication of ATO/rGO nanocomposites. The ATO/GO composites were prepared by a one-pot solvothermal route in *tert*-butyl alcohol. The synthesis quantities are summarized in Table 4.4. For a ATO/GO nanocomposite with 10% GO and an antimony doping concentration of 10%, 566.0 mg (2.17 mmol) of tin(IV) chloride, 55.1 mg (0.24 mmol) of antimony(III) chloride and 1.485 mL GO (corresponding to 27.3 mg/mL in water) were dissolved in 18 mL of *tert*-butyl alcohol and heated in a hermetically sealed Teflon lined autoclave at temperatures of 80 °C, 100 °C or 150 °C for 20 h in an oven or for 90 min in microwave autoclaves with an initial heating power of 900 W (Synthos 3000, Anton Paar), respectively. For the oven-heated samples,

the size of the ATO/SnO_2 nanoparticles within the composites is 3.7/3.5 nm, 4.6/4.7 nm and 6.1/5.8 nm at synthesis temperatures of 80 °C, 100 °C and 150 °C, respectively. For the microwave-heated samples the size of the ATO/SnO_2 nanoparticles is significantly smaller of 2.5/2.0 nm, 3.3/3.5 nm and 3.7/4.0 nm at the same temperatures. We note that only amorphous phase was observed at reaction temperatures below 80 °C. Formation of the ATO nanoparticles is favored by adding small amounts of water to the *tert*-butyl alcohol reaction mixture. Under synthesis conditions without water the reaction time has to be prolonged and/or the precursor concentration increased. The nanocomposites were separated by centrifugation (47800 rcf for 15 min) and washed once with 20 mL water and once with 20 mL ethanol by repeated redispersion and centrifugation. Finally the nanocomposites were dried in air at 60 °C for 10 h and pyrolyzed in nitrogen at 400 °C for 2 h (reached with a ramp of 2 °C min^{-1}).

Table 4.4: Synthesis quantities for ATO/GO and SnO_2/GO nanocomposites as well as pure ATO nanoparticles.

	Precursor		GO [27.3 mg/mL] in water		Water	*tert*-butyl alcohol
	$SnCl_4$ [µL]	$SbCl_3$ [mg]	[mL]	[mass %]	[mL]	[mL]
SnO^2/GO	630	-	1.485	10	-	18
ATO/GO	566	55.1	1.485	10	-	18
ATO	566	55.1	-	-	1.485	18

Fabrication of ATO nanoparticles. The antimony doped tin oxide (ATO) nanoparticles with a doping level of 10 % were prepared by a modified solvothermal route in *tert*-butyl alcohol described by some of the authors.[35] In brief, 566.0 mg (2.17 mmol) tin(IV) chloride and 55.1 mg (0.24 mmol) antimony(III) chloride were dissolved in a mixture of 18 mL of *tert*-butyl alcohol and 1.485 mL water. The mixtures were heated in a hermetically sealed Teflon lined autoclave at different temperatures for 20 h in an oven or for 90 min using an initial heating power of 900 W (Synthos 3000, Anton Paar). The nanoparticles were flocculated by the addition of 20 mL dichloromethane, separated by centrifugation (47800 rcf for 10 min), washed in 20 mL acetone and centrifuged again at 47800 rcf for 10 min.

Fabrication of ATO/rGO nanocomposites-"dispersion-mixing" approach. ATO nanoparticles with a doping concentration of 10 % were dispersed in 2 mL ethanol and mixed with 1.4 mL GO

(concentration: 27.3 mg/mL in water). The resulting mixture was stirred for two days. Afterwards the nanocomposites were dried at 60 °C for 10 h and pyrolyzed in nitrogen at 400 °C for 2 h.

Battery assembly. Electrochemical measurements were carried out using ECC-PAT-Core electrochemical test cells (EL-Cell). The working electrode was prepared by coating homogeneous slurries containing the pyrolyzed active materials (ATO, ATO/rGO and SnO_2/rGO nanocomposites), PVDF and black carbon at a mass ratio of 80:10:10 in NMP. The slurries were stirred overnight and uniformly coated onto Cu foil (Targray Technology) with a coater (wet film thickness: 50-100 µm, corresponding to a loading of 0.2 mg cm^{-2} – 0.6 mg cm^{-2}). The electrodes were die-cut into round disks with a diameter of 18 mm (254.5 mm^2) and pyrolyzed at 400°C for 2 h in nitrogen (achieved with a ramp of 2 °C min^{-1}). The electrodes were dried at 120°C for 3 h in vacuum before being used as anodes. The cells were assembled in an argon filled glove box using lithium metal as the counter and reference electrode and an EL-CELL ECC1-01-0011-A/L glass fiber membrane as separator. As electrolyte, we used a commercial mixture of 1.15 M $LiPF_6$ in EC/EMC/DMC at a 2:2:6 volume to volume ratio and 1.0 % wt fluoroethylene carbonate (FEC).

Characterization methods: Wide angle X-ray diffraction analysis was carried out in transmission mode using a STOE STADI P diffractometer with $CuK_{\alpha 1}$-radiation (λ = 1.54060 Å) and a Ge(111) single crystal monochromator equipped with a DECTRIS solid state strip detector MYTHEN 1K. Powder XRD patterns of the samples were collected in a 2θ range from 5° to 70° with a step size of 1° and a fixed counting time of 45 seconds per step. The size of the crystalline domains was calculated from the XRD patterns for the most intensive ATO signal (110 reflection) using the Scherrer equation.

X-ray photoelectron spectroscopy (XPS) measurements of the composites on a silicon substrate were performed using a VSW TA10 X-ray source, providing non-monochromatic Al K_α radiation, and a VSW HA100 hemispherical analyzer. The samples were cleaned by Ar^+ sputtering (VSW AS10 ion source) for 5 min at 1 keV. The recorded elemental peaks were fitted with a Doniach-Sunjic function[60] convoluted with a Gaussian and linear background subtraction. As the O 1s and Sb $3d_{5/2}$ peaks overlap, we used the Sb $3d_{3/2}$ and the Sn $3d_{3/2}$ peaks (SnO_2 $3d_{3/2}$ at 495.0 eV) to derive the chemical composition from the ratio of the Sb $3d_{3/2}$ peak area to the sum of the Sb $3d_{3/2}$ and Sn $3d_{3/2}$ peak areas from the measured integral intensity of the peaks.[61] The composition of the valence states was evaluated by the $Sb^{5+}/(Sb^{3+} + Sb^{5+})$ ratio of the Sb $3d_{3/2}$

peak following the method developed by Terrier *et al.*[61, 62] Thereby the Sb $3d_{3/2}$ peak was split into two Doniach-Sunjic function Gaussian lines centered at 540.04 eV[63] for Sb^{5+} and 539.24 eV[63] for Sb^{3+}. This variation of the binding energy of the Sb $3d_{3/2}$ peak is significant in XPS measurements and clearly indicates the presence of two oxidation states of antimony.

Thermogravimetric analysis (TGA) was performed on a NETZSCH STA 440 C TG/DSC instrument using a heating rate of 10 K min^{-1} in a stream of synthetic air of about 25 mL min^{-1}.

Raman spectroscopy was carried out on a LabRAM HR UV/Vis Raman instrument from HORIBA Jobin Yvon with an Olympus BX41 microscope, a Symphony CCD detection system and a He-Ne laser (λ = 633 nm).

Nitrogen sorption measurements were performed on a Quantachrome Autosorb-1 instrument at the boiling point of liquid nitrogen (approximately 77 K). Prior to the sorption experiments, the samples were degassed for 12 h at 150 °C under vacuum. The specific surface area was determined with the Brunauer-Emmett-Teller (BET) method at p/p_0 = 0.05−0.2. The pore size distribution was calculated using the DFT/Monte Carlo method and the nonlocal density functional theory (NLDFT) adsorption model with cylindrical/spherical pores.

SEM images were obtained with a FEI Helios NanoLab G3 UC scanning electron microscope equipped with a field emission gun operated at 3 kV. The powders were measured on carbon tabs glued onto a sample holder.

TEM measurements were carried out using a FEI Tecnai G2 20 S-TWIN or a Titan Themis 300 operated at 200 kV or 300 kV, respectively. For TEM sample preparation the powders were gently crushed with mortar and pestle or dispersed in absolute ethanol, placed on a holey carbon coated copper grid and dried.

Electrochemical measurements were performed at room temperature with ECC-PAT-Core (EL-Cell) battery test cells using an Autolab potentiostat/galvanostat (PGSTAT302N) with a FRA32M module or a Autolab Multipotentiostat M101 with a 8AUT.M101 module operated with Nova 1.11 software. Cyclic voltammograms were recorded in a potential range of 0.01–3.0 V vs. Li/Li^+ using a scan rate of 0.5 mV s^{-1} and a step potential of 2.44 mV. The cells were charged and discharged galvanostatically at different C rates (1 C - 60 C) in a voltage range of 0.01 – 3.0 V vs. Li/Li^+.

The theoretical capacity C_{theo} of the SnO_2 and ATO was calculated assuming that all Li per formula unit participate in the electrochemical reaction using the following equation (Equation 4.3):

$$C_{theo} = \frac{F \cdot n_{Li}}{M \cdot 3.6} \qquad 4.3$$

where F is Faraday's constant, n_{Li} - the number of lithium ions per formula unit and M - the molecular mass of the electrode material.

The overall electro-chemical process involves 8.4 and 8.33 Li^+ ions for one SnO_2 and $Sb_{0.10}Sn_{0.90}O_2$ (ATO) formula unit corresponding to a theoretical capacity of 1494 $mAhg^{-1}$ and 1466 $mAhg^{-1}$, respectively. Furthermore, reversible Li intercalation/deintercalation in graphene at E = 0.1 V with an uptake of up to 2 mol Li per mol graphene should be taken into account in the composite anodes as follows from Equation 4.4:[54]

$$6C\ (rGO) + 2Li^+ + e^- \rightleftharpoons Li_2C_6 \qquad 4.4$$

The theoretical capacity of the nanocomposites $C_{ATO/rGO\ theo}$ was calculated from the stoichiometric amounts of SnO_2 or ATO and GO in the composition according to the following equation (Equation 4.5):[14, 26]

$$C_{ATO/rGO\ theo} = C_{ATO\ theo} \cdot x\%\ ATO + C_{rGO\ theo} \cdot y\%\ rGO \qquad 4.5$$

with a theoretical capacity of 1494 $mAhg^{-1}$ for SnO_2, 1466 $mAhg^{-1}$ for ATO and 744 mAh g^{-1} for rGO. The specific capacity is based to the weight of the active material, namely the ATO nanoparticles or the ATO/rGO nanocomposites, while the masses of the additives such as carbon black, PVDF and NMP are not taken into account.

Galvanostatic charge and discharge curves were recorded at room temperatures at various C-rates ranging from 1C – 60C in a voltage window of 3.0 V to 0.01 V vs. Li^+/Li. The corresponding current densities of the different materials investigated in this publication are summarized in Table 4.5:

Table 4.5: Current densities of ATO_{70}/rGO_{30}, $SnO_{2,70}/rGO_{30}$ and pure ATO nanoparticles at different C-rates (1C–60C) and a mass loading of 0.2 mg cm^{-2}.

	Current densities [A g^{-1}]		
C-rate	ATO_{70}/rGO_{30}	$SnO_{2,70}/rGO_{30}$	ATO
Theoretical capacity	1249 [Ah g^{-1}]	1269 [Ah g^{-1}]	1466 [Ah g^{-1}]
1C	1.25	1.27	1.47
2C	2.50	2.54	2.90
5C	6.25	6.35	7.30
10C	12.49	12.69	14.66
20C	24.98	25.38	29.32
40C	49.96	50.76	58.64
60C	74.94	76.14	87.96

4.6 References

[1] S. Goriparti, E. Miele, F. De Angelis, E. Di Fabrizio, R. Proietti Zaccaria, C. Capiglia. *Journal of Power Sources* **2014**, *257*, 421-443.
[2] P. Roy, S. K. Srivastava. *Journal of Materials Chemistry A* **2015**, *3*, 2454-2484.
[3] J. Tollefson. *Nature news* **2008**, *456*, 436-440.
[4] V. Etacheri, R. Marom, R. Elazari, G. Salitra, D. Aurbach. *Energy & Environmental Science* **2011**, *4*, 3243-3262.
[5] C. Liu, F. Li, L.-P. Ma, H.-M. Cheng. *Adv Mater* **2010**, *22*, E28-E62.
[6] K. M. Abraham. *The Journal of Physical Chemistry Letters* **2015**, *6*, 830-844.
[7] M. R. Palacin. *Chemical Society Reviews* **2009**, *38*, 2565-2575.
[8] Y. Deng, C. Fang, G. Chen. *Journal of Power Sources* **2016**, *304*, 81-101.
[9] J. M. Feckl, K. Fominykh, M. Döblinger, D. Fattakhova-Rohlfing, T. Bein. *Angewandte Chemie International Edition* **2012**, *51*, 7459-7463.
[10] K. Naoi, W. Naoi, S. Aoyagi, J.-i. Miyamoto, T. Kamino. *Accounts of Chemical Research* **2012**, *46*, 1075-1083.
[11] L. Liu, H. Zhang, J. Yang, Y. Mu, Y. Wang. *Chemistry – A European Journal* **2015**, *21*, 19104-19111.
[12] M. Odziomek, F. Chaput, A. Rutkowska, K. Świerczek, D. Olszewska, M. Sitarz, F. Lerouge, S. Parola. *Nature Communications* **2017**, *8*, 15636.
[13] X. Wang, B. Liu, X. Hou, Q. Wang, W. Li, D. Chen, G. Shen. *Nano Research* **2014**, *7*, 1073-1082.
[14] X. Zhao, J. Zhang, J. Zhang, C. Gong, X. Gu, Z. Ma, J. Zhou, L. Yu, Z. Zhang. *J Power Sources* **2015**, *294*, 223-231.
[15] V. Raju, X. Wang, W. Luo, X. Ji. *Chemistry – A European Journal* **2014**, *20*, 7686-7691.
[16] Q. Guo, S. Chen, X. Qin. *Materials Letters* **2014**, *119*, 4-7.
[17] L. Liu, M. An, P. Yang, J. Zhang. *Sci Rep* **2015**, *5*, 9055.
[18] M. S. A. Sher Shah, J. Lee, A. R. Park, Y. Choi, W.-J. Kim, J. Park, C.-H. Chung, J. Kim, B. Lim, P. J. Yoo. *Electrochim Acta* **2017**, *224*, 201-210.
[19] B. Chen, H. Qian, J. Xu, L. Qin, Q.-H. Wu, M. Zheng, Q. Dong. *J Mater Chem A* **2014**, *2*, 9345-9352.
[20] Z. Wang, M. A. Fierke, A. Stein. *Journal of The Electrochemical Society* **2008**, *155*, A658-A663.
[21] O. Cevher, M. O. Guler, U. Tocoglu, H. Akbulut. *Int J Energy Res* **2014**, *38*, 499-508.
[22] O. Cevher, U. Tocoglu, H. Akbulut. *International Journal of Hydrogen Energy* **2014**, *39*, 21429-21434.
[23] J. Liang, X.-Y. Yu, H. Zhou, H. B. Wu, S. Ding, X. W. Lou. *Angewandte Chemie International Edition* **2014**, *53*, 12803-12807.
[24] P. Lian, X. Zhu, S. Liang, Z. Li, W. Yang, H. Wang. *Electrochimica Acta* **2011**, *56*, 4532-4539.
[25] N. Li, H. Sonsg, H. Cui, C. Wang. *Electrochim Acta* **2014**, *130*, 670-678.
[26] M. Zhang, Z. Sun, T. Zhang, D. Sui, Y. Ma, Y. Chen. *Carbon* **2016**, *102*, 32-38.
[27] T. Gao, K. Huang, X. Qi, H. Li, L. Yang, J. Zhong. *Ceramics International* **2014**, *40*, 6891-6897.
[28] R. Tian, Y. Zhang, Z. Chen, H. Duan, B. Xu, Y. Guo, H. Kang, H. Li, H. Liu. *Sci Rep* **2016**, *6*, 19195.
[29] F. Ye, B. Zhao, R. Ran, Z. Shao. *Chemistry – A European Journal* **2014**, *20*, 4055-4063.

[30] Y. Jiang, T. Yuan, W. Sun, M. Yan. *ACS Appl Mater Interfaces* **2012**, *4*, 6216-6220.
[31] X. Li, X. Meng, J. Liu, D. Geng, Y. Zhang, M. N. Banis, Y. Li, J. Yang, R. Li, X. Sun, M. Cai, M. W. Verbrugge. *Advanced Functional Materials* **2012**, *22*, 1647-1654.
[32] X. Zhou, L.-J. Wan, Y.-G. Guo. *Adv Mater* **2013**, *25*, 2152-2157.
[33] Y. Sun, C. Zhao, M. Shen, Z. Pan, X. Liu. *J Alloy Compd* **2016**, *683*, 191-197.
[34] Y. S. Kim, W. B. Kim, Y. L. Joo. *Journal of Materials Chemistry A* **2014**, *2*, 8323-8327.
[35] K. Peters, P. Zeller, G. Stefanic, V. Skoromets, H. Nemec, P. Kuzel, D. Fattakhova-Rohlfing. *Chem Mater* **2015**, *27*, 1090-1099.
[36] V. Müller, M. Rasp, G. Štefanić, J. Ba, S. Günther, J. Rathousky, M. Niederberger, D. Fattakhova-Rohlfing. *Chem Mater* **2009**, *21*, 5229-5236.
[37] G.-H. An, D.-Y. Lee, Y.-J. Lee, H.-J. Ahn. *ACS Appl Mater Interfaces* **2016**, *8*, 30264-30270.
[38] Y. Liu, A. Palmieri, J. He, Y. Meng, N. Beauregard, S. L. Suib, W. E. Mustain. *Sci Rep* **2016**, *6*, 25860.
[39] P. Dou, Z. Cao, C. Wang, J. Zheng, X. Xu. *Chemical Engineering Journal* **2017**, *320*, 405-415.
[40] D. Pan, N. Wan, Y. Ren, W. Zhang, X. Lu, Y. Wang, Y.-S. Hu, Y. Bai. *ACS Appl Mater Interfaces* **2017**, *9*, 9747-9755.
[41] X. Zhang, X. Huang, X. Zhang, L. Xia, B. Zhong, T. Zhang, G. Wen. *Electrochimica Acta* **2016**, *222*, 518-527.
[42] F. Mueller, D. Bresser, V. S. K. Chakravadhanula, S. Passerini. *Journal of Power Sources* **2015**, *299*, 398-402.
[43] X. Wang, Z. Li, Z. Zhang, Q. Li, E. Guo, C. Wang, L. Yin. *Nanoscale* **2015**, *7*, 3604-3613.
[44] C. Ba, L. Shi, Z. Wang, G. Chen, S. Wang, Y. Zhao, M. Zhang, S. Yuan. *Research on Chemical Intermediates* **2017**, *43*, 5857-5869.
[45] S. Wang, L. Shi, G. Chen, C. Ba, Z. Wang, J. Zhu, Y. Zhao, M. Zhang, S. Yuan. *ACS Appl Mater Interfaces* **2017**.
[46] J. Sun, L. Xiao, S. Jiang, G. Li, Y. Huang, J. Geng. *Chemistry of Materials* **2015**, *27*, 4594-4603.
[47] A. A. K. King, B. R. Davies, N. Noorbehesht, P. Newman, T. L. Church, A. T. Harris, J. M. Razal, A. I. Minett. *Sci Rep* **2016**, *6*, 19491.
[48] C. Zhao, H. Gao, C. Chen, H. Wu. *Journal of Materials Chemistry A* **2015**, *3*, 18360-18364.
[49] Y.-X. Wang, S.-L. Chou, H.-K. Liu, S.-X. Dou. *Carbon* **2013**, *57*, 202-208.
[50] S. Dubin, S. Gilje, K. Wang, V. C. Tung, K. Cha, A. S. Hall, J. Farrar, R. Varshneya, Y. Yang, R. B. Kaner. *ACS Nano* **2010**, *4*, 3845-3852.
[51] E. A. Bondarenko, A. V. Mazanik, E. A. Streltsov, A. I. Kulak, O. V. Korolik. *Materials Science and Engineering: B* **2015**, *202*, 61-67.
[52] W. C. Lee, K. Kim, J. Park, J. Koo, H. Y. Jeong, H. Lee, D. A. Weitz, A. Zettl, S. Takeuchi. *Nature Nanotechnology* **2015**, *10*, 423.
[53] D. C. Marcano, D. V. Kosynkin, J. M. Berlin, A. Sinitskii, Z. Sun, A. Slesarev, L. B. Alemany, W. Lu, J. M. Tour. *ACS Nano* **2010**, *4*, 4806-4814.
[54] Z. Chen, H. Li, R. Tian, H. Duan, Y. Guo, Y. Chen, J. Zhou, C. Zhang, R. Dugnani, H. Liu. *Scientific Reports* **2016**, *6*, 27365.
[55] Y. Chen, B. Song, R. M. Chen, L. Lu, J. Xue. *J Mater Chem A* **2014**, *2*, 5688-5695.
[56] H. Wang, J. Wang, D. Cao, H. Gu, B. Li, X. Lu, X. Han, A. L. Rogach, C. Niu. *J Mater Chem A* **2017**.

[57] D. Hoon Suh, S. K. Park, P. Nakhanivej, S.-W. Kang, H. S. Park. *J Alloy Compd* **2017**, *702*, 636-643.
[58] M.-S. Wang, Z.-Q. Wang, Z.-L. Yang, Y. Huang, J. Zheng, X. Li. *Electrochim Acta* **2017**, *240*, 7-15.
[59] T. Sun, J. Yu, Q. Yang, J. Ma. *Ionics* **2017**, *23*, 1059-1066.
[60] S. Doniach, M. Sunjic. *Journal of Physics C: Solid State Physics* **1970**, *3*, 285.
[61] C. Terrier, J. P. Chatelon, R. Berjoan, J. A. Roger. *Thin Solid Films* **1995**, *263*, 37-41.
[62] C. Terrier, J. P. Chatelon, J. A. Roger. *Thin Solid Films* **1997**, *295*, 95-100.
[63] T. Krishnakumar, R. Jayaprakash, N. Pinna, A. R. Phani, M. Passacantando, S. Santucci. *Journal of Physics and Chemistry of Solids* **2009**, *70*, 993-999.

5 Nanosized lithium-rich cobalt oxide particles and their transformation to lithium cobalt oxide cathodes with optimized high-rate morphology

This chapter is based on the following publication:

Nanosized lithium-rich cobalt oxide particles and their transformation to lithium cobalt oxide cathodes with optimized high-rate morphology

Peter M. Zehetmaier, Arnaud Cornélis, Bernhard Böller, Andreas Wisnet, Thomas Bein, Dina Fattakhova-Rohlfing, manuscript in preparation.

5.1 Abstract

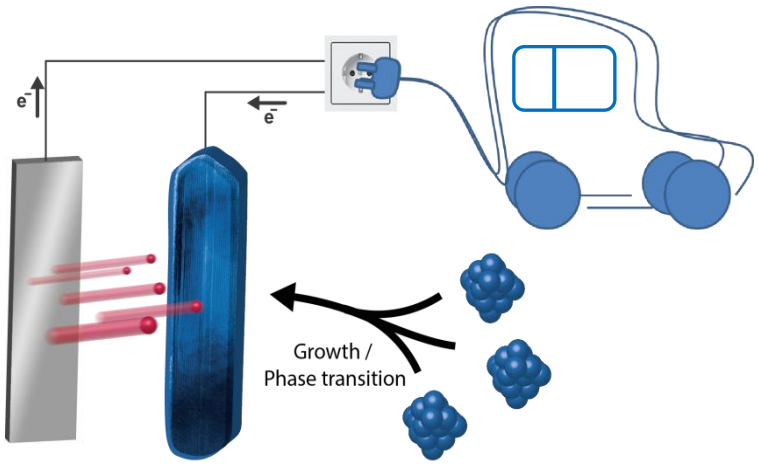

Figure 5.1: ToC image: Ultrasmall $Li_xCo_{1-x}O$ nanoparticles with a Li content of about 15% are synthesized in a solvothermal approach in *tert*-butanol and can be transformed together with an overstoichiometric lithium source in a simple rather low-temperature calcination step into HT-LCO nanoparticles. After calcination block-copolymer-templated self-assembled films produce a structured cathode material for lithium ion batteries showing high, stable and reversible gravimetric capacity even at high charge/discharge rates.

We report the formation of crystalline dispersible $Li_xCo_{1-x}O$ nanoparticles with an unusual rock-salt phase containing ~15 at% Li in the crystalline structure. This is the first time that this composition was formed at temperatures as low as 150 °C under conditions of a solvothermal process, although it is referred to as a high temperature metastable phase in a very limited number of known publications. The $Li_{0.15}Co_{0.85}O$ nanoparticles of 2-3 nm in size completely transform to high-temperature $LiCoO_2$ (HT-LCO) nanoparticles at 560 °C in the presence of slightly overstoichiometric amounts of Li source. The presence of lithium in the CoO lattice slows down the kinetics of its phase transformation, enabling to obtain very small HT-LCO nanocrystals during the subsequent calcination. The HT-LCO particles formed after this transformation have an elongated shape with a mean size of about 17 nm x 60 nm, which is targeted as an optimum size for battery applications. An attractive feature of the $Li_{0.15}Co_{0.85}O$ nanoparticles is their high dispersibility enabling their assembly into different nanostructures with optimized morphology. Open porous HT-LCO electrodes prepared via self-assembly of $Li_{0.15}Co_{0.85}O$ nanoparticles and Pluronic F127 as a structure-directing agent demonstrate very good performance at high current densities representing short charge/discharge times below 10 minutes. Even at charge/discharge times of 72 seconds (50C), 50% of the theoretical capacity has been preserved. After 250 cycles at charge/discharge times of 6 minutes (10C), over 60% of the initial discharge capacity was retained.

5.2 Introduction

Since the introduction of the high-temperature modification of $LiCoO_2$ (HT-LCO) as a suitable cathode material for lithium ion batteries (LIBs) and its commercialization by Sony in 1991, HT-LCO is still one of the prevailing cathode materials in LIBs.[1-3] Over the years, a family of promising new cathode materials was directly derived from HT-LCO by substituting Co^{3+}-ions at different degrees by metals such as nickel, manganese or aluminum to obtain materials with lower overall cost, higher energy density and lower environmental toxicity.[3-13] Nevertheless, HT-LCO still plays an important role as cathode material and as a model system for all its derivatives. Basic understanding of the processes accompanying electrochemical transformations of HT-LCO as well as the development of design guides to optimize its performance in batteries are important for the further improvement of LIB technology and are applicable also for all its derivatives.

Relatively long charging times are still a known drawback of the state of the art lithium ion batteries. Nanostructuring and accompanied morphology optimization are established means to overcome this issue by increasing the power density of the electrode materials. Thereby, nanoscaling the active material powders significantly shortens the diffusion path lengths for electrons and ions resulting in a full utilization of accessible capacity even at high charging rates. Furthermore, electrodes with nanosized active material generally better cope with structural changes induced during lithium extraction/insertion to accommodate the resulting strains. Besides nanoscaling, the electrode nanomorphology including porosity, pore size and surface area are key factors for the battery performance. A high accessible surface area provides an enlarged electrode-electrolyte interface beneficial for the flux of lithium ions and hence allows for increased charging rates. On the other hand, the increase in the surface area results in an accompanied scale up of undesired side reactions resulting in cathodic SEI formation. Furthermore, the diminishing size of crystalline domains often leads to a decreased electronic and ionic conductivity of the scaffold caused by the deteriorated crystalline periodicity existing in the bulk phase and due to an increased contribution of grain boundaries. Therefore, an optimum particles size exists for different electrode materials to improve their rate capability without compromising other important materials properties for LIB application.[9, 14-16] As the lithium ion diffusion coefficient of HT-LCO is estimated to be around 10^{-11} cm^2 s^{-1} - 10^{-12} cm^2 s^{-1} that the lithium ion diffusion length is between 10 nm to 20 nm during a 1 s charge/discharge process, the

nanoparticles have to be smaller than 30 nm to be effectively charged/discharged within 1 s.[17] Even smaller particle sizes are, however, not desired; the very small nanoparticles compromise the specific capacity of the HT-LCO material as Co^{3+}-ions are reduced to Co^{2+}-ions on the surface layers causing a lattice expansion and a loss of Li^{+}-ions. In the literature, the critical size of HT-LCO nanoparticles is estimated to be 15 nm.[17] Therefore, nanoparticles with at least one dimension in the size range of 15 nm to 30 nm are targeted to obtain high-power HT-LCO without significant loss in specific capacity.[17-20] Nanosized HT-LCO has been synthesized via different approaches such as precipitation[21], coprecipitation[22], mechano-chemical[23], molten salt[24, 25], ultrasonic[26, 27], hydrothermal[17] and sol-gel[28-30] methods and the beneficial impact of the small particle size on the enhanced electrochemical cyclability at high rates has been demonstrated. The reported approaches, however, lack the flexibility of tuning the nanomorphology of the obtained HT-LCO electrode materials to improve their rate capability and cycling stability even further. Aiming to enhance tenability, we intended to synthesize nanosized dispersible HT-LCO nanoparticles that could be assembled into desired nanostructures using different structure-directing templates – an approach that has been already successfully applied in our group to provide nanomaterials with greatly improved performance in different electrochemical applications.[16, 31-38]

5.3 Results and discussion

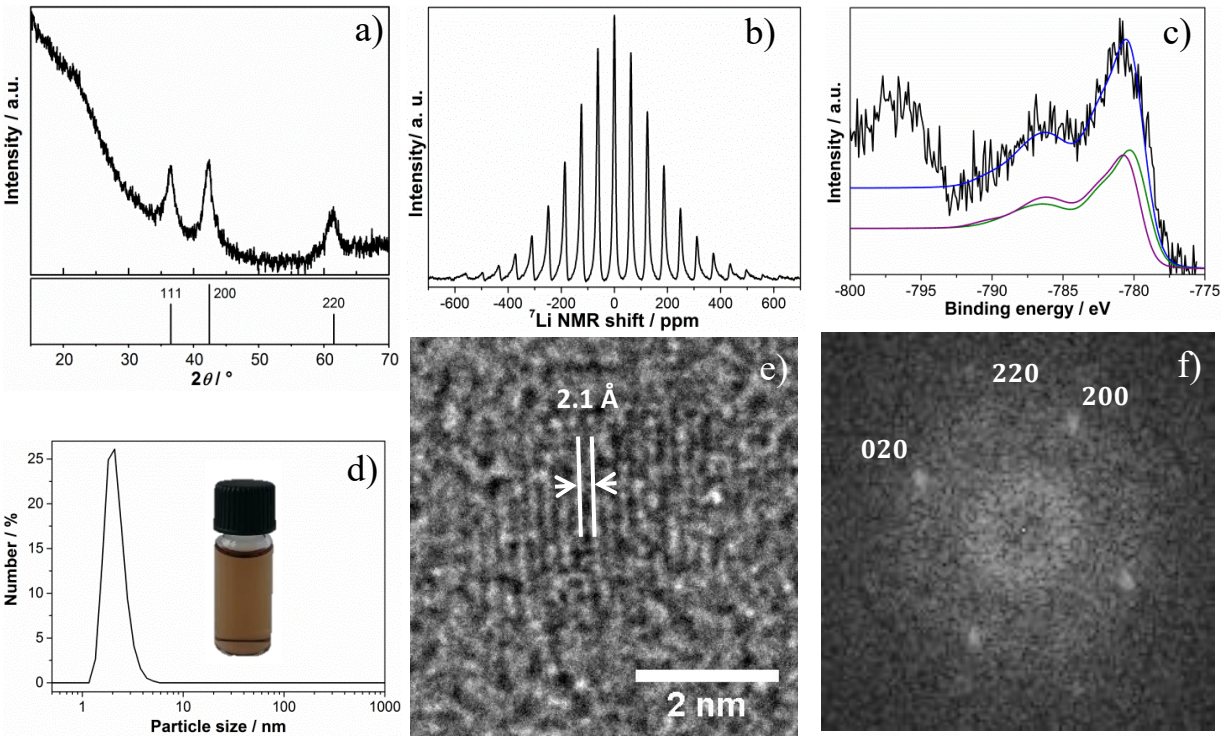

Figure 5.2: (a) XRD of $Li_{0.15}Co_{0.85}O$ nanoparticles in comparison to ICDD card 00-043-1004 of CoO. The background in the X-ray diffractogram is caused by fluorescence produced by measuring Co-containing samples with Cu-$K_{\alpha 1}$-radiation. (b) ^{7}Li solid state MAS-NMR of the washed $Li_{0.15}Co_{0.85}O$ nanoparticles. (c) XPS of the Co $2p_{3/2}$ peak on the washed $Li_{0.15}Co_{0.85}O$ nanoparticles. (d) DLS measurement of a diluted dispersion of $Li_{0.15}Co_{0.85}O$ nanoparticles in ethanol with the picture of a highly concentrated dispersion in the insert. (e) TEM micrograph of a single $Li_{0.15}Co_{0.85}O$ nanoparticle with the (200) lattice plane distance indicated. (f) Fourier transform of the HRTEM image of a single $Li_{0.15}Co_{0.85}O$ nanoparticle in Figure 5.9b with indicated diffraction pattern.

In an attempt to produce dispersible $LiCoO_2$ nanoparticles we performed a solvothermal reaction in *tert*-butanol that has already proven to be successful for the synthesis of a variety of nanosized transition metal oxides.[16, 31-38] With this purpose, $Co(OAc)_2$ and LiO*i*Pr taken at molar ratio of 1.00:1.05 were dispersed in *tert*-butanol and heated at 150 °C for 17 h in sealed autoclaves. The powder obtained after drying the reaction product is easily dispersible in ethanol to provide clear brownish dispersions containing nanoparticles with an average size of 2–3 nm and a narrow particle size distribution, as follows from dynamic light scattering (DLS) measurements (Figure 5.2d). The X-ray diffraction (XRD) pattern of the as-prepared dried powder shows the formation of a crystalline phase different from that of the precursor compounds together with a large amount of an amorphous phase (Figure 5.2a). The amorphous contribution in the XRD pattern was significantly reduced by washing the nanocrystals in ethanol, subsequent centrifugation for 15 min at 50000 rcf and removing the supernatant solution (Figure 5.3).

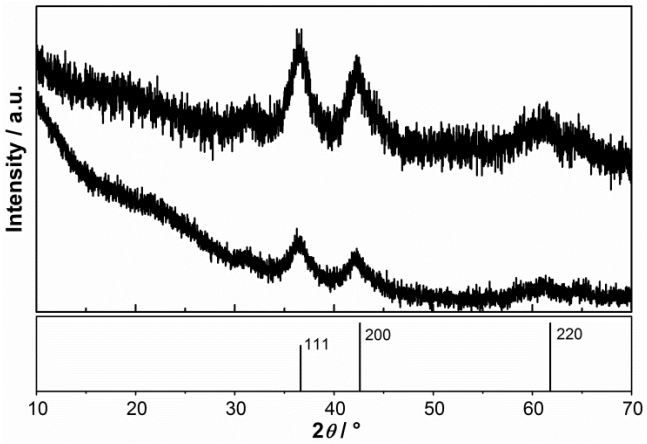

Figure 5.3: XRD patterns of as-prepared (bottom) and washed (top) $Li_xCo_{1-x}O$ nanoparticles.

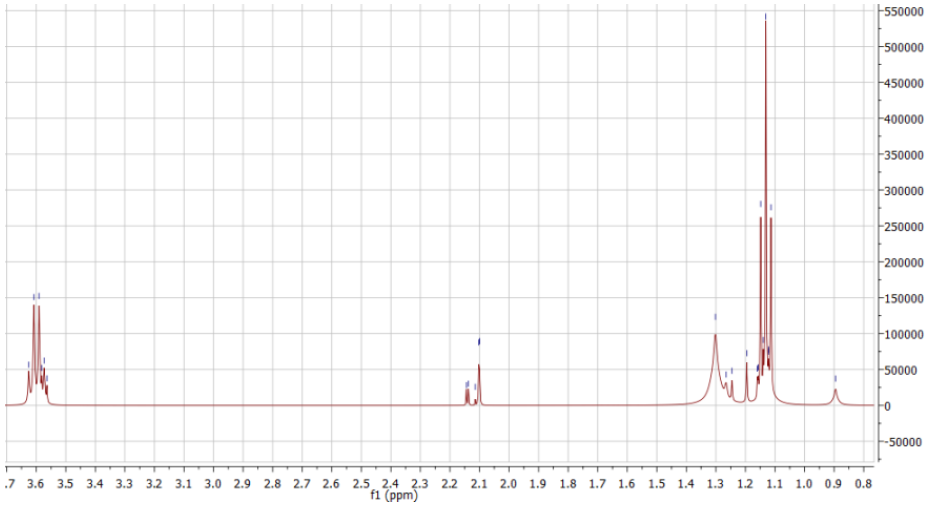

Figure 5.4: ^{1}H NMR of the dried supernatant obtained after separation of $Li_xCo_{1-x}O$ nanoparticles and dissolved in acetone-D_6. The signals correspond to ethanol, acetate and isopropoxide ions, *tert*-butanol, grease and other unidentified impurities.[39]

Gravimetric analysis in combination with the XRD measurements reveals that the weight of the as-prepared dried product consists to one third of the crystalline and to two thirds of the amorphous products; the latter are highly soluble and remain in a bluish supernatant solution. According to inductively coupled plasma optical emission spectroscopy (ICP-OES) measurements, the powder obtained by drying supernatant solution contains cobalt and lithium ions in a molar Li:Co ratio of 2.5:1, however they make up only around 18% of the total mass. The rest consists mainly of ethanol used for washing, isopropoxide and acetate-ions from the precursor salts, *tert*-butanol from the solvothermal reaction and organic impurities according to ^{1}H nuclear magnetic resonance spectroscopy (NMR) (Figure 5.4).[39] Around one third of the initially used cobalt ions remain in the supernatant solution after the reaction. The cobalt ions in

the supernatant solution are present prevalently as Co^{3+} as indicated by the typical blue color of cobalt(III)-complexes in the solution as well as the chemical shift in ^{59}Co NMR (Figure 5.5).[40] We assume that the reaction residues together with the excess of the metal ions are equally distributed in the as-prepared product and that the crystalline nanoparticles are embedded in this amorphous matrix.

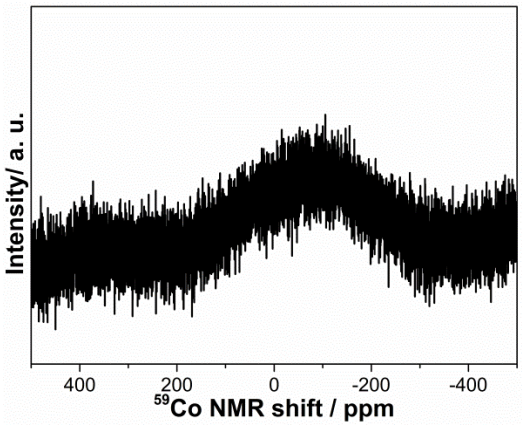

Figure 5.5: ^{59}Co NMR of the dried supernatant obtained after separation of $Li_xCo_{1-x}O$ nanoparticles and dissolved in acetone-D_6. The signal corresponds to the Co^{3+}-ions.

The XRD pattern of the crystalline material contains broad diffraction lines that do not correspond to the targeted $LiCoO_2$. However, the obtained structure is closely related to rock-salt type CoO (ICDD card 00-043-1004). The mean particle size calculated using Scherrer´s equation on the 200 reflection corresponds to 2 - 3 nm, which is in good agreement with the value obtained from DLS for dispersed particles. ICP-OES analysis of the carefully washed crystalline particles reveals that the product contains a significant amount of Li with a molar Li:Co ratio being approximately 0.2:1. The results indicate that the solvothermal reaction actually does not produce CoO, but $Li_xCo_{1-x}O$ nanoparticles crystallizing in the rock-salt type structure of CoO. According to the ICP-OES analysis the molar fraction of lithium (x) is determined to be ~0.15, hence we will refer to the obtained phase as $Li_{0.15}Co_{0.85}O$ in the following. The incorporation of Li^+ in the rock-salt CoO lattice is confirmed by the ^7Li magic angle spinning solid state NMR (^7Li MAS-NMR) spectra of washed (Figure 5.2b) and of as-prepared particles (Figure 5.6), which show an incorporation of Li^+ into the structure by an unusual broad signal splitting of about 1200ppm. The coupling of the unpaired electron of Co^{2+} with Li^+ leads to the exceptionally broad spectrum.

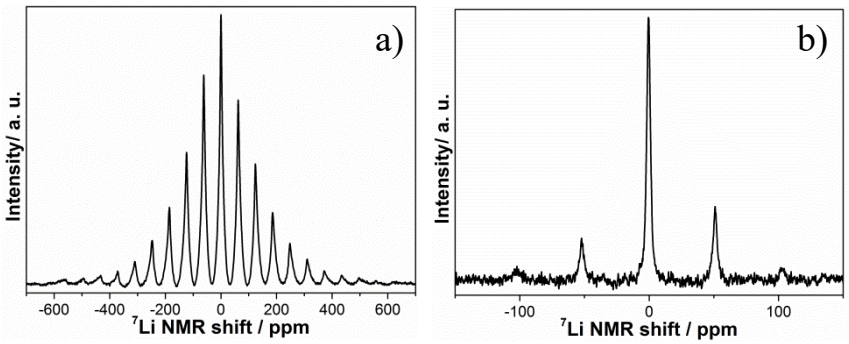

Figure 5.6: ^{7}Li solid state MAS-NMR of (a) as-prepared $Li_xCo_{1-x}O$ nanoparticles and (b) HT-LCO nanoparticles obtained after their calcination at 560 °C.

X-ray photoelectron spectroscopy (XPS) reveals the presence of Co^{3+} besides Co^{2+} species in the unwashed sample (Figure 5.7a). The ratio of Co^{2+} to Co^{3+} is found to be 2:1. After removal of the amorphous phase by washing, no Co^{3+}-ions were detected in the XPS (Figure 5.2c). The $Co2p_{3/2}$ peak of the washed crystalline product can be successfully fitted by a linear superposition of peaks of CoO and $Co(OH)_2$ according to Biesinger *et al.*[41] We can therefore assume that the washed product consists of the crystalline $Li_{0.15}Co_{0.85}O$ nanoparticles terminated with surface adsorbed OH groups, while the Co^{3+}-ions can be attributed to the non-incorporated cobalt in the amorphous phase. In contrast to ICP-OES analysis, XPS does not provide information about the lithium in the structure as the incorporation of Li does not alter the local electronic structure of CoO.[42] Raman spectroscopy characterization of cobalt-containing compounds is challenging due to their strong interaction with the Raman laser beam that converts the material irreversibly. Rivas-Murias *et al.* reported this phenomenon for the transformation of pure CoO to Co_3O_4 by local laser-induced heat.[43] As can be seen in the upper graph in Figure 5.8, high-power laser irradiation of the as-prepared unwashed $Li_{0.15}Co_{0.85}O$ nanoparticles leads to the formation of Co_3O_4[44] as well as a smaller amount of high-temperature $LiCoO_2$[45] with bands at 590 cm^{-1} and 475 cm^{-1}, which overlap with the corresponding band of Co_3O_4. At very low laser intensity however the broad band of CoO around 530 cm^{-1} is visible together with signals of instantly formed Co_3O_4 (Figure 5.8, lower graph).

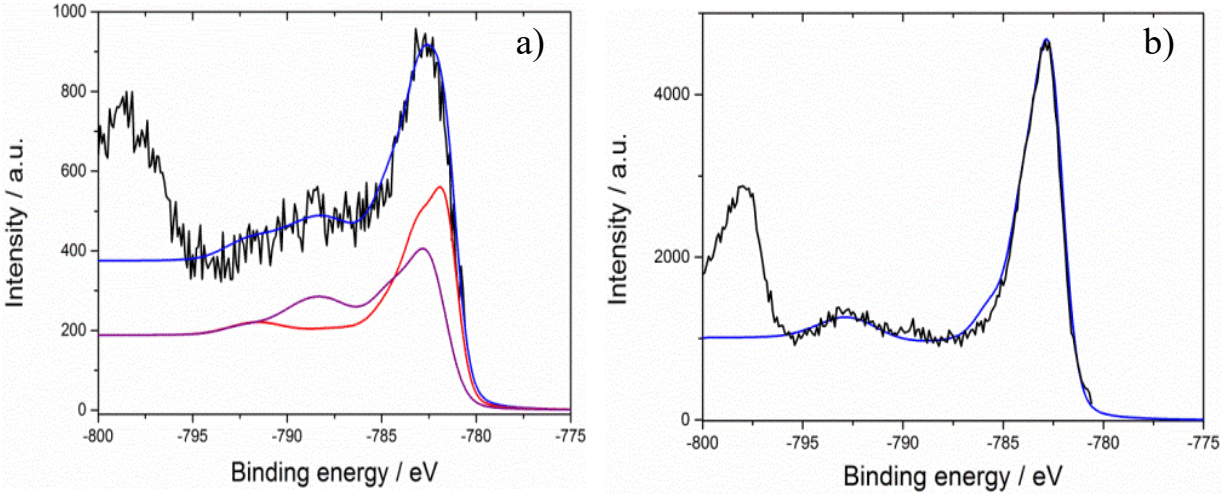

Figure 5.7: XPS of the Co $2p_{3/2}$ peak on (a) as-prepared $Li_xCo_{1-x}O$ nanoparticles and (b) HT-LCO nanoparticles obtained after their calcination at 560 °C.

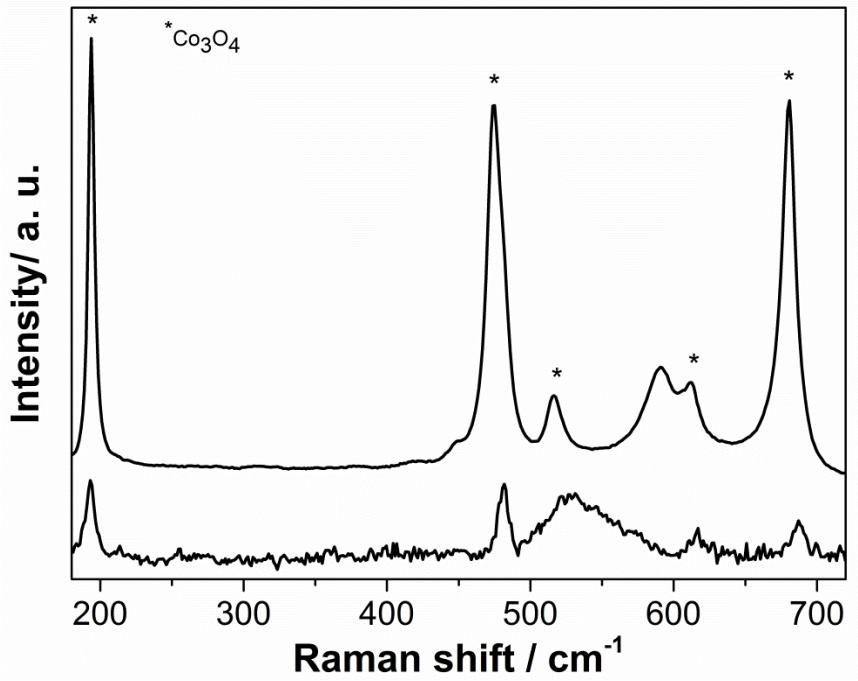

Figure 5.8: Raman spectra of as-prepared $Li_xCo_{1-x}O$ nanoparticles at 1.7 mW (lower spectrum) and 8.5 mW laser power (upper spectrum). Impurities of Co_3O_4 are indicated.

High-resolution transmission electron microscopy (HRTEM) shows the presence of very small non-agglomerated particles. The size of the nanoparticles ranges between 2 – 3 nm and is in a good agreement with the results of XRD and DLS measurements (Figure 5.9a). The presence of well-developed lattice fringes reveals the crystalline structure of the particles (Figure 5.2e). The (200) lattice fringe distance of 2.1 Å and the Fourier transforms of the images are in a good agreement with the rock-salt structure for $Li_{0.15}Co_{0.85}O$ (Figure 5.2f, Figure 5.9b).

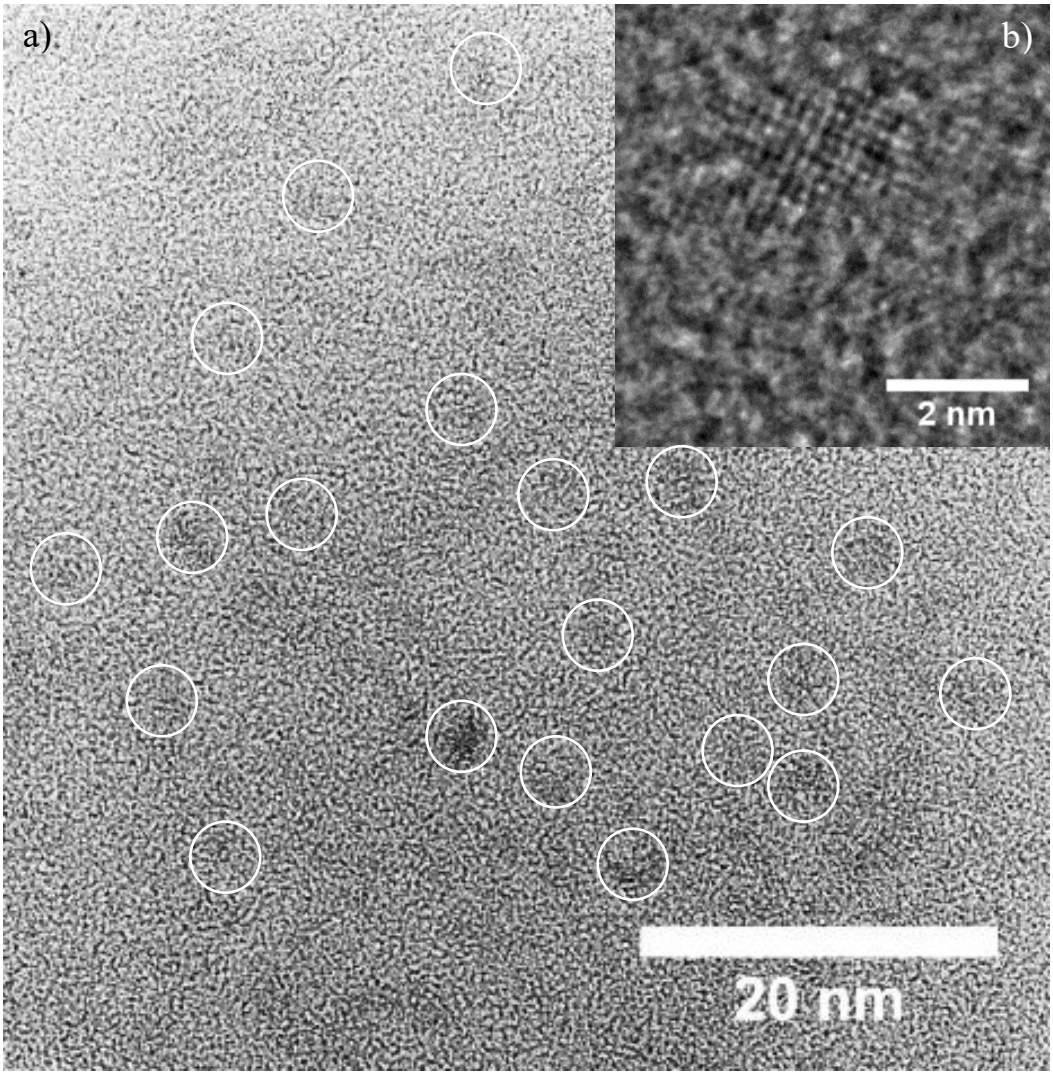

Figure 5.9: (a) TEM overview image of dispersed and non-agglomerated $Li_xCo_{1-x}O$ nanoparticles after washing (selection of the individual nanoparticles is circled). (b) TEM image of a single $Li_xCo_{1-x}O$ nanoparticle.

We note that the presence of Li^+-ions in the reaction mixture significantly alters the course of the solvothermal reaction. *tert*-Butanol synthesis performed with $Co(OAc)_2$ precursor only, without any addition of LiO*i*Pr, leads to the formation of Co_3O_4 nanoparticles instead of CoO, along with some significant amount of an unidentified nanocrystalline phase with a size around 40 nm (Figure 5.10b). The size of the resulting Co_3O_4 nanoparticles is around 4 - 6 nm. Addition of up to equimolar amount of LiO*i*Pr to the solvothermal reaction leads to the formation of $Li_{0.15}Co_{0.85}O$, however Co_3O_4 nanoparticles also form as a co-product. Only a slight excess of 5mol% Li with respect to Co prevents the nanoparticles from incorporating the Co^{3+} species and therefore from forming Co_3O_4. To summarize, the presence of Li^+-ions seems to significantly

stabilize Co^{2+}-ions under given synthesis conditions and promotes the formation of the rock-salt type oxide.

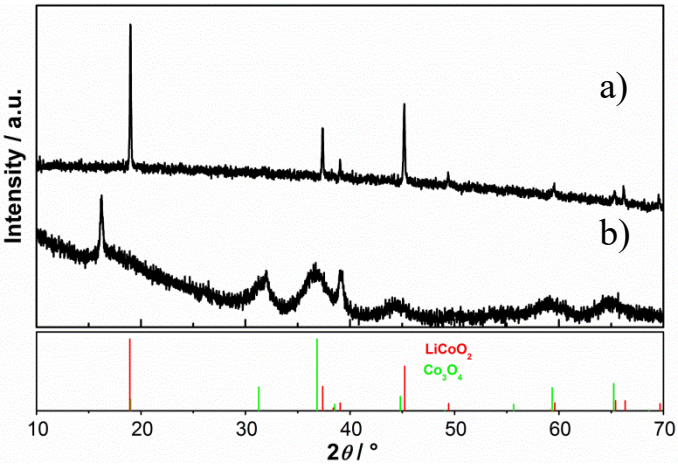

Figure 5.10: (a) XRD pattern of the product of solvothermal synthesis in *tert*-butanol performed with only $Co(OAc)_2$ without addition of Li*O*i*Pr (b) and the product of its calcination at 560 °C after mixing with lithium Li*O*i*Pr in a molar ratio of 1:1.05.

Literature reports on the rock-salt $Li_xCo_{1-x}O$ phase are very rare, beginning with a first proposed synthesis route and description of the crystal structure by Johnston *et al.* in 1958.[46] They found phase pure rock salt-type material incorporating Li of up to x = 0.2 by solid state synthesis at elevated temperatures of 700 - 900 °C; the obtained structure was described as a high-temperature phase.[46] Later in 1994 Antaya *et al.* extended the system by producing $Li_{0.5}Co_{1.5}O_2$ and $Li_{0.75}Co_{1.25}O_2$ (or, alternatively, $Li_{0.25}Co_{0.75}O$ and $Li_{0.375}Co_{0.625}O$) by laser ablation deposition.[47] Both publications assume random substitution of cobalt in the rock-salt CoO lattice by lithium, leading to an oxidation of neighboring Co^{2+} ions to Co^{3+}. In contrast to this statement, the publications of other groups oppose the formation of Co^{3+} in the rock-salt structure upon incorporation of Li^+. According to their conclusions, the formed holes are located primarily in the 2p states of the nearest lithium neighbor oxygen.[42, 48] As Li^+-ions are smaller than the substituted Co^{2+}-ions, the size of the unit cell was found to decrease with the increasing lithium content.[46, 47] Furthermore, besides the direct solid state syntheses carried out above 900 °C, $Li_xCo_{1-x}O$ was also found as combustion product of HT-LCO emerging at temperatures above 1000 °C besides Co_3O_4.[49, 50]

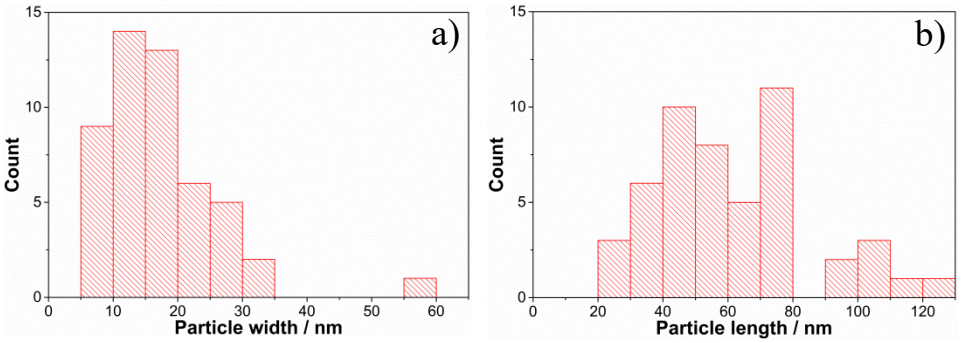

Figure 5.11: Width (a) and length (b) of the HT-LCO nanoparticles obtained by measurement of 50 particles in HRTEM images.

However, no literature reports on the nanosized $Li_xCo_{1-x}O$ exist so far; in fact to the best of our knowledge we are the first to obtain phase-pure $Li_{0.15}Co_{0.85}O$ nanoparticles. Strikingly, the nanosized rock-salt type $Li_{0.15}Co_{0.85}O$ crystallizes at the very low temperature of 150 °C under solvothermal conditions in contrast to the reported solid state syntheses that require high temperatures to obtain phase-pure material.

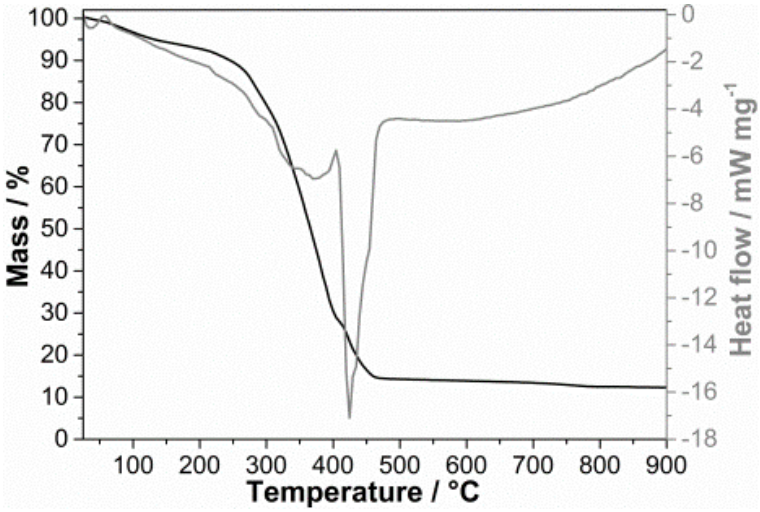

Figure 5.12: TGA (left axis) and DSC (right axis) of the mixture of as-prepared $Li_xCo_{1-x}O$ nanoparticles and Pluronic F127 in air.

To investigate the phase stability of the $Li_{0.15}Co_{0.85}O$ nanoparticles, we performed in situ heating XRD measurements (Figure 5.13a) and thermogravimetric / differential scanning calorimetry analysis (TGA/DSC, Figure 5.13b). TGA/DSC measurements reveal that a structure transition takes place at a temperature of around 425 °C, which is confirmed by in situ XRD measurements. At temperatures beyond 425 °C the XRD patterns drastically change and only one phase can be indexed corresponding to the so called high-temperature modification of lithium cobalt oxide with α-$NaFeO_2$ structure (HT-$LiCoO_2$, space group R-3m, ICDD card 01-070-2685). In the

Raman spectrum (Figure 5.14b) of the product formed at this temperature the pronounced peaks of the E_g and A_{1g} modes of the HT-$LiCoO_2$ are visible. Furthermore, small amounts of Co_3O_4 were detectable, which were presumably formed *via* the laser-induced local heating of lithium deprived particle regions with a subsequent phase transformation. $LiCoO_2$ is known to crystallize in two main modifications: low-temperature modification (LT-$LiCoO_2$, space group Fd3m) and the already mentioned high-temperature modification targeted for battery applications. Due to the structure similarity the unambiguous determination of these polymorphs using XRD analysis is not always possible.[45] Cyclic voltammograms (CV) (Figure 5.13c) of the two phases however differ significantly, which provides a convenient tool for their qualitative determination. In contrast to the results of XRD analysis that point to the formation of HT-$LiCoO_2$ already at 425 °C, cyclic voltammograms of thin films of the powder calcined at temperatures from 350 °C to 560 °C (Figure 5.13c) show a pair of peaks at around 3.6 V typical for the LT-$LiCoO_2$. Only at a temperature beyond 560 °C the redox peaks around 3.9 V characteristic for the HT-$LiCoO_2$ phase are observed. Therefore, we choose a calcination temperature of 560 °C to fully convert $Li_xCo_{1-x}O$ nanoparticles to HT-LCO for all further experiments. ^{7}Li MAS-NMR (Figure 5.6b) and XPS (Figure 5.7b) measurements of HT-$LiCoO_2$ phase obtained after calcination at 560 °C revealed the sole formation of Co^{3+} species. In ^{7}Li MAS-NMR the initially broad spectrum narrows down to a width of around 200ppm as there is no longer an unpaired spin within Co^{3+} for lithium to couple with. Additionally, the Co $2p_{3/2}$ spectrum in XPS of a sample calcined at 560 °C was fitted by using only the peak shape of a CoOOH reference according to Biesinger *et al.*[41]

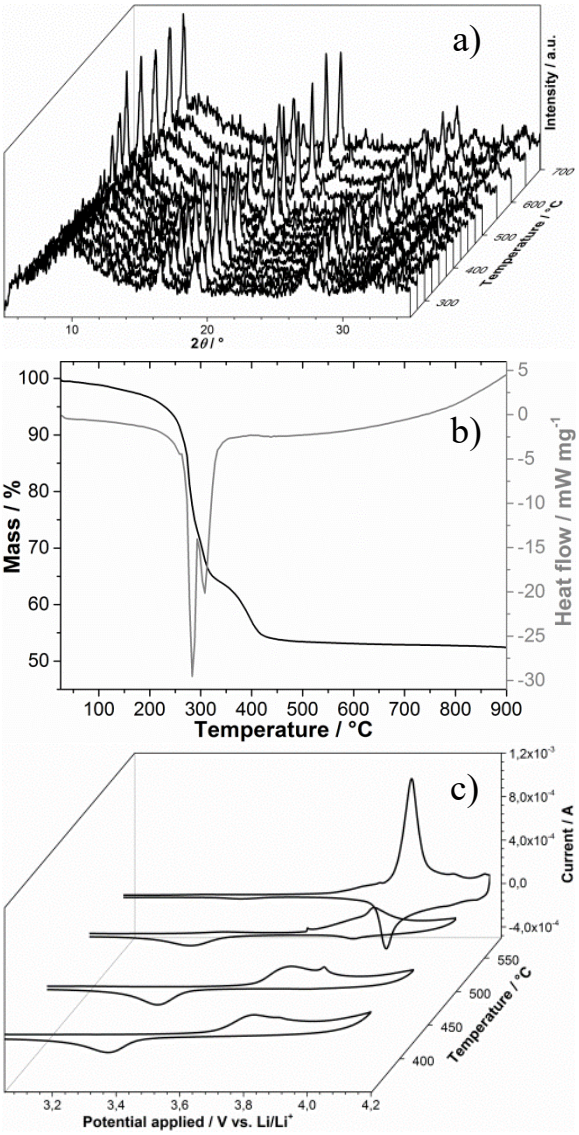

Figure 5.13: (a) In-situ XRD of the oxidation process of as-prepared $Li_{0.15}Co_{0.85}O$ to HT-LCO nanoparticles using Mo-K_α-radiation. (b) TGA (left y-axis) and DSC (right y-axis) of the as-prepared $Li_{0.15}Co_{0.85}O$ nanoparticles in air. (c) CV measurements of thin films (~200 nm) of the calcined as-prepared $Li_{0.15}Co_{0.85}O$ powder on FTO after calcination at 350 °C, 425 °C, 500 °C and 560 °C for 5 hours, respectively.

HRTEM images demonstrate that the calcination of the as-prepared spherical $Li_xCo_{1-x}O$ nanoparticles at 560 °C leads to their anisotropic growth with the formation of elongated nanoparticles (Figure 5.14c, d). The presence of well-developed lattice fringes reveals high crystallinity of the particles. The lattice fringe distances of 4.7 Å (Figure 5.14c) and the Fourier transform of the HRTEM image of the nanoparticles (Figure 5.14e) are in a good agreement with the α-$NaFeO_2$ structure of HT-$LiCoO_2$ deduced from the XRD patterns. The width of the elongated HT-$LiCoO_2$ nanoparticles ranges from 5 nm to 30 nm (Figure 5.11a) with a weighted average of 17 nm, which is in excellent agreement with the value derived from XRD. The particle

length observed is between 20 nm and 80 nm (Figure 5.11b) with a weighted average of around 60 nm.

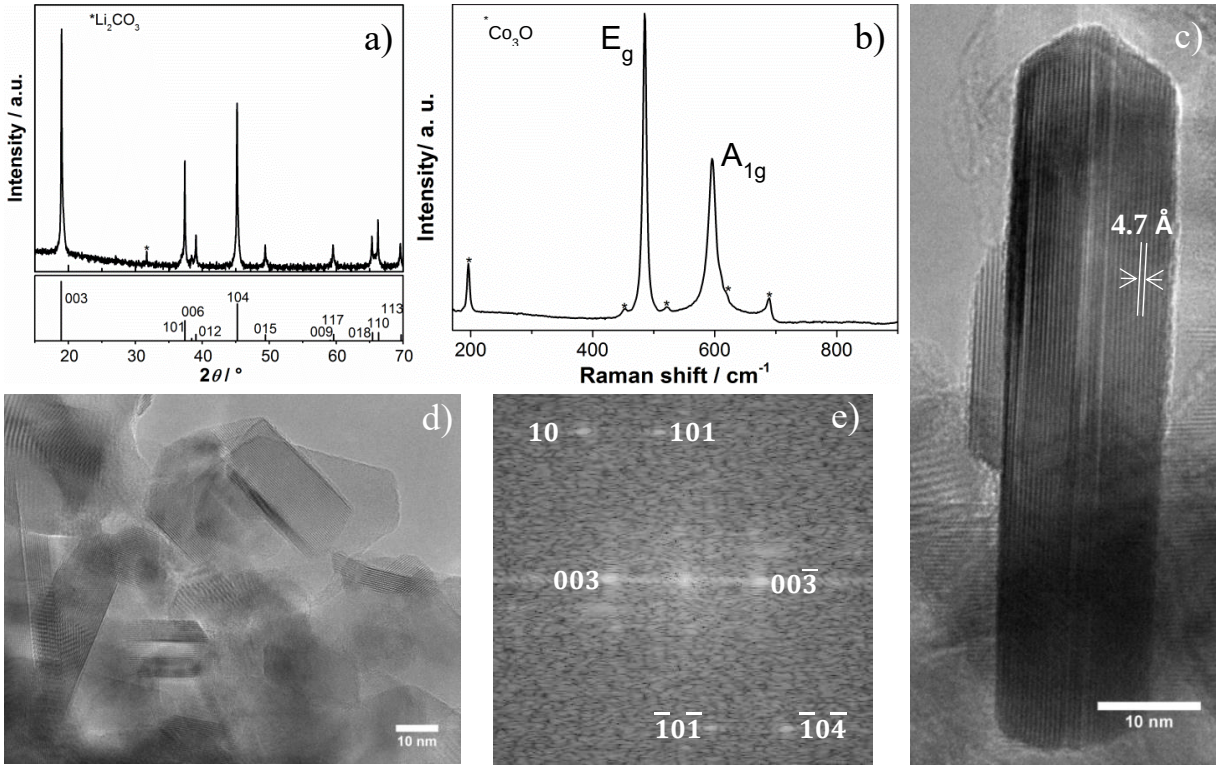

Figure 5.14: (a) XRD of HT-LCO nanoparticles calcined at 560 °C in comparison to ICDD card 01-070-2685 of HT-LCO. Particle width is calculated as 16 nm from the broadening in the 003 reflex according to the Scherrer equation. (b) Raman spectrum of HT-LCO nanoparticles. Impurities of Co_3O_4 are indicated. (c) HRTEM micrograph of a single HT-LCO nanoparticle with the (003) lattice plane distance indicated. (d) HRTEM image of the intergrown nanoparticle network scratched off a thin film calcined at 560 °C. (e) Fourier transform of the HRTEM image of (c) with indicated diffraction pattern.

As follows from the results of the different complementary measurements described above, calcination of the as-prepared product of the solvothermal reaction composed of crystalline $Li_{0.15}Co_{0.85}O$ nanoparticles embedded in an amorphous phase containing Co^{3+}-ions and an excess of Li^+-ions results in a complete transformation of the rock-salt $Li_xCo_{1-x}O$ structure to HT-$LiCoO_2$ structure upon calcination above 425 °C. This process is accompanied by an oxidation of Co^{2+}-ions to Co^{3+}-ions within the nanoparticles and diffusion of Li^+- (and probably also Co^{3+}-) ions from the surrounding amorphous phase to the nanoparticles. An excess amount of Li^+-ions is needed to obtain the Li : Co stoichiometry required for the synthesis of phase pure HT-LCO. Lithium ions can be supplied by the non-reacted precursor from the amorphous phase as it was shown above for the non-washed and as-prepared reaction product. Alternatively, Li^+-ions can also be added separately in excess. Thus, calcination of washed $Li_{0.15}Co_{0.85}O$ nanoparticles in

presence of added LiO*i*Pr produces HT-LCO nanoparticles with a size of around 50 nm (Figure 5.15a). In contrast to that, the calcination of $Li_{0.15}Co_{0.85}O$ alone (washed $Li_{0.15}Co_{0.85}O$ nanoparticles) results in the formation of a lithium-containing compound structurally similar to Co_3O_4 spinel, as follows from the XRD analysis. ICP-OES analysis of the obtained product indicates that the Co_3O_4 spinel contains 15% of Li (Figure 5.15b).

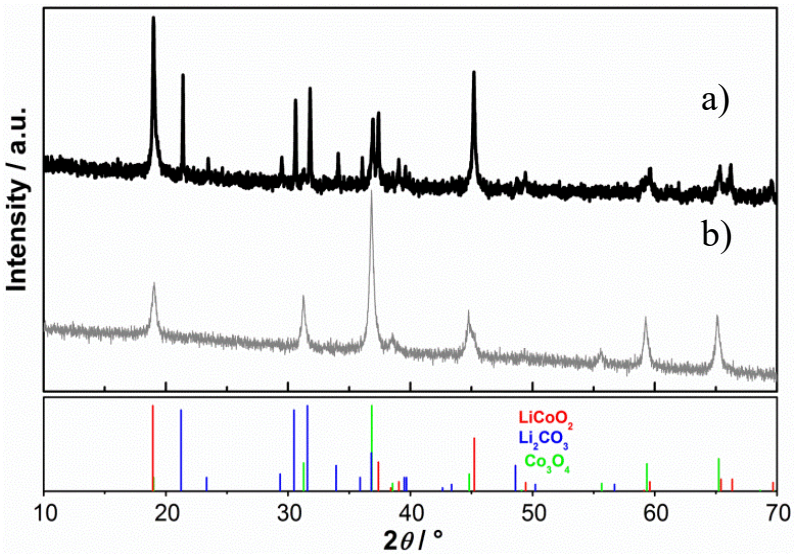

Figure 5.15: (a) XRD pattern of the reaction product obtained after calcination of washed $Li_{0.15}Co_{0.85}O$ nanoparticles and added LiO*i*Pr mixed in molar ratio of 1:0.95 at 560 °C. (b) XRD pattern of the reaction product obtained after calcination of washed $Li_{0.15}Co_{0.85}O$ nanoparticles at 560 °C without any additional Li source.

It should be noticed that the phase transformation of the $Li_xCo_{1-x}O$ at elevated temperatures was not investigated so far. The only publication dealing with this process describes the oxidation of $Li_xCo_{1-x}O$ at around 850 °C leading to a mixture of Co_3O_4 and HT-LCO.[51]

In order to tackle the role of Li^+-ion substitution in the rock-salt CoO structure in its phase transformation to LCO, we have investigated the temperature-induced transformation of Li-free cobalt oxide. Li-free Co_3O_4 nanoparticles synthesized in a similar solvothermal reaction as described above were mixed with an over-stoichiometric amount of LiO*i*Pr (1:1.05) added after the synthesis as a Li source. Calcination of the mixture at 560 °C results in the formation of HT-LCO, similar to the calcination of $Li_{0.15}Co_{0.85}O$ nanoparticles. The size of the crystalline domains of HT-LCO obtained by the transformation of Co_3O_4 is however much larger, with a particle size being over 300 nm according to XRD analysis (Figure 5.10a). Based on these results, we assume that the presence of lithium in the CoO lattice slows down the kinetics of

phase transformation to HT-LCO at elevated temperatures, enabling us to obtain very small HT-LCO nanocrystals during the subsequent calcination.

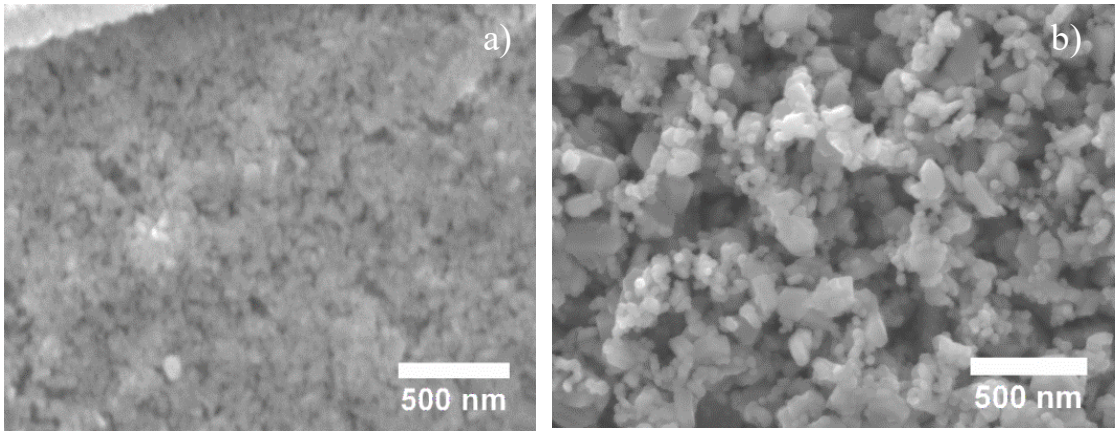

Figure 5.16: SEM micrographs of (a) LCO film resulting after calcination of as-prepared $Li_xCo_{1-x}O$ nanoparticles without any templating agent, and (b) Pluronic F127-templated HT-LCO film after calcination at 560 °C.

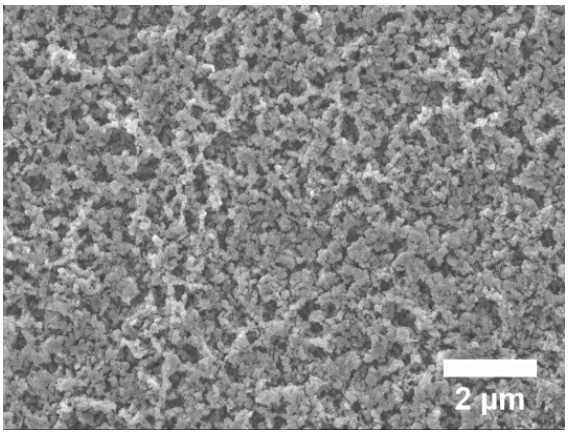

Figure 5.17: SEM image of a LCO film resulting after calcination of as-prepared $Li_xCo_{1-x}O$ nanoparticles with templating agent in low magnification.

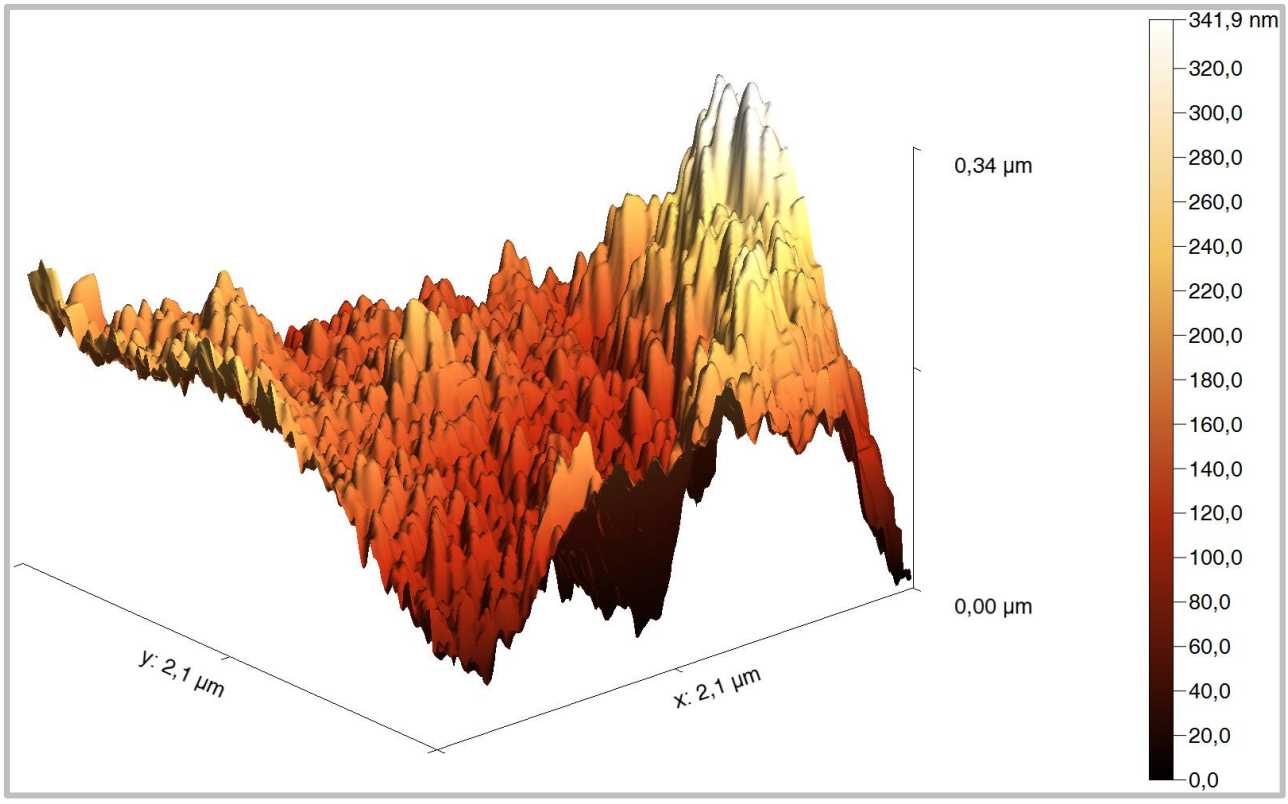

Figure 5.18: AFM image (three-dimensional plot) of the nanostructured HT-LCO film after calcination.

An attractive feature of the $Li_{0.15}Co_{0.85}O$ nanoparticles is their good dispersibility in ethanol, which enables their assembly into nanostructures with optimized morphology for LIB applications. As can be seen in scanning electron microscopy (SEM) images, the LCO films obtained by the direct sintering of $Li_{0.15}Co_{0.85}O$ nanoparticles show only textural porosity with small pores resulting from random packing of sintered agglomerates (Figure 5.16a). To optimize the morphology and to increase the accessible interface area, the block co-polymer Pluronic F127 was added to the dispersion as a structure-directing agent (in a mass ratio of as-prepared nanoparticles : Pluronic 1 : 2). The dispersion was drop-cast on FTO glass and resulting films were calcined at 560 °C. Pluronic F127 combusts at temperatures of around 400 °C as follows from the TGA/DSC measurements (Figure 5.12). The HT-LCO layers obtained in this way feature a uniform highly porous structure with large open voids accessible from the surface, as follows from the SEM images (Figure 5.16b, Figure 5.17) and atomic force microscopy (AFM) measurements (Figure 5.18). Nitrogen sorption isotherms (Figure 5.19) reveal a comparably high BET surface area of 23 $m^2 g^{-1}$ of the nanostructured LCO resulting from the high porosity with a broad pore size distribution ranging from micro- to macropores (Figure 5.19, inset). The surface area is large enough to provide an extended contact interface with the electrolyte for facilitated

lithium ion diffusion but at the same time it is small enough not to significantly increase undesired side-reactions at the interface between active material and the electrolyte. Therefore, it has the optimal properties of being an appropriate cathode material for fast lithium insertion/extraction.

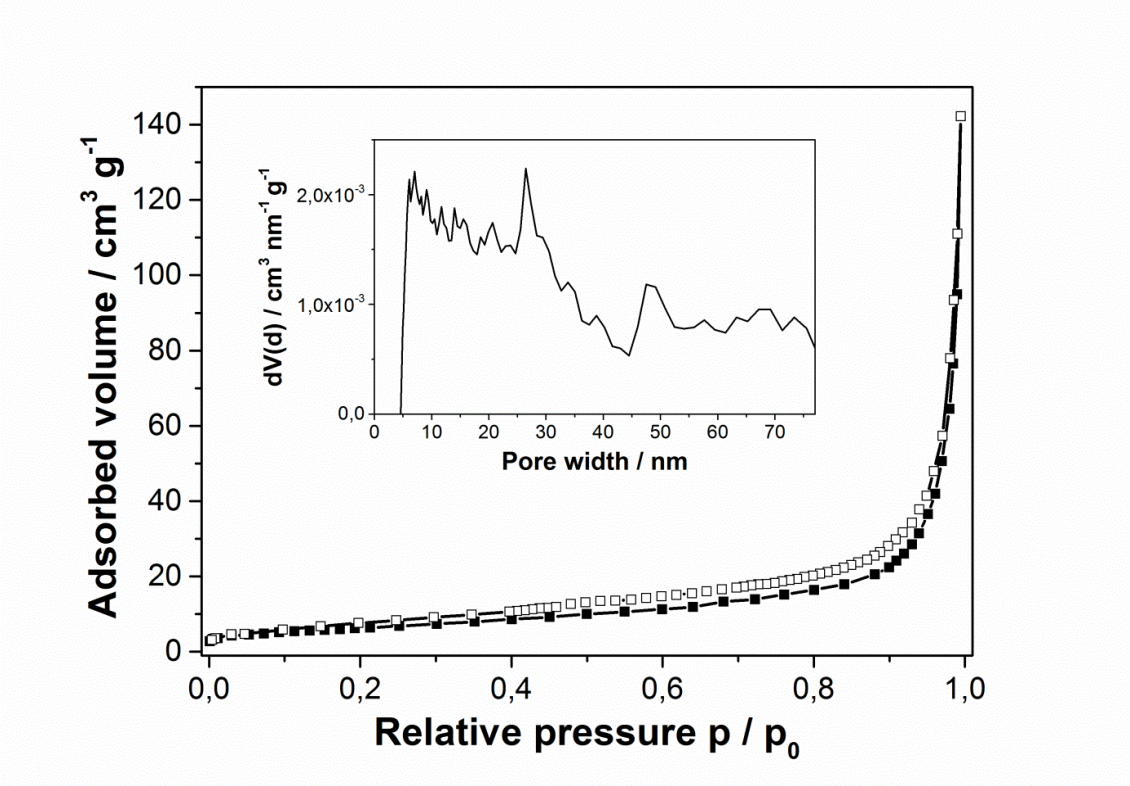

Figure 5.19: Nitrogen sorption experiment on nanostructured HT-LCO. Inserted is the pore size distribution obtained with the NLDFT method.

Comparison of electrochemical properties of non-templated and nanostructured films shows distinct differences in their performance (Figure 5.20a). The nanostructured HT-LCO film reveals a narrower separation between oxidation and reduction peaks as well as a higher current density than the flat film. Upon prolonged cycling the peak to peak separation of the flat film increases, while the peaks of the nanostructured HT-LCO remain closer together with less change in the difference of the peak potentials. The most remarkable difference between the non-templated and templated films is observed in their insertion capacities. Although the charge capacities are nearly the same for both HT-LCO structures, the discharge capacities of the nanostructured HT-LCO are almost twice as large as those of the non-templated one (Figure 5.20b).

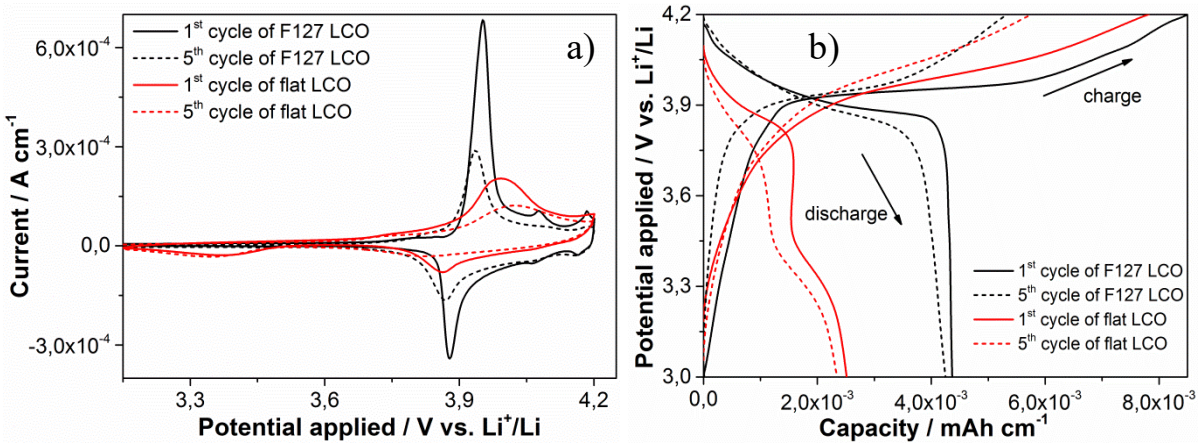

Figure 5.20: (a) CVs of flat (red) and Pluronic F127 structured LCO (black) and (b) their integrated capacities.

Galvanostatic charge/discharge measurements performed at different rates are shown in Figure 5.21a. 1C corresponds to a full charge (or discharge) of the active material within one hour, which equals a current density of 137 mA g^{-1} for HT-LCO up to a terminal voltage of 4.2 V vs. Li/Li^+. The nanostructured HT-LCO films exhibit an initial discharge capacity of 132 mAh g^{-1} at 1C, which is very close to the theoretical limit of 137 mAh g^{-1}. At higher charge/discharge rates, at which the accessible capacity in typical LCO cathodes drops significantly, the nanostructured LCO electrodes show remarkably high capacity retention. At a rate of 2C (274 mA g^{-1}) still 89% of the initial capacity is maintained (118 mAh g^{-1}) and even after ten cycles at 50C (6850 mA g^{-1}) 53% of the initial capacity can be retrieved (Figure 5.21a). Subsequent cycling at 1C yields 77% capacity retention. The irreversible capacity loss is presumably due to mechanical interruptions caused by the high current densities at 50C, leading to a loss of a portion of the active material. Comparison of rate performance of our nanostructured HT-LCO with other reported materials is not straightforward as the measurement conditions and procedures differ strongly. Further below, we provide an overview of the relevant literature and how different procedures can be related to make the results more comparable. Taking all these considerations into account, the only publication reporting slightly better performance of LCO at the rates of up to 15C is by Yadav *et al.*[52] They use a microemulsion derived HT-LCO which exhibits discharge capacities of 123 mAh g^{-1}/ 118 mAh g^{-1} for 5C/ 10C, respectively. Our nanostructured HT-LCO demonstrates, however, better performance at very high charging rates and at 20C and 50C it reveals the highest capacity retention reported so far. Furthermore, the plateaus corresponding to oxidation/reduction process of HT-LCO during galvanostatic charge/discharge, respectively, are observed at practically the same potential of 3.9 V at different C-rates (Figure 5.21b). Only at C rates higher

than 10C the plateaus are getting less distinct and drift apart due to higher overpotentials caused by the electrode resistance and the capacitive effects.[17, 53]

Long-time measurement at 10C (1370 mA g^{-1}) in Figure 5.21c shows a Coulomb efficiency of 87.6% in the first cycle and therefore an irreversible capacity loss of 12.4% due to the formation of a cathodic solid-electrolyte-interphase. For all other cycles, the Coulomb efficiency stays constant over 95%. This is a typical behavior already reported for sub-micron-sized LCO particles.[54] Especially, the long term experiment at a rather high current density shows that our nanostructured HT-LCO material has a superior discharge capacity as well as stability compared to other published HT-LCO materials. For a rate as high as 10C (6 minutes discharge) a discharge capacity of still 116 mAh g^{-1} was measured for the first cycle corresponding to 85% of the theoretical available capacity, which is relatively high compared to reported values in the literature. Subsequently, for even higher C rates up to 50C the discharge capacity only slowly decreases in contrast to the electrochemical behavior of non-nanoscaled HT-LCO.

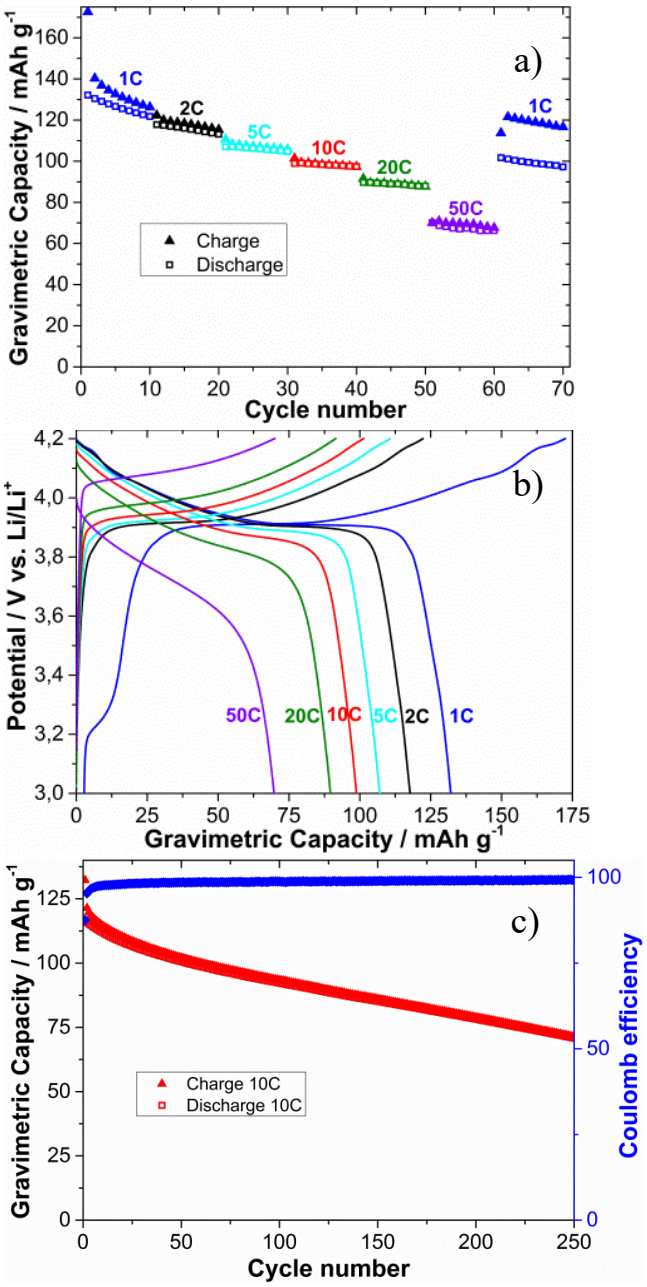

Figure 5.21: Electrochemical Li insertion/extraction with nanostructured HT-LCO heated at 560 °C: (a) Multicycling stability at different rates (ten cycles each are shown); (b) Corresponding galvanostatic charge/discharge (first curves); (c) Multicycling stability at the rate 10C showing gravimetric capacity on the left and Coulomb efficiency on the right y-axis.

Generally, a direct comparison of the rate performance of different electrodes with literature data is complicated, as the performance strongly depends on the electrode thickness and the mode of the electrode fabrication. A more detailed comparison of different reported HT-LCO electrodes is given in the following:

One of the fastest HT-LCO electrodes was prepared by Okubo *et al.*[17] from hydrothermally-grown 17 nm wide nanoparticles. The authors have used, however, a very high

content of carbon black (45%) that drastically enhances the conductivity even at very high current densities. The electrodes by Okubo *et al.* show a high value of 90 mAh g^{-1} compared to 72 mAh g^{-1} for our nanostructured HT-LCO electrode charged at 50C. However, it should be noted that our material yields a higher discharge capacity at 1C (132 mAh g^{-1}) as compared to 120 mAh g^{-1} by Okubo *et al.* Taking the masses of the additional conducting material, mostly carbon black, and the polymeric binder into account, we can re-evaluate and compare the capacity per ink mass. This reduces the values of Okubo *et al.*[17] to 60 mAh g_{ink}^{-1} and 45 mAh g_{ink}^{-1} at 1C and 50C, respectively, while our material still yields 106 mAh g_{ink}^{-1} and 56 mAh g_{ink}^{-1}, respectively. This alternative point of view drastically changes the relations towards our material and is a more realistic approach with respect to commercial use. Additionally, it should be noted that the capacity drops quite strongly between first and second cycle due to the formation of a cathodic surface-electrolyte-interphase. In this study, the discharge capacity at 50C was determined after the overall 51st cycle and not after the 1st and does not overestimate the discharge capacity by taking non-reversible charges of the cathodic SEI formation into account. Therefore, some groups normalize their data to the values of the fourth cycle to make a more realistic comparison.[10]

Another parameter which makes the comparison of the electrodes difficult is the different cut-off potential used for charging. At a cut-off potential of 4.2 V vs. Li/Li^+, half of all lithium ions are extracted. Higher cut-off voltages, such as 4.3 V, 4.5 V or even 4.8 V vs. Li/Li^+, result in a stronger lithium ion extraction from the HT-LCO. Therefore, discharge capacities far beyond 137 mAh g^{-1} can be reached and theoretical capacity limits can be derived from the literature (see Table 5.1).[55] Hence, in order to compare the performance of materials at different C rates properly the theoretical capacity for the material at each cut-off voltage should be taken into account. By this approach, the mobility of the lithium ions within the different materials expressed as the respectively achieved capacities can be compared in a more direct way as at least the time parameter is fixed.

Table 5.1: Minimal expected theoretical capacities of HT-LCO for different cut-off voltages.[55]

Cut-off voltage / V vs. Li/Li^+	4.2	4.3	4.4	4.5	4.8
Minimal theoretical capacity / mAh g^{-1}	137	156	167	192	241

Wu *et al.*[56] showed flake-like HT-LCO by a solid state synthesis and cycled them with an upper cut-off of 4.5 V *vs.* Li/Li^+. The maximum discharge capacity they obtained was 179 mAh g^{-1} for the first cycle at 0.1C (14 mA g^{-1}). This is around 93% of the possible achievable capacity. Each individual C-rate cycling step was repeated five times which returned 166 mAh g^{-1} for 1C which is significantly higher than reported in this work. Taking into account the 300 mV higher cut-off voltage, the actual C-rate reduces to 0.7C and hence, only 86% of the theoretical capacity are reached. In this work over 92% of the theoretical capacity is retained at a cut-off potential of 4.2 V vs. Li/Li^+ in all ten cycles at 1C. Further correction of the values at higher C-rates of Wu *et al.* returned 159 mAh g^{-1} and 116 mAh $g^{-1}$for 1.5C and 3.6C, respectively, where 118 mAh g^{-1} and 107 mAh g^{-1} for the higher C-rates 2C and 5C, respectively, are reported in this work. Another possibility of comparing stated literature values with this work is the collation of the relative capacity retention at different C-rates. Measurement values of Wu *et al*. show a 82% capacity retention which is opposed by 86% retention at 1.5C/2C as well as 3.6C/5C shown by the material introduced in this work. Furthermore, our material was able to deliver a superior absolute capacity of 99 mAh g^{-1} in comparison to 96 mAh g^{-1} reported for the HT-LCO flakes of Wu *et al*. Absolute capacities stated were thereby extracted from the overall 31st discharge cycle at C-rates of 10C with regard to this work and 7.3C for the value reported by Wu *et al*.

Qi and Koenig reported submicron-sized HT-LCO particles cycled up to 4.5 V with a proportionally higher current density.[54] By this, the actual C-rates get nearly the same and the results are comparable. Nevertheless, our material showed a better high-rate capability with discharge capacities of 107 mAh g^{-1} and 99 mAh g^{-1} at 5C and 10C, respectively, compared to 94 mAh g^{-1} and 70 mAh g^{-1} achieved by Qi and Koenig for the respective C-rates.[54] Reddy *et al.*[57] used procedures similar to ours for their sol-gel derived cherry-blossom-leaf-templated HT-LCO, but measured only a capacity of 69 mAh g^{-1} at 2C compared to 118 mAh g^{-1} obtained for nanosized HT-LCO introduced in this work.

Comparing our material with a desert-rose-type HT-LCO of Chen and Grey, HT-LCO presented in this work exhibits a capacity retention of 95% up to the 14th cycle at 10C versus a literature reported 75% retention obtained for a corrected rate of only 5C (1000 mA g^{-1}) resulting from an increased potential window of up to 4.5 V.[24]

Okubo *et al.* showed for bulk and nanoparticles discharge capacity retention of 93% and 70%, respectively, after 20 cycles at 10C. HT-LCO introduced in this work thereby maintained 93% of the initial discharge capacity under comparable conditions.[17] This shows that the cycling stability of our nanosized HT-LCO material is comparable to that of bulk material.

Hydrothermally prepared nanoparticles by Jo *et al.* show a discharge retention of 90% after 30 cycles at a corrected C-rate of 5C (1000 mA g^{-1}) which is just below the discharge retention of 91% at 10C reported in this work.[58] With ongoing cycling at high current density, the advantage of our nanosized HT-LCO material gets more and more pronounced.

Liang *et al.* report a capacity retention of 77% after 50 cycles at corrected 5C with their synthesized nanoparticles, while nanoparticles presented in this work preserve 87% of the initial discharge capacity after 50 cycles at 10C.[59]

Only a few groups report the performance of their HT-LCO after more than 50 cycles at high current densities. For example, Yadav *et al.* whose microemulsion derived HT-LCO nanostructures already performed well at various lower C-rates showed a decreased performance at the lower constant C-rate of 5C. Their initial discharge capacity of 110 mAh g^{-1} is reduced to 82 mAh g^{-1} after 80 cycles leading to a retention of 75% which is lower than 82% capacity retention at 10C obtained after the same number of charge/discharge cycles shown in our work.[52]

In conclusion, the only competitive high rate LCO materials demonstrating similar performance as our nanostructured HT-LCO were described by Xiao *et al.* who prepared HT-LCO with nanowire[60] and nanoplate morphology.[61] The HT-LCO nanowires reported by Xiao *et al.* preserve 79% of their initial discharge capacities after 100 cycles at 1000 mA g^{-1} (7C).[60] The HT-LCO nanoplates show a slightly higher capacity retention of 85% of the initial discharge capacity under the same experimental conditions.[61] Our nanostructured HT-LCO shows similar capacity retention after 100 cycles at an even higher C-rate of 10C (1370 mA g^{-1}). Moreover, it still retains 71 mAh g^{-1}corresponding to over 60% of the initial discharge capacity after the 250th cycle at a rate of 10C (1370 mA g^{-1}).

5.4 Conclusion

Solvothermal reaction of $Co(OAc)_2$ and LiO*i*Pr in *tert*-butanol results in the formation of crystalline dispersible nanoparticles with an unusual rock-salt $Li_xCo_{1-x}O$ phase containing around 15at% Li in the crystalline structure. This is the first time that this composition was obtained as single nanoparticles. It is also noteworthy that the rock-salt $Li_{0.15}Co_{0.85}O$ phase was formed at temperatures as low as 150 °C under the conditions of a solvothermal process, although it is referred to as high temperature metastable phase in a very limited number of known publications. A thorough investigation of the obtained nanoparticles reveals several benefits of this morphology that can be of advantage for the fabrication of HT-LCO cathodes with an optimized performance. We observed that the synthesized $Li_{0.15}Co_{0.85}O$ nanoparticles completely transform to HT-LCO nanoparticles at 560 °C in the presence of slightly overstoichiometric amounts of a lithium source. Thereby, the Li^+-ions can be supplied by the non-reacted precursor from the reaction mixture or added separately after the synthesis. The HT-LCO particles formed after this transformation have an elongated shape with a mean size of ca. 17 nm x 60 nm, which is targeted as an optimum size for high-rate battery applications. Although HT-LCO can be obtained in a similar way also from lithium-free cobalt oxide nanoparticles, the resulting particles are much larger with a size of about 300 nm. We attribute the difference in the particle sizes to slower kinetics of the phase transformation of lithium-containing nanoparticles to HT-LCO at elevated temperatures, enabling us to obtain very small HT-LCO nanocrystals during the subsequent calcination. Another attractive feature of the $Li_xCo_{1-x}O$ nanoparticles besides their small size is their high dispersibility, enabling their assembly into different nanostructures with optimized morphology. As an example we prepared porous electrodes composed of HT-LCO nanoparticles by using Pluronic F127 as a structure-directing agent, which has not been reported before. Porous HT-LCO resulting after calcination at 560 °C demonstrates very good performance at high current densities representing short charge/discharge times below 10 minutes. Even at charge/discharge times of only 72 seconds, corresponding to 50C, half of the theoretical capacity was preserved. After 250 cycles at charge/discharge times of 6 minutes (10C), still over 60% of the initial discharge capacity was retained. We suggest that further modifications of our nanostructured HT-LCO such as surface coatings with Al_2O_3[10-12], doping[13], and novel conductivity-enhancing composites[13] will help towards improving stability at higher current densities.

5.5 Experimental

Synthesis of $Li_xCo_{1-x}O$ nanoparticles: LCO nanoparticles were synthesized in a two-step synthesis. Pure cobalt(II) acetate was purchased from AppliChem. Pure lithium *iso*-propoxide was purchased from Acros Organics and *tert*-butanol was purchased from Grüssing (99% purity). All chemicals were used as received.

In a typical synthesis, 349 mg (1.4 mmol) of $Co(OAc)_2$ tetrahydrate and 97 mg (1.5 mmol) were dispersed in 180 mL *tert*-butanol within a Parr Instruments 300 mL General Purpose & High Temperature Pressure Vessel steel autoclave with internal temperature and pressure sensor. The autoclave was sealed, heated with 10 °Cmin^{-1} to 150 °C and kept at this temperature for 17 h and stirred during the reaction at 1000 rpm. The nanoparticles were collected by drying the processed solution at 70 °C. The atomic ratio of lithium to cobalt in the dried product was 1.06 in average according to ICP-OES. In order to prepare a dispersion of the preliminary particles, 100 mg of the dried solid was treated with 100 mg of concentrated acetic acid, then redispersed in 4 mL ethanol and stirred overnight. This dispersion was filtered afterwards with a 220 nm syringe filter (Sartorius minisart cellulose acetate membrane) to remove remaining agglomerates and the atomic proportion of lithium to cobalt in the resulting dispersion was determined by ICP-OES to be 1.3:1. This dispersion was diluted in a ratio of 1:50 with ethanol for DLS measurements and the preparation of TEM samples. For the production of nanostructured LCO, 200 mg of Pluronic F127 was added to the dispersion and stirred at room temperature for at least one hour.

Thin film LCO electrode preparation: Thin film electrodes for the *ex-situ* CVA measurements to determine the dependency on the calcination temperature were prepared by simply drop-casting 10 µL of the dispersion on a defined area, 1.0 cm x 1.5 cm, of a 1.0 cm x 3.0 cm FTO glass substrate. The specimen were calcined under air by heating up with a heat rate of 3 °C min^{-1} to the respective calcination temperature and a dwell time of 5 h. Afterwards the samples cooled down to room temperature with an estimated cooling rate of about 1 °C min^{-1}. To provide good electrical contact to the attached electrodes a small strip of silver varnish was attached to the upper part of the uncoated side of the FTO glass substrate.

LCO compound electrode preparation: Nanostructured LCO powder was obtained by drop-casting 6.7 µL cm^{-2} of the as-prepared dispersion (25 mg mL^{-1}) containing Pluronic F127 (50 mg mL^{-1}) on FTO glass sheets and calcination at 560 °C achieved with a heating rate of

3 °C $min^{-1}$and a dwell time of 5 hours. Afterwards the sheets were cooled down to RT with a cooling rate of 1 °C min^{-1} and the nanostructured LCO powder was scratched off the FTO glass sheets.

The nanostructured LCO powder was mixed together with carbon black Super C65 purchased from TIMCAL and poly(vinylidene fluoride) (PVdF) from Aldrich in a ratio of 80:10:10. 7 µL mg^{-1} 1-methyl-2-pyrrolidinone purchased from Sigma-Aldrich (99% purity) was added to the mixture. The ink was stirred overnight and treated for 20 min with an ultrasonic horn (Vibra Cell VC 250 of Sonics Materials) at half power. A wet film of 100 µm of the ink was coated on aluminum foil with an automatic film applicator coater ZAA 2300 from Zehntner with a coating speed of 5 mm s^{-1} and dried afterwards at 60 °C for 3 h. Circular electrodes of 18 mm in diameter were punched out and then dried at 120 °C for 5 h under vacuum. The average active mass loading was 0.7 mg.

Materials characterization: Wide angle X-ray diffraction analysis of the powders was performed in transmission mode (Debye-Scherrer geometry) using a STOE STADI P diffractometer with a Ge single crystal monochromator for either Cu-$K_{\alpha 1}$ (λ = 1.54060 Å) or Mo-$K_{\alpha 1}$-radiation (λ = 0.709300 Å) and both equipped with a DECTRIS solid state strip detector MYTHEN 1K.

Raman spectra were acquired with a Jobin Yvon Horiba HR800 UV Raman microscope (OLYMPUS BX41) using a HeNe laser (632.8 nm) and a SYMPHONY CCD detection system. Spectra were recorded using a lens with a 100-fold magnification. To prevent the samples of local heating, the power of the laser beam was normally adjusted to about 8.5 mW and for extremely sensitive samples to 1.7 mW with filters of various optical densities.

Scanning electron microscopy (SEM) was carried out on a JEOL JSM-6500F scanning electron microscope equipped with a field emission gun operating at 5 kV. The films were prepared on FTO glass substrates and glued onto a brass sample holder with silver lacquer.

TEM analysis was carried out on a FEI Titan Themis 300 instrument equipped with a field emission gun operating at 300 kV. Pure $Li_xCo_{1-x}O$ nanoparticles were drop-coated out of strongly diluted dispersions on a copper grid with a holey carbon film and plasma cleaned for 9 s at 50 mW to remove contaminations. In contrast to that, lithium cobalt oxide film material was scratched off a FTO substrate, deposited on the same type of copper grid and used without plasma cleaning.

Dynamic light scattering (DLS) of the $Li_xCo_{1-x}O$ nanoparticles was performed using a Malvern Zetasizer-Nano with a 4 mW He-Ne laser (633 nm) and an avalanche photodiode detector. The scattering data were evaluated on particle number.

Thermogravimetric analysis (TGA) and differential scanning calorimetry (DSC) was carried out with a NETZSCH STA 440 C TG/DSC instrument (heating rate 10 K min^{-1} in a stream of synthetic air of about 25 $mLmin^{-1}$).

Inductively coupled plasma optical emission spectroscopy was performed on a VARIAN VISTA RL CCD Simultaneous ICP-OES.

XPS analysis of the particles was performed on a silicon substrate using a VSW HA 100 electron analyzer and the Kα radiation provided by a non-monochromatized Mg anode system (Mg-K_α = 1253.6 eV). Fitting of the $Co2p_{3/2}$ peaks are based on a linear combination of Co^0, Co^{2+}, Co^{3+}, and Co_3O_4 spectra published by Biesinger *et al.*[41]

^{7}Li magic angle spinning solid state nuclear magnetic resonance (MAS-NMR) were recorded on a Bruker DSX Avance 500 FT spectrometer with a magnetic field of 11.7 T. The zirconia rotor with an outer diameter of 2.5 mm was spun at a rotation frequency of 12 kHz.

^{59}Co and ^{1}H NMR were measured on a Bruker Avance 400 MHz spectrometer.

Nitrogen sorption measurement was performed at 77 K with the scratched powder of nanostructured $LiCoO_2$ using a QUANTACHROME Autosorb iQ instrument. The powders were degassed at 120 °C for at least 12 h before measurement. The specific surface area was determined with the Brunauer−Emmett−Teller method. The pore size distribution was calculated using a non-local density functional theory (NLDFT) approach on silica cylindrical pores.

AFM characterization was performed using a NANOINK NScriptor DPN System working in tapping mode.

Electrochemical Measurements: Electrochemical measurements were performed in a three-electrode setup using an Autolab potentiostat/galvanostat PGSTAT302N with FRA32M module operating with Nova 1.10.4 software.

Thin film electrodes on FTO were measured in a custom made three electrode setup with Lithium wire as both, reference and counter electrode, and the nanostructured LCO film as working electrode. A 1 M $LiN-(SO_2CF_3)_2$ solution in a mixture of ethylene carbonate (EC) and 1,2-dimethoxyethane (DME) (1:1 by weight) that was dried over 3 Å molecular sieves for at least 24 h was used as electrolyte.

LCO compound electrodes were measured in an EL-CELL ECC-PAT-Core three electrode setup. The cathode material electrode was separated from the Li metal foil anode by an insulation sleeve equipped with a WHATMAN glass-fiber separator and a lithium metal reference ring. As electrolyte we used a commercial PuriEL 1.15 M $LiPF_6$ in EC/ethyl-methyl-carbonate (EMC)/dimethylcarbonate (DMC) in a 2:2:6 volume to volume ratio and 1.0 % wt fluoroethylene carbonate (FEC) purchased from Soulbrain MI.

Cyclic voltammetry measurements were usually performed between 3 V and 4.2 V vs. Li/Li^+ and with a scan speed of 2 mV s^{-1}.

Galvanostatic measurements were performed using off voltages of 3 V and 4.2 V vs. Li/Li^+, respectively. Both charge and discharge steps were performed at the same current density. A potentiostatic step at 4.2 V was performed between the galvanostatic charge and discharge step until the charge/discharge current density was reached.

5.6 References

[1] K. Mizushima, P. C. Jones, P. J. Wiseman, J. B. Goodenough. *Materials Research Bulletin* **1980**, *15*, 783-789.
[2] K. Ozawa. *Solid State Ionics* **1994**, *69*, 212-221.
[3] G. E. Blomgren. *Journal of The Electrochemical Society* **2017**, *164*, A5019-A5025.
[4] M. Ma, N. A. Chernova, B. H. Toby, P. Y. Zavalij, M. S. Whittingham. *Journal of Power Sources* **2007**, *165*, 517-534.
[5] M. Sathiya, G. Rousse, K. Ramesha, C. P. Laisa, H. Vezin, M. T. Sougrati, *et al. Nat Mater* **2013**, *12*, 827-835.
[6] Y. Wang, J. Jiang, J. R. Dahn. *Electrochemistry Communications* **2007**, *9*, 2534-2540.
[7] J. W. Fergus. *Journal of Power Sources* **2010**, *195*, 939-954.
[8] X. Xu, S. Lee, S. Jeong, Y. Kim, J. Cho. *Materials Today* **2013**, *16*, 487-495.
[9] Y. Tang, Y. Zhang, W. Li, B. Ma, X. Chen. *Chemical Society Reviews* **2015**, *44*, 5926-5940.
[10] I. D. Scott, Y. S. Jung, A. S. Cavanagh, Y. Yan, A. C. Dillon, S. M. George, S.-H. Lee. *Nano Lett* **2011**, *11*, 414-418.
[11] Y. S. Jung, P. Lu, A. S. Cavanagh, C. Ban, G.-H. Kim, S.-H. Lee, S. M. George, S. J. Harris, A. C. Dillon. *Advanced Energy Materials* **2013**, *3*, 213-219.
[12] Y. S. Jung, A. S. Cavanagh, A. C. Dillon, M. D. Groner, S. M. George, S.-H. Lee. *Journal of The Electrochemical Society* **2010**, *157*, A75-A81.
[13] L. Liu, H. Zhang, J. Yang, Y. Mu, Y. Wang. *Chemistry – A European Journal* **2015**, *21*, 19104-19111.
[14] A. S. Arico, P. Bruce, B. Scrosati, J.-M. Tarascon, W. van Schalkwijk. *Nat Mater* **2005**, *4*, 366-377.
[15] P. G. Bruce, B. Scrosati, J.-M. Tarascon. *Angewandte Chemie International Edition* **2008**, *47*, 2930-2946.
[16] J. M. Feckl, K. Fominykh, M. Döblinger, D. Fattakhova-Rohlfing, T. Bein. *Angewandte Chemie International Edition* **2012**, *51*, 7459-7463.
[17] M. Okubo, E. Hosono, J. Kim, M. Enomoto, N. Kojima, T. Kudo, H. Zhou, I. Honma. *J Am Chem Soc* **2007**, *129*, 7444-7452.
[18] L. Maugeri, A. Iadecola, B. Joseph, L. Simonelli, L. Olivi, M. Okubo, I. Honma, H. Wadati, T. Mizokawa, N. L. Saini. *Journal of Physics: Condensed Matter* **2012**, *24*, 335305.
[19] L. Maugeri, L. Simonelli, A. Iadecola, B. Joseph, M. Okubo, I. Honma, H. Wadati, T. Mizokawa, N. L. Saini. *Journal of Power Sources* **2013**, *229*, 272-276.
[20] L. Simonelli, N. L. Saini, M. Moretti Sala, M. Okubo, I. Honma, T. Mizokawa, G. Monaco. *Applied Physics Letters* **2013**, *103*, 083111.
[21] D. Larcher, B. Delobel, L. Dantras-Laffont, E. Simon, J.-F. Blach, E. Baudrin. *Inorg Chem* **2010**, *49*, 10949-10955.
[22] H. Chen, X. Qiu, W. Zhu, P. Hagenmuller. *Electrochemistry Communications* **2002**, *4*, 488-491.
[23] E. Grigorova, T. S. Mandzhukova, M. Khristov, M. Yoncheva, R. Stoyanova, E. Zhecheva. *Journal of Materials Science* **2011**, *46*, 7106-7113.
[24] H. Chen, C. P. Grey. *Adv Mater* **2008**, *20*, 2206-2210.
[25] D. Qian, Y. Hinuma, H. Chen, L.-S. Du, K. J. Carroll, G. Ceder, C. P. Grey, Y. S. Meng. *J Am Chem Soc* **2012**, *134*, 6096-6099.

[26] K. H. Kim, K. B. Kim. *Ultrason Sonochem* **2008**, *15*, 1019-1025.
[27] J.-P. Park, J.-Y. Park, C.-H. Hwang, M.-H. Choi, J.-E. Kim, K.-M. Ok, I.-W. Shim. *Bulletin of the Korean Chemical Society* **2010**, *31*, 327-330.
[28] M. Okubo, E. Hosono, T. Kudo, H. S. Zhou, I. Honma. *Journal of Physics and Chemistry of Solids* **2008**, *69*, 2911-2915.
[29] T. Kawamura, M. Makidera, S. Okada, K. Koga, N. Miura, J.-i. Yamaki. *Journal of Power Sources* **2005**, *146*, 27-32.
[30] R. B. Khomane, A. C. Agrawal, B. D. Kulkarni, S. Gopukumar, A. Sivashanmugam. *Materials Research Bulletin* **2008**, *43*, 2497-2503.
[31] Y. Liu, J. M. Szeifert, J. M. Feckl, B. Mandlmeier, J. Rathousky, O. Hayden, D. Fattakhova-Rohlfing, T. Bein. *ACS Nano* **2010**, *4*, 5373-5381.
[32] J. M. Szeifert, J. M. Feckl, D. Fattakhova-Rohlfing, Y. Liu, V. Kalousek, J. Rathousky, T. Bein. *J Am Chem Soc* **2010**, *132*, 12605-12611.
[33] K. Fominykh, J. M. Feckl, J. Sicklinger, M. Döblinger, S. Böcklein, J. Ziegler, L. Peter, J. Rathousky, E.-W. Scheidt, T. Bein, D. Fattakhova-Rohlfing. *Advanced Functional Materials* **2014**, *24*, 3123-3129.
[34] Y. Liu, K. Peters, B. Mandlmeier, A. Müller, K. Fominykh, J. Rathousky, C. Scheu, D. Fattakhova-Rohlfing. *Electrochimica Acta* **2014**, *140*, 108-115.
[35] J. M. Feckl, H. K. Dunn, P. M. Zehetmaier, A. Müller, S. R. Pendlebury, P. Zeller, *et al.* *Advanced Materials Interfaces* **2015**, *2*, 1500358-n/a.
[36] K. Fominykh, P. Chernev, I. Zaharieva, J. Sicklinger, G. Stefanic, M. Döblinger, A. Müller, A. Pokharel, S. Böcklein, C. Scheu, T. Bein, D. Fattakhova-Rohlfing. *ACS Nano* **2015**, *9*, 5180-5188.
[37] K. Fominykh, G. C. Tok, P. Zeller, H. Hajiyani, T. Miller, M. Döblinger, R. Pentcheva, T. Bein, D. Fattakhova-Rohlfing. *Advanced Functional Materials* **2017**, *27*, 1605121-n/a.
[38] K. Peters, P. Zeller, G. Stefanic, V. Skoromets, H. Němec, P. Kužel, D. Fattakhova-Rohlfing. *Chemistry of Materials* **2015**, *27*, 1090-1099.
[39] G. R. Fulmer, A. J. M. Miller, N. H. Sherden, H. E. Gottlieb, A. Nudelman, B. M. Stoltz, J. E. Bercaw, K. I. Goldberg. *Organometallics* **2010**, *29*, 2176-2179.
[40] N. Juranić, M. B. Ćelap, D. Vućelić, M. J. Malinar, P. N. Radivojša. *Journal of Magnetic Resonance (1969)* **1979**, *35*, 319-327.
[41] M. C. Biesinger, B. P. Payne, A. P. Grosvenor, L. W. M. Lau, A. R. Gerson, R. S. C. Smart. *Applied Surface Science* **2011**, *257*, 2717-2730.
[42] J. van Elp, J. Wieland, H. Eskes, P. Kuiper, G. Sawatzky, F. de Groot, T. Turner. *Physical Review B* **1991**, *44*, 6090-6103.
[43] B. Rivas-Murias, V. Salgueiriño. *Journal of Raman Spectroscopy* **2017**, *48*, 837-841.
[44] V. G. Hadjiev, M. N. Iliev, I. V. Vergilov. *Journal of Physics C: Solid State Physics* **1988**, *21*, L199-L201.
[45] H. Porthault, R. Baddour-Hadjean, F. Le Cras, C. Bourbon, S. Franger. *Vibrational Spectroscopy* **2012**, *62*, 152-158.
[46] W. D. Johnston, R. R. Heikes, D. Sestrich. *Journal of Physics and Chemistry of Solids* **1958**, *7*, 1-13.
[47] M. Antaya, K. Cearns, J. S. Preston, J. N. Reimers, J. R. Dahn. *Journal of Applied Physics* **1994**, *76*, 2799-2806.
[48] E. Iguchi, T. Hashimoto, S. Yokoyama. *Journal of the Physical Society of Japan* **1996**, *65*, 221-229.
[49] E. Antolini. *Ceramics International* **2001**, *27*, 675-679.
[50] E. Antolini. *International Journal of Inorganic Materials* **2001**, *3*, 721-726.

[51] Y. Wu, D. Pasero, E. E. McCabe, Y. Matsushima, A. R. West. *Journal of Materials Chemistry* **2009**, *19*, 1443.
[52] G. G. Yadav, A. David, H. Zhu, J. Caruthers, Y. Wu. *Nanoscale* **2014**, *6*, 860-866.
[53] P. Simon, Y. Gogotsi, B. Dunn. *Science* **2014**, *343*, 1210-1211.
[54] Z. Qi, G. M. Koenig. *ChemistrySelect* **2016**, *1*, 3992-3999.
[55] N. Yabuuchi, Y. Kawamoto, R. Hara, T. Ishigaki, A. Hoshikawa, M. Yonemura, T. Kamiyama, S. Komaba. *Inorg Chem* **2013**, *52*, 9131-9142.
[56] N. Wu, Y. Zhang, Y. Guo, S. Liu, H. Liu, H. Wu. *ACS Appl Mater Interfaces* **2016**, *8*, 2723-2731.
[57] M. J. K. Reddy, S. H. Ryu, A. M. Shanmugharaj. *Electrochimica Acta* **2016**, *189*, 237-244.
[58] M. Jo, Y.-S. Hong, J. Choo, J. Cho. *Journal of The Electrochemical Society* **2009**, *156*, A430-A434.
[59] H. Liang, X. Qiu, H. Chen, Z. He, W. Zhu, L. Chen. *Electrochemistry Communications* **2004**, *6*, 789-794.
[60] X. Xiao, L. Yang, H. Zhao, Z. Hu, Y. Li. *Nano Research* **2012**, *5*, 27-32.
[61] X. Xiao, X. Liu, L. Wang, H. Zhao, Z. Hu, X. He, Y. Li. *Nano Research* **2012**, *5*, 395-401.

6 Nanocellulose-mediated transition of lithium-rich pseudo-quarternary metal oxide nanoparticles into lithium nickel cobalt manganese oxide (NCM) nanostructures

This chapter is based on the following publication:

Nanocellulose-mediated transition of lithium-rich pseudo-quarternary metal oxide nanoparticles into lithium nickel cobalt manganese oxide (NCM) nanostructures

Peter M. Zehetmaier, Maximilian A. Plass, Florian Zoller, Michael Beetz, Franziska Friedrich, Sebastian Häringer, Bernhard Böller, Markus Döblinger, Thomas Bein, Dina Fattakhova-Rohlfing, manuscript in preparation.

6.1 Abstract

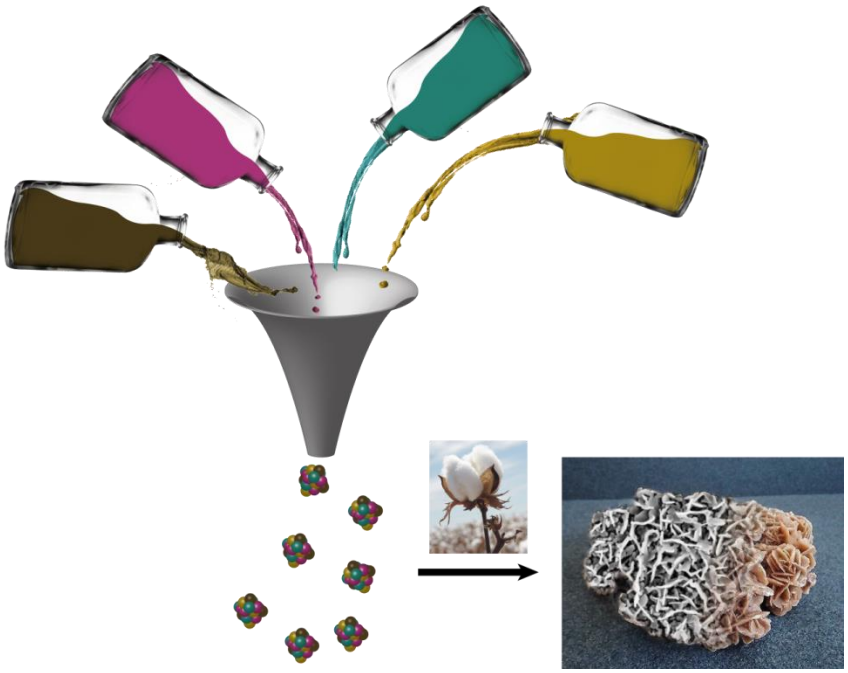

Figure 6.1: ToC image: Ultrasmall nanoparticles of the pseudo-quaternary phase $Li_wNi_xCo_yMn_zO$ were deliberately synthesized in four different compositions by a solvothermal approach in *tert*-butanol for the first time. All four different types of nanoparticles can be transformed together with an overstoichiometric lithium source and through templating with nanocellulose in a simple low-temperature calcination step into desert-rose type $Li(Ni_xCo_yMn_z)O_2$ (NCMs) with the respective compositions. These NCMs serve as cathode materials in lithium ion batteries with stable gravimetric capacities even at high charge/discharge rates.

We report the syntheses of various compounds within the pseudo-quaternary system of the type $Li_wNi_xCo_yMn_zO$ (pre-NCMs). Four different compositions of this compound were realized as ultrasmall crystalline nanoparticles of 1-4 nm diameter using low-temperature solvothermal reaction conditions in *tert*-butanol at only 170 °C. All of the pre-NCMs crystallize in the rock-salt structure and their lithium content is between 20% and 30% with respect to the complete metal content. By adjusting the lithium content to 105% stoichiometry in the solvothermal reaction, the pre-NCMs can easily react to the respective $Li(Ni_xCo_yMn_z)O_2$ (NCM) nanoparticles. Furthermore, nanosized desert-rose structured NCMs were obtained after addition of nanocellulose during the synthesis. By using the mixed metal monoxides as precursor for the NCMs, cation mixing between lithium and nickel is favored and gets more pronounced with increasing nickel content. The cation mixing effect compromises good electrochemical capacity retention, but the desert-rose structure nevertheless enables enhanced stability at high power conditions, especially for NCM333.

6.2 Introduction

Oxide compounds of cobalt, nickel and manganese play an important role in electrochemical energy storage as positive electrodes (cathodes) for lithium ion batteries (LIBs). Thus, $LiCoO_2$ (LCO) is the first commercialized cathode material and it is still used in a considerable number of LIBs over a quarter of a century after market introduction in 1991.[1-3] LCO is attractive because of its theoretical capacity of about 140 mAh g^{-1} up to 4.2 V, the low self-discharge and good cycling performance. However, major drawbacks of this material are the high cost and toxicity of cobalt within LCO, as well as a moderate energy density.[3-9] In order to overcome these problems without compromising the advantages, much research has been conducted to substitute cobalt in the layered $LiMO_2$. Complete substitution of Co by Ni leads to $LiNiO_2$ (LNO) with, on the one hand, a similar specific capacity, a higher energy density and lower cost compared to LCO. On the other hand, LNO exhibits higher thermal instability and the Ni^{2+}-ions have the tendency to substitute Li^+-sites during synthesis and delithiation and consequently block the lithium ion diffusion pathways. Complete substitution with Mn leads to the low-cost layered $LiMnO_2$, which shows a high practical specific capacity of around 200 mAh g^{-1}. However, manganese compounds face structural instability problems due to Jahn-Teller distortion, as well as Mn dissolution, followed by a loss of active material and a low cyclability. The best strategy so far is the combination of different metals within the MO_2 layers of $LiMO_2$, resulting in $Li(Ni_xCo_yMn_z)O_2$ (NCM) compounds that increasingly gain importance as cathodes in advanced LIBs.[4, 10-12],[3]

Besides the high specific capacity and energy density, high power density (high charging rate) is another important requirement for the electrode materials in advanced LIBs. Control of morphology and in particular nanoscaling are very efficient ways to boost the power density of electrode materials.[13-16] Reduction of the particle size of the active materials to the submicron region or even to tens of nanometers drastically shortens the diffusion path lengths of electrons as well as of lithium ions. This can lead to higher accessible capacities even at high charging or discharging rates. Moreover, active materials in the nanosize region are known to cushion the volume changes of structural changes and strains during the lithium insertion and extraction.

Submicron sized particles of $LiNi_{1/3}Co_{1/3}Mn_{1/3}O_2$ (NCM333) can be produced with different methods. Especially sol-gel,[17-19] modified Pechini,[20] plasma pyrolysis,[21] coprecipitation[22] and

hydrothermal[23] approaches lead to particle sizes of over 100 nm after additional calcination steps at over 750 °C. The synthesis of smaller particles, which are expected to further increase the power density, is much more challenging. So far only a few groups have developed techniques to obtain NCM333 nanocrystals between 10 nm and 100 nm including hydrothermal,[24] reverse-microemulsion[25] and combustion[26] strategies.

In our previous publications we have described a novel approach to fabricate nanostructured and nanosized lithium cobalt oxide (LCO) cathode materials, which is based on the synthesis of lithium-rich rock salt type CoO nanoparticles ("pre-LCO") followed by the temperature-assisted transformation to the electrochemically active high temperature LCO (HTO-LCO) phase. The benefit of using pre-LCO nanoparticles as nanostructured building blocks are the slow kinetics of their phase transformation to HT-LCO, enabling to obtain much smaller HT-LCO nanocrystals after the subsequent calcination as compared to other reported approaches. It is appealing to extend this approach to more complex Li-Ni-Co-Mn quaternary oxide structures to enable the fabrication of high-voltage NCM cathodes with an optimized nanomorphology. Different pseudo-binary and pseudo-ternary monoxide compounds of the system Li-Ni-Co-Mn adopting rock-salt structure such as $Li_xCo_{1-x}O$,[27-32] $Li_xNi_{1-x}O$,[33-41] $Co_xNi_{1-x}O$,[42-47] $Mn_xNi_{1-x}O$,[48] $Mn_xCo_{1-x}O$[49] and $Li_xMn_yNi_zO$[50] are already described in literature. However, there are no reports on pseudo-quaternary rock-salt type $Li_wNi_xCo_yMn_zO$ (pre-NCM) so far. Here, we show for the first time the fabrication of dispersible crystalline pre-NCM particles of various compositions and in the size range of 1-4 nm *via* the *tert*-butanol solvothermal route that was already successfully used in the syntheses of various metal oxides.[13-16, 47, 51-57] These pre-NCM building blocks form, after a combustion step, the respective NCM nanoparticles ($LiNi_{1/3}Co_{1/3}Mn_{1/3}O_2$ (NCM333), $LiNi_{0.5}Co_{0.2}Mn_{0.3}O_2$ (NCM523), $LiNi_{0.6}Co_{0.1}Mn_{0.3}O_2$ (NCM613) and $LiNi_{0.8}Co_{0.1}Mn_{0.1}O_2$ (NCM811)) intergrown in a desert-rose-like morphology.

6.3 Results and Discussion

Lithium-rich rock salt-type nickel cobalt manganese oxide $Li_wNi_xCo_yMn_zO$ (pre-NCM) nanoparticles of different compositions were obtained in a *tert*-butanol solvothermal route that has been proven successful for the syntheses of numerous metal oxide nanoparticles of very small size.[14-16, 47, 52-57] In a typical synthesis, $Ni(OAc)_2$, $Co(OAc)_2$ and $Mn(acac)_2$ were mixed in the respective molar ratios to obtain the four NCM materials. Afterwards, LiO*i*Pr was added in slight excess to the transition metal precursors (TM) in a molar ratio of 1.05:1.00 Li:TM. The resulting mixture was suspended in *tert*-butanol and heated in sealed autoclaves at 165 °C for 17 h.

XRD patterns of the as-prepared dried reaction products indicate the presence of undefined organic compounds detected as strong reflections at 5-15° 2ϑ (Figure S 6.1 in supporting information) that are most presumably derived from not-fully reacted precursors. The lithium organic compounds can be easily removed by washing with ethanol. After the washing step the rock-salt phase and an additional side phase whose reflections can be assigned to Mn_3O_4 are detectable in the XRD patterns (Figure 6.2a). Inductively-coupled plasma optical emission spectroscopy (ICP-OES) analysis reveals that the stoichiometry of Ni, Co and Mn ions for all washed pre-NCM nanoparticles is practically the same as in the initial reaction mixture. However, the molar ratio of the sum of transition metals to lithium in the washed nanoparticles is in the range of 0.25 to 0.43, hence, significantly lower than in the reaction mixture. According to the results of ICP-OES and XRD analyses, the obtained pre-NCM products crystallize in a rock salt type structure with the composition of $Li_{0.30}Ni_{0.27}Co_{0.23}Mn_{0.20}O$ (pre-NCM333), $Li_{0.23}Ni_{0.40}Co_{0.17}Mn_{0.20}O$ (pre-NCM523), $Li_{0.25}Ni_{0.47}Co_{0.08}Mn_{0.20}O$ (pre-NCM613) and $Li_{0.22}Ni_{0.62}Co_{0.08}Mn_{0.08}O$ (pre-NCM811) (Table 6.1).

Table 6.1: Compositions of the as-prepared and the washed nanoparticles of pre-NCMs in comparison. The average nanoparticle sizes calculated from the line broadening in the XRD pattern are given as well.

Sample assignment	Stoichiometry in the reaction mixture according ICP-OES (Li : Ni : Co : Mn)	Phase and chemical composition of washed reaction products according to XRD and ICP-OES	Particle size according XRD / nm
pre-NCM333	1.06 : 0.32 : 0.35 : 0.33	$Li_{0.30}Ni_{0.27}Co_{0.23}Mn_{0.20}O$	1.5
pre-NCM523	1.11 : 0.48 : 0.22 : 0.30	$Li_{0.23}Ni_{0.40}Co_{0.17}Mn_{0.20}O$	1.4
pre-NCM613	1.06 : 0.60 : 0.11 : 0.29	$Li_{0.25}Ni_{0.47}Co_{0.08}Mn_{0.20}O$	1.3
pre-NCM811	1.08 : 0.79 : 0.11 : 0.10	$Li_{0.22}Ni_{0.62}Co_{0.08}Mn_{0.08}O$	1.9

The results derived from ICP-OES concerning the compositions of the different materials and the molar ratios between Ni, Co and Mn are also confirmed by X-ray photoelectron spectroscopy (XPS) data for all of the washed pre-NCM nanoparticles. Furthermore, the $2p_{3/2}$ peaks of all three transition metals can be fitted with the respective peaks of $M(OH)_2$ according to Biesinger *et al.*,[58] confirming that all three metals are in the same oxidation state of +II (Figure 6.2c). Nevertheless, XPS cannot give evidence of Li, since Li is not directly detectable and does not distinctly affect the local electronic structure of Co and Ni.[28, 40]

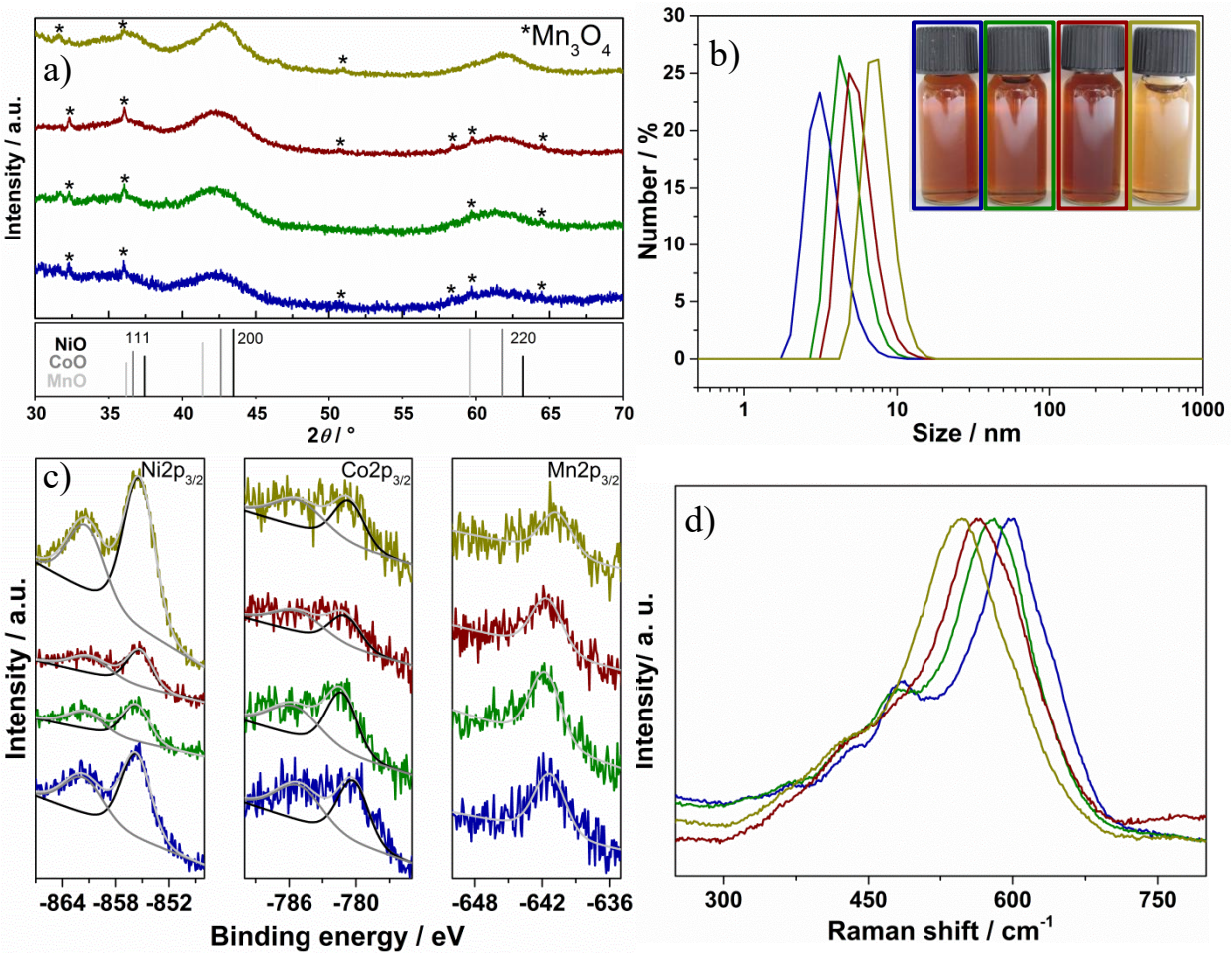

Figure 6.2: For all graphs the different pre-NCM materials are assigned the same color: pre-NCM333 (blue), pre-NCM523 (green), pre-NCM613 (red) and pre-NCM811 (dark yellow): (a) XRD pattern of washed pre-NCM nanocrystals in comparison to ICDD card 00-001-1239 (NiO), ICDD card 00-001-1227 (CoO) and ICDD card 00-003-1145 (MnO). Impurities of Mn_3O_4 (ICDD card 00-001-1127) are indicated with stars. Fluorescence arising from measuring Co-containing samples with Cu$K_{\alpha 1}$-radiation causes the background in the X-ray diffractogram. (b) DLS measurements of diluted dispersions in ethanol of the various pre-NCM. The insets show pictures of the respective dispersions at higher concentration. (c) XPS spectra of the Ni $2p_{3/2}$, Co $2p_{3/2}$ and Mn $2p_{3/2}$ peaks of the washed pre-NCM nanoparticles. (d) Raman spectra of pre-NCM nanoparticles.

The phase purity of the obtained particles was characterized using Raman spectroscopy (Figure 6.2d), as well. For the pure binary metal oxides NiO, CoO and MnO crystallizing in the rock-salt

structure only weak Raman scattering can be expected due to the high symmetry of their unit cells.[59, 60] Surprisingly, the Raman spectra of all washed pre-NCM particles demonstrate strong and distinct signals. The presence of such signals can be explained only by formation of mixed Ni-Co-Mn compounds in which the symmetry is broken by the different neighboring transition metals.[61] This assumption is further supported by the position of the most pronounced peak. In the literature this peak is referred to as a first order one phonon (1P) longitudinal optical (LO) mode and is found to locate between 560 cm^{-1} and 570 cm^{-1} for NiO,[53, 61, 62], 530-560 cm^{-1} for CoO[13, 59] and around 530-540 cm^{-1} for MnO.[60, 63] For the pre-NCM333 the 1P LO mode is strongly red-shifted to 599 cm^{-1}, followed by 581 cm^{-1} for pre-NCM523, 563 cm^{-1} for pre-NCM613 and 547 cm^{-1} for pre-NCM811. It is known that the peak position can be significantly shifted by doping or substitution and is not just a superposition of the peaks in a pure physical mixture.[47, 64] Moreover, the first order 1P transversal optical (TO) mode of NiO can be seen for all compositions in the region from 430 cm^{-1} for pre-NCM811 to 441 cm^{-1} for pre-NCM333.[60] We assume that the signals located around 480 cm^{-1} and only distinctly visible for pre-NCM333 and pre-NCM523 correspond to the 1P TO mode of CoO[59] and the signals around 370 cm^{-1} are assigned to the 1P TO mode of MnO.[60] Therefore, the results of the Raman spectroscopy confirm the formation of a chemical mixture of the three transition metals and lithium within the single nanoparticles.

The mean size of the crystalline domains of pre-NCM particles corresponds to 1-2 nm as estimated from the broadening of the most pronounced (200) reflection in the XRD using the Scherrer equation. The same particle size was also determined also by using dynamic light scattering (DLS) on dispersions of the different pre-NCM materials (Figure 6.2b, inset). In order to obtain a homogenous dispersion the particles were dissolved in ethanol and acetic acid. The latter is necessary to enhance the electrostatic repulsion of the individual particles. Interestingly, to stabilize these nanoparticles we needed the double amount of acetic acid in comparison to pure $Li_{0.15}Co_{0.85}O$ reported previously.[13] Additionally, for pre-NCM811 we even needed four times the amount of acetic acid in comparison to the nickel-free oxide. This leads to the assumption that the nickel content influences the point of zero charge of the particles. With higher nickel amount more acetic acid is needed to disperse the nanoparticles. The DLS data (Figure 6.2b) further confirm the higher tendency for agglomeration with increasing nickel content, as the hydrodynamic diameter rises. Pre-NCM333 shows, for example, a nanocrystal size in ethanol of

2-4 nm which is in accordance with the XRD-derived size. However, pre-NCM811 exhibits a size of 6-10 nm and this indicates a slight agglomeration of a few nanoparticles. Size analysis in scanning transmission electron microscopy (STEM) further confirms a size of 2-3 nm for all pre-NCM nanoparticles (Figure S 6.2 in supporting information).

The morphology of the washed pre-NCM nanoparticles was investigated using STEM (Figure 6.3). The electron diffraction patterns of all pre-NCM (insets in Figure 6.3b, d, f and h) can be indexed to the (111), (200) and (220) reflections typical for the cubic rock-salt structure.

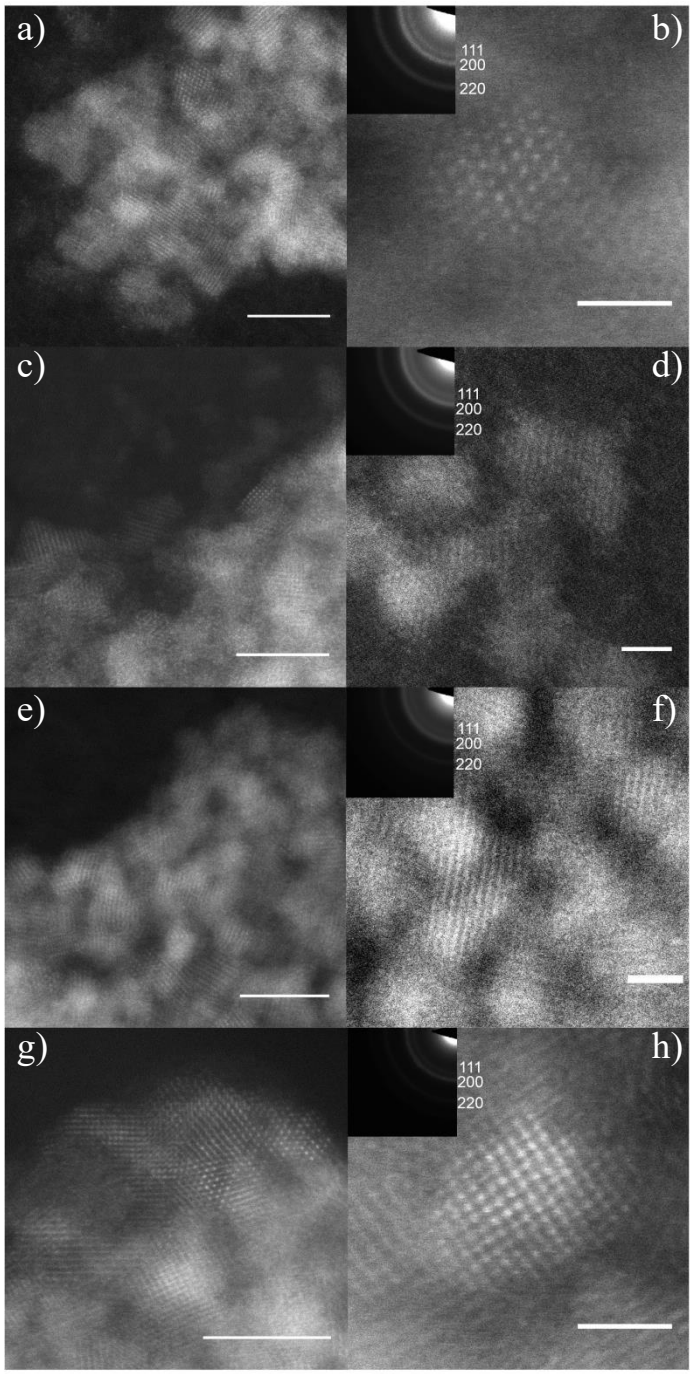

Figure 6.3: **STEM images of pre-NCM333 (a, b), pre-NCM523 (c, d), pre-NCM613 (e, f) and pre-NCM811 (g, h). Overview images with a scale bar of 5 nm (a, c, e, g) and single particles in detail with scale bar of 1.5 nm and the indicated electron diffraction pattern of the respective materials as insets (b, d, f, h).**

In order to further confirm the results gathered from XPS and ICP-OES analysis, the composition of the different washed pre-NCMs was determined by energy-dispersive X-ray spectroscopy (EDX) measurements, which were performed during STEM. Furthermore, the uniformity of the metal distribution in the particles was exemplarily investigated in case of the pre-NCM523 using

EDX and electron energy loss spectroscopy (EELS) in the STEM. While EDX was performed on areas larger than 100 nm x 100 nm, providing information about the average chemical composition, EELS can be measured on very small areas down to single nanoparticles. In Figure 6.4c, different element maps of Ni (Figure 6.4d), Co (Figure 6.4e) and Mn (Figure 6.4f) derived from EDX measurements are combined. It can be seen that for a major part of the sample all elements are equally distributed and the transition metal stoichiometry of pre-NCM523 agrees well with that determined by other methods. It should be noted that although the element distribution is predominantly homogeneous throughout the whole of the samples, small regions with inhomogeneous elemental distribution have been observed as well. In Figure S 6.3b in the supporting information, distinct bluish areas for Mn-rich parts, greenish areas for Co-rich parts and reddish areas for Ni-rich parts can be observed.

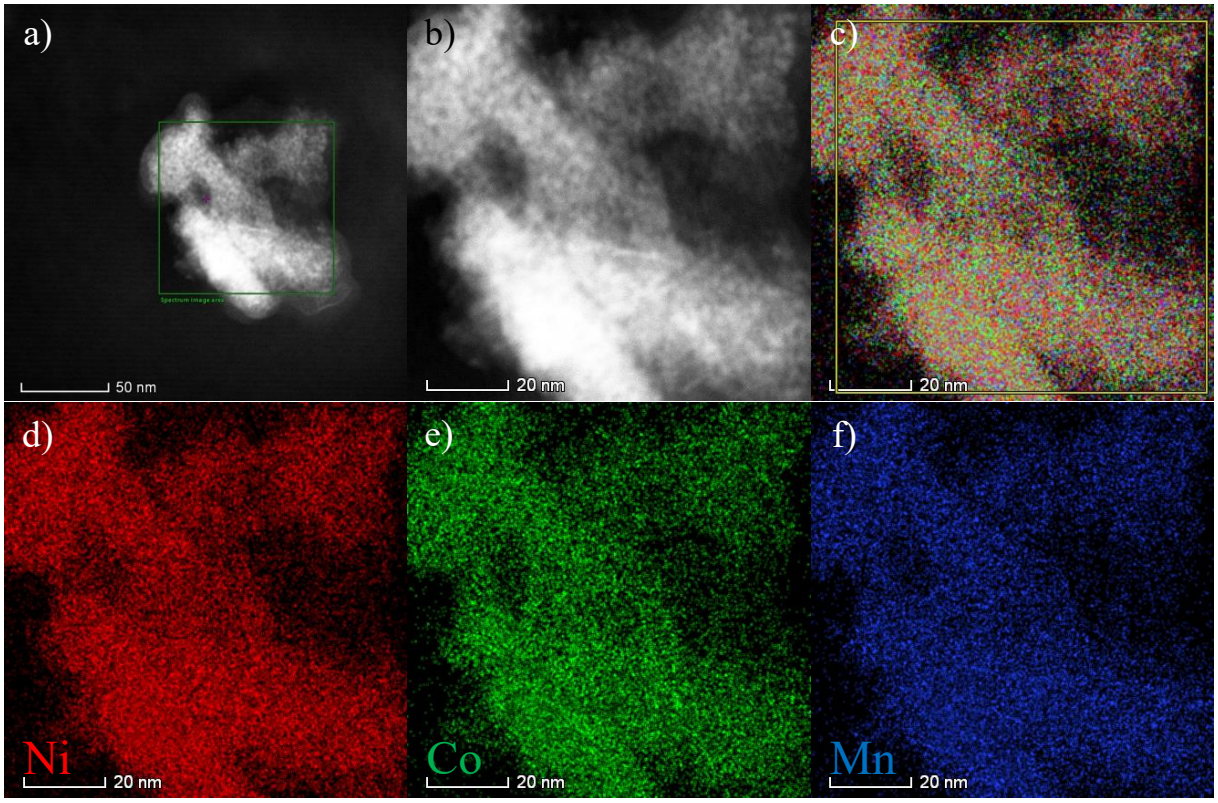

Figure 6.4: STEM image of pre-NCM523 nanoparticles (a) including the selected area for the EDX acquisition (b). (c) Overlay of the detected Ni (d), Co (e) and Mn (f) EDX maps.

EELS analysis of selected single nanoparticles confirms that the transition metal stoichiometry in each nanoparticle perfectly agrees with the average composition determined by ICP-OES, XPS and EDX. We have, however, observed minor variations in composition for individual

nanoparticles. Thus, for six particles studied the Ni:Co:Mn ratio varies from 0.64:0.24:0.12 to 0.47:0.21:0.32, which is very close to the expected composition within the measurement error of EELS.

The results of different characterization methods confirm that the solvothermal synthesis in *tert*-butanol leads to the formation of very small pre-NCM nanoparticles, whose composition can be described as a solid solution of NiO, CoO and MnO crystallizing in a rock salt structure with a homogeneous distribution of transition metal ions. Unfortunately, the accurate determination of the Li content within each nanoparticle remains challenging as none of the used methods enable an accurate determination of the Li content within the extremely high spatial resolution of only 1-2 nm. Quantification of Li with EELS is hardly possible as the $M_{2,3}$ edges of Ni, Co and Mn are in the same region as the K edge of Li.[65] Therefore, we can only determine an average Li content based on the results of ICP-OES analysis.

As mentioned above, one possible application of dispersible pre-NCM nanoparticles is their use as building blocks for nanostructured NCM cathode materials with tunable nanomorphologies for high power applications. As a suitable template for the nanostructure assembly we have tested nanocrystalline cellulose (NCC), a biogenic template that can be easily extracted from natural sources such as bacteria or cotton plants.[66, 67] Besides being environmentally benign, the attractive features of NCC are its rod-like anisotropic shape (5-10 nm width and 100-300 nm length for cotton NCC) and the shape persistence, enabling the synthesis of different metal oxide motifs with a unique anisotropic nanomorphology.[67-72]

For the fabrication of electrochemically active nanostructured NCM, the as-prepared reaction product containing pre-NCM nanoparticles as well as non-reacted lithium compounds was filtered to remove remaining large aggregates, then diluted with water and finally mixed with a stock dispersion of the nanocellulose. The presence of an extra Li source is necessary to reach the right stoichiometry, as the amount of Li in pre-NCM nanoparticles is not sufficient for the formation of targeted NCM phase. The weight ratio between the nanocellulose and the pre-NCM particles was taken as 1:1 and the overall nanocellulose concentration in the coating dispersion was adjusted to be 0.8 wt%. The mixture was drop-cast on a glass substrate, dried at room temperature and calcined at 560 °C for 5 h. XRD patterns of the obtained products demonstrate that the calcination of cubic pre-NCM333 nanoparticles in the presence of nanocellulose results

in the formation of hexagonal layered NCM333 (ICDD card 01-077-9286) crystallizing in the α-$NaFeO_2$ structure with space group R-3m (Figure 6.5a). Similar XRD patterns were also obtained also for other pre-NCM compositions. While the 003 reflection remains at the same position for all NCM compositions indicating that the layers of the hexagonal lattice have the same distance, the 104 reflection shifts to lower °2θ values for higher nickel content. One explanation for this could be that for higher Ni content more of the large Ni^{2+}-ions have to be incorporated into the crystal lattice of the α-$NaFeO_2$ structure, which leads to an expansion of the lattice and hence in a shift to lower angles. Additionally, the 104 reflections of NCM333 and NCM523 seem to consist of two superimposed reflections of two structurally equivalent materials with different compositions, which will be discussed later in the context of the results obtained by EDX. The nanoparticle size can be calculated by using the Scherrer equation for the broadening of the 003 reflection. The result shows that with increasing Ni content the width of the nanoparticles decreases from 19 nm for NCM333 over 16 nm for NCM523 and 11 nm NCM613 to 10 nm for NCM811.

ICP-OES analysis of different NCM compositions confirms that the stoichiometry of transition metal ions in the calcined samples is practically the same as in the pre-NCM nanoparticles, however, the total amount of lithium slightly decreases from 5% overstoichiometry to a nearly stoichiometric amount. Based on the results of ICP-OES analysis, the compositions of $LiNi_{0.33}Co_{0.33}Mn_{0.33}O_2$ (NCM333), $LiNi_{0.50}Co_{0.20}Mn_{0.30}O_2$ (NCM523), $LiNi_{0.60}Co_{0.10}Mn_{0.30}O_2$ (NCM613) and $LiNi_{0.50}Co_{0.20}Mn_{0.30}O_2$ (NCM523) for hexagonal NCM materials were obtained.

To unravel the nature of the individual transition metals in each compound XPS was used. For Ni, Co and Mn, their $2p_{3/2}$ peak (Figure 6.5b) was fitted with the corresponding reference spectra according to Biesinger *et al.*[58] Ni was fitted with $Ni(OH)_2$ due to the surface adhering OH groups, Co with CoOOH, and Mn with MnO_2. This means that for all different NCM compositions we found the same oxidation state (Ni^{2+}, Co^{3+}, Mn^{4+}) for each individual transition metal. Quantification with XPS confirmed the results already obtained with ICP-OES for the NCM compositions.

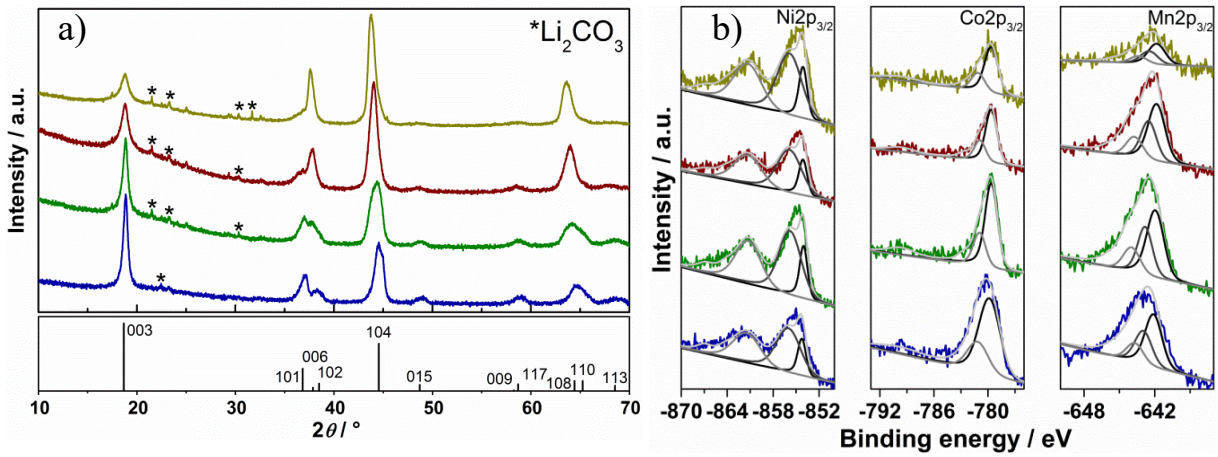

Figure 6.5: For all graphs the different NCM material are assigned the same color: NCM333 (blue), NCM523 (green), NCM613 (red) and NCM811 (dark yellow): (a) XRD of NCM nanocrystals in comparison of ICDD card 01-077-9286 of $LiNi_{0.33}Co_{0.33}Mn_{0.33}O_2$ (NCM333). Impurities of Li_2CO_3 (ICDD card 00-009-0359) are indicated with stars. (b) XPS of the Ni $2p_{3/2}$, Co $2p_{3/2}$ and Mn $2p_{3/2}$ peaks on the NCM nanoparticles.

Scanning electron microscopy (SEM) images (Figure 6.6) demonstrate for each composition that the calcination of the self-assembly product of pre-NCM and nanocellulose results in the formation of an anisotropic desert-rose structure with intergrown walls perpendicular to the surface. In contrast to that, only dense nonporous material was obtained without using the nanocellulose as a template (Figure S 6.4 in supporting information). Using nitrogen sorption experiments (Figure S 6.5 in supporting information) the BET-surfaces of the different structures can be determined. For the NCM333, NCM523, NCM613 and NCM811 samples, surface areas of 10 $m^2 g^{-1}$, 11 $m^2 g^{-1}$, 15 $m^2 g^{-1}$ and 13 $m^2 g^{-1}$, respectively, were obtained. All BET surfaces are in the same range and small enough to not promote unfavorable side reactions as cathode material in LIBs. Furthermore, the pore size distributions (PSDs) derived from the individual isotherms by DFT calculations (Figure S 6.5, insets) show a broad range of porosity for all NCM materials, from microporosity, due to textural porosity produced by agglomeration of the ultrasmall nanoparticles, to NCC induced meso- and macroporosity.

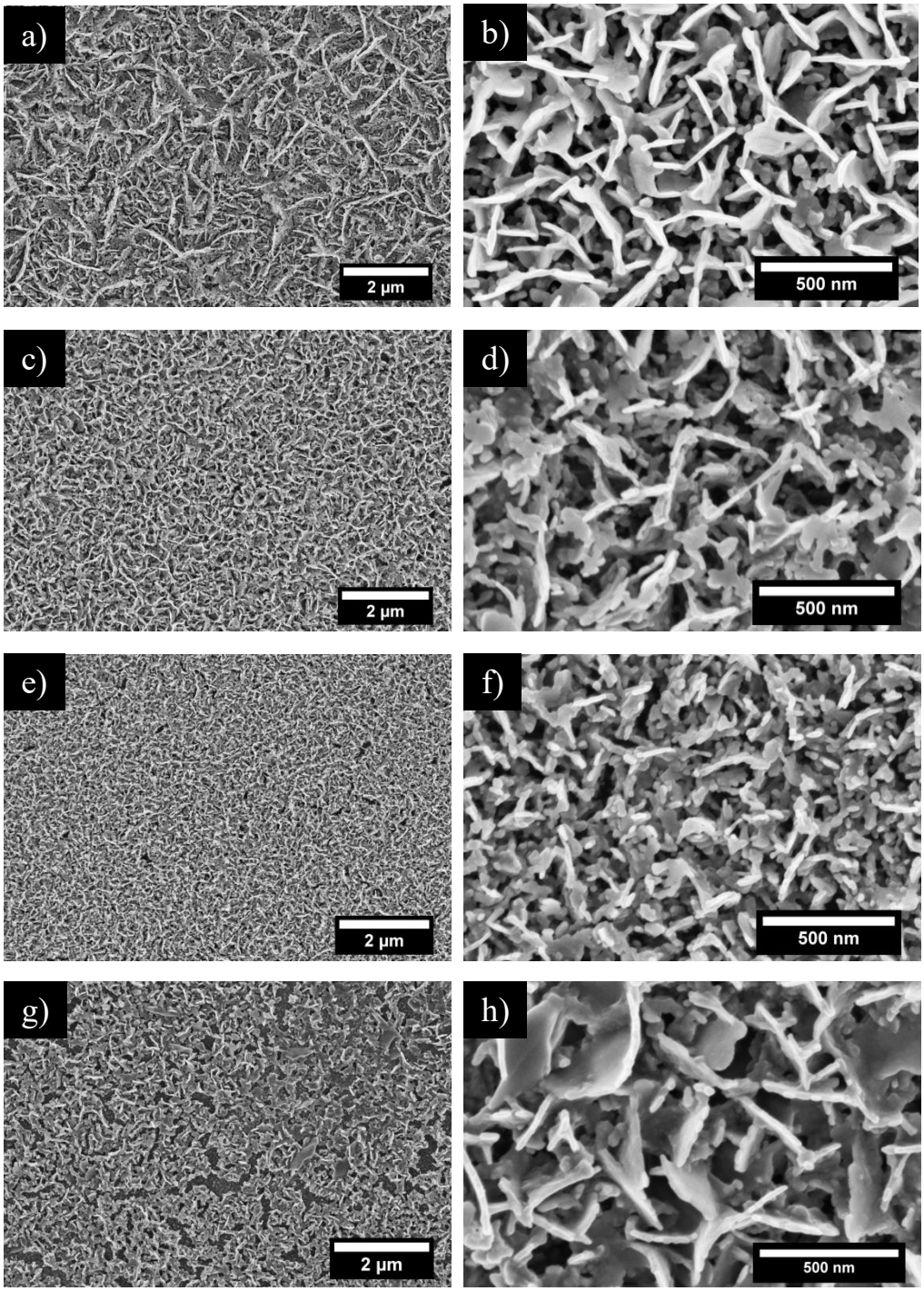

Figure 6.6: SEM micrographs of NCC-nanostructured NCM333 (a, b), NCM523 (c, d), NCM613 (e, f) and NCM811 (g, h) all exhibiting a desert-rose morphology. Overview images in low magnification (a, c, e, g) are shown in comparison to high-magnification micrographs (b, d, f, h).

EDX analysis of different elements in SEM (Figure S 6.6, Figure S 6.7, Figure S 6.8, Figure S 6.9) reveal that the transition metal ions are uniformly distributed over large areas in a stoichiometry expected for the respective NCM materials within the error bar of EDX.

To investigate the structure and composition of each single nanoparticle, STEM measurements were performed. On the STEM micrographs of larger areas (Figure 6.7a, c, e, g) and of single nanoparticles (Figure 6.7b, d, f, h) for all compositions the fine structure of the desert-rose morphology can be clearly seen and the diffraction patterns (insets in Figure 6.7b, d, f, h) of the respective areas prove that they are crystallized in the layered α-$NaFeO_2$ structure. For NCM333 and NCM523, however, square-like nanoplatelets (Figure S 6.10) have also been observed in addition to the already mentioned rod-like morphology. Increasing Ni content generally leads to a smaller particle size (Figure S 6.11). Thus, for NCM333 nanorods the average width and length is around 20 nm and 160 nm, respectively, for NCM523 12 nm x 110 nm, for NCM613 13 nm x 60 nm and for NCM811 10 nm x 55 nm, respectively. The width of the nanorods is in a good approximation comparable to the sizes already derived from the XRD patterns. Compared to this, we found sizes for the nanoplatelets of 28 nm for NCM333 and 22 nm for NCM523 (Figure S 6.12). Furthermore, the elemental compositions of the different morphologies were measured using EDX in the STEM. While the nanorods were the only type of crystals found in NCM613 and NCM811 and while they showed the expected molar ratios between the different transition metals, for NCM333 and NCM523 the composition varied drastically between the two morphologies. While the nanoplatelet structures almost exhibited the estimated composition with around $LiNi_{0.25}Co_{0.40}Mn_{0.35}O_2$ for NCM333 and $LiNi_{0.48}Co_{0.22}Mn_{0.30}O_2$ for NCM523, the rod-like nanoparticles showed a lack of Ni lack and an excess of Co. The NCM333 nanorods consisted in average of $LiNi_{0.13}Co_{0.60}Mn_{0.27}O_2$ and the one of NCM523 of $LiNi_{0.15}Co_{0.48}Mn_{0.37}O_2$.

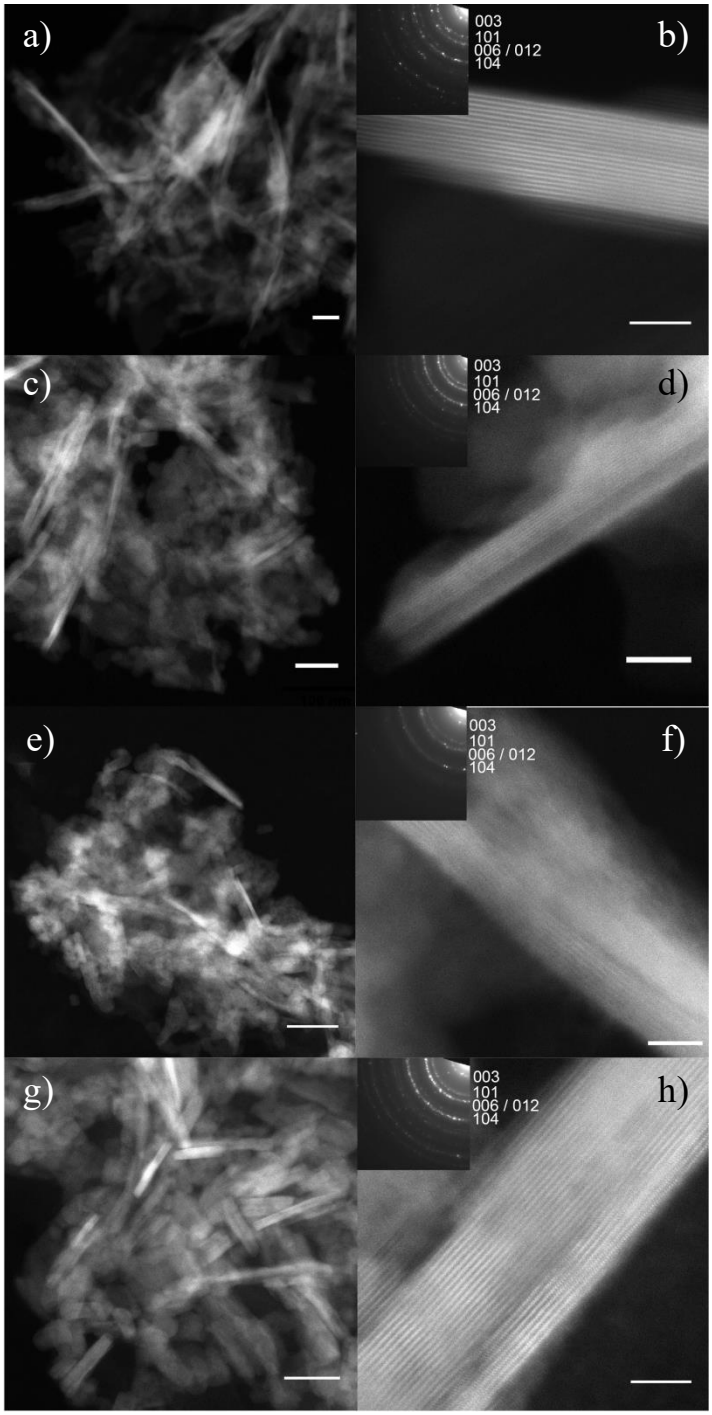

Figure 6.7: STEM images of NCM333 (a, b), NCM523 (c, d), NCM613 (e, f) and NCM811 (g, h). Overview images of desert-rose agglomerates with a scale bar of 50 nm (a, c, e, g) and single rod-like nanoparticles in detail with scale bar of 5 nm, and the indicated electron diffraction pattern of the respective materials as insets (b, d, f, h).

In order to complete the full characterization of the NCM materials, ^{7}Li magic angle spinning nuclear magnetic resonance spectroscopy (MAS-NMR) was performed (Figure S 6.13). All spectra of the NCMs show an unusually broad signal splitting of about 1400ppm. The coupling of the unpaired electrons of Mn^{4+} and Ni^{2+} with Li^{+} leads to the exceptionally broad spectrum.

Moreover, Raman spectroscopy was also performed on the material (Figure S 6.14) and compared with the literature values for the Raman shifts of $LiNiO_2$,[73] $LiCoO_2$[74] and $LiMnO_2$.[75] Hereby, in a first approximation we assume that the Raman signal for the NCMs may derive from the superposition of the pure phases $LiNiO_2$, $LiCoO_2$ and $LiMnO_2$. Therefore, we deal with in total two peaks, the A_{1g} and E_g for the rhombohedral $LiNiO_2$ and $LiCoO_2$ and three signals, two A_g modes and one B_g mode, for the monoclinic layered $LiMnO_2$.[73-76] While the E_g band is not clearly visible as it overlaps with the A_{1g} peak, the latter can be determined for all NCMs. For NCM333 the peak is at 588 cm^{-1} and slightly decreases to 553 cm^{-1} with rising Ni content since the A_{1g} peak appears at 544 cm^{-1} for pure $LiNiO_2$.[73] Furthermore, for moderate Mn content, for NCM333, NCM523 and NCM613, the A_g mode is also visible at around 420 cm^{-1} as described in the literature.[75]

In order to get insight into the phase transformation of pre-NCM nanoparticles to layered NCM in the presence of nanocellulose, we performed thermogravimetric analysis (TGA) and differential scanning calorimetry (DSC) analysis of the respective dry pre-NCM/nanocellulose mixtures (Figure S 6.17). The combustion of pure nanocellulose is completed at temperatures as high as 534 °C (Figure S 6.15 in supporting information). In contrast, it can be seen that the presence of pre-NCM significantly reduces the combustion temperature of the nanocellulose, which is also influenced by the relative fraction of Ni ions in the nanoparticles.

Thus, the NCC is fully combusted already at 420 °C and 490 °C for the pre-NCM811/nanocellulose and the pre-NCM333/nanocellulose, respectively (Figure S 6.17 in supporting information). Interestingly, the transformation of the pre-NCMs to the NCMs is completed much earlier than the full combustion of NCC. The transformation of the Ni-rich phases is completed again at lower temperatures (around 400 °C for pre-NCM811) than for Ni-poor pre-NCM333 (at 475 °C). Comparing the pre-NCM/nanocellulose composite with as-prepared pre-NCM, we can attribute the first major weight loss in the TGA diagrams at around 300 °C (Figure S 6.16) to the oxidation of the pre-NCMs to NCMs, including the accompanying metal migration into the nanoparticles and the combustion of the residual precursor organics. The second large weight loss step at 400-450 °C can be assigned to the total combustion of NCC. Moreover, both processes occur already at lower temperatures compared to the separate processes in pre-NCM and pure NCC.

The addition of extra Li source is necessary to reach the correct stoichiometry and to prevent the pre-NCM nanoparticles to form other phases (see Figure S 6.18 in the supporting information). To illustrate this, after calcination at 560 °C for 5 h we observe the separation of the different transition metals under formation of their most stable oxide phases. Ni^{2+} remains still in NiO, while Co^{2+} is partly oxidized forming Co_3O_4, and Mn^{2+} is fully oxidized, most likely forming $LiMn_2O_4$ or a small amount of MnO_2. To prevent this, in our dispersions we use the as-prepared pre-NCM powders with a slight overstoichiometric Li-content (as confirmed by ICP-OES).

Finally, the electrochemical properties of the NCMs were also investigated. Cyclic voltammograms (CVs) of the cathodes containing the individual nanostructured NCMs (Figure S 6.19a) feature oxidation and the respective reduction peaks at potentials around 3.6 V and 4.0 V typical for the Ni^{2+}/Ni^{4+} redox couple.[17, 77] Furthermore, for all materials the first cycle exhibits a drastically higher current density than for the following cycles due to the formation of the cathodic solid-electrolyte interface (SEI). In contrast to the potential values of the redox peaks which remain practically the same for different NCM cathodes, the current densities differ significantly for different compositions. Thus, the current density of NCM333 is more than five times higher than that of the sample NCM811. The specific capacities obtained by the integration of the corresponding CV peaks also show a strong variation depending on the composition (Figure S 6.19b). Thus, 70 mAh g^{-1} discharge capacity was obtained for NCM333, but only around 15 mAh g^{-1} for NCM811. These values are much lower than the expected values of 150-160 mAh g^{-1} for NCM333,[78] NCM523[79] and 203 mAh g^{-1} for NCM811,[80][81] respectively. In the literature two quality criteria for the NCM materials are currently used. The first is the ratio between the integrated intensities of the 003 to the 104 reflection I_{003}/I_{104} in X-ray diffractograms, which should be around 1.4 for NCM cathode materials with high capacity.[11, 77, 82, 83] Values below 1.4 are interpreted as evidence for cation mixing, namely a displacement, between Ni^{2+} and Li^{+} where the nickel ions occupy sites in the Li^{+}-ion layer. The higher the degree of displacement the weaker the intensity of the 003 reflection while the 104 reflection remains unaffected.[83] The second quality criterion is the so-called R value, the ratio between the integrated intensities of the combined 006 and 102 reflections to the 101 one. This value is a measure for the hexagonal ordering and should be as small as possible.[82, 84] In Table 6.2 both values are given for our NCM materials.

Table 6.2: Comparison of the parameters for cation mixing and hexagonality for all NCMs.

NCM Material	I_{003}/I_{104}	R
NCM333	1.01	0.83
NCM523	0.74	0.80
NCM613	0.65	0.83
NCM811	0.48	1.46

The rather low values for I_{003}/I_{104} and the very high values for R suggest a high degree of cation mixing in our NCM materials, which increases with the increased Ni content. The cation mixing leads to blocking of mobile Li^+-ions that cannot further participate in the lithium extraction/insertion. This conclusion is further confirmed by galvanostatic measurements at different current densities (Figure 6.8a) and long-time measurements at high current densities (Figure 6.8b). Both measurements show capacities far below expected values for all NCM materials. It is obvious that the lower the ratio between I_{003}/I_{104}, the lower the discharge capacities, which strongly suggests that most of the lithium is blocked by cation mixing. It appears that the synthesis procedure using an intermediate step of cubic rock-salt type pre-NCM favors the cation mixing, as all the metal ions are already equally distributed within the rock-salt lattice. With this in mind a synthesis *via* hexagonal layered transition metal hydroxides with lithium precursor might be more appropriate route to avoid the cation mixing.[77]

However, even in spite of the unfavorable cation mixing, the obtained NCM nanostructures exhibit very good capacity retention and cycling stability even at extremely high charging and discharging current densities of 5600 mA g^{-1} and 8400 mA g^{-1}. For NCM333 at a charge/discharge current density of 140 mA g^{-1} (corresponding to 1C, which means the charge/discharge of the full capacity within one hour) only half of the expected capacity is reached with 72 mAh g^{-1}. Nevertheless, with current densities of 5600 mA g^{-1} (40C, charge/discharge process of 90 s) and 8400 mA g^{-1} (60C, charge/discharge process of 60 s) 37 mAh g^{-1} and 31 mAh g^{-1}, respectively, can still be achieved. These values are still around 25% and 20%, respectively, of the theoretical expected specific capacity for NCM333. With rising nickel content, we expect an increase in overall theoretical capacity, but here we observe capacity values much lower than those for NCM333.

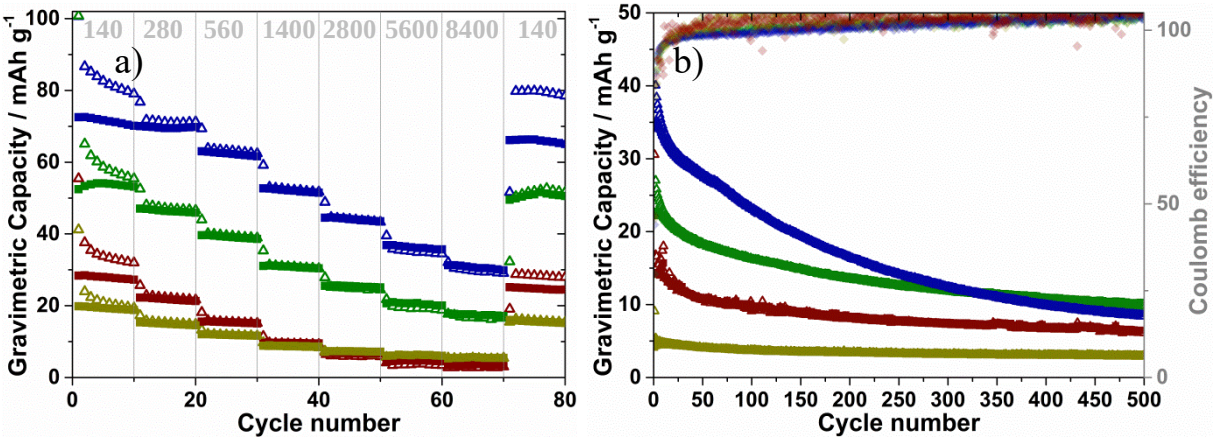

Figure 6.8: Electrochemical Li insertion/extraction with NCC-nanostructured NCM333 (blue), NCM523 (green), NCM613 (red) and NCM811 (dark yellow): Rate capabilities at different current densities (140, 280, 560, 1400, 2800, 5600 and 8400 mA g^{-1}) with ten cycles each (a) and long term cyclic performance at 1400 mA g^{-1} showing gravimetric capacity on the left (same symbols as in (a))and Coulomb efficiency (diamond symbols with the same color codes as in (a)) on the right y-axis (b). Open triangular symbols: Li extraction (charging), full square-like symbols: Li insertion (discharging).

6.4 Conclusion

We performed solvothermal reactions of $Ni(OAc)_2$, $Co(OAc)_2$ and $Mn(acac)_2$ in different stoichiometries together with LiO*i*Pr in *tert*-butanol in order to obtain four different compositions of the pseudo-quaternary phase of $Li_wNi_xCo_yMn_zO$ (pre-NCM). The Li content was varying between 20-30at% within the four different crystalline materials, all adopting the cubic rock-salt structure. Here, we describe for the first time the formation of all four pseudo-quaternary phases and were further able to synthesize them as ultrasmall dispersible nanoparticles in the size range of 1-4 nm and at very low temperatures such as 170 °C in a solvothermal environment. These different pre-NCM nanoparticles can be completely transformed into the respective NCM nanoparticles with fixed transition metal ratio by addition of a slightly overstoichiometric amount of lithium precursor at the rather low temperature of 560 °C. Moreover, we were able to obtain NCMs with a desert-rose type interconnected nanoparticle morphology by nanocellulose-mediated calcination of the pre-NCM nanocrystals. The size and the morphology of the NCM nanoparticles strongly depend on the nickel content. The higher the nickel content the smaller and less elongated are the resulting NCM nanoparticles. Furthermore, with rising nickel content an increased mixing of the cations within the NCM phase is observed. This leads to poor capacity retention of the NCMs, especially for NCM631 and NCM811. Nevertheless, in high rate performance tests at charge/discharge times of only 90 s (40C) or 60 s (60C) 25% and 20% of the theoretical capacity of NCM333 can preserved, respectively.

6.5 Experimental

Syntheses of $Li_wNi_xCo_yMn_zO$ (pre-NCM) nanoparticles: Pure cobalt(II) acetate tetrahydrate ($Co(OAc)_2$) was purchased from AppliChem, nickel(II) acetate tetrahydrate ($Ni(OAc)_2$), 98% purity) and pure manganese(II) acetylacetonate ($Mn(acac)_2$) both from Aldrich, pure lithium *iso*-propoxide (LiO*i*Pr) from Acros Organics and *tert*-butanol from VWR Chemicals (100% purity). All chemicals were used as received.

For the syntheses of the pre-NCM nanoparticles with the different compositions, typically 1.47 mmol (97.1 mg) of LiO*i*Pr was mixed with a total of 1.40 mmol of the transition metal compounds with ratios according to the desired final composition of NCM. Hereby, in all formulations LiO*i*Pr is added at 5% in excess to the necessary stoichiometric amount. For example, for NCM811 279.0 mg (1.12 mmol) of $Ni(OAc)_2$, 35.4 mg (0.14 mmol) of $Co(OAc)_2$ and 34.8 mg (0.14 mmol) of $Mn(acac)_2$ are weighed in together with the LiO*i*Pr. All metal salts were then dispersed in 180 mL *tert*-butanol in a Parr Instruments 300 mL General Purpose & High Temperature Pressure Vessel steel autoclave with internal temperature and pressure sensor. The sealed autoclave was heated at 10 °C min^{-1} to 165 °C and kept there for 17 h. During this time, the reaction dispersion was stirred at 1000 rpm. After cooling down to room temperature with an approximately cooling rate of 2 °C min^{-1}, the different pre-NCM nanoparticles were collected by simply drying the processed dispersion at 70 °C. For the preparation of stock dispersions of the pre-NCM nanoparticles, 100 mg of the as-prepared and dried solid was wetted with 200 mg, for pre-NCM811 with 400 mg acetic acid. Afterwards, 4 mL ethanol was added to all dispersions, which were then stirred for two days. Afterwards, remaining agglomerates were removed by filtration with a 220 nm syringe filter (Sartorius minisart cellulose acetate membrane) For DLS measurements, the dispersions were diluted at a ratio of 1:50 with ethanol.

For TEM measurements, the as-prepared pre-NCM solids were washed with ethanol, subsequently centrifuged for 15 min at 50000 rcf (relative centrifugal force) and the supernatant solutions removed. The remaining powders were again dried at 70 °C in air.

Extraction of cellulose nanocrystals: For the extraction of nanocrystalline cellulose, cotton linters CP20 (Peter Temming AG) were hydrolyzed in concentrated sulfuric acid.[85] The linters were washed with water and dried at 60 °C. 1 mL of 64% H_2SO_4 was added to 8.75 g cellulose fibers, letting the linters soak in the acid for 25 min at room temperature. Thereafter, the mixture was

heated to 55 °C for 45 min under vigorous stirring. Hereby, large cellulose aggregates dissolved. Afterwards, the suspension was diluted with 10 times the volume of deionized water and kept in this stage overnight. The formed supernatant was decanted and the NCC-rich phase on the bottom was washed three times with water and subsequent centrifugation at 50000 rcf for 15 min. The last centrifugation step was performed at 70 rcf for 10 min to remove sedimented cellulose aggregates and to collect the NCC dispersion. In the end, the dispersion was concentrated in a rotary evaporator to a stock solution with 6.2wt% NCC at pH 2.55.[69]

Fabrication of NCC-templated NCMs: For the preparation of NCC-templated NCM material, 1 mL of the filtered pre-NCM dispersion was diluted with 1.697 mL deionized water and mixed with 0.403 mL of the NCC stock solution under vigorous stirring for 5 min. 1.25 mL of the resulting suspension with an NCC content of 0.8wt% was drop-cast on a 6 cm x 6 cm fluorine doped tin oxide (FTO) glass substrate, dried at 60 °C in an oven and afterwards heated up to 560 °C with a 3 °C min^{-1} heating rate. The dwell time of the calcination under air was 5 h and the FTO glass substrates were immediately cooled down to room temperature on a stainless-steel rack. The NCC nanostructured NCM was scratched off the FTO glass using stainless-steel razor blades and used for further characterization and processing.

NCM compound electrode preparation: NCC nanostructured NCM powders were mixed together with carbon black Super C65 (TIMCAL) and poly(vinylidene fluoride) (PVdF) from Aldrich a ratio of 80:10:10, respectively. 1-methyl-2-pyrrolidinone (Sigma-Aldrich, 99% purity) was added the ratio of 3.7 µL : 1 mg of the composite mixture. The inks were all stirred overnight, vortexed thoroughly for 10 min (Vortex Mixer ZX3 of fisherbrand) and treated for 30 min with an ultrasonic horn (Sonopuls GM 4100 of Bandelin) at half power. Wet films of the ink with a thickness of 100 µm were coated on aluminum foil with an automatic film applicator coater ZAA 2300 from Zehntner with a coating speed of 7 mm s^{-1} and dried afterwards at 60 °C for 3 h. Circular electrodes of 18 mm in diameter were punched out and then dried at 120 °C for 5 h under vacuum. The average active mass loading was 0.5 mg cm^{-2}.

Materials characterization: Wide angle X-ray diffraction analysis of the powders was performed in transmission mode (Debye-Scherrer geometry) using a STOE STADI P diffractometer with a Ge single crystal monochromator for Cu-$K_{\alpha 1}$ (λ = 1.54060 Å) equipped with a DECTRIS solid state strip detector MYTHEN 1K.

Raman spectra were acquired with a Jobin Yvon Horiba HR800 UV Raman microscope (OLYMPUS BX41) using a HeNe laser (632.8 nm) and a SYMPHONY CCD detection system. Spectra were recorded using a lens with a 10-fold magnification. The power of the laser beam was normally adjusted to about 8.5 mW.

Scanning electron microscopy (SEM) was carried out on a JEOL JSM-6500F scanning electron microscope equipped with a field emission gun operating at 5 kV an FEI Helios NanoLab G3 UC scanning electron microscope equipped with a field emission gun usually operated at 3 kV. The films were prepared on FTO glass substrates and glued onto a brass sample holder with silver lacquer.

(S)TEM analysis was carried out on an FEI Titan Themis 300 instrument equipped with a field emission gun operating at 300 kV, a high angle annular dark field (HAADF) detector, an EDAX energy-dispersive X-ray spectrometer and a Gatan EELS spectrometer. Pure washed pre-NCM nanoparticles were drop-coated from strongly diluted dispersions on a copper grid with a holey carbon film and plasma cleaned for 9 s at 50 mW to remove contaminations. NCM materials were scratched off the FTO substrate, wetted with ethanol and deposited on the same type of copper grid. Here, the samples were plasma cleaned in the same way.

Dynamic light scattering (DLS) of the pre-NCM nanoparticles was performed using a Malvern Zetasizer-Nano with a 4 mW He-Ne laser (633 nm) and an avalanche photodiode detector. The scattering data were evaluated based on particle number.

Thermogravimetric analysis (TGA) and differential scanning calorimetry (DSC) was carried out with a NETZSCH STA 440 C TG/DSC instrument (heating rate 10 K min^{-1} in a stream of synthetic air of about 25 mL min^{-1}).

Inductively coupled plasma optical emission spectroscopy was performed on a VARIAN VISTA RL CCD Simultaneous ICP-OES.

XPS analyses of the washed and calcined particles were performed with the non-monochromatized Mg-K_α radiation of a VSW TA10 X-ray source (Mg-K_α = 1253.6 eV) and a VSW HA100 electron analyzer. Fitting of the $Co2p_{3/2}$ peaks was based on a convolution of a Doniach-Šunjić-function and a Gaussian function with a linear background subtraction. To eliminate peak shifts due to charging of the nanoparticles the carbon 1s peak was calibrated to 284.5 eV. Determination of the chemical state of Co, Ni and Mn is based on fit parameters published by Biesinger *et al.*[58]. For the XPS measurements the particles were drop-casted on a gold-coated silicon substrate.

^{7}Li magic angle spinning solid state nuclear magnetic resonance (MAS-NMR) spectra were recorded on a Bruker DSX Avance 500 FT spectrometer with a magnetic field of 11.7 T. The zirconia rotor with an outer diameter of 2.5 mm was spun at a rotation frequency of 12 kHz.

Nitrogen sorption measurements were performed at 77 K with the scratched-off powder of nanostructured $LiCoO_2$ using a QUANTACHROME Autosorb iQ instrument. The powders were degassed at 120 °C for at least 12 h before measurement. The specific surface area was determined with the Brunauer−Emmett−Teller method. The pore size distribution was calculated using a non-local density functional theory (NLDFT) approach for silica cylindrical pores.

Electrochemical Measurements: Electrochemical measurements were performed in an EL-CELL ECC-PAT-Core three-electrode setup using an Autolab potentiostat/galvanostat PGSTAT302N with FRA32M module operating with Nova 1.10.4 software. The NCM compound electrodes were separated from the Li metal foil anode by an insulation sleeve equipped with a WHATMAN glass-fiber separator and a lithium metal reference ring. We used the commercial electrolyte PuriEL 1.15 M $LiPF_6$ in ethylene carbonate (EC)/ethyl-methyl-carbonate (EMC)/dimethylcarbonate (DMC) in a 2:2:6 volume to volume ratio and 1.0wt% fluoroethylene carbonate (FEC) purchased from Soulbrain MI.

Cyclic voltammetry measurements were usually performed between 3 V and 4.3 V vs. Li/Li^+ and with a scan speed of 0.5 mV s^{-1}.

Galvanostatic measurements were performed using off voltages of 3 V and 4.3 V vs. Li/Li^+, respectively. Both charge and discharge steps were performed at the same current density. A potentiostatic step at 4.3 V was performed between the galvanostatic charge and discharge steps until the charge/discharge current density was reached.

6.6 Supporting information

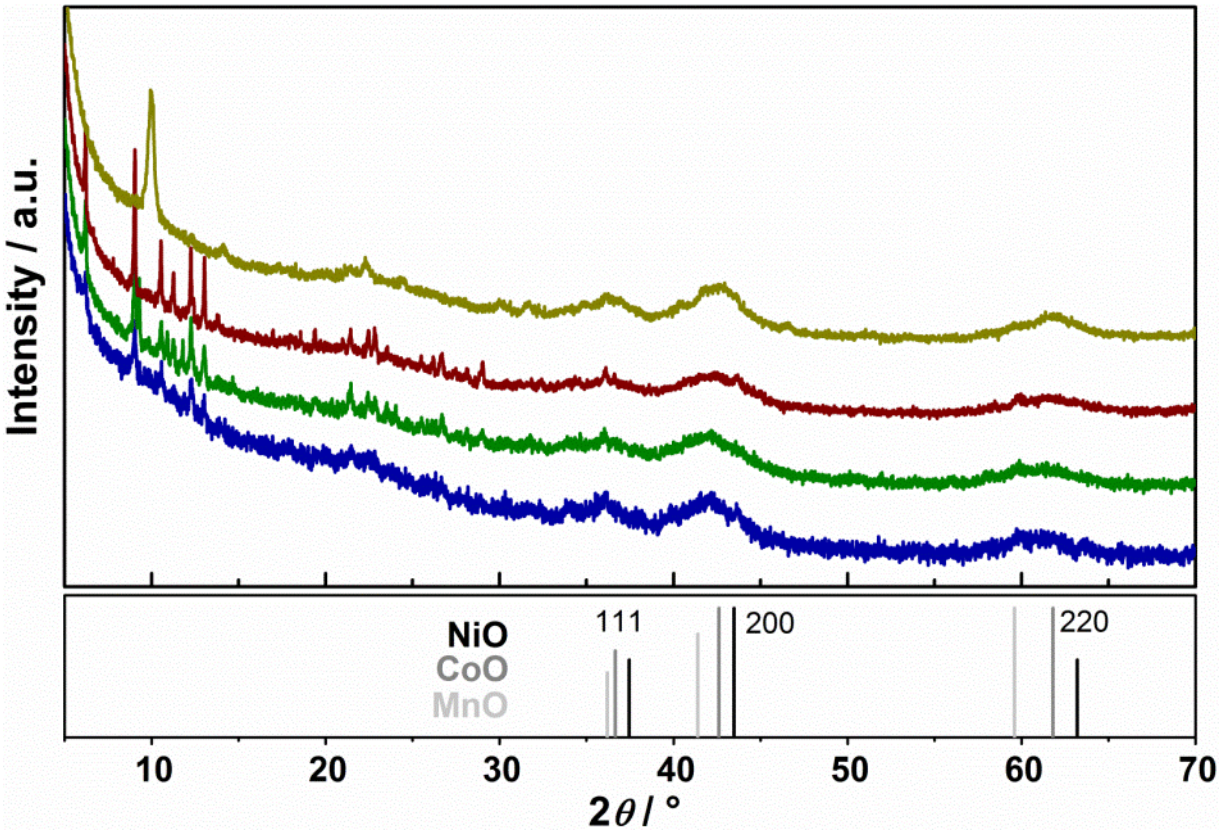

Figure S 6.1: XRDs of the as-prepared powders of pre-NCM333 (blue), pre-NCM523 (green) pre-NCM613(red) and pre-NCM811 (dark yellow) in comparison ICDD card 00-001-1239 of NiO, ICDD card 00-001-1227 of CoO and ICDD card 00-003-1145 of MnO.

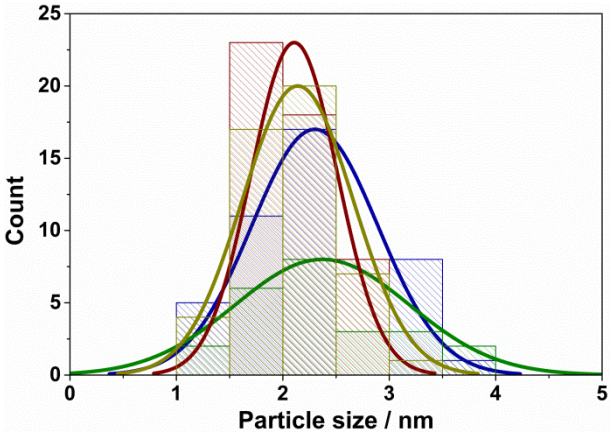

Figure S 6.2: Sizes of pre-NCM333 (blue), pre-NCM523 (green), pre-NCM613 (red) and pre-NCM811 (dark yellow) nanoparticles obtained by measurement of 50 particles each in STEM images. For the size determination of pre-NCM523 (green) 25 particles were measured.

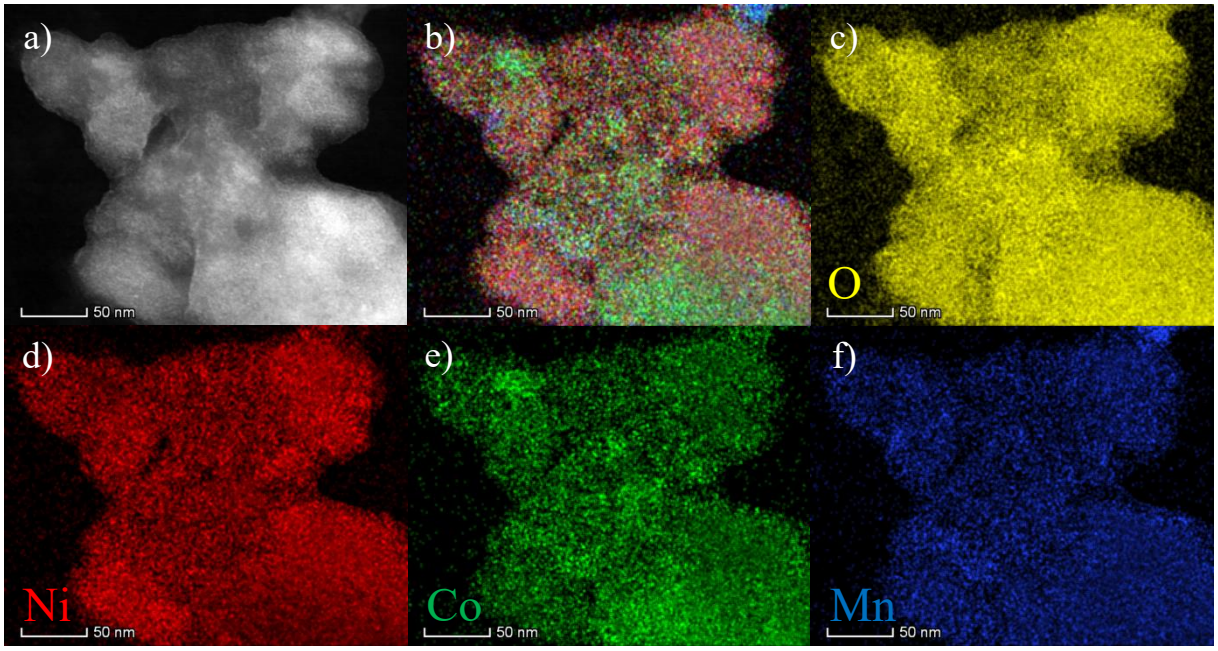

Figure S 6.3: STEM image of pre-NCM523 nanoparticles (a). (b) Overlay of the detected Ni (d), Co (e) and Mn (f) EDX maps. (c) O EDX map.

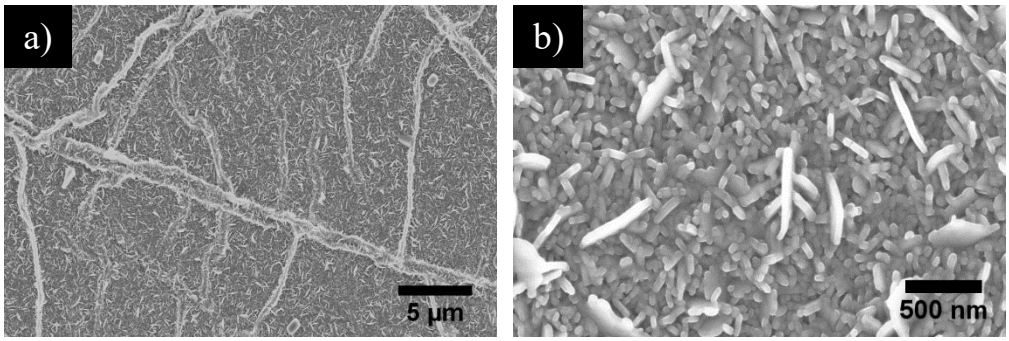

Figure S 6.4: SEM micrographs of pure NCM333 in low magnification (a) and for more details in high-magnification (b).

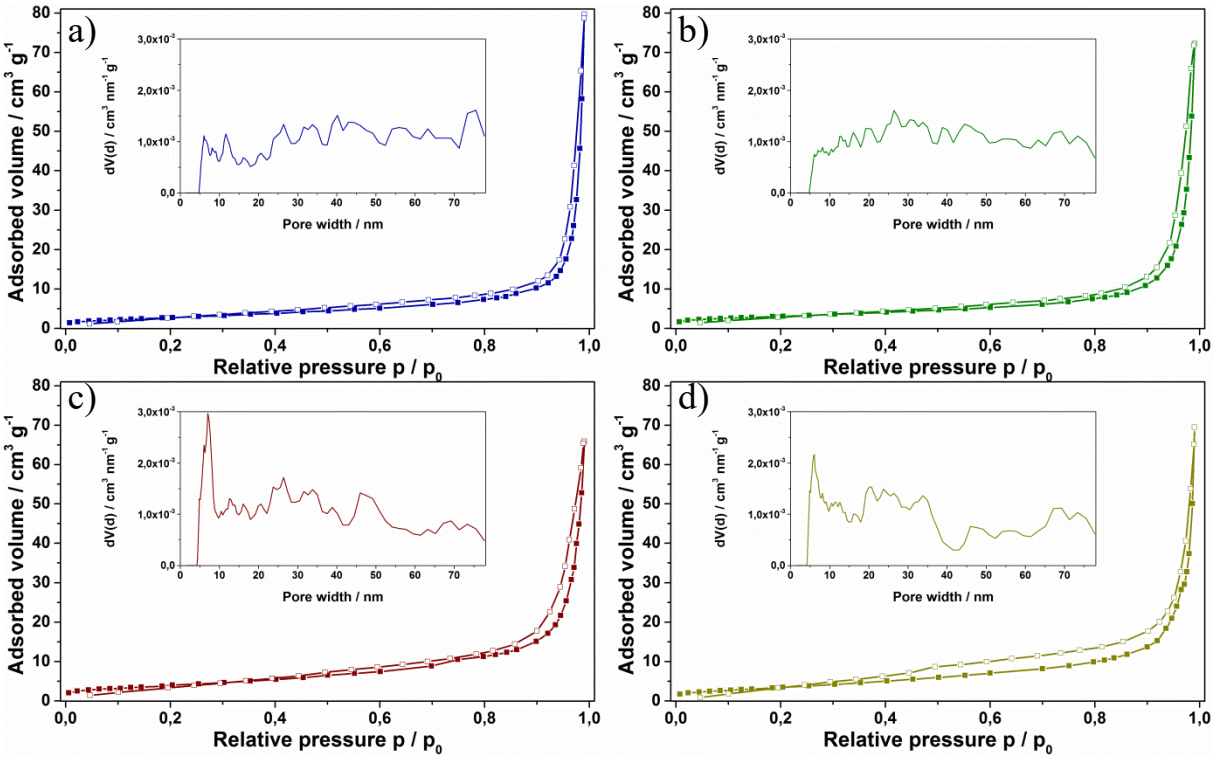

Figure S 6.5: Nitrogen sorption isotherms of NCC-nanostructured NCM333 (a), NCM523 (b), NCM613 (c) and NCM811 (d). Inserted in each is the pore size distribution obtained with the NLDFT method.

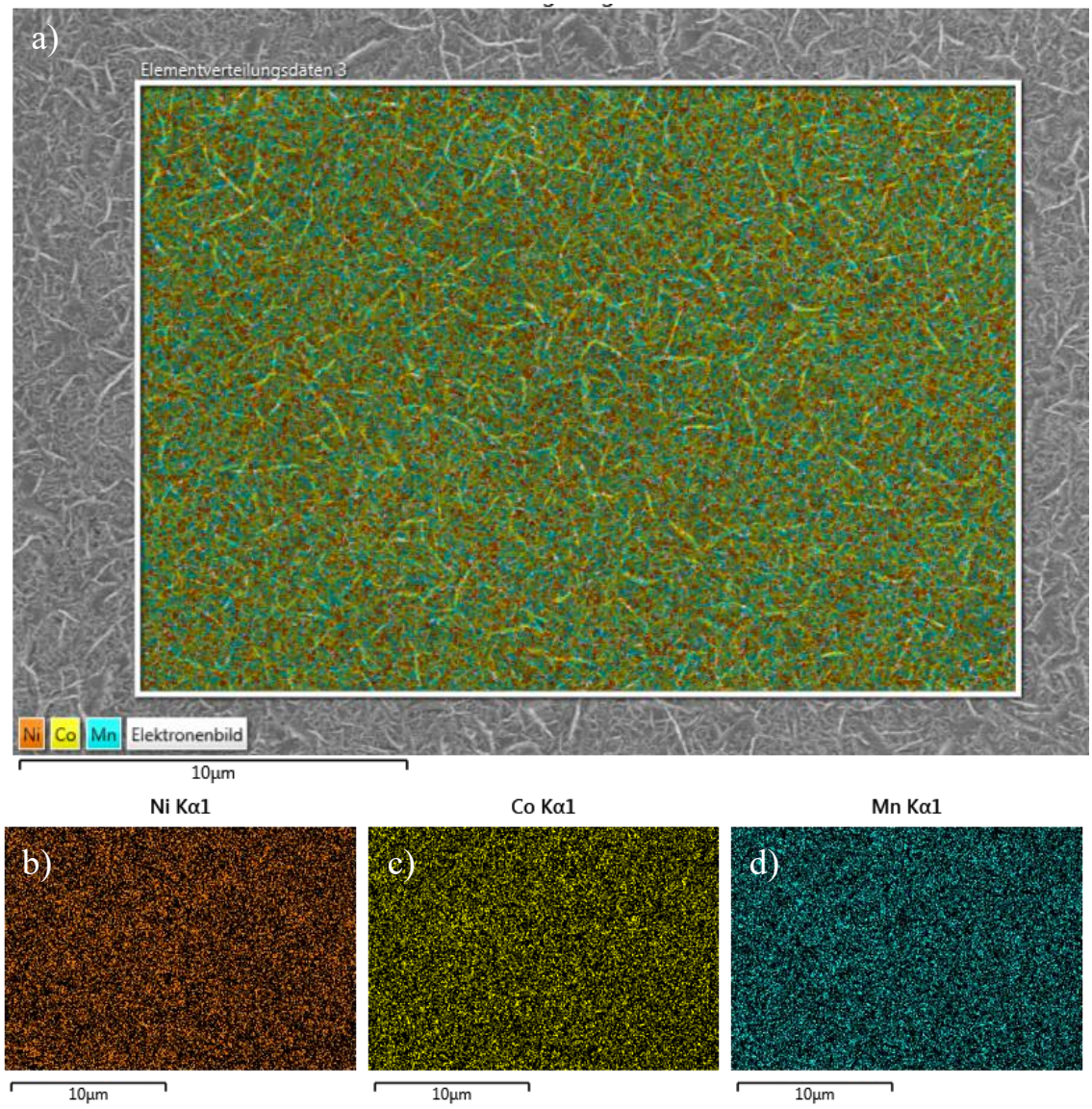

Figure S 6.6: EDX elemental maps of NCM333 in the SEM. Overlay (a) of the Ni (b), Co (c) and Mn (d) maps.

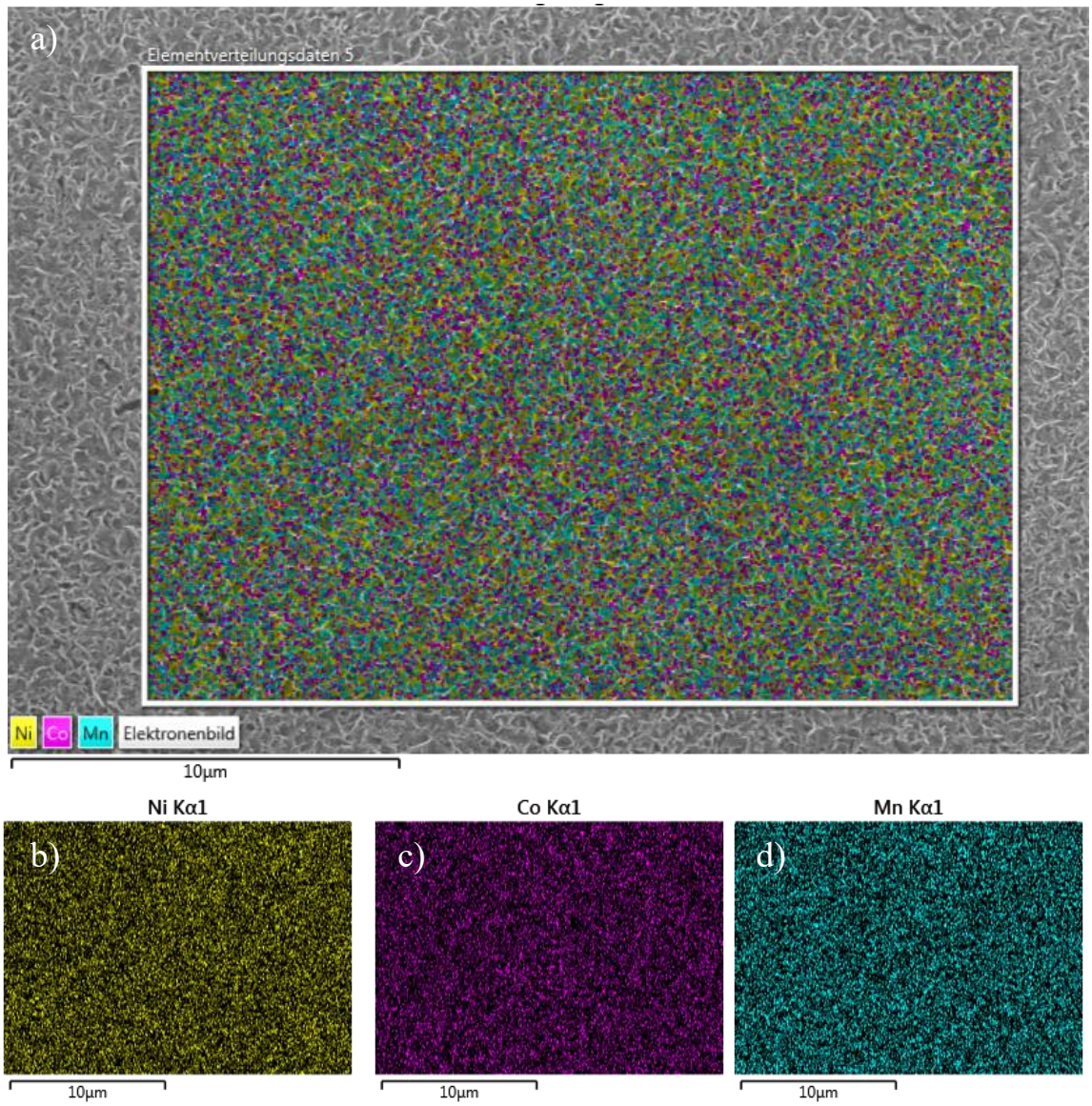

Figure S 6.7: EDX elemental maps of NCM523 in the SEM. Overlay (a) of the Ni (b), Co (c) and Mn (d) maps.

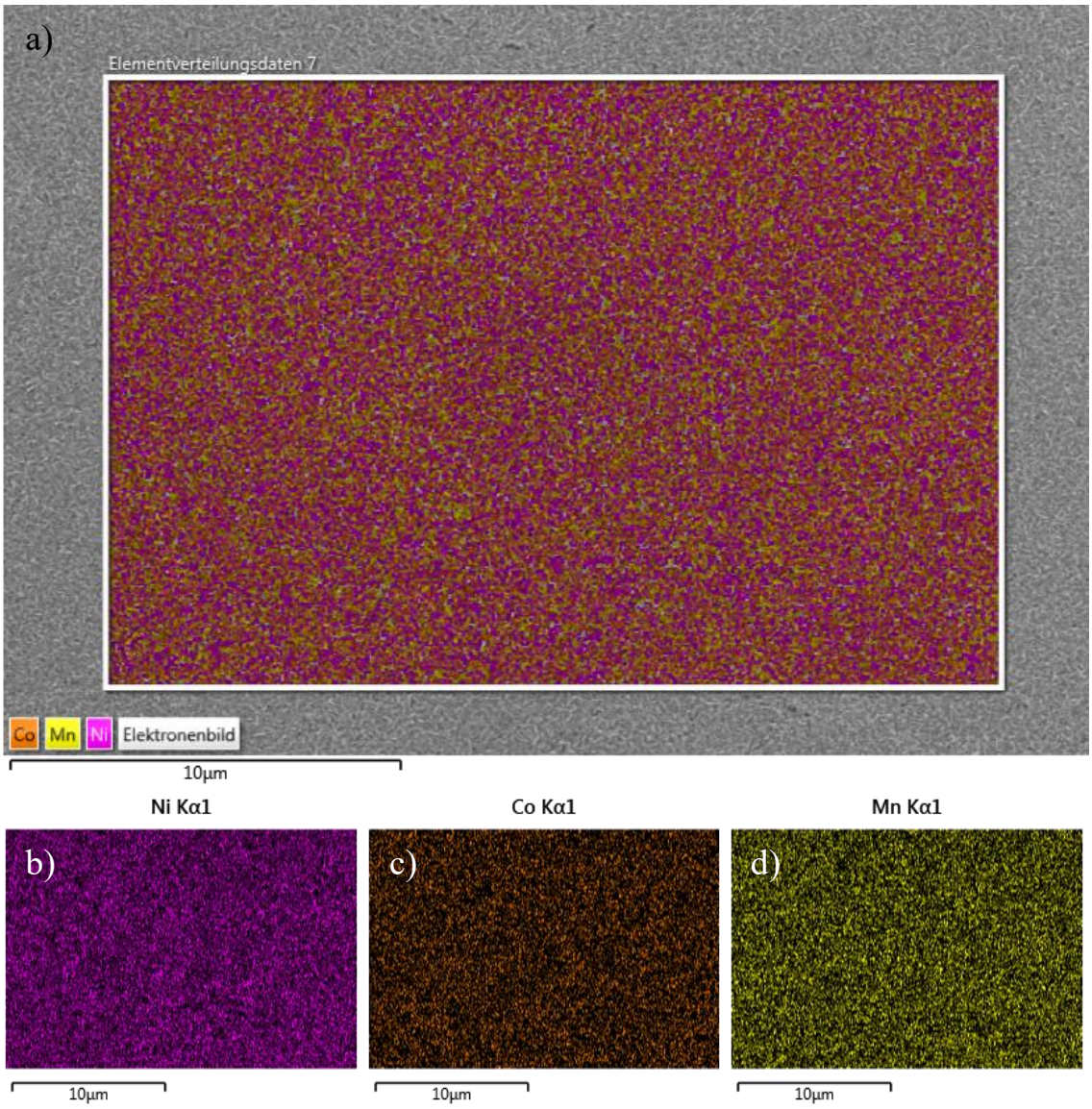

Figure S 6.8: EDX elemental maps of NCM613 in the SEM. Overlay (a) of the Ni (b), Co (c) and Mn (d) maps.

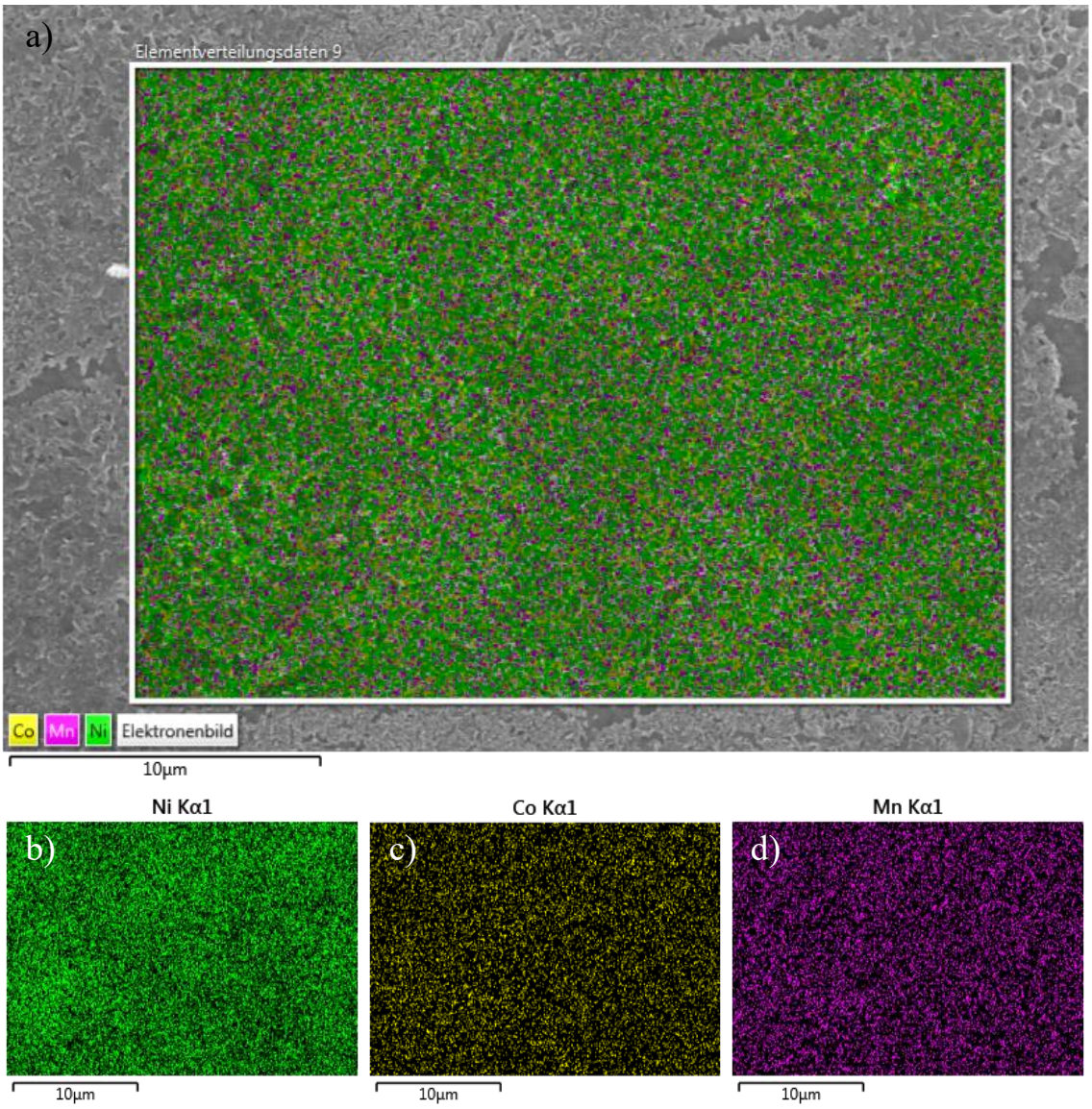

Figure S 6.9: EDX elemental maps of NCM811 in the SEM. Overlay (a) of the Ni (b), Co (c) and Mn (d) maps.

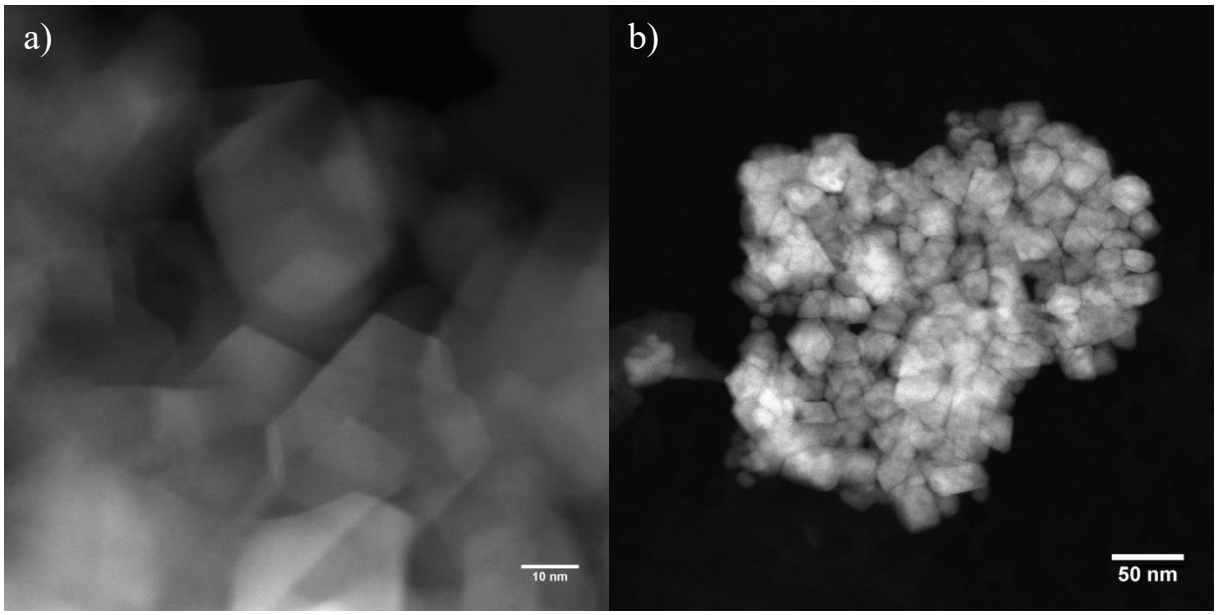

Figure S 6.10: STEM images of square-like nanoparticles of NCM333 (a) and NCM523 (b).

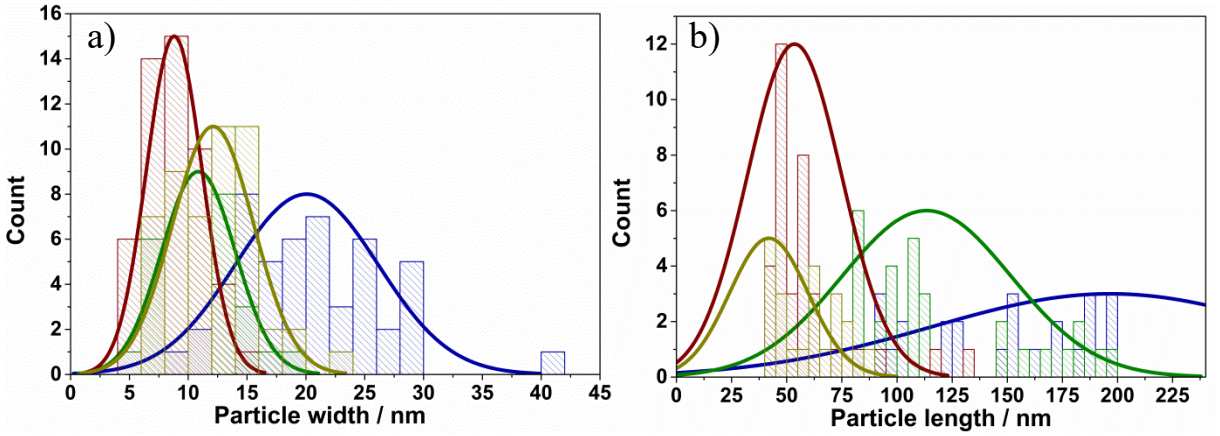

Figure S 6.11: Widths (a) and lengths (b) of NCM333 (blue), NCM523 (green), NCM613 (red) and NCM811 (dark yellow) rod-like nanoparticles obtained by measurement of 50 particles each in STEM images. For the width and length determination of NCM523 (green) 40 particles were measured.

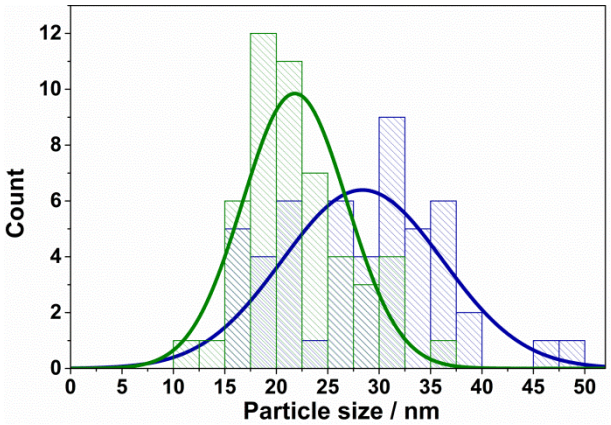

Figure S 6.12: Sizes of NCM333 (blue) and NCM523 (green) square-like nanoparticles obtained by measurement of 50 particles each in STEM images.

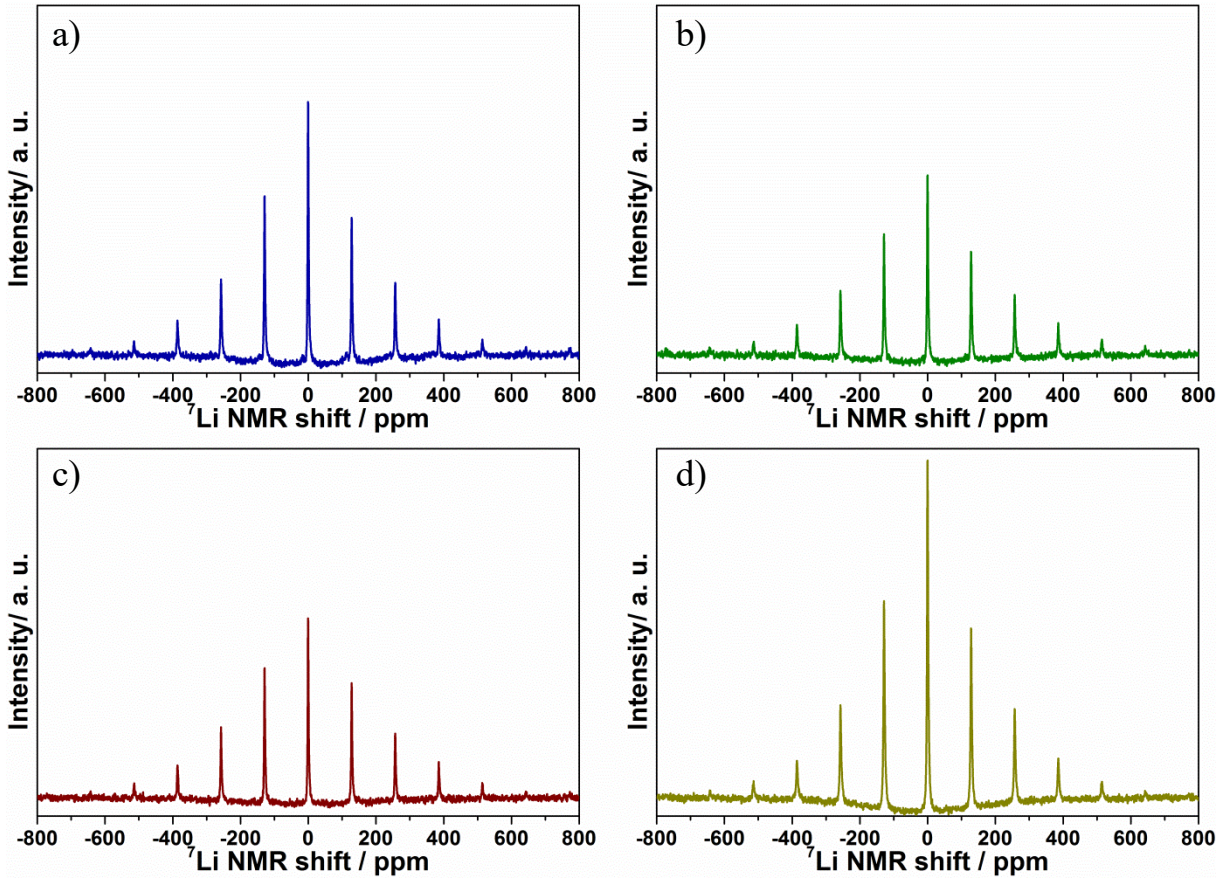

Figure S 6.13: ^{7}Li solid state MAS-NMR of NCM333 (a), NCM523 (b), NCM613 (c) and NCM811 (d) nanoparticles.

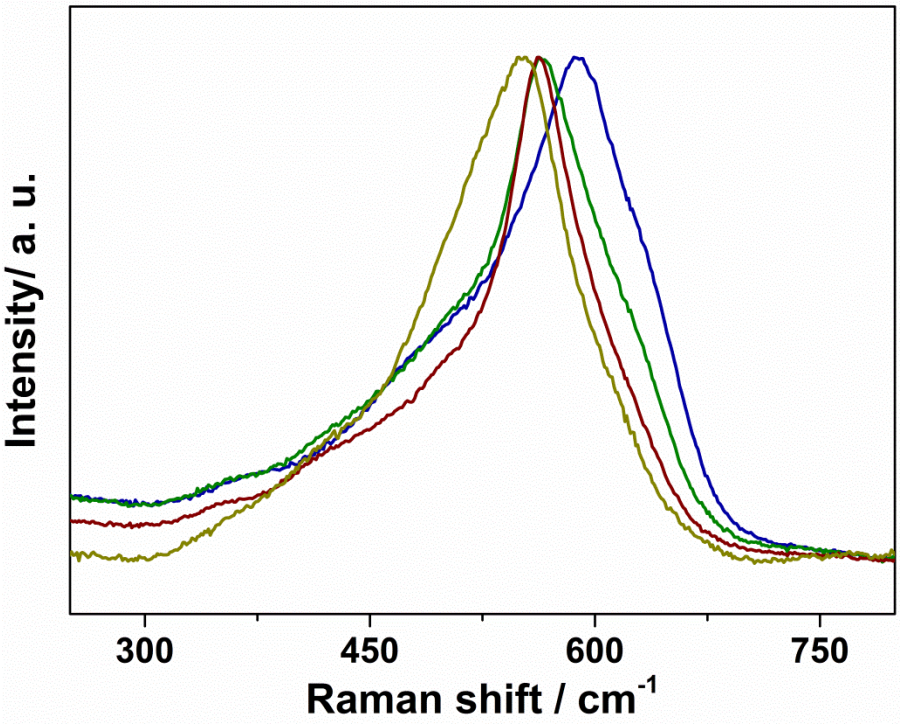

Figure S 6.14: Raman spectra of NCM333 (blue), NCM523 (green), NCM613 (red) and NCM811 (dark yellow) nanoparticles.

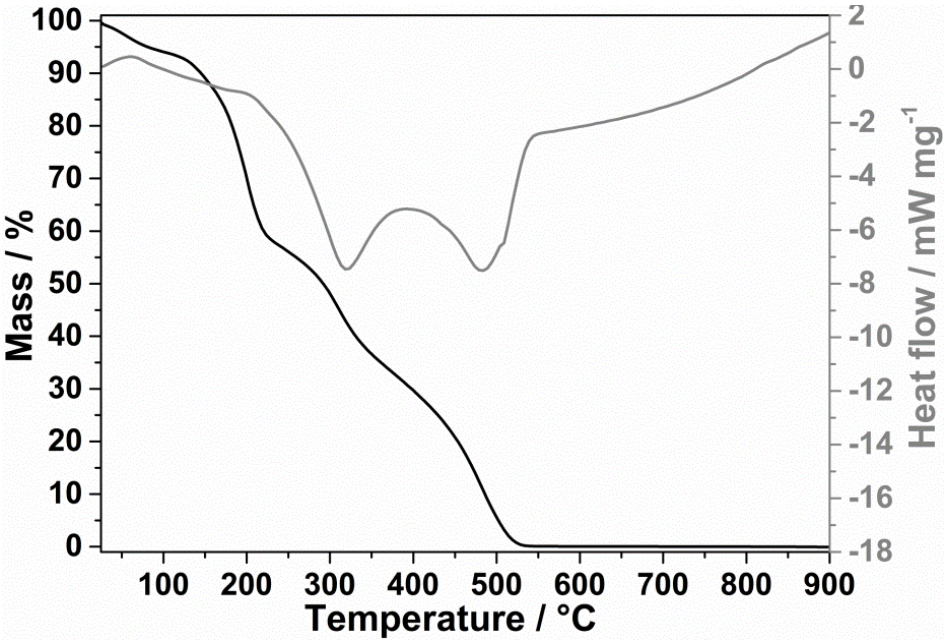

Figure S 6.15: TGA (left y-axis) and DSC (right y-axis) of pure NCC in air.

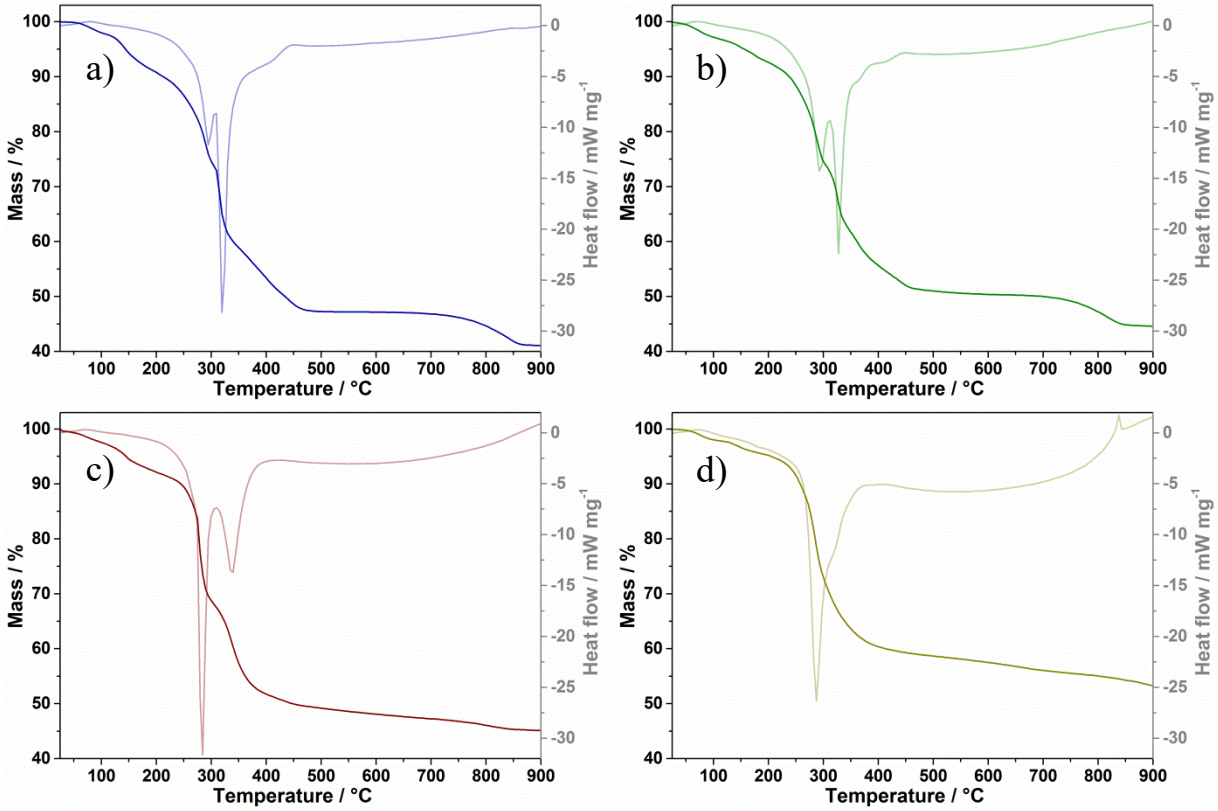

Figure S 6.16: TGA (left y-axis) and DSC (right y-axis) of the as-prepared pre-NCM333 (a), pre-NCM523 (b), pre-NCM613 (c) and pre NCM811 (d) nanoparticles in air.

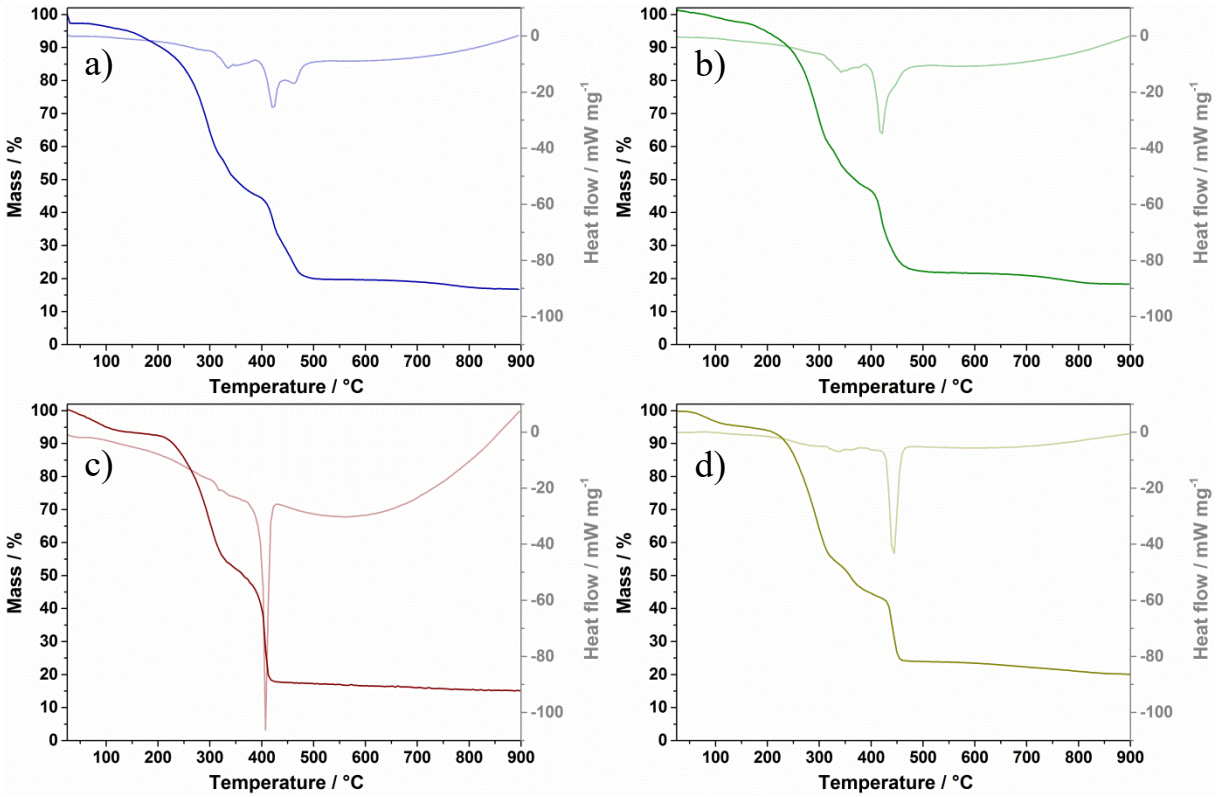

Figure S 6.17: TGA (left y-axis) and DSC (right y-axis) of the as-prepared pre-NCM333 (a), pre-NCM523 (b), pre-NCM613 (c) and pre NCM811 (d) nanoparticles each mixed with NCC. The combustion process was performed in air.

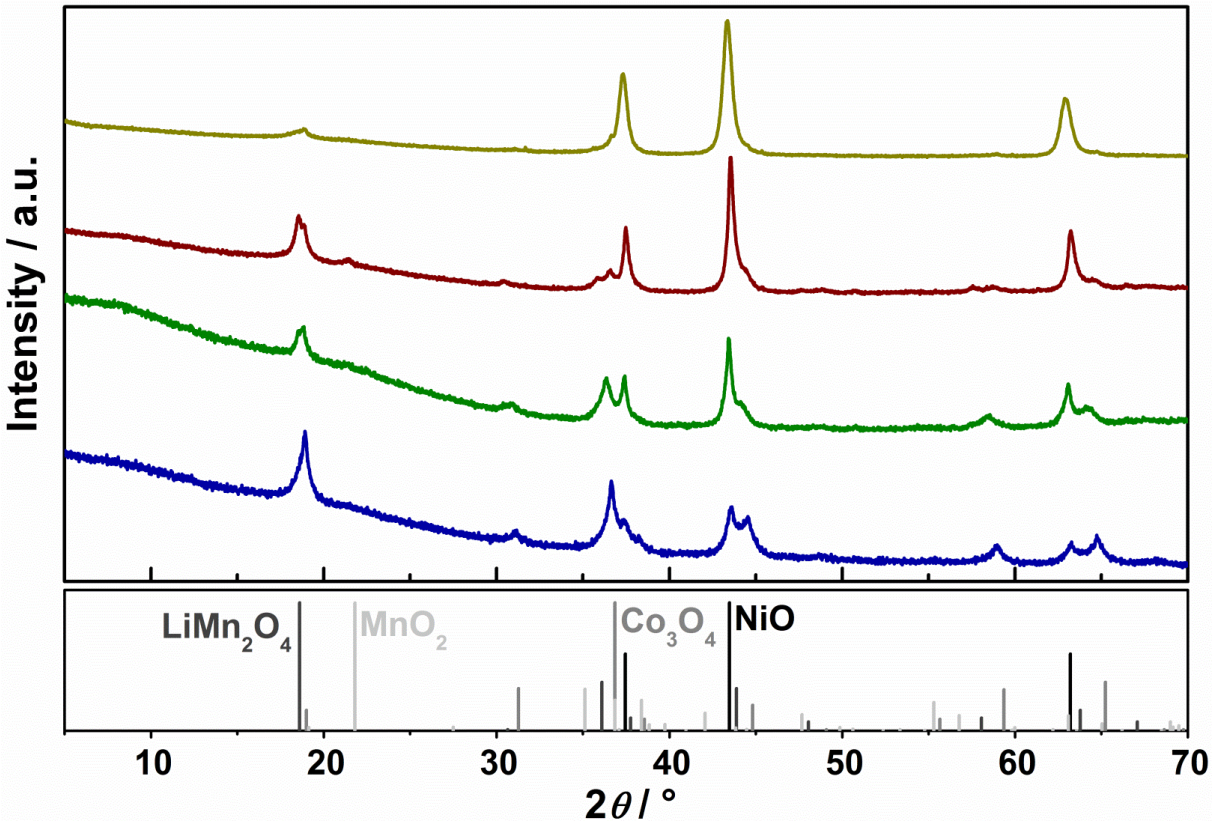

Figure S 6.18: XRDs of the products after calcination of pre-NCM333 (blue), pre-NCM523 (green), pre-NCM613 (red) and pre-NCM811 (dark yellow) in comparison with ICDD card 00-001-1239 of NiO, ICDD card 00-043-1003 of Co_3O_4, ICDD card 00-035-0782 of $LiMn_2O_4$ and ICDD card 01-073-1539 of MnO_2.

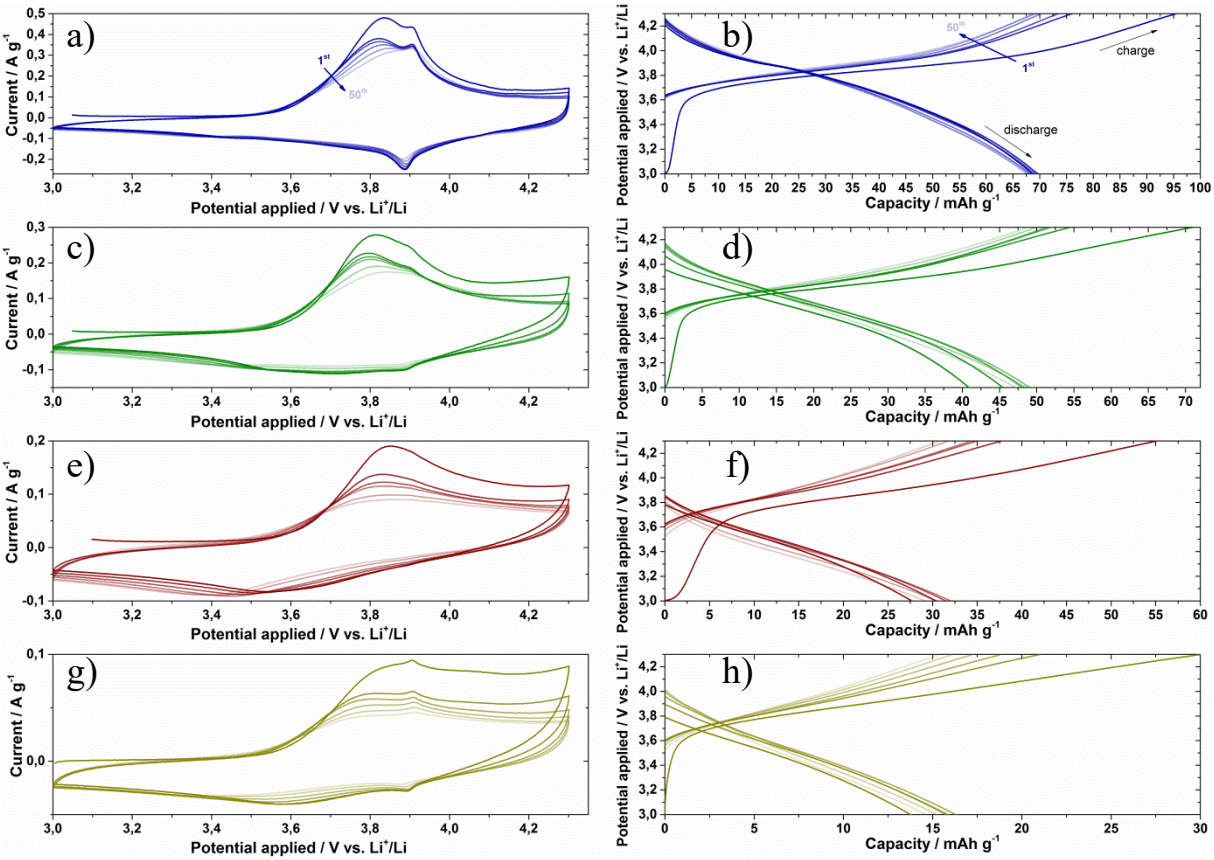

Figure S 6.19: CVs at a scan speed of 0.5 mV s^{-1} (a, c, e, g) and derived from those, the integrated capacities (b, d, f, h) of NCC-templated desert-rose-like NCM333 (a, b), NCM 523 (c, d), NCM613 (e, f) and NCM811 (g, h). Depicted are the 1st, 2nd, 5th, 10th, 25th and 50th cycle, respectively, and with more transparent color at the higher cycle numbers.

6.7 References

[1] K. Mizushima, P. C. Jones, P. J. Wiseman, J. B. Goodenough. *Materials Research Bulletin* **1980**, *15*, 783-789.
[2] K. Ozawa. *Solid State Ionics* **1994**, *69*, 212-221.
[3] G. E. Blomgren. *Journal of The Electrochemical Society* **2017**, *164*, A5019-A5025.
[4] M. Ma, N. A. Chernova, B. H. Toby, P. Y. Zavalij, M. S. Whittingham. *Journal of Power Sources* **2007**, *165*, 517-534.
[5] M. Sathiya, G. Rousse, K. Ramesha, C. P. Laisa, H. Vezin, M. T. Sougrati, *et al. Nat Mater* **2013**, *12*, 827-835.
[6] Y. Wang, J. Jiang, J. R. Dahn. *Electrochemistry Communications* **2007**, *9*, 2534-2540.
[7] J. W. Fergus. *Journal of Power Sources* **2010**, *195*, 939-954.
[8] X. Xu, S. Lee, S. Jeong, Y. Kim, J. Cho. *Materials Today* **2013**, *16*, 487-495.
[9] Y. Tang, Y. Zhang, W. Li, B. Ma, X. Chen. *Chemical Society Reviews* **2015**, *44*, 5926-5940.
[10] M. Park, X. Zhang, M. Chung, G. B. Less, A. M. Sastry. *Journal of Power Sources* **2010**, *195*, 7904-7929.
[11] K. M. Shaju, G. V. Subba Rao, B. V. R. Chowdari. *Electrochimica Acta* **2002**, *48*, 145-151.
[12] S. H. Kang, J. Kim, M. E. Stoll, D. Abraham, Y. K. Sun, K. Amine. *Journal of Power Sources* **2002**, *112*, 41-48.
[13] P. M. Zehetmaier, A. Cornélis, B. Böller, A. Wisnet, T. Bein, D. Fattakhova-Rohlfing. *manuscript in preparation*.
[14] J. M. Szeifert, J. M. Feckl, D. Fattakhova-Rohlfing, Y. Liu, V. Kalousek, J. Rathousky, T. Bein. *J Am Chem Soc* **2010**, *132*, 12605-12611.
[15] J. M. Feckl, K. Fominykh, M. Döblinger, D. Fattakhova-Rohlfing, T. Bein. *Angewandte Chemie International Edition* **2012**, *51*, 7459-7463.
[16] F. Zoller, K. Peters, P. M. Zehetmaier, P. Zeller, M. Döblinger, T. Bein, Z. k. Sofer, D. Fattakhova-Rohlfing. *Advanced Functional Materials* **2018**, *28*, 1706529.
[17] Z.-D. Huang, X.-M. Liu, S.-W. Oh, B. Zhang, P.-C. Ma, J.-K. Kim. *Journal of Materials Chemistry* **2011**, *21*, 10777-10784.
[18] C. Yang, J. Huang, L. Huang, G. Wang. *Journal of Power Sources* **2013**, *226*, 219-222.
[19] C. Li, Q. Hou, S. Li, F. Tang, P. Wang. *Journal of Alloys and Compounds* **2017**, *723*, 887-893.
[20] X.-M. Liu, W.-L. Gao, B.-M. Ji. *Journal of Sol-Gel Science and Technology* **2012**, *61*, 56-61.
[21] K. Myoujin, T. Ogihara, N. Ogata, K. Nakane, T. Kodera, S. Omura, M. Uede, K. Higeta. *Key Engineering Materials* **2006**, *320*, 255-258.
[22] J. Zhu, K. Yoo, A. Denduluri, W. Hou, J. Guo, D. Kisailus. *Journal of Materials Research* **2014**, *30*, 286-294.
[23] F. Wu, M. Wang, Y. Su, L. Bao, S. Chen. *Journal of Power Sources* **2010**, *195*, 2362-2367.
[24] J. Xie, X. Huang, Z. Zhu, J. Dai. *Ceramics International* **2010**, *36*, 2485-2487.
[25] C.-H. Lu, Y.-K. Lin. *Journal of Power Sources* **2009**, *189*, 40-44.
[26] S. Patoux, M. M. Doeff. *Electrochemistry Communications* **2004**, *6*, 767-772.
[27] W. D. Johnston, R. R. Heikes, D. Sestrich. *Journal of Physics and Chemistry of Solids* **1958**, *7*, 1-13.

[28] J. van Elp, J. Wieland, H. Eskes, P. Kuiper, G. Sawatzky, F. de Groot, T. Turner. *Physical Review B* **1991**, *44*, 6090-6103.
[29] M. Antaya, K. Cearns, J. S. Preston, J. N. Reimers, J. R. Dahn. *Journal of Applied Physics* **1994**, *76*, 2799-2806.
[30] E. Iguchi, T. Hashimoto, S. Yokoyama. *Journal of the Physical Society of Japan* **1996**, *65*, 221-229.
[31] E. Antolini. *International Journal of Inorganic Materials* **2001**, *3*, 721-726.
[32] Y. Wu, D. Pasero, E. E. McCabe, Y. Matsushima, A. R. West. *Journal of Materials Chemistry* **2009**, *19*, 1443.
[33] J. B. Goodenough, D. G. Wickham, W. J. Croft. *Journal of Physics and Chemistry of Solids* **1958**, *5*, 107-116.
[34] S. Van Houten. *Journal of Physics and Chemistry of Solids* **1960**, *17*, 7-17.
[35] J. C. Danko, G. R. Kilp, H. M. Ferrari. *Solid-State Electronics* **1961**, *3*, 233-238.
[36] W. Bronger, H. Bade, W. Klemm. *Zeitschrift für anorganische und allgemeine Chemie* **1964**, *333*, 188-200.
[37] P. Kuiper, G. Kruizinga, J. Ghijsen, G. A. Sawatzky, H. Verweij. *Physical Review Letters* **1989**, *62*, 221-224.
[38] V. Berbenni, V. Massarotti, D. Capsoni, R. Riccardi, A. Marini, E. Antolini. *Solid State Ionics* **1991**, *48*, 101-111.
[39] W. Li, J. N. Reimers, J. R. Dahn. *Physical Review B* **1992**, *46*, 3236-3246.
[40] J. van Elp, H. Eskes, P. Kuiper, G. A. Sawatzky. *Physical Review B* **1992**, *45*, 1612-1622.
[41] Z. Li, C. Wang, X. Ma, L. Yuan, J. Sun. *Materials Chemistry and Physics* **2005**, *91*, 36-39.
[42] S. Holgersson, A. Karlsson. *Zeitschrift für anorganische und allgemeine Chemie* **1929**, *182*, 255-271.
[43] Y. J. Mai, J. P. Tu, X. H. Xia, C. D. Gu, X. L. Wang. *Journal of Power Sources* **2011**, *196*, 6388-6393.
[44] G. Natu, P. Hasin, Z. Huang, Z. Ji, M. He, Y. Wu. *ACS Appl Mater Interfaces* **2012**, *4*, 5922-5929.
[45] W. Du, Y. Gao, Q. Tian, D. Li, Z. Zhang, J. Guo, X. Qian. *Journal of Nanoparticle Research* **2015**, *17*, 368.
[46] T. V. Thi, A. K. Rai, J. Gim, J. Kim. *Journal of Power Sources* **2015**, *292*, 23-30.
[47] K. Fominykh, G. C. Tok, P. Zeller, H. Hajiyani, T. Miller, M. Döblinger, R. Pentcheva, T. Bein, D. Fattakhova-Rohlfing. *Advanced Functional Materials* **2017**, *27*, 1605121-n/a.
[48] C. A. BARRETT, E. B. EVANS. *Journal of the American Ceramic Society* **1964**, *47*, 533-533.
[49] W. Wei, W. Chen, D. G. Ivey. *Chemistry of Materials* **2008**, *20*, 1941-1947.
[50] E. McCalla, J. R. Dahn. *Solid State Ionics* **2013**, *242*, 1-9.
[51] J. M. Szeifert, D. Fattakhova-Rohlfing, D. Georgiadou, V. Kalousek, J. Rathouský, D. Kuang, S. Wenger, S. M. Zakeeruddin, M. Grätzel, T. Bein. *Chemistry of Materials* **2009**, *21*, 1260-1265.
[52] Y. Liu, J. M. Szeifert, J. M. Feckl, B. Mandelmeier, J. Rathousky, O. Hayden, D. Fattakhova-Rohlfing, T. Bein. *ACS Nano* **2010**, *4*, 5373-5381.
[53] K. Fominykh, J. M. Feckl, J. Sicklinger, M. Döblinger, S. Böcklein, J. Ziegler, L. Peter, J. Rathousky, E.-W. Scheidt, T. Bein, D. Fattakhova-Rohlfing. *Advanced Functional Materials* **2014**, *24*, 3123-3129.
[54] Y. Liu, K. Peters, B. Mandlmeier, A. Müller, K. Fominykh, J. Rathousky, C. Scheu, D. Fattakhova-Rohlfing. *Electrochimica Acta* **2014**, *140*, 108-115.

[55] J. M. Feckl, H. K. Dunn, P. M. Zehetmaier, A. Müller, S. R. Pendlebury, P. Zeller, *et al.* *Advanced Materials Interfaces* **2015**, *2*, 1500358-n/a.
[56] K. Fominykh, P. Chernev, I. Zaharieva, J. Sicklinger, G. Stefanic, M. Döblinger, A. Müller, A. Pokharel, S. Böcklein, C. Scheu, T. Bein, D. Fattakhova-Rohlfing. *ACS Nano* **2015**, *9*, 5180-5188.
[57] K. Peters, P. Zeller, G. Stefanic, V. Skoromets, H. Němec, P. Kužel, D. Fattakhova-Rohlfing. *Chemistry of Materials* **2015**, *27*, 1090-1099.
[58] M. C. Biesinger, B. P. Payne, A. P. Grosvenor, L. W. M. Lau, A. R. Gerson, R. S. C. Smart. *Applied Surface Science* **2011**, *257*, 2717-2730.
[59] B. Rivas-Murias, V. Salgueiriño. *Journal of Raman Spectroscopy* **2017**, *48*, 837-841.
[60] N. Mironova-Ulmane, A. Kuzmin, M. Grube. *Journal of Alloys and Compounds* **2009**, *480*, 97-99.
[61] N. Mironova-Ulmane, A. Kuzmin, I. Steins, J. Grabis, I. Sildos, M. Pärs. *Journal of Physics: Conference Series* **2007**, *93*, 012039.
[62] L. D. L. S. Valladares, A. Ionescu, S. Holmes, C. H. W. Barnes, A. B. Domínguez, O. A. Quispe, J. C. González, S. Milana, M. Barbone, A. C. Ferrari, H. Ramos, Y. Majima. *Journal of Vacuum Science & Technology B* **2014**, *32*, 051808.
[63] K. Ramesh, L. Chen, F. Chen, Y. Liu, Z. Wang, Y.-F. Han. *Catalysis Today* **2008**, *131*, 477-482.
[64] J. B. Wang, G. J. Huang, X. L. Zhong, L. Z. Sun, Y. C. Zhou, E. H. Liu. *Applied Physics Letters* **2006**, *88*, 252502.
[65] S. Muto, K. Tatsumi. *Microscopy* **2017**, *66*, 39-49.
[66] Y. Habibi, L. A. Lucia, O. J. Rojas. *Chem Rev* **2010**, *110*, 3479-3500.
[67] A. Dufresne. *Materials Today* **2013**, *16*, 220-227.
[68] A. Ivanova, D. Fattakhova-Rohlfing, B. E. Kayaalp, J. Rathouský, T. Bein. *J Am Chem Soc* **2014**, *136*, 5930-5937.
[69] A. Ivanova, K. Fominykh, D. Fattakhova-Rohlfing, P. Zeller, M. Döblinger, T. Bein. *Inorg Chem* **2015**, *54*, 1129-1135.
[70] A. Ivanova, M. C. Fravventura, D. Fattakhova-Rohlfing, J. Rathouský, L. Movsesyan, P. Ganter, T. J. Savenije, T. Bein. *Chemistry of Materials* **2015**, *27*, 6205-6212.
[71] E. Dujardin, M. Blaseby, S. Mann. *Journal of Materials Chemistry* **2003**, *13*, 696-699.
[72] D. Klemm, F. Kramer, S. Moritz, T. Lindström, M. Ankerfors, D. Gray, A. Dorris. *Angewandte Chemie International Edition* **2011**, *50*, 5438-5466.
[73] C. Julien. *Solid State Ionics* **2000**, *136-137*, 887-896.
[74] M. Inaba, Y. Iriyama, Z. Ogumi, Y. Todzuka, A. Tasaka. *Journal of Raman Spectroscopy* **1997**, *28*, 613-617.
[75] S.-J. Hwang, H.-S. Park, J.-H. Choy, G. Campet, J. Portier, C.-W. Kwon, J. Etourneau. *Electrochemical and Solid-State Letters* **2001**, *4*, A213-A216.
[76] A. M. Hashem, R. S. El-Taweel, H. M. Abuzeid, A. E. Abdel-Ghany, A. E. Eid, H. Groult, A. Mauger, C. M. Julien. *Ionics* **2012**, *18*, 1-9.
[77] L.-j. Li, X.-h. Li, Z.-x. Wang, H.-j. Guo, P. Yue, W. Chen, L. Wu. *Powder Technology* **2011**, *206*, 353-357.
[78] H.-J. Noh, S. Youn, C. S. Yoon, Y.-K. Sun. *Journal of Power Sources* **2013**, *233*, 121-130.
[79] S.-K. Jung, H. Gwon, J. Hong, K.-Y. Park, D.-H. Seo, H. Kim, J. Hyun, W. Yang, K. Kang. *Advanced Energy Materials* **2014**, *4*, 1300787.
[80] C. Zhang, M. Liu, G. Pan, S. Liu, D. Liu, C. Chen, J. Su, T. Huang, A. Yu. *ACS Applied Energy Materials* **2018**, *1*, 4374-4384.

[81] ICDD card No. 00-043-1003
[82] T. Ohzuku, A. Ueda, M. Nagayama. *Journal of The Electrochemical Society* **1993**, *140*, 1862-1870.
[83] T. Ohzuku, A. Ueda, M. Nagayama, Y. Iwakoshi, H. Komori. *Electrochimica Acta* **1993**, *38*, 1159-1167.
[84] J. R. Dahn, U. von Sacken, C. A. Michal. *Solid State Ionics* **1990**, *44*, 87-97.
[85] X. M. Dong, T. Kimura, J.-F. Revol, D. G. Gray. *Langmuir* **1996**, *12*, 2076-2082.

7 Conclusion and Outlook

The objective of this thesis was the extension of the solvothermal *tert*-butanol route towards multinary metal oxide nanoparticles with sizes down to 1 nm. Due to the small size and the high dispersibility all the different metal oxide nanoparticles could be used for energy applications, in particular electrochemical energy storage.

In Chapter 3 we discuss the synthesis of Co_3O_4 nanoparticles that were further used in a water splitting experiment to suppress the electron hole recombination at the hematite surface. Since the time scale of recombination is extended up to milliseconds and even seconds, almost five times higher photocurrents were measured in comparison to untreated hematite.

In Chapter 4 antimony-doped tin oxide (ATO) nanoparticles were grown on reduced graphene oxide, building up nanocomposites that were then tested as active anode materials in lithium ion batteries. The nanocomposites exhibited very good electrical conductivity as well as a good buffering of the drastic volume changes during the electrochemically induced conversion and lithium alloying/de-alloying reactions. Thus, the electrochemistry of the nanocomposite consisting of ATO and reduced graphene oxide becomes completely reversible, and furthermore the processes were accelerated due to the nanosizing.

Chapter 5 and Chapter 6 cover the syntheses of lithium containing cathode materials for lithium ion batteries. Chapter 5 deals with the two-step synthesis of $LiCoO_2$, where in the first step the pseudo-binary metal oxide $Li_{0.15}Co_{0.85}O$ was produced *via* the solvothermal approach in *tert*-butanol. Subsequently, in the second step the previous reaction product was calcined together with the block-copolymer Pluronic F127 to form nanostructured $LiCoO_2$ with improved capacity retention at exceedingly high charging/discharging rates.

In the project described in Chapter 6 we have demonstrated that the two-step synthesis procedure described in the previous chapter could be generalized and extended for the first time to a pseudo-quaternary system consisting of lithium, nickel, cobalt and manganese. Here, dispersible nanoparticles in a size range of 1-4 nm of four different compounds of the type $Li_wNi_xCo_yMn_zO$ adopting the cubic rock-salt structure were synthesized as intermediates. Calcination of the as-prepared intermediate products together with nanocellulose used as a microstructure-directing template led to the formation of desert-rose nanostructured $Li(Ni_xCo_yMn_z)O_2$ with the respective

compositions. This specific nanostructure enabled still reasonably large specific capacities even at charging/discharging times of 60 s, although rising nickel content favored cation mixing of lithium and nickel and therefore reduced the specific capacities.

In conclusion, we have extended the already existing solvothermal *tert*-butanol synthesis route to fabricate different multinary, up to pseudo-quaternary metal oxide nanoparticles. The nanocrystals were ultrasmall, below 7 nm, highly dispersible and were therefore used to build up nanostructures with the help of combustible surfactants or in nanocomposite materials. Except Co_3O_4, which was successfully tested as a co-catalyst in electrochemical water splitting, all other synthesized materials in this thesis were investigated with respect to their electrochemical energy storage performance as active electrode materials in lithium ion batteries.

Possible future work could focus on the syntheses of further multinary metal oxide nanoparticles and a targeted distribution of single ions on specific crystal sites. To achieve this, further insights have to be gained about the mechanisms forming the nanocrystals during the synthesis. Additional efforts should focus on introducing novel composite systems in which the individual materials can interact in synergy, yielding higher performance for better batteries.